

UNIVERSITY OF SOUTHAMPTON

Power Scaling of Tm:YLF-pumped Ho:YAG Lasers

by

Sik So

A thesis submitted in partial fulfillment for the
degree of Doctor of Philosophy

in the
Faculty of Engineering, Science and Mathematics
Optoelectronics Research Center

December 2007

Declaration of Authorship

I, Sik So, declare that this thesis titled, ‘Power Scaling of Tm:YLF-pumped Ho:YAG Lasers’ and the work presented in it are my own. I confirm that:

- This work was done wholly or mainly while in candidature for a research degree at this University
- Where any part of this thesis has previously been submitted for a degree or any other qualification at this University or any other institution, this has been clearly stated
- Where I have consulted the published work of others, this is always clearly attributed
- Where I have quoted from the work of others, the source is always given. With the exception of such quotations, this thesis is entirely my own work
- I have acknowledged all main sources of help
- Where the thesis is based on work done by myself jointly with others, I have made clear exactly what was done by others and what I have contributed myself

Signed:

Date:

UNIVERSITY OF SOUTHAMPTON

Abstract

Faculty of Engineering, Science and Mathematics
Optoelectronics Research Center

Doctor of Philosophy

by Sik So

Reported in this thesis are methodologies for power-scaling Ho:YAG lasers for both the continuous-wave (CW) and Q-switched regime. Advancement in Ho:YAG laser power is made possible through the improvements in output power of the Tm:YLF pump lasers. The slab geometry provides good thermal management characteristics which helps to overcome the limitations set by the thermally-induced stress fracture when scaling output power of Tm:YLF lasers. In conjunction with the use of novel holmium cavity designs that allow the use of slab pump lasers, high-power Ho:YAG lasers are realised.

Conflicting requirements on the thulium doping concentration in Tm:YLF provided motivation for the preliminary experiments of laser performance characterisation to find the optimum doping concentration. The optimum doping concentration is defined as that which gives the highest output power before fracture. These experiments show that 2 at.% is the optimum thulium doping concentration, which is then used with the slab geometry to demonstrate 100 W of high M^2 thulium output.

Two different Ho:YAG cavity designs are detailed that make use of the power-scaled Tm:YLF slab pump lasers. An intra-cavity side-pumping scheme involves the Tm:YLF slab laser side-pumping a Ho:YAG slab laser within its own cavity. This simple and compact resonator design allows efficient operation of the holmium laser. An output power of 13 W was obtained at an incident diode power of 200 W with an M^2 of 140×1.7 . The slope efficiency was nearly 16 % with respect to the diode incident power, with a lasing wavelength of 2097 nm. The second cavity design used for the Ho:YAG laser is an external end-pumping arrangement. A pump-guiding rod was employed in order to minimise the pump size, and thus threshold, and allow the use of spatially multiplexed pump lasers. A maximum output power of 38 W was achieved at an incident thulium pump power of ~ 70 W with an M^2 of 18.3×3.3 . The slope efficiency was 61 % with respect to the thulium incident power, and the lasing wavelength was 2090 nm. Pulse energies as high as 14 mJ were achieved when Q-switched at 20 Hz, with a pulse duration of 17 ns. Further future improvements in output power and beam quality are also discussed.

Acknowledgements

Firstly, I would like to thank my supervisors, Prof. David Shepherd, Prof. Andy Clarkson, for their continual support, guidance and patience throughout my studies in the ORC. I would like to particularly thank my post-doc, Dr. Jacob Mackenzie for all the effort and patience used in guiding and teaching me. Without his help, I could never have finished my work. I would like to thank members of the Advance Solid-State Sources group for the many helpful discussion and advice, especially Dr. Deyuan Shen, Dr. Ji Won Kim and Dr. Pu Wang.

Thank you Simon Butler, Timothy McIntyre and Chris Nash for all the technical advice and support, as well as the bits and pieces made for my experiments along with the fun during the years. I would like to thank Dr Eleanor Tarbox for the guidance and support especially with the help on my thesis writing. Thank you to all the ORC stuff such as Eveline Smith, Jenny Morley, Dina Smith for the helpful support. Thank you Arthur Longhurst, David Oliver and Kevin Sumner for their help in solving my computer problems. Thank you Lee Whitelock with my purchase orders and patients with my enquiries. Thank you to all the members in the ORC with whom I have had fun and pints with and ones whom I share my office with in particular: Mark Darby, Vincent Tse, Fei He, Weijia Yang, Andy Piper, Jing Wang, Ian Wellington, Ed Aronson, Robert Simpson, Tipsuda Chaipiboonwong, Chun Tian, Hazel Hung, David Banks, Jaclyn Chan, Lee Pearson.

I acknowledge QinetiQ for their financial and resource support that makes the project possible. I also acknowledge the EPSRC studentship that I received throughout my research studies. There are many others who have contributed to this work which I might have left out. I would like to thank them for their support.

Finally I have to say a big thank you to my family who have support me throughout my life, particularly my Mum, Dad and brother. I would also like to thank my fiancée Slaker Cheung for all her support and care. Oh, and my dog Bobby...

Peace,

Sik So (Matthew)

Contents

Abstract	ii
Acknowledgements	iii
List of Figures	vii
List of Tables	ix
1 Introduction	1
1.1 Topic overview	1
1.2 Background	3
1.2.1 History	3
1.2.2 Comparison of different laser architectures	4
1.2.2.1 Co-doping	4
1.2.2.2 Intra-cavity pumping	5
1.2.2.3 Externally pumped with a separate laser	6
1.3 Power-scaling method investigated	8
1.3.1 Intra-cavity side-pumping	9
1.3.2 External end-pumping pump-guided Ho:YAG rod	10
1.4 Synopsis	11
2 Tm:YLF rod laser characterisation	13
2.1 Spatial rate equation model	15
2.2 Energy-transfer upconversion, cross-relaxation and quantum yield	16
2.2.1 Energy-transfer upconversion	16
2.2.2 Cross-relaxation	18
2.2.3 Quantum yield	19
2.3 Energy-transfer upconversion and cross-relaxation modelling	20
2.3.1 Effect of energy-transfer upconversion on laser performance	20
2.3.2 Effect of cross-relaxation on laser performance	22
2.4 Thermally induced stress fracture	23
2.5 Tm:YLF laser characterisation setup	24
2.6 Laser characterisation and analysis	26
2.6.1 Slope efficiency and quantum yield	28
2.6.2 Threshold and upconversion rate	29
2.7 Power limit	30

2.8	Gain medium geometry	32
2.9	Conclusion	33
3	Power scaling of end-pumped Tm:YLF slab lasers	34
3.1	Plane-wave analysis	35
3.1.1	Single-pass absorption	36
3.1.2	Rate of excitation	38
3.1.3	Single-pass emission	38
3.1.4	Rate of de-excitation	39
3.1.5	Steady-state operation	40
3.1.6	Excited ion population at threshold	40
3.1.7	Output channels	41
3.2	Experimental setup	42
3.2.1	Pump configurations	42
3.2.1.1	Single diode stack pumping	43
3.2.1.2	Spatially multiplexed diode stack pumping	45
3.2.2	Laser configuration	47
3.2.3	Slab aspect ratio considerations	49
3.3	Power-scaling of the single-slab geometry	50
3.4	Power-scaling of a two-slab Tm:YLF laser	56
3.5	Tm:YLF fracture limit	58
3.6	Conclusion	59
4	Intra-cavity side-pumping	61
4.1	Intra-cavity side-pumped plane-wave analysis	62
4.1.1	Absorption	65
4.1.2	Emission	68
4.1.3	Rate of excitation and de-excitation	70
4.1.4	Equating excitation and de-excitation rate	71
4.2	Laser design	72
4.2.1	Gain and absorption for different holmium output coupler reflectivities	73
4.2.2	Holmium cavity optimisation	75
4.2.3	Optimisation of the Ho:YAG slab design	78
4.3	Intra-cavity side-pumping experimental setup	78
4.3.1	Pump laser	79
4.3.2	Holmium cavity	80
4.4	Intra-cavity side-pumped Ho:YAG experimental results	80
4.5	Laser result discussion and modelling	84
4.6	Second threshold condition	85
4.7	Conclusion	87
5	Externally-pumped Ho:YAG laser	88
5.1	Externally-pumped Ho:YAG laser cavity	89
5.1.1	Pump configuration	89
5.1.2	Thulium pump	90
5.1.3	Ho:YAG laser	91

5.2	Laser characterisation with focused y-axis thulium pump beam	93
5.3	Laser characterisation with collimated y-axis thulium pump beam	96
5.4	Plane-plane mirror cavity	97
5.5	Intra-cavity and external-pumping comparison	100
5.6	Conclusion	102
6	A Q-switched Ho:YAG laser pumped by Tm:YLF slab lasers	104
6.1	Q-switching theory	105
6.2	Q-switching method	108
6.3	Q-switching experimental setup	109
6.3.1	Pump configuration	110
6.3.2	Holmium cavity configuration	110
6.3.2.1	Laser cavity for CW performance characterisation	110
6.3.2.2	Laser cavity for Q-switching	111
6.4	CW performance comparison for different holmium rods	112
6.5	CW performance comparison for different intra-cavity elements	112
6.6	Q-switching performance discussion	114
6.7	Scaling prediction	119
6.8	Conclusion	120
7	Conclusions	121
7.1	Summary of work presented	121
7.1.1	Tm:YLF pump laser design	121
7.1.2	Intra-cavity side-pumping	123
7.1.3	External pumping and Q-switching	123
7.2	Future work	124
7.2.1	Power-scaling Ho:YAG lasers	125
7.2.1.1	Power-scaling Ho:YAG laser through spatially multiplex	125
7.2.1.2	Power-scaling Tm:YLF slab pump lasers	125
7.2.2	Slab lasers with good beam quality	126
A	Rate equation model	128
B	Publication list	136
B.1	Journal publications	136
B.2	Conference publications	136
	References	137

List of Figures

1.1	Schematic for diode end-pumped sensitised Ho:YAG	5
1.2	Schematic for intra-cavity end-pumping scheme	6
1.3	Schematics for external pumping	7
1.4	Schematic for intra-cavity side-pumping	10
2.1	Tm:YLF energy level diagram	17
2.2	Modelled upconversion effect	21
2.3	Modelled cross-relaxation effect	22
2.4	Pump configuration for Tm:YLF rod laser experiment	25
2.5	Laser performance for 2, 4 and 6 at.% Tm:YLF rod lasers	27
2.6	Tm:YLF emission cross-section	28
2.7	Tm:YLF rod laser operating wavelength	28
2.8	Quantum yield prediction for Tm:YLF	29
2.9	Laser performance for diode-stack-pumped Tm:YLF rod lasers	32
3.1	Slab dimensions and axes direction	36
3.2	Measured Tm:YLF absorption cross-section	44
3.3	Pump configuration for end-pumped Tm:YLF slab laser	45
3.4	Spatial beam combination setup and output profile	45
3.5	Photo of the diode box with slotted mirrors for spatial beam combination	46
3.6	Tm:YLF slab coatings reflectivity	48
3.7	Tm:YLF two-slab system	50
3.8	Measured Tm:YLF slab laser lasing wavelength (resolution: 0.2 nm) . . .	51
3.9	Laser performance of a single Tm:YLF slab laser system	52
3.10	Calculated power in different output channels	54
3.11	Experimental setup for slab laser spot size measurement	55
3.12	Measured Tm:YLF beam profile on plane input coupler	56
3.13	Laser performance of two-slab system	57
3.14	Measured temperature of heat-sink	58
3.15	Measured Tm:YLF absorption cross-section and diode wavelength	59
4.1	The axes and dimensions variables of the slabs used in the model	63
4.2	Intra-cavity elements for the laser cavity model	64
4.3	Energy level diagram of Tm:YLF and Ho:YAG	66
4.4	Effect of holmium output coupler reflectivity on gain and absorption . . .	74
4.5	Tm:YLF emission and Ho:YAG absorption cross-sections	75
4.6	Theoretical reflectivity of “edge mirror”	76
4.7	Calculated laser performance of Ho and Tm system	77

4.8	Calculated holmium laser performance vs slab width and doping	79
4.9	Intra-cavity side-pumping experimental setup	80
4.10	Ho:YAG slab design	81
4.11	Photo of intra-cavity side-pumping cavity	81
4.12	Damage on pump-reflective coatings of 2 mm thick Tm:YLF slab	82
4.13	Laser performance of the intra-cavity side-pumped Ho:YAG laser	82
4.14	Emission cross-section of Ho:YAG	83
4.15	Measured beam profile of Ho:YAG	84
4.16	Calculated passive Q-switch operating threshold equality	86
5.1	Experimental setup of pump-guiding Ho:YAG rod laser	89
5.2	Thulium pump beam propagation path in holmium rod	93
5.3	Measured Ho:YAG CW laser performance and beam profile	95
5.4	Measured collimated pump profile at pump waist	96
5.5	Measured Ho:YAG laser performance and output beam profile	97
5.6	Measured laser performance of Ho:YAG using plane-plane cavity	98
5.7	Cavity stability as a function of thermal lens	99
5.8	Output power of Ho:YAG plane plane cavity	100
6.1	Loss, inversion and output intensity under Q-switch and CW operation .	107
6.2	Q-switch cavity configuration and pumping arrangement	109
6.3	CW laser performance with 88 % reflectivity output coupler	112
6.4	CW laser performance with various intra-cavity elements	113
6.5	Beam profile on output coupler using 2.5 mm holmium rod	114
6.6	Measured pulse energy and pulse width at 20 Hz	115
6.7	Pulse energy as a function of Q-switch frequency	116
6.8	Measured pulse width as a function of Q-switch frequency at maximum thulium pump power	117
6.9	Measured Q-switch pulse at 20 Hz: (a) pulse profile and build-up time; (b) pulse train	117
6.10	Measured beam quality of Q-switched output as a function of Q-switch frequency	119
7.1	Spatially multiplex several Tm:YLF slab lasers	126
7.2	Side-pumped slab	127
7.3	Hybrid stable-unstable resonator	127
A.1	Quasi-3-level energy level diagram based on Tm:YLF	129

List of Tables

2.1	Upconversion modelling parameters	21
2.2	Power-scaling calculations	31
3.1	Measured single Tm:YLF slab laser characteristics	51
3.2	Laser performance model parameter for Tm:YLF	53
3.3	Parameters used for temperature modelling	54
3.4	Tm:YLF slab fracture limit model parameters	60
3.5	Predicted power-scaling using Tm:YLF two-slab laser	60
4.1	Parameters used for intra-cavity modelling	73
5.1	Laser performance model parameters for Ho:YAG	95
5.2	Thermal lens modelling parameters	99
5.3	Comparison of internal and external pumping scheme summary	101

Chapter 1

Introduction

1.1 Topic overview

Since the introduction of holmium lasers in the 1960s [1–3], much progress has been made in improving the output power, slope efficiency and laser designs. There are various spectroscopic properties of Ho^{3+} that make it a useful ion for laser sources; such as a long upper laser level lifetime, and the potential for operation at a wavelength that is both “eye-safe” and has a high transmission through the atmosphere. This lasing wavelength at $2.1\ \mu\text{m}$ is the wavelength of interest throughout this thesis. Important applications based on the unique properties of holmium lasers include medical, military, machining and remote sensing. As new applications arise, demands on output power and pulse energy also increase. This thesis describes significant accomplishments towards the power-scaling of Ho:YAG lasers, and presents novel laser configurations, which may be applied to other laser hosts.

Yttrium aluminium garnet (YAG) is an optically isotropic crystal with many advantageous properties, e.g. it is mechanically and chemically robust with good thermal and optical characteristics, which have led it to be one of the host laser materials of choice. Ho:YAG has a long upper laser level lifetime of 8.5 ms [4] ($\sim 30\times$ that of Nd:YAG [5]), thus provides good energy storage in the crystal and therefore the potential for high energy Q-switched pulses. The possibility of extracting high energy pulses has enabled it to be used for many material processing applications, one specific example being laser machining [3]. If in-band pumping of Ho:YAG is used, i.e. exciting the crystal with a pump wavelength that couples the ground energy state with the metastable upper laser manifold, a low quantum defect of only $\sim 9\%$ can be realised. This offers the potential for efficient operation and good power-scalability, similar to Yb:YAG lasers, due to

the low thermal contribution. The reduced thermal load also minimises thermal problems such as: lensing, which limits laser performance at high pump powers; increased population in the lower laser Stark level, the source of reabsorption losses and thus increased threshold pump powers; stress birefringence that can again lead to increased losses; and stress fracture that sets the maximum power-scalability of a laser system. An “eye-safe” lasing wavelength in the 2 μm regime, in conjunction with good atmospheric transmission, has meant that holmium lasers are an excellent source for remote sensing [6] and environmental monitoring [4, 7–10]. The longer lasing wavelength with respect to thulium based lasers makes it an important pump source for ZGP and GaAs based Optical Parametric Oscillators (OPO)s for generating mid-IR wavelengths (3–5 μm). The mid-IR window has various applications for gas sensing, laser ranging and counter measures in the military sector [11–15], and use as a surgical tool in the medical sector [16–21].

Next generation technologies call for even higher average and peak powers. Currently available commercial Ho:YAG lasers have reached an output power of 80 W, and 3.5 J in the Q-switched regime¹. As high as 30 J has been achieved in single-pulse mode [22]. This work concentrates on power-scaling methodologies for lasers in both the CW and Q-switched regimes, where higher pulse energy in the Q-switched regime, would for example, allow faster material processing or longer range remote sensing, whereas, higher CW powers would find use in the scientific and research field [23]. However, several underlying problems hold back the progression towards higher output powers. Most significant is the quasi-three-level nature of the 2 μm transition for Ho^{3+} , which has a significant thermal population in the lower laser level. This thermal population results in high threshold pump power. Moreover, the lack of commonly available laser diodes at suitable pump wavelengths prevents direct diode pumping. Thus typical approaches for power scaling Ho:YAG lasers involve a two step process, e.g. excitation through energy transfer in co-doping, or pumping in-band with a diode pumped source. Therefore, a suitable pumping scheme is required in order to power-scale Ho:YAG to over 100 W.

There are two different pumping schemes employed in this work, the intra-cavity side-pumping scheme and the external end-pumping. Both of these schemes are designed to allow the use of a more power-scalable slab pump laser. The slab is a rectangular shaped geometry that is more power-scalable due to its good thermal management from its two large surfaces. The ability to use a slab pump laser allows high-power Ho:YAG laser to be realised.

¹<http://www.trimeddyne.com/txmax.htm>

1.2 Background

1.2.1 History

The first holmium laser, demonstrated in 1966 [1], was a holmium erbium co-doped system ($\text{Ho}^{3+}:\text{Er}_2\text{O}_3$). Erbium co-doping was used to provide a broader absorption band for lamp pumping. The operating temperature in [1] was at 77 K to minimise the threshold pump power due to the thermal population in the holmium lower laser Stark level. Everitt then demonstrate the first Ho:YAG laser in 1969 [3], co-doped with both erbium and thulium to enhance the absorption of the lamp pump light. Lamp pumped systems have shown output powers as high as 50 W CW operated with direct cryogenic cooling [24] using Ho,Er,Tm:YAG, over 60 W from Ho:YLF [25], and 17 J Q-switched for a chromium and thulium co-doped system [26]. However, it was not until 1971 that the first room temperature Ho:YAG laser was demonstrated under Q-switched operation [27], and recently, pulse energies as high as 4 J has been achieved by Li et al. [28], using a lamp-pumped, thulium and chromium co-doped Ho:YAG system.

Following the demonstration of laser diodes, a diode-pumped cryogenically cooled Ho:YAG laser was demonstrated in 1986 [29], where the cryogenic operating temperature was necessary due to the relatively low diode pump power available at the time. The holmium crystal was again co-doped with thulium and erbium due to the lack of a suitable holmium absorption band at the diode wavelength of $0.79\text{ }\mu\text{m}$. An output power of 5.6 mW at $2.1\text{ }\mu\text{m}$ was obtained for 34 mW of incident pump power. The laser threshold was as low as 2.7 m W due to the low operating temperature and the use of a diode pump source with a good beam quality.

Co-doping holmium-doped materials with thulium was found to reduce the lifetime of the upper holmium laser level from the intrinsic lifetime. Therefore, one approach for improving the storage capability was to split the different dopants out to two separate crystals. Here an intra-cavity pumping scheme was introduced where the Tm:YAG and Ho:YAG crystals share the same laser cavity [30]. A Ti:sapphire, at a wavelength of 785 nm, was used as the Tm:YAG pump source, which gave over 120 mW of holmium output at $2.09\text{ }\mu\text{m}$ from 450 mW of absorbed pump power. Employing a similar intra-cavity configuration but with a beam shaped diode-bar as the thulium pump source, an output power of 7.2 W was demonstrated by Hayward et al. [31] in 2000. This also involves the use of Tm:YAG to convert the $0.8\text{ }\mu\text{m}$ to $2.0\text{ }\mu\text{m}$ laser wavelength, suitable for pumping the holmium 5I_7 upper laser manifold.

As Ho:YAG has good absorption in the $1.9\text{ }\mu\text{m}$ region, one approach that has been used is end-pumping with $1.9\text{ }\mu\text{m}$ diode lasers [32]. Unfortunately, due to the limited

efficiency and pump power from these diodes, this approach has only generated 0.7 W of 2.1 μm output power at an operating temperature of $-53\text{ }^{\circ}\text{C}$. The incident threshold pump power was $\sim 0.5\text{ W}$ and the slope efficiency was 35 % with respect to the absorbed pump power.

Thulium doped yttrium lithium fluoride (YLF) is another suitable candidate for pumping the strong absorption peak of the Ho:YAG around the 1.9 μm region, having a much stronger absorption than the output from Tm:YAG. Moreover, it has a “two-for-one” cross-relaxation process that allows efficient operation when pumped around 790 nm, where there are commercially available efficient high-power diodes. Budni et al. used a Tm:YLF laser to end-pump a Ho:YAG laser, generating 20 W of 2.1 μm output from 120 W of incident diode power [33], and 50 mJ from a 270 mJ thulium laser pump pulse. However, YLF is a relatively fragile crystal which is limited to $\sim 20\text{ W}$ of CW output power in standard end-pump single-rod configurations. Recently, a tunable thulium glass fiber laser has also been demonstrated as a good pump source for Ho:YAG lasers [34–36], generating 15.3 W of holmium average output [37].

1.2.2 Comparison of different laser architectures

The lack of suitable holmium absorption bands at the commonly available laser diode wavelengths makes it a difficult laser source to be efficiently power-scaled. Various laser architectures have been developed for Ho³⁺ systems operating at 2.1 μm , which can be classified by the following:

- Co-doping with suitable sensitizers and lamp or diode pumping
- Intra-cavity pumping by separated active media
- External pumping with high brightness pump sources, based on semiconductor or dielectric gain media

1.2.2.1 Co-doping

The earliest form of the solid-state laser used flash lamps as the pump source. The flash lamp has a broad emission spectrum with a relatively poor overlap with the absorption spectra of rare-earth ions. For the holmium laser, additional rare earth ions such as erbium and thulium were introduced into the host media to sensitise it to the pump spectral content and improve the absorption efficiency. The co-dopants provide extra absorption bands, whereby these additional ions, once excited, undergo an energy transfer process that then excites the holmium ions [24, 29, 38–41]. Chromium and thulium

co-doping has also been used for lamp pumping [42–44], while thulium, co-doped with holmium, has mainly been used with diode pumping due to its good absorption at available diode lasing wavelengths [45–47], as shown in figure 1.1.

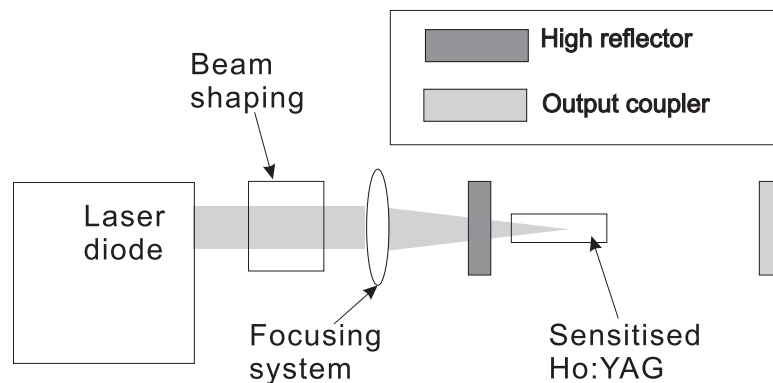


FIGURE 1.1: Schematic for diode end-pumped sensitised Ho:YAG

Co-doping provides the simplest and most compact holmium laser architecture, as it involves only one laser cavity and gain element. Unfortunately, sensitised holmium gain media suffer severe additional co-operative upconversion between the different dopants that significantly reduce the effective holmium energy storage lifetime [17, 48]. Moreover, the upconversion loss leads to an increase in the thermal load, associated with the non-radiative relaxation of the higher excited state ions, exacerbating thermal problems.

1.2.2.2 Intra-cavity pumping

To avoid upconversion between co-dopants, Stoneman and Esterowitz, and other workers demonstrated that by separating the thulium and holmium into separate crystals, efficient energy transfer between the thulium and holmium ions could still be achieved via a purely radiative mechanism, i.e. intra-cavity pumping [7, 11, 30], as shown in figure 1.2. This cavity configuration solves the co-operative upconversion loss problem between the co-dopants thus improving the energy storage lifetime of the holmium upper laser level, while maintaining a compact cavity design. The use of intra-cavity pumping is essential because Ho^{3+} is a quasi-three-level ion and thus needs a pump source intensity that is comparable to the saturation intensity for efficient operation. Moreover, the thermal load was split between two crystals and could be managed separately. Despite this, however, one notes that Tm:YAG suffers strong thermal lensing at high pump powers, which complicates the intra-cavity pumped resonator design, especially when combined with a separate thermal lens in Ho:YAG, ultimately limiting the power-scalability of this configuration [49].

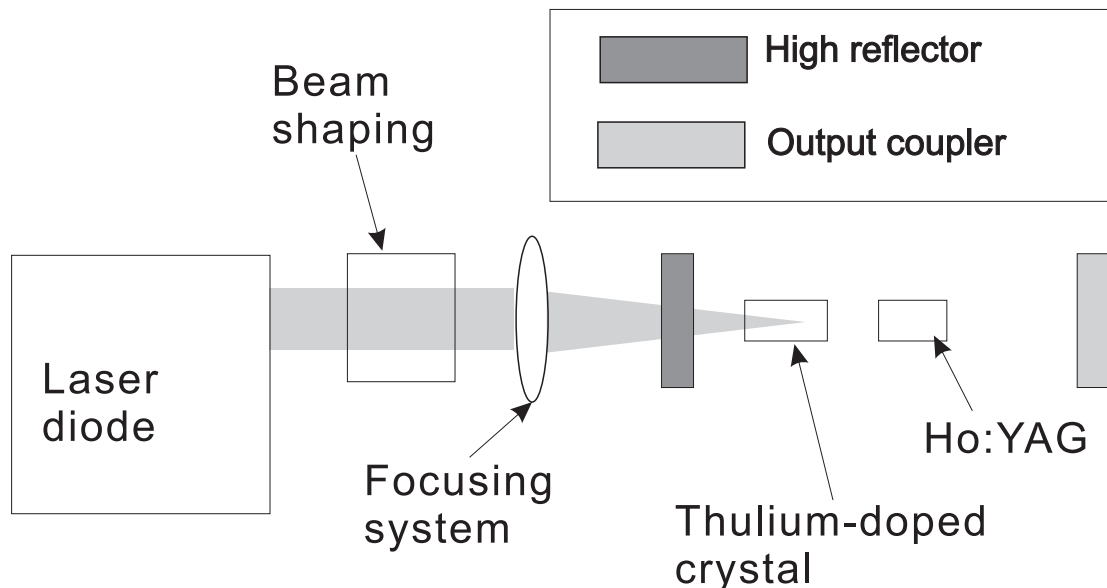


FIGURE 1.2: Schematic for intra-cavity end-pumping scheme

Using a separate thulium-doped crystal from the holmium-doped crystal, one can obviously use a different host besides YAG. Such a host that has proven successful with thulium-doping is YLF [33, 50]. Tm:YLF has a negative $\frac{dn}{dT}$ which can over-power the positive thermal lensing from crystal distortions resulting in a weak negative thermal lens [51]. However, Tm:YLF suffers a low thermally-induced stress fracture limit [4], restricting its power-scalability as the pump source of the holmium laser, in the collinear intra-cavity pumping configuration.

1.2.2.3 Externally pumped with a separate laser

The advent of alternative high-power laser sources such as Tm:YLF with the strongest wavelength that coincides with a Ho:YAG absorption peak around $1.9 \mu\text{m}$, led to a reduction of required saturation intensity to only $\sim 1.5 \text{ kW/cm}^2$. This saturation intensity is an order of magnitude smaller than that for the lasing wavelength of Tm:YAG, thus allowing the thulium laser to be positioned outside the cavity. In the scheme shown in figure 1.3(a), most of the thermal load that occurs in the system is in the thulium system due to its larger quantum defect between the diode pump wavelength and the thulium lasing wavelength, even including the advantageous two-for-one cross-relaxation. Therefore, as this approach effectively pumps the holmium laser in-band with a low quantum defect, it has a relatively good environment for obtaining good beam quality.

Thulium fibre lasers are another attractive source for end-pumping Ho:YAG lasers [34, 52], where figure 1.3(b) shows the schematic of such a pumping scheme. Fibre lasers have the benefit of using low doping levels and hence having long absorption lengths that

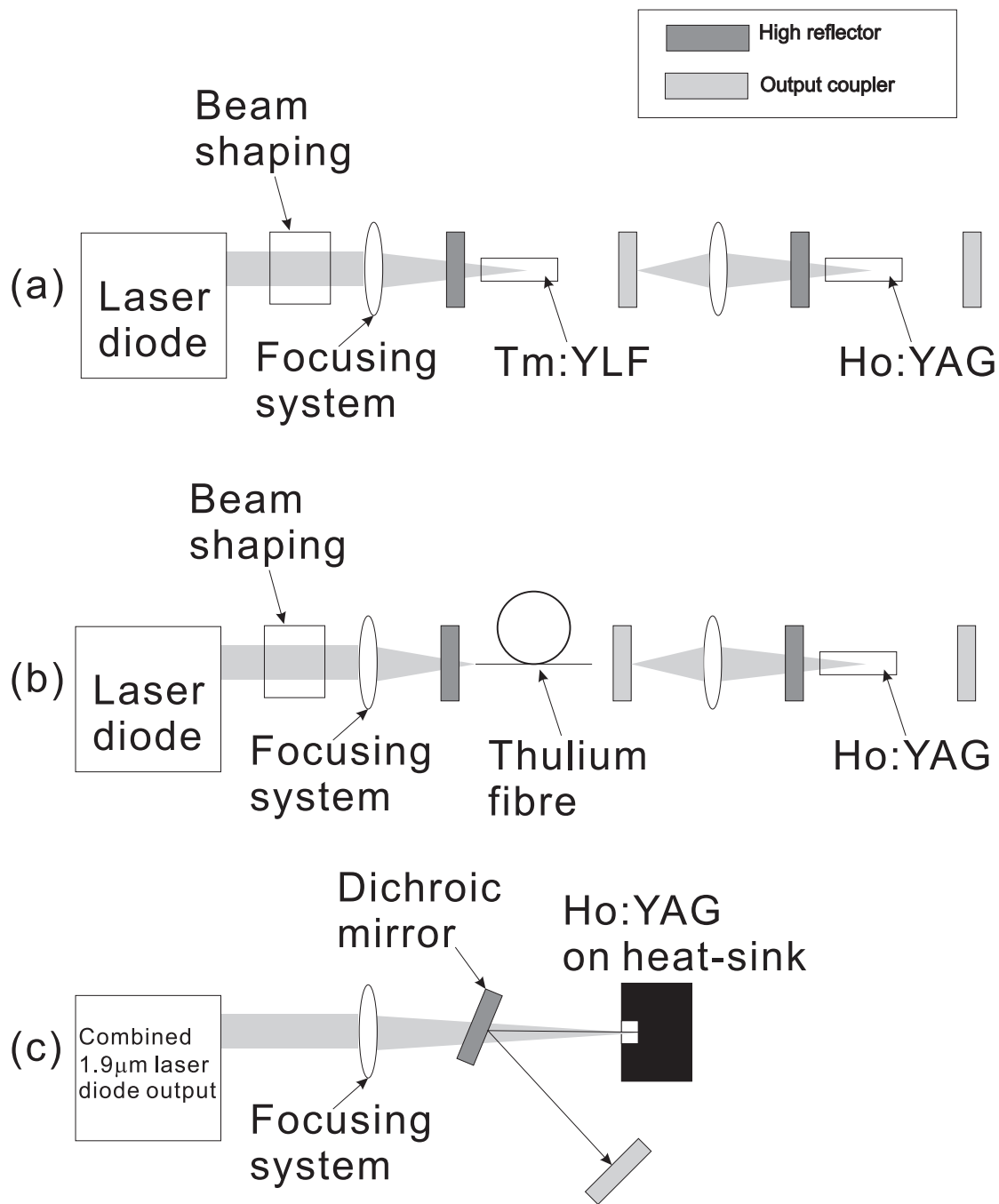


FIGURE 1.3: Schematics for external pumping. (a) Tm:YLF end-pumping; (b) thulium fibre laser; (c) 1.9 μ m diode laser

distribute the thermal load over a long distance, which has been exploited to scale output power levels into the kW regime for Yb^{3+} based devices. However, in order to make fibre lasers into 2 μm regime based on thulium efficient two-for-one cross-relaxation process, high doping concentrations are required. This reduces the absorption length, thus increasing the thermal load per unit length significantly. These conflicting requirements between doping concentration and power handling capability of such fibres has restricted the output power achievable. The solution to this was double-clad fibres. Double-clad thulium fibre lasers with high doping concentration and improved characteristics have achieved good overall laser performance and power-scalability in pumping Ho:YAG [36]. Thulium fibre has a broad emission bandwidth therefore, in order to have a wavelength that matches the holmium absorption, the laser requires the use of wavelength selection techniques, such as intra-cavity gratings. Recent development in fibre laser systems have pushed the output power levels to 150 W (see footnote²), however there are still other practical limitations for the thulium-doped fibres to be overcome such as fibre quality for even greater power levels.

Direct pumping of Ho:YAG using mixed GaInAsSb and InGaAsP diodes operating at a wavelength of 1.9 μm has also been demonstrated [32]. Using a pumping scheme shown in figure 1.3(c), it potentially offers similar advantages to thulium laser pumping, but with a single step between the electrical power source and optical pumping of the holmium crystal. The scheme combines six diode output using angle multiplexing [53] and polarisation beam combining to give about 4 W of 1.9 μm incident power. To date, demonstration has only been in the low power regime, and further power-scalability is unclear, limited by the diode pump power and beam quality.

Tm:YLF has a suitable lasing wavelength to be a good pump source for Ho:YAG. However, once again the fragile nature of Tm:YLF limits its brightness-scalability [33], which in turn limits the scalability of holmium lasers.

1.3 Power-scaling method investigated

In our power-scaling strategy, diode lasers were chosen over lamp pumping as the pump source for a thulium laser due to their good wall-plug efficiency [54], a narrow spectral bandwidth for improved absorption and lower heat deposition, and lower divergence allowing a small pump area, thus a higher pump intensity that is comparable to the saturation intensity of the active crystal. Moreover, multiple diode pump sources, such as a diode laser bar or a stack, can be used to increase the pump power of the system. Although the increased number of diodes degrades the pump beam quality, techniques

²http://www.ipgphotonics.com/products_2micron_lasers_cw_tlr-series.htm

such as two-mirror beam shaping [55], polarisation beam combining [56] and spatial multiplexing, can be used to reclaim part of the lost beam quality.

Given diode lasers are used as the pump source to convert electrical to optical power, thulium-doped crystals make a good intermediate medium to convert the diode wavelength to a suitable excitation wavelength for the holmium crystal. The demonstrated power-scalability of Tm:YAG would normally suggest it to be a good choice as a high-power pump source. However, Ho:YAG has a low absorption at the Tm:YAG lasing wavelength.

Thulium-doped material has been reported in several host materials including YAG [11, 49], YLF [33, 50], YAP [57], KY_3F_{10} [58] and $LiTaO_3$ [59]. Both KY_3F_{10} and $LiTaO_3$ offer a high emission cross section and long fluorescence lifetimes. However, they have not been proven to lase efficiently and thus are not considered as a good host material for this project. On the other hand, YAP, YAG and YLF are very popular laser host materials and have demonstrated good lasing performance. Apart from laser performance, emission and absorption cross-sections, lasing wavelengths, upper-state lifetimes, three-level character, thermo-mechanical properties, thermal-optical properties, rates for upconversion and cross-relaxation are all very important as they all affect the efficiency of the laser. Of all the host materials, Tm:YLF provides a lasing wavelength that is well matched to the absorption peak of Ho:YAG at $1.91\ \mu\text{m}$. Spectroscopically, this makes Tm:YLF a good laser medium for pumping Ho:YAG, both intra- and extra-cavity. Unfortunately, the relatively poor mechanical property of YLF makes it vulnerable to thermally-induced stress fracture.

Given the fragile nature of YLF, the power-scaling bottle-neck is now in the thulium laser. Lowering the doping concentration to increase the absorption length is restricted for a thulium laser, due to the need for high doping concentration in order to benefit from two-for-one cross-relaxation. Another way of increasing the fracture limit is to use the slab geometry, [60, 61]. Here we describe two different cavity designs that make use of a Tm:YLF slab pump laser for the purpose of power-scaling Ho:YAG lasers. Both of these schemes do not require good pump beam quality.

1.3.1 Intra-cavity side-pumping

Figure 1.4 shows a schematic outline of a novel intra-cavity side-pumping scheme that we have investigated as a route to power-scaling of a Ho:YAG laser. It has all the advantages of intra-cavity pumping such as long holmium energy storage lifetime, a compact cavity configuration and separated thermal loads. Besides, the side-pumping configuration allows the use of a slab geometry for the thulium pump laser, increasing

the power-scalability of the system. The holmium cavity is naturally de-coupled from the thulium cavity in side-pumping, reducing the effect of the thermal lens in the thulium crystal from affecting the holmium cavity stability and its output beam quality. Finally, the low single-pass absorption across the width of the holmium and the side-pumping with a top-hat profile gives a relatively uniform gain and thermal load.

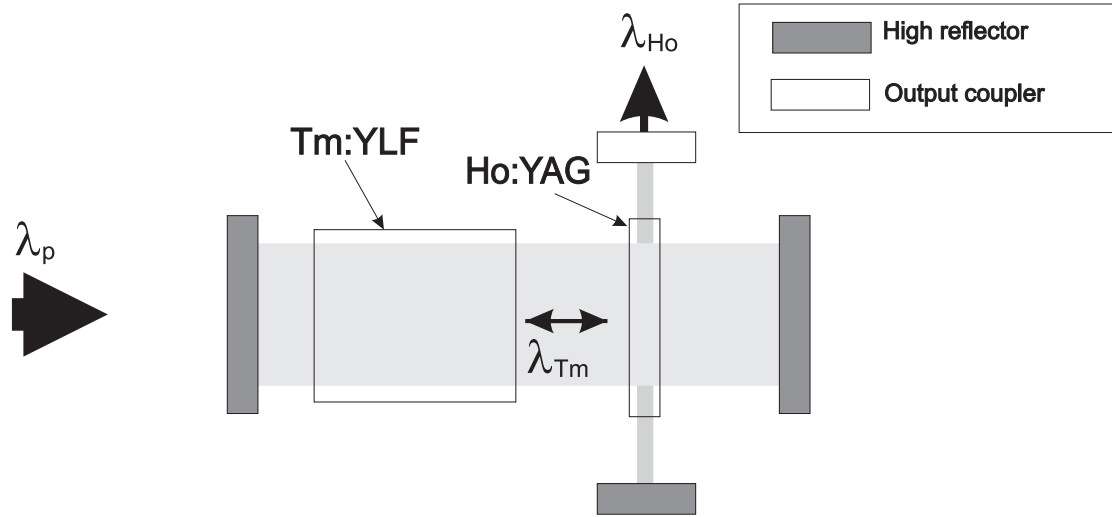


FIGURE 1.4: Schematic for intra-cavity side-pumping

Slab lasers were first introduced in the 1970s [62, 63]. This concept is well known to have a higher thermally-induced stress fracture limit than the standard rod geometry due to the large cooling surfaces and a one-dimensional heat flow [60, 61, 64]. This geometry mostly benefits the Tm:YLF pump laser, which is limited by thermal fracture at pump intensities of $\sim 5 \text{ kWcm}^{-2}$ [33]. Moreover, a slab gain element has a relatively relaxed requirement on the pump beam quality in the slow-axis, which reduces the complexity of the focussing arrangement and allows a high delivery efficiency from non-diffraction limited high-power diode sources. These properties makes the slab geometry a good option for power-scaling, with the only drawback being a typically poor output beam quality, particularly in one axis. Luckily, this is another advantage for this intra-cavity side-pumped approach as it provides a uniform thermal load along the length of the holmium crystal and hence minimal potential for stress due to thermal inhomogeneities. In active medium that has a broad gain such as thulium, the lasing wavelength would shift to avoid the holmium absorption. An increase in holmium doping concentration or the length of absorption is therefore required to compensate this for efficient operation.

1.3.2 External end-pumping pump-guided Ho:YAG rod

The high aspect ratio gain volume of the Tm:YLF slab does not have a particularly good overlap with a standard laser resonator mode, leading to poor beam quality in one axis.

Ways to improve this beam quality could include the use of an unstable resonator [65–67], multi-passing the fundamental mode through the active medium [61, 68, 69], or by defining an asymmetric cavity mode compatible with the geometry of the pumped region [70, 71]. Alternatively, and the simplest solution for Tm:YLF slabs that are to be used for end-pumping Ho:YAG, is to operate the slab laser in a multi-mode regime and utilise pump-guiding in the Ho:YAG rod, similar in concept to one of the first configurations that was used for kW class Yb:YAG lasers, which was end-pumped with large diode-stacks.

We used a Ho:YAG rod with a polished barrel finish over its length, providing pump-guiding and a directly water cooled interface, to which we could couple the Tm:YLF slab pump-lasers in an end-pump configuration. Since the slab laser gave a good beam quality in one axis, it is possible to spatially multiplex multiple thulium pump-laser beams in this axis to increase the pump power. Effectively the concept is to actively convert the diode light to a suitable wavelength that has a strong absorption, or low saturation intensity, for Ho:YAG. This approach has significant potential due to its simplicity for diode pump coupling, and subsequently power-scaling possibilities through multiplexing many high-power Tm:YLF slab lasers. Beam quality issues can then be addressed in the Ho:YAG laser itself.

1.4 Synopsis

This thesis describes the progress made in power-scaling of Tm:YLF pumped Ho:YAG lasers. Due to the lack of available data for the properties of Tm:YLF, such as quantum yield and upconversion, and their influence on the stress fracture limit, the investigation of laser performance and the fracture limit as a function of doping concentration is first reported in chapter 2. The laser performance for various doping concentrations was obtained and used to find the optimum doping concentration that gives the maximum output power before fracture.

Both of the power-scaling strategies explored in this body of work use Tm:YLF slab lasers because of the lasing wavelength match to the Ho:YAG absorption. Moreover, the slab geometry is used, as it is more power-scalable due to its better thermal management properties. This was experimentally verified in chapter 3 with the observed laser performance supported by modelling with a plane-wave theory and a 100 W class two-slab Tm:YLF laser was demonstrated, the additional slab was only required because sufficiently large slabs were not available from our commercial supplier. This represents the highest reported Tm:YLF laser power to our knowledge.

Equipped with our high-power Tm:YLF slab pump laser, a very compact intra-cavity side-pumping scheme was implemented. A plane-wave intra-cavity side-pumping model is presented in chapter 4, which was used to optimise the holmium laser design. Experimental results are discussed in comparison with the theoretical predictions. Further improvements are suggested to enhance the power scaling potential and to achieve a better performance.

Chapter 5 contains a report of the laser performance of a power-scaled pump-guided Ho:YAG rod laser, externally end-pumped by two spatially multiplexed Tm:YLF slab lasers. The laser performance was characterised and compared to the laser performance of the intra-cavity side-pumping scheme. Q-switched performance for this laser is also presented and discussed in chapter 6, and future possibilities for the pump-guiding rod are presented.

This thesis finishes in chapter 7 with a conclusion of the results and suggestions for further work.

Chapter 2

Tm:YLF rod laser characterisation

Ho:YAG is an attractive laser source with medical, military, industrial, and research applications. It has features such as a long upper-state lifetime and laser emission at an eye-safe wavelength, as well as good thermal and mechanical properties associated with the YAG host. However, it does not have an absorption band that coincides with commonly available commercial diodes; therefore a separate thulium-based pump laser is often used to directly excite the holmium upper laser level.

YLF is a well-known good laser host for rare-earth ions that has various benefits such as strong birefringence, which leads to minimal depolarisation loss, and relatively long upper state lifetimes when doped with many rare-earth ions. When doped with thulium, it provides a lasing wavelength that has an especially strong overlap with an absorption band in Ho:YAG, and is thus commonly used as the pump laser of choice for Ho:YAG systems.

However, YLF is also a relatively fragile crystal with a low tensile strength and stress-fracture limit. Thermally induced stress-fracture has been reported to occur when end-pumping Tm:YLF with 790 nm diodes and beam-waist pump intensities of $\sim 5 \text{ kWcm}^{-2}$ [72]. Typically, if pump beam quality allows, this limit can be increased by reducing the doping concentration of the host crystal, thus reducing its absorption coefficient at the pump wavelength and distributing the heat power over longer lengths. Unfortunately, this simple strategy cannot be followed in the case of thulium-doped solid-state lasers when pumping the 3H_4 level at around $0.8 \mu\text{m}$, because of two different properties. Firstly, moderate concentrations of thulium doping leads to an increase in the slope efficiency due to a “two-for-one” cross-relaxation process between neighbouring ions, therefore lowering the doping concentration would not only increase the

absorption length but also reduce the overall efficiency, resulting in an increase in the thermal load. Secondly, energy-transfer upconversion, a loss process that is dependent on the excited-state population density, should also be considered. Similar to cross-relaxation, upconversion involves the exchange of energies between neighbouring excited ions, therefore the upconversion rate increases with increasing doping concentration. When operating Tm:YLF in the 2 μm regime, a quasi-three-level transition, high inversion densities are typically required to overcome the reabsorption losses as well as other cavity losses. This leads to a higher upconversion loss that increases depopulation rate of the upper laser level, therefore a shorter effective lifetime, ultimately leading to an increased threshold and thermal load within the crystal. These processes are shown in figure 2.1. Note that the operating temperature is ideal to be as low as possible to reduce thermal population in the lower laser level.

A trade off exists between increasing laser performance and absorption by using a higher doping level, and reducing the upconversion rate through reducing the doping level. This requires knowledge of the upconversion and cross-relaxation rate parameters, which can be measured spectroscopically as a function of thulium doping concentration, but can be a very difficult process and often the results are dependent on the measurement technique. A more meaningful result is to determine the relative laser performance that simultaneously includes all the inter-dependent processes, such as cross-relaxation, upconversion and ultimately the thermo-optical and mechanical properties, occurring within the gain medium. These results can then be used to optimise the laser cavity design in terms of its power scaling performance and limit.

In this chapter we introduce the background theory for the laser performance including cross-relaxation, upconversion, and thermally induced stress fracture, followed by the characterisation of the laser performance for several different Tm:YLF rods. The laser performance results are discussed with the intention of obtaining a better understanding of the upconversion and cross-relaxation processes, and the thermally induced stress fracture limit. Doping concentrations of 2, 4, and 6 at.% were characterised with rod lengths that corresponded to two pump absorption lengths (24 mm, 12 mm and 8 mm respectively). The relative cross-relaxation efficiency and thus quantum yield were extracted from the laser performance. Moreover, the fracture pump intensity of Tm:YLF, determined in our experimental configuration, was used to define a figure of merit for the other dopant concentrations, including quantum yield and upconversion processes, which could then be used to optimise the design for other Tm:YLF lasers. Therefore, this technique allowed us to estimate the power scalability of Tm:YLF laser systems without actually determining the exact figure for the upconversion parameter.

2.1 Spatial rate equation model

There are a number of models for end-pumped laser systems described in the literature [17, 73–75], many of which use spatial rate equations and provide solutions for determining the laser threshold and slope efficiency for a particular laser system. The model presented here is based upon the work of T. Taira et al. [76], and is extended to take into account the effects of cross-relaxation and upconversion. As such, the modelling provides an understanding of how these processes affect the laser performance, and can be used for designing other laser systems that suffer the same problems. A similar approach was also reported by Bjurshagen [77] and the derivation is shown in appendix A for completeness.

We describe here a formula for calculating the inversion density of the pumped active medium, which takes into account the spatial distribution and overlap of the pump and laser fields, reabsorption loss, upconversion and cross-relaxation. The model assumes fast relaxation between the terminal pump level (3H_4) and the upper laser level 3F_4 (see figure 2.1 for energy level diagram), no ground-state depletion (GSD), and no diffraction inside the active media. From equation A.21, the inversion density is given by

$$\Delta N = \Delta N^0 + \frac{2f\tau_U Rr_p - 2f\tau_U\sigma_{21}\frac{c}{n}\Phi\phi_0\Delta N^0}{1 + f\tau_U\sigma_{21}\frac{c}{n}\Phi\phi_0 + \sqrt{(1 + f\tau_U\sigma_{21}\frac{c}{n}\Phi\phi_0)^2 + 4\gamma\tau_U(\tau_U Rr_p - \tau_U\sigma_{21}\frac{c}{n}\Phi\phi_0\Delta N^0)}}, \quad (2.1)$$

where $\Delta N(r, z) = N_2(r, z) - N_1(r, z)$ is the population inversion density in the active medium, $\Delta N^0 = N_2^0 - N_1^0$ is the unpumped population inversion density or the thermal population inversion density, τ_U is the upper laser manifold lifetime including both radiative and non-radiative decay, but excluding upconversion, $f = f_1 + f_2$ is the sum of the Boltzmann occupation factors of the initial and final laser Stark levels, σ_{21} is the spectroscopic emission cross-section at the lasing wavelength, c is the speed of light, n is the refractive index of the active medium, Φ is the total number of photons in the active medium, $\phi_0(r, z)$ is the normalized spatial distribution of the laser photon field, γ is the manifold upconversion parameter, R is the rate of pumping to the upper laser manifold and $r_p(r, z)$ is the normalized spatial distribution of the excited ions. Note that only the negative part of the quadratic equation solution is taken into account, because the other solution is not physically meaningful. This equation can be substituted into the gain-loss equality equation, which can be solved numerically to give the output power as a function of input power, and is then used to find the threshold and slope efficiency.

From equation A.25, the gain-loss equality is given by

$$2\sigma_{21}l_{rod} \int \int \int_{crystal} \Delta N(x, y, z) \phi_0(x, y, z) dV = L - \ln R_{oc} , \quad (2.2)$$

where l_{rod} is the rod length, L is the intrinsic cavity loss and R_{oc} is the output coupler reflectivity.

2.2 Energy-transfer upconversion, cross-relaxation and quantum yield

The upconversion and cross-relaxation processes involve exchange of energy between two neighbouring ions. They are important parameters that affect the thulium laser performance and maximum achievable output power. Understanding of these processes is essential in order to develop power-scalable efficient lasers with Tm:YLF.

2.2.1 Energy-transfer upconversion

Energy-transfer upconversion, also known as cooperative upconversion, is the effect where two excited ions interact, promoting one ion to a higher excited state while the other relinquishes its energy and returns to its ground state. The higher excited state ion then typically decays non-radiatively, thus contributing to the thermal loading of the host crystal. When returned to the upper laser level, it creates a net loss of one excited ion in the overall process. In Tm:YLF, this involves two interacting ions in the 3F_4 manifold, resulting in an ion in the ground state, 3H_6 , and promoting the other ion to either 3H_4 or 3H_5 , where the promoted ion would decay back to 3F_4 , as shown in figure 2.1. This affects the maximum power achievable due to the increased heat deposition.

From equation A.14, it can be shown that the upconversion loss can be combined with the fluorescence lifetime of the upper manifold to give an effective lifetime, τ_{eff} . Although, strictly, the effective lifetime is based on a plane-wave analysis, it is a simple way of understanding the effect of upconversion on the laser performance. The effective lifetime is given by

$$\frac{1}{\tau_{eff}} = \frac{1}{\tau_U} + \gamma N_U(x, y, z) , \quad (2.3)$$

where γ is the overall upconversion parameter accounting for all upconversion pathways from this manifold [9] and N_U is the population density in the upper laser manifold.

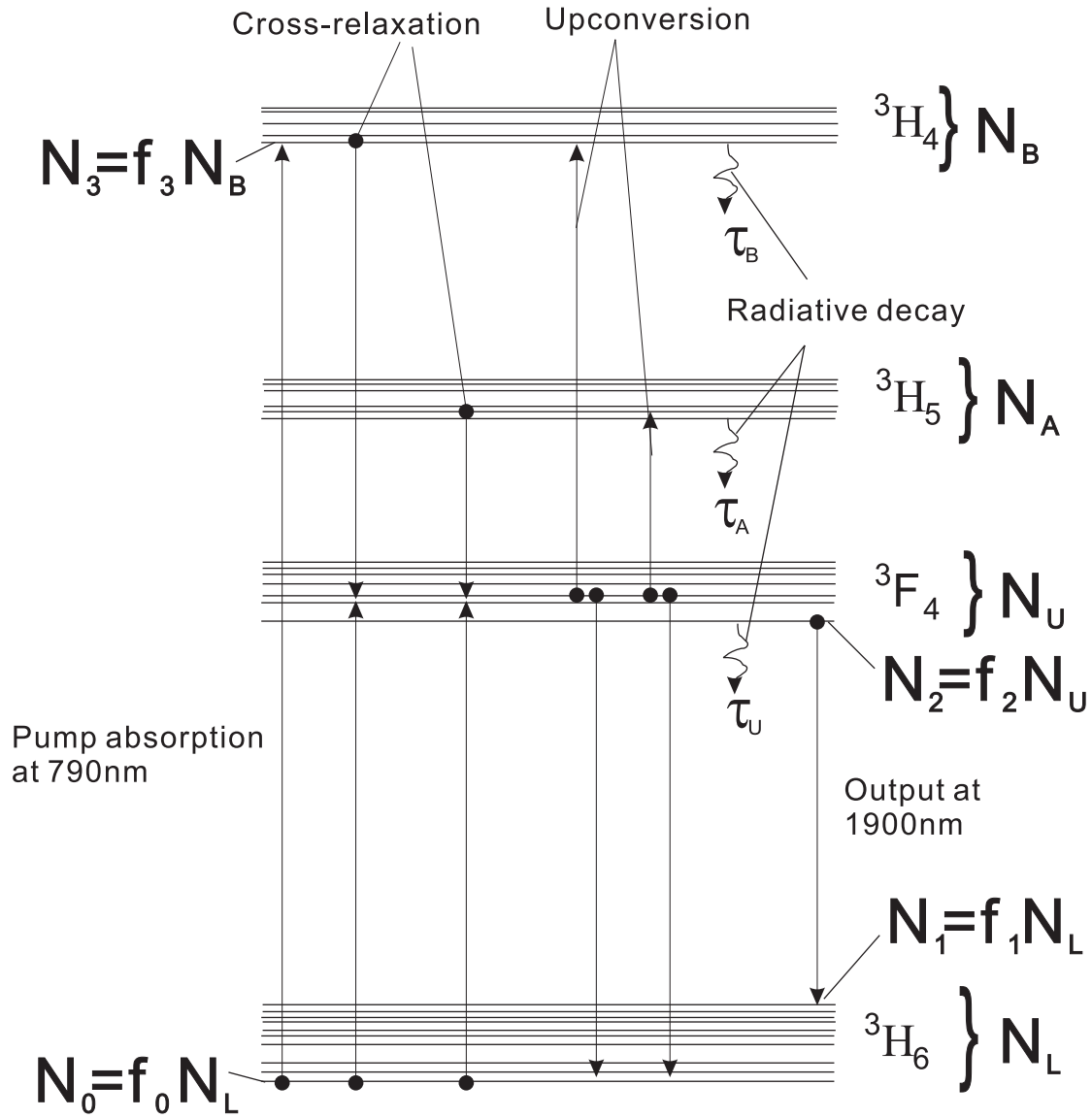


FIGURE 2.1: Tm:YLF energy level diagram

The upper laser level lifetime, τ_U , can be replaced by the effective lifetime, τ_{eff} , to take into account upconversion loss in threshold calculations, as will be discussed in chapter 3. This shows that upconversion has a direct effect upon the upper laser level lifetime, such that a high upconversion rate would reduce the upper laser level lifetime, and thus increase the threshold for laser operation (see equation A.27). However, as the laser reaches threshold, the population inversion will be clamped by the balance of the excitation and de-excitation processes. Therefore, thus upconversion has little effect upon the slope efficiency which, as shown in equation A.34, is not affected by the lifetime. In calculating heat deposition, the upconversion loss output channel, P_{UC} , does not change significantly with pump power after threshold is reached and can be expressed as

$$P_{UC} = h\nu_l \gamma N_c^2 V, \quad (2.4)$$

where $h\nu_l$ is the energy of the laser photon, N_c is the clamped population density of the upper laser manifold and V is the pumped volume.

It should be noted that this argument is based upon a plane-wave analysis and if transverse spatial profiles are taken into account then it is possible for upconversion to have an effect on the slope efficiency as will be seen in section 2.3.1. This is because it is the inversion averaged over the laser mode profile which becomes clamped at the threshold value, however, the spatial profile of the inversion will change above laser threshold as discussed in section 2.3. In the case of uniform pumping, the inversion will initially be more strongly depleted at the centre by the lasing mode, causing a reduction in upconversion in this region compared to the edges. Numerical simulations of the laser performance, accounting for such spatial profiles, are shown later in figure 2.2, including the effect of upconversion on threshold and slope efficiency.

2.2.2 Cross-relaxation

The cross-relaxation process between Tm^{3+} ions, also known as “two-for-one”, is essentially the reverse of the upconversion process. It involves one excited ion in a higher energy level than the metastable laser level, 3H_4 in figure 2.1, and a ground state ion (3H_6) exchanging energy, resulting in two excited ions in the upper laser level in 3F_4 . This effect can therefore lead to two excited ions in the upper laser level per absorbed pump-photon. Without cross-relaxation, the maximum possible slope efficiency is the stokes efficiency, $\eta_{st} = \frac{\lambda_p}{\lambda_l}$, $\sim 40\%$ for Tm:YLF, would imply a significant thermal load in the active crystal. With the “two-for-one” process the efficiency may approach 80% .

Starting from Honea’s et al. analysis [49], we know that the cross-relaxation rate is proportional to the square of the doping concentration, which is given by the equation

$$\gamma_x = \frac{1}{\tau_0} \left(\frac{C}{C_0} \right)^2, \quad (2.5)$$

where C is the doping concentration and C_0 is a fitted parameter. τ_0 is the low concentration lifetime of the 3H_4 manifold and is defined by

$$\frac{1}{\tau_0} = \frac{1}{\tau_r} + \frac{1}{\tau_{nr}}, \quad (2.6)$$

where τ_r is the radiative lifetime and τ_{nr} is the non-radiative lifetime of the 3H_4 manifold.

Thus the 3H_4 manifold has a measured lifetime, τ , in the form

$$\frac{1}{\tau} = \frac{1}{\tau_r} + \frac{1}{\tau_{nr}} + \gamma_x, \quad (2.7)$$

where γ_x is the rate of cross-relaxation. Note that the higher the cross-relaxation rate, the shorter the lifetime.

Therefore, although for example reducing the doping level to lower the heat deposition caused by the upconversion effect has been successfully employed in end-pumped Nd:YLF, [78], the counteracting effect, cross-relaxation, restricts the use of this strategy for Tm:YLF. Several routes exist for the excited population in the 3H_4 manifold to relax to the lower lying energy states, only a proportion of which will find its way into the upper laser level, 3F_4 , through cross-relaxation. The portion that make its way through cross-relaxation is defined by the factor quantum yield.

2.2.3 Quantum yield

Quantum-yield is the average number of excited ions in the upper laser level created per absorbed photon. For thulium systems, this parameter normally falls between 1 and 2, and varies with doping concentration. The quantum yield of a thulium doped material with certain doping concentration can be obtained from the equation [49]

$$\eta_{QY} = \frac{1 + 2 \left(\frac{C}{C_0} \right)^2 - \frac{\tau_0}{\tau_r} (1 - \beta)}{1 + \left(\frac{C}{C_0} \right)^2}, \quad (2.8)$$

where β is the branching ratio for radiatively populating the 3F_4 manifold from the 3H_4 manifold.

The quantum yield has a direct effect on the slope efficiency, as seen in equation A.34. In addition, with this in mind the power that goes into heat due to the quantum defect, P_{QD} , where quantum defect, is defined by the energy difference between the pump and laser photon, given by

$$P_{QD} = P_p \eta_a \left(1 - \eta_{QY} \frac{\lambda_p}{\lambda_l} \right), \quad (2.9)$$

where P_p is the incident pump power. The quantum yield therefore plays a very important role in both the output efficiency and the quantum defect, affecting both the laser performance and the heat load in the active medium.

Thus based on these equations, we have seen that quantum yield affects both the threshold and slope efficiency of the laser in a linear fashion, while upconversion primarily affects the threshold power. Therefore, by comparing the slope efficiency and threshold corresponding to differently doped crystals, with the same laser configuration, a relative figure for the quantum yield can be obtained for each concentration, and therefore helps to estimate a value for the quantum yield as a function of doping concentration. With

this knowledge, it is also possible to estimate the power lost to upconversion channels and the associated heat load. It should be noted that this relies on the validity of the model, which has not been firmly established.

2.3 Energy-transfer upconversion and cross-relaxation modelling

The equations in section 2.1 can be used to estimate the performance of a quasi-three-level laser, and also to demonstrate how it can be affected by upconversion and cross-relaxation. In this section, we show how these effects affect on measurable parameters such as the laser threshold and slope efficiency through modelled results. The aim is to demonstrate that these parameters are relatively independent and therefore in our experiments, where we used a multi-mode pump and signal system, they can be approximated as such.

The parameters used in the modelling are listed in table 2.1. They are based on a 2 at.% Tm:YLF rod with Gaussian pump and signal profiles. The pump size radius, w_p , of 500 μm is similar to the pump size used in the experiment as will be seen in section 2.5. The laser is assumed to be always operating, with equal laser and pump mode dimensions giving the ratio, $a \sim 1$, where a is defined by

$$a = \frac{w_p}{w_L}, \quad (2.10)$$

where w_L is the laser mode radius.

2.3.1 Effect of energy-transfer upconversion on laser performance

Figure 2.2 shows the predicted laser performance of a Tm:YLF laser with parameters detailed in table 2.1 for various upconversion rates, γ . The rates were chosen to vary by several orders of magnitude around the reported Tm:YAG upconversion rate of 10^{-18} [79–82]. When the upconversion strength increases from negligible to strong, the threshold increases by over 700 %, showing that upconversion can have a severe effect on the threshold power. Looking at the slope efficiency however, the same increase in upconversion has reduced the slope efficiency only by slightly more than 5 %, which is insignificant in comparison to the change in threshold. Therefore, under these conditions upconversion can be considered to affect threshold, with negligible effect on the slope efficiency.

Description	Symbol	Value
Doping density (cm^{-3})	N_0	2.64×10^{20}
Crystal length (cm)	l_r	2.4
Upper level effective lifetime (ms)	τ_{eff}	14
Boltzmann occupation factor for initial laser Stark level	f_2	0.286
Boltzmann occupation factor for final laser Stark level	f_1	0.033
Boltzmann occupation factor for initial pump Stark level	f_0	0.191
Lasing wavelength (nm)	λ_l	1909
Pump wavelength (nm)	λ_p	790
Spectroscopic emission cross-section at lasing wavelength (cm^2)	σ_{21}	8×10^{-21}
Spectroscopic absorption cross-section at pump wavelength (cm^2)	σ_{03}	18.3×10^{-21}
Pump radius (cm)	w_p	0.05
Laser mode radius (cm)	w_l	0.05
Intrinsic double-pass cavity loss	L	0.015
Output coupler reflectivity	R_{oc}	0.87
Quantum yield	η_{QY}	1.68

TABLE 2.1: Upconversion modelling parameters. Boltzmann factors calculated from NASA's energy level data at 300 K, lifetime and cross-sectional areas from reference [7] and the rest are experimental data.

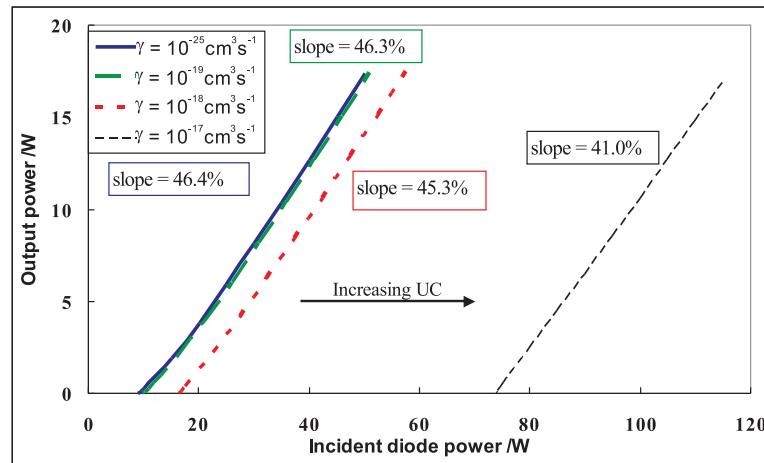


FIGURE 2.2: Modelled upconversion effect on threshold and slope efficiency based on equation A.21 and A.25

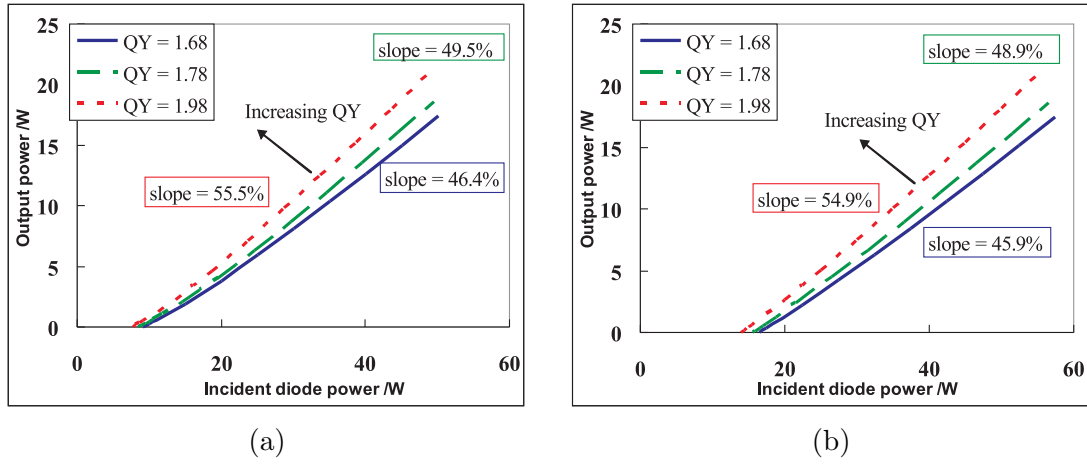


FIGURE 2.3: Modelled cross-relaxation effect on threshold and slope efficiency based on equation A.21 and A.25 (a) $\gamma = 10^{-25}$; (b) $\gamma = 10^{-18}$.

2.3.2 Effect of cross-relaxation on laser performance

In contrast to the previous section, figure 2.3 shows the predicted laser performance for various values of the quantum yield, η_{QY} , for negligible and a moderate strength upconversion rate. An important point is that output coupling is set to dominate other cavity losses. For increasing quantum yield, the slope efficiency also increases in all cases, while the threshold decreases proportionally. This is expected as quantum yield is directly proportional to the pump rate (see equation A.3), and laser threshold is dependent on the inversion. Therefore, according to the model, it is concluded that cross-relaxation affects the efficiency and the threshold pump power while upconversion only affects the threshold as discussed in section 2.2.

If the slope efficiencies for different concentration Tm:YLF crystals are compared in over-coupled lasers, where the output coupling is much larger than the cavity loss, the above analysis shows that this effectively provides the ratio of the quantum yield of each doping concentration. This result implies that the quantum yield may be separated from the upconversion effect, and when combined with the model for how quantum yield varies with concentration (equation 2.8) and the measured lifetimes of the upper laser level, an estimated quantum yield for each doping level can be obtained. Note that if enough data points were available, the quantum yield could be determined directly without the use of equation 2.8. This would require a very low or high doping concentration rod that had a quantum yield of one or two as reference; thus the quantum yield of the other doping crystals could be obtained directly from their relative slope efficiency. Note that a quantum yield of two is better due to the fact there could be some bad ions that could cause a quantum yield of lower than one in low doping concentration.

2.4 Thermally induced stress fracture

When a laser is being pumped, heat is generated in the excitation region according to the quantum defect and, if present, upconversion. In general, the generated heat is removed from the crystal via conductive cooling to a heat sink, creating a temperature gradient. Consequently, there is a non-uniform thermal expansion throughout the crystal leading to stress.

The thermally induced stress fracture is a limiting factor in power-scaling Tm:YLF lasers. Thus in order to design a power-scaled laser system, the ability to predict the maximum output power achievable by a certain system before fracture occurs is essential. Firstly, it is important to have an understanding of the parameters that thermal fracture depends on, being the material properties and thermal load per unit length, P_h/L . Secondly, it is important to understand how the absorbed power is converted, and to estimate how much is responsible for heating the crystal, including the quantum defect and upconversion processes. Armed with these predictive tools, a figure of merit can be defined for the maximum possible stress, allowing the determination of the fracture limit for other doping concentrations, and the design of a system that gives the maximum output power before fracture.

Thermally induced stress fracture is caused by non-uniform thermal expansion, therefore it is dependent on the thermal conductivity, thermal expansion coefficient, and stiffness (young modulus) of the material. A high conductivity would result in a smaller gradient, and combined with low thermal expansion coefficient, would lead to lower stress. Moreover, a distributed heat load is also important as it would help lower the peak temperature rise and thus the temperature gradient, which is why the thermal load per unit length should be considered instead of the total thermal load. The thermal load per unit length at which thermally induced fracture occurs in a uniformly-pumped, end-pumped rod is given by [60, 83],

$$\frac{P_h^{max}}{L} = \frac{8\pi\kappa(1-\nu)\sigma_{max}}{E\alpha_T}, \quad (2.11)$$

where κ is the thermal conductivity, ν is the Poisson's ratio, E is the Young's modulus, α_T is the thermal expansion coefficient and σ_{max} is the maximum stress the host can tolerate before fracture. All parameters on the right hand side of the equation are dependent on the host material. In the case of thulium-doped media, the cross-relaxation processes mean that the fraction of absorbed power converted to heat and the length over which this power is absorbed are both dependent upon the dopant concentration. Note that in non-uniform pumping where the pump size is smaller than the rod, the maximum stress occurring on the surface of the rod can increase by as much as a factor of 2 for a small pump size [84].

The absorbed power for the diode pumped laser crystal is converted into different output channels. The output channels comprise of useful radiant energy (output power) and non-useful radiant energy (fluorescence and cavity losses), which will be further discussed in section 3.1.7. The rest are non-radiative channels, caused by coupling to lattice phonons through the quantum defect and upconversion processes, causing heat deposition in the crystal lattice.

The power converted into heat due to the quantum defect is simply given by equation 2.9. On the other hand, upconversion increases proportionally with pump power until threshold, where the inversion is clamped (see section 2.2.1). Therefore, an estimate of the total heat input, P_h , combining heat deposition by quantum defect and upconversion, is given by

$$P_h = \left(1 - \eta_{QY} \frac{\lambda_p}{\lambda_l}\right) (P_{abs} - P_{DUC}) + P_{DUC} , \quad (2.12)$$

where P_{abs} is the absorbed pump power and P_{DUC} is the increase in threshold power due to upconversion; a quantity that is totally converted to heat. This equation can be used to find the heat load for a certain system, and combined with experimentally determined fracture limits to obtain a figure of merit of P_h/L for estimating the maximum achievable power for various Tm:YLF laser systems. Note that this assumes the average fluorescence wavelength is at the lasing wavelength, thus radiation balanced effect in athermal laser is not considered.

2.5 Tm:YLF laser characterisation setup

The laser characterisation experiment was performed with the help of Dr J.I. Mackenzie. Tm:YLF rods of doping concentration 2, 4 and 6 at.%, each of which were designed to be two absorption lengths long for a pump wavelength of 792 nm, giving 24 mm, 12 mm and 8 mm respectively, were used for laser performance characterisation. The characterisation setup was designed to give the same threshold in absence of cross-relaxation and upconversion processes. All rods were 3 mm in diameter, a-cut, had a fine ground finish on the barrel, and both ends were polished with antireflection coatings for the pump and lasing wavelengths at 790 nm and 1910 nm. All rods were mounted by sliding into drilled circular holes of heated copper blocks, where the blocks were the same length as the rods. Wax was applied to the interior surfaces of the holes in the blocks, liquified at the heated temperature before inserting the rods. This technique provides a very thin layer of wax to improve the surface contact between the heat-sink and the rod. The wax layer, with a thickness of only a few 10s μm , should only give a

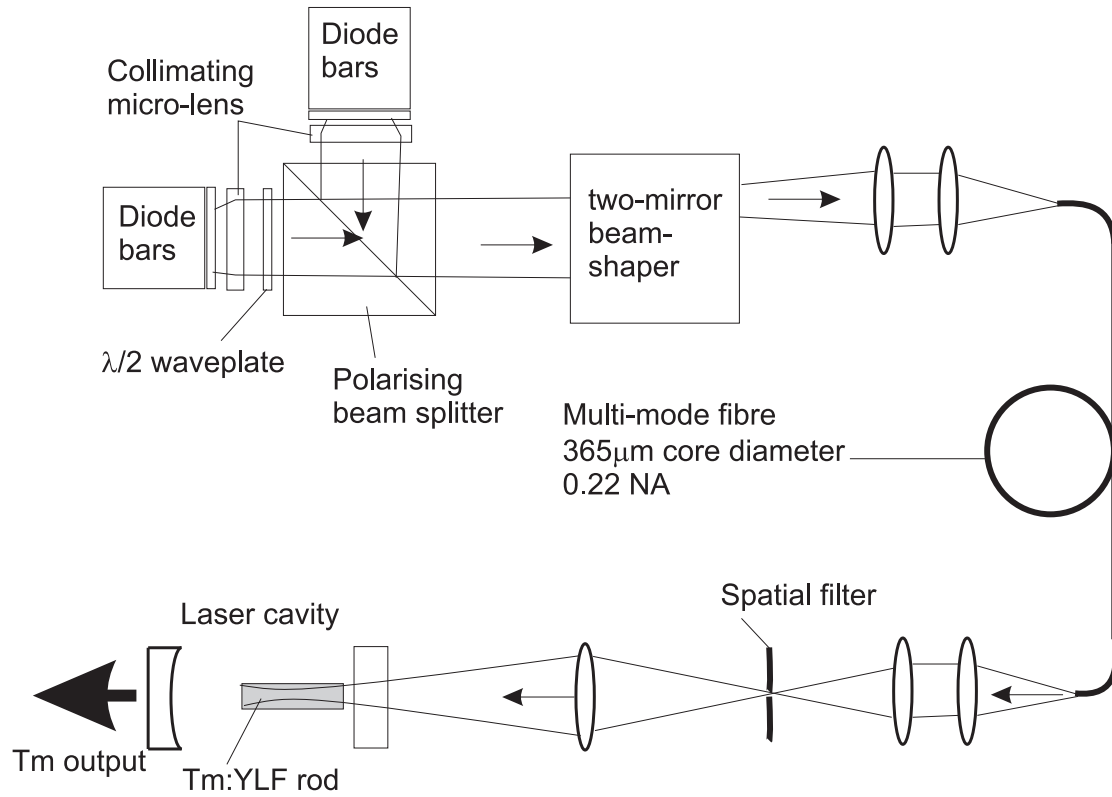


FIGURE 2.4: Pump configuration for Tm:YLF rod laser experiment

modest thermal resistance. The blocks were attached to water-cooled copper heat-sinks, maintained at 18 °C, with thermal paste in between to assist heat removal.

As shown schematically in figure 2.4, each crystal was end-pumped by two high-power, low-fill-factor, water-cooled diode bars that was setup by my colleagues. Micro-lenses were used to collimate the diode output in both fast and slow-axes, after which the two diode beams were polarisation combined to produce a single beam. The combined diode beams were then reshaped with a two-mirror beam-shaper [55] to roughly equalised beam propagation factors in the orthogonal planes, giving $M_x^2 \approx 80$ (parallel to array) and $M_y^2 \approx 52$ (perpendicular to array), with a maximum transmitted power of ~ 52 W. The beam was then ‘homogenised’ by coupling it into a multi-mode fibre of core diameter 365 μm and 0.22 NA. This creates a uniform quasi-top-hat pump profile, desirable for comparative studies between the three dopant concentrations.

The resultant output from the fibre gave an M^2 value of ~ 130 in a circular beam. A spatial filter was then employed to reduce the M^2 to ~ 100 , reducing the maximum pump power to ~ 33 W. This better beam quality was selected as it gave a longer Rayleigh range, making it possible to use confocal pumping in the longest rod.

A simple two-mirror cavity was used for the experiment, consisting of a plane input coupler and various reflectivity curved mirrors as output couplers. The plane pump input coupling mirror was coated for high reflectance at the lasing wavelength of ~ 1910 nm, and high transmission at pump wavelength of ~ 790 nm. Two concave output couplers were used with a radius of curvature, R_{OC} , of 200 mm, and transmission of 7.5 % and 13.5 % at the lasing wavelength. A cavity length of 100-120 mm was chosen to produce a calculated cold cavity TEM₀₀ mode radius of ~ 260 μm inside the crystal, which was predicted to only slightly increase when pumped due to weak negative thermal lensing in YLF, where the negative lensing from the $\frac{dn}{dT}$ is partially compensated by the positive lensing from the surface bulging [85, 86].

The pump beam was focused to a waist of ~ 470 μm radius, which is roughly equal to what is required for confocal pumping of the 2 at.% rod (i.e. $w_p = \left(\frac{M^2 \lambda_p l}{2n\pi}\right)^{\frac{1}{2}}$), and positioned at the mid-point of each laser rod. In this configuration, the Tm:YLF lasers were operated in a multi-transverse-mode regime to minimise the effect of thermally-induced lens aberrations on output power and efficiency.

2.6 Laser characterisation and analysis

Figure 2.5(a) and (b) show the output power versus incident pump power for the three Tm:YLF rods and the two output coupler transmissions of 7.5 % and 13.5 % respectively. A linear fit to the data points for pump powers greater than three times threshold was used to estimate the slope efficiency, which increases until the laser is operating several times above threshold, as is typical for quasi-three-level lasers [7].

Tm:YLF, due to its quasi-three-level nature and relatively broad emission spectrum (see figure 2.6), has an operation wavelength that is dependant upon the population inversion [7]. The operating wavelength for each output coupler was measured using a computer controlled $f=0.5$ m monochromator equipped with an extended-InGaAs detector. Approximately five peaks within an overall bandwidth of ~ 8 -9 nm was observed for both output couplers and rods of all doping concentrations. The centre wavelengths were 1.928 μm and 1.909 μm for the 7.5 % and 13.5 % output couplers respectively as shown in figure 2.7. Each laser operated on the σ -polarisation ($E \perp c$ -axis) without polarisation selection element.

The laser performance was also characterized for a range of heat sink temperatures from 15 °C to 45 °C, to determine the threshold power and lasing wavelength dependence on temperature. Absorbed power thresholds were measured, showing a linear increase of ~ 20 % over the temperature range. The lasing wavelength suffered a very slight

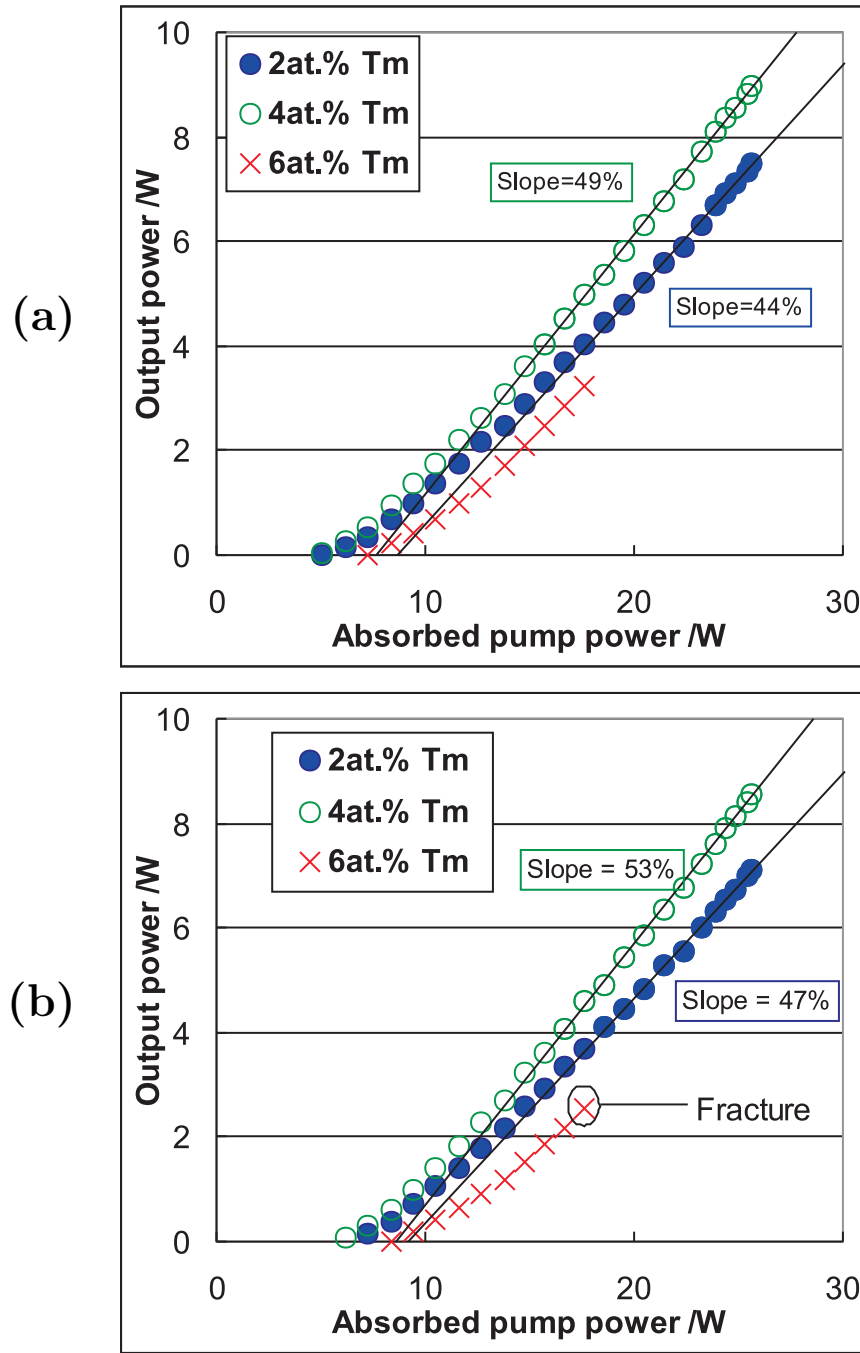


FIGURE 2.5: Laser performance for 2, 4 and 6 at.% Tm:YLF single-end-pumped rods with (a) 7.5 % and (b) 13.5 % output coupler transmission

change of <1 nm. The pump absorption over the crystal length for the same conditions decreased by only ~ 1.5 %.

It can be seen from figure 2.5(a) and (b) that increasing the output coupling transmission from 7.5 % to 13.5 % did not have a very marked effect on the slope efficiency indicating that the cavity loss was low compared to the output coupling, as expected. However, there is clearly a very pronounced effect of Tm doping level on the performance. Given

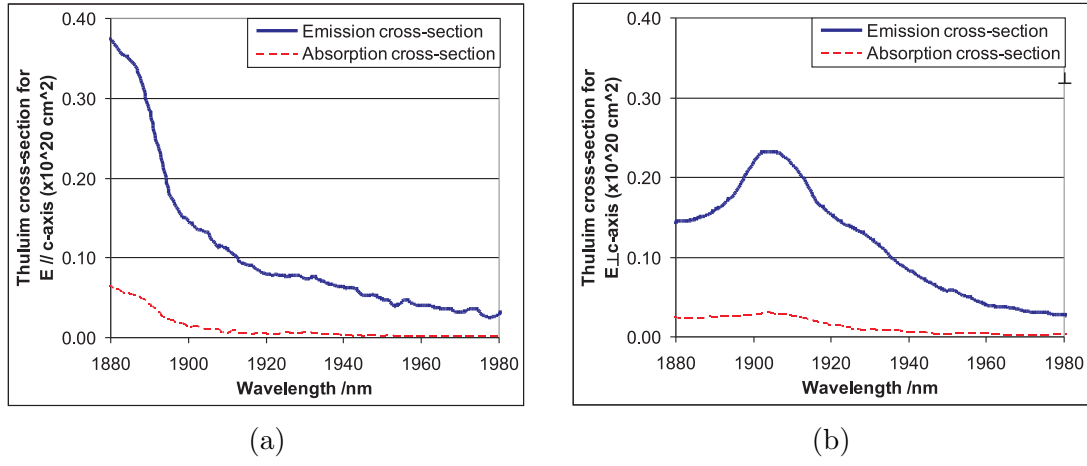


FIGURE 2.6: Tm:YLF emission cross-section [87] for (a) $E // c$ -axis; (b) $E \perp c$ -axis

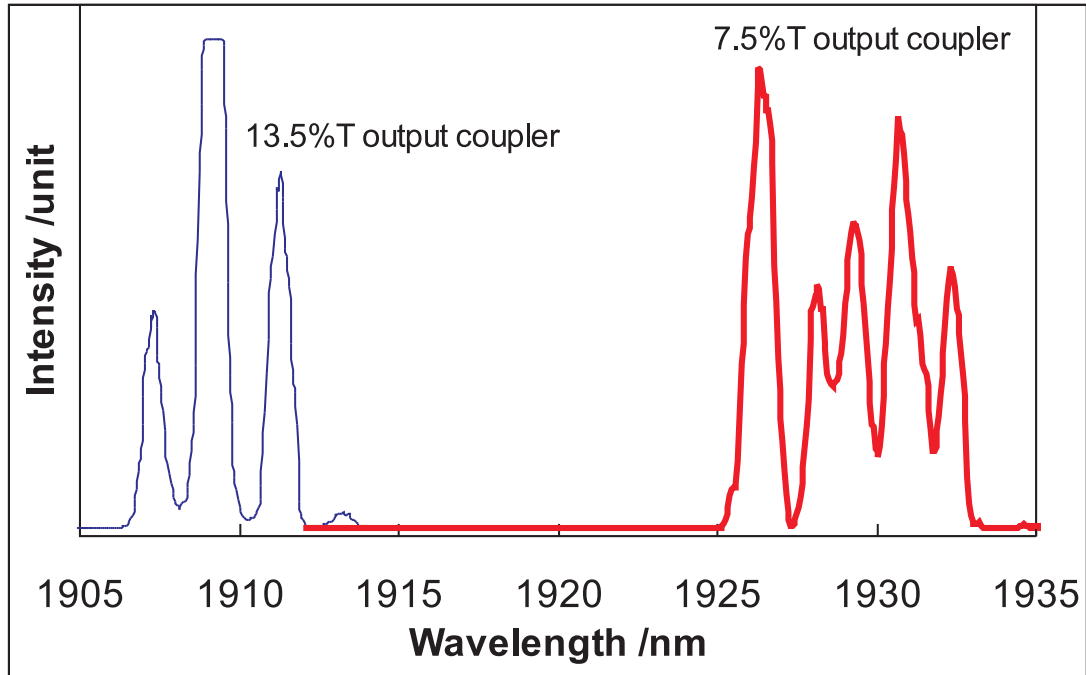


FIGURE 2.7: Tm:YLF rod laser measured operation wavelength for output coupler of 7.5 % and 13.5 % transmission

that all three Tm:YLF rods were operated under nearly identical conditions in terms of absorbed pump power, cavity loss, pump and laser mode sizes and re-absorption loss, we can draw the following conclusions.

2.6.1 Slope efficiency and quantum yield

From figure 2.5(a) and (b) we note that the 2 at.% crystal has on average a 0.89 times lower slope efficiency than the 4 at.% crystal. Given that upconversion has negligible effect on the slope efficiency according to the modelled results discussed in section 2.3.1),

we attribute the difference in slope efficiency to differences in quantum yield, η_{QY} , (see section 2.3.2). However, we are unable to draw any conclusion concerning the 6 at.% rod as thermal induced stress fracture occurred when only 2.4 times above threshold pump power when using the 13.5 % output coupler and thus an equivalent slope efficiency could not be derived. An estimate of the quantum yield as a function of doping concentration can be calculated, shown in figure 2.8, using equations described in section 2.2 and data in references [87, 88], and predicts a very similar ratio of 0.88. We are therefore confident in using the theoretical quantum yield versus doping level values in further power-scaling calculations. It should also be noted that the 53 % slope efficiency is much greater than the maximum possible in absence of cross-relaxation (41 %), and that the relatively small increase in slope efficiency from doubling the thulium doping concentration from 2 to 4 at.% is indicative of being in the nearly saturated quantum yield ≈ 2 regime.

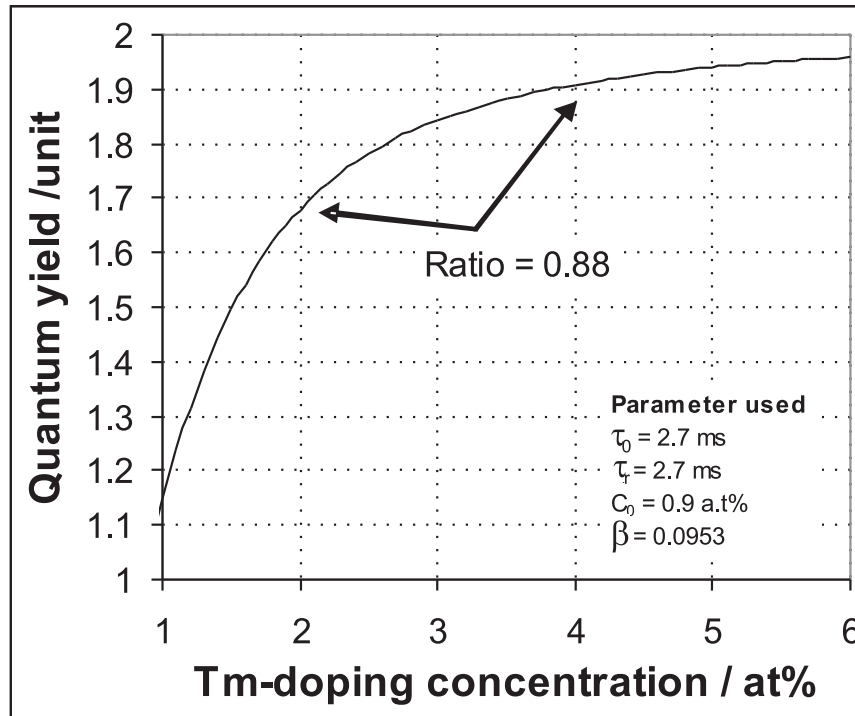


FIGURE 2.8: Quantum yield prediction for Tm:YLF

2.6.2 Threshold and upconversion rate

The relative quantum yield not only gives us the relative slope efficiency, it should also give the relative threshold in the absence of upconversion. Results in figure 2.5 shows a very small decrease in threshold from 5.9 W to 5.6 W in going from 2 to 4 at.% thulium doping, which is mostly accounted for by the change in quantum yield. The small increase in threshold after doubling the doping concentration suggested the

upconversion effects are small in this regime. It is therefore safe to make the assumption that the upconversion loss is zero for the 2 at.% doping for future calculations.

However, rather than a lower threshold due to a higher quantum yield, we find that the 6 at.% rod had a significantly higher threshold and indeed fractures at just 17 W of absorbed pump power. The observed threshold of 8.0 W is 2.9 W higher than we would expect from scaling the observed threshold from the 2 at.% rod solely accounting for the higher quantum yield. This power difference, P_{DUC} , is attributed to upconversion and is totally converted into heating the YLF crystal.

Note that both the diode and thulium power was measured with a 40 W power meter and digital display to an accuracy of 0.1 W. The power was incident directly onto the centre of the power meter without magnifying the spot size and gives a relatively stable reading for both the diode and thulium output. The accuracy of the measurement only has minimal effect on the laser performance result. On the other hand, the accuracy could affect the fracture limit prediction through the inaccurate prediction of thermal load due to upconversion.

2.7 Power limit

There are various factors that limit the power scalability of a laser system, such as available pump power, coating damage, thermal-optical properties and mechanical stress. The thermal-mechanical properties of the host material is a dominant failure mechanism, especially for YLF, and one of the aims of this experiment is to determine its stress-fracture limit as a function of doping level. The fracture limit mainly depends on the host material properties. However, there is also a dependence on the pump beam size, rod diameter and power distribution, which can be optimised by choosing the appropriate pump size and geometry for the active media. Using the laser performance result discussed in section 2.6 and the estimated value of quantum yield, a measure of the heat loading in the system is found. As such, a figure of merit at which fracture of the crystal is likely to occur can be defined to assist in finding the optimum configuration and design to maximize the pump power limit.

As shown in table 2.2, the estimated heat power at which fracture occurred for the 6 at.% rod was 5.5 W. The thermal load per length in the first absorption length, $\frac{P_h^{max}}{L} \approx 10.8 W cm^{-1}$, can be used as the figure of merit for thermal fracture limit calculations when comparing various doping levels and rod lengths.

Given our experimental results for the slope efficiency (with respect to absorbed power), η_s^{abs} , for the 2 and 4 at.% doped rods, we are able to make an estimate of the maximum

Thulium doping level (at.%)	1	2	3	4	6
Quantum yield	1.15	1.68	1.84	1.91	1.96
Slope efficiency (%)	32	47*	51	53	55
Absorption coefficient (cm ⁻¹)	0.36	0.71*	1.07	1.43*	2.14*
Absorbed threshold power (W)	7.9	5.9*	5.6**	5.6*	8.0*
Threshold in absence of UC (W)	7.9	5.9	5.6**	5.2	5.1
P_{UC} (W)	0	0	0**	0.4	2.9
P_h^{max} (W)	33.0	16.5	11.0	8.2	5.5
Maximum absorbed power (W)	63.4	55.1	47.2	38.7	17.0*
Effective threshold	13.4	9.2*	8.4	8.7*	-
Maximum output power (W)	16.0	21.6	19.8	15.9	2.5*

TABLE 2.2: Power-scaling calculations. *indicates an experimental value. ** indicates assumed values for 3 at.% leading to an optimistic power scaling. All other values are either theoretical or scaled from experimental values

output power achievable, P_o^{max} , for the various doping concentration using a plane wave equation

$$P_{out}^{max} = \eta_s^{abs} (P_p^{abs-max} - P_{th}^{abs}) , \quad (2.13)$$

where $P_p^{abs-max}$ is the maximum absorbed power before thermally induced stress fracture occurs and P_{th}^{abs} is the threshold absorbed power as shown in table 2.2. The maximum absorbed power for each rod is calculated using equation 2.12 as referenced to the figure of merit determined from the 6 at.% rod, with the results shown in table 2.2.

The results in table 2.2 predict the optimum doping of 2 at.%, is lower than the 3 at.% used by previous workers [33, 89]. This is despite the fact that we take the optimistic power-scaling assumption that the upconversion is still negligible at the 3 at.% doping level. It should be noted that the prediction for output powers used effective thresholds found from the slope efficiency fits shown in figure 2.5, or by scaling from them.

In order to gain some experimental verification of these power-scaling predictions we increased the power of the pump source to allow us to reach fracture point of the 4 at.% rod. This experiment, performed by my colleague Dr. Jacob Mackenzie, using a new pump source consisting of a six-bar low-fill-factor diode stack, with each bar collimated in the fast and slow axes with micro-lenses. The final beam-shaped diode stack beam quality was $M_x^2 \approx 160$ and $M_y^2 \approx 100$ with a maximum pump power of 265 W. To produce a similar beam quality from the diode stack as had been used previously, a spatial filtering slit was employed in the x-axis only, limiting the available incident

power to 115 W. With identical pump parameters and cavity configurations as used for diode-bar pumping, the results shown in figure 2.9 were obtained. Once again the ratio of the slope efficiencies fitted three times above threshold (0.92) was in fair agreement with that expected from the theoretical quantum yield curve of figure 2.8(0.88). Furthermore, the 4 at.% rod fractured at an absorbed power of 38.5 W and an output power of 14.5 W, in good agreement with our scaling predictions of 38.7 W and 15.9 W, respectively.

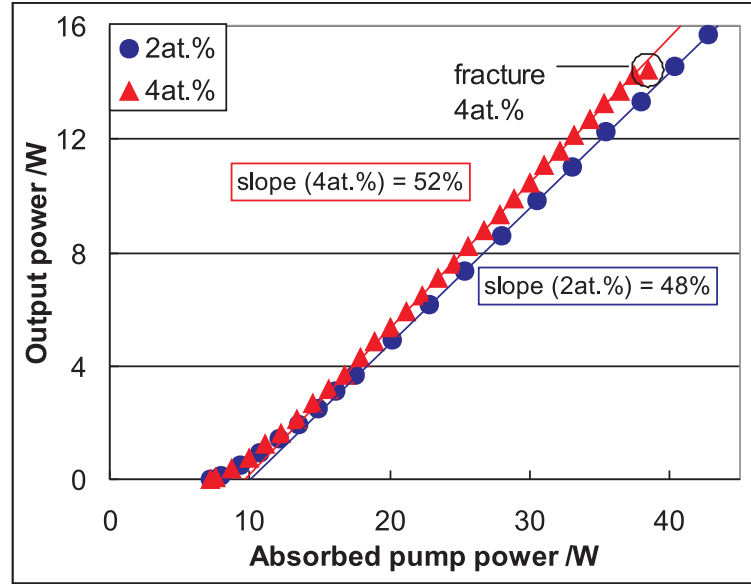


FIGURE 2.9: Laser performance for Tm:YLF rods of 2 and 4 at.% using diode-stack pumping

The results not only indicate that 2 at.% is the optimum doping concentration for end-pumped power scaling, but also that end-pumping of a single Tm:YLF rod will not achieve output powers much greater than 20 W. This is consistent with the work of Budni et al. [33, 89], who have demonstrated 22 W from a single 3 at.% doped Tm:YLF rod, with undoped end-caps, to further increase the stress fracture limit. A factor-of-two improvement should be available, according to theory [84], if the pump nearly fills the rod aperture, but this is not sufficient to reach the 100 W output power regime. To go beyond this power level requires the use of multiple rods in one cavity. It should be noted that one could also use a slab geometry to elevate this power limitation.

2.8 Gain medium geometry

It is well known that a uniformly pumped slab geometry, with its large cooling surfaces, benefits from an increase in fracture limit when compared to a rod. In the case of a

uniformly pumped slab, the maximum heat input per unit length is given by [60, 83]

$$\frac{P_h^{max}}{L} = \frac{12\kappa(1-\nu)\sigma_{max}}{\alpha_T E} \frac{2w_{px}}{t}, \quad (2.14)$$

where $\frac{2w_{px}}{t}$ is the ratio of the pump width diameter to thickness of the slab [83]. Making the comparison between equations 2.11 and 2.14, for the rod and slab geometries, it suggests that the slab can accept $\sim \frac{w_{px}}{t}$ times higher $P_h\alpha_{abs}$ [60, 61]. Therefore a 10 mm-wide and 1 mm-thick slab with the pump width filling most of the slab, gives a five fold improvement in the maximum heat load before fracture over the rod. Moreover, because the slab geometry is highly compatible with the diode pump sources, the requirements on the pump beam size and quality in the slow axis are not very demanding thus simplifying the overall pump focusing system. This clearly gives greater freedom on the choice of pump size and quality for power scaling. The down-side for the slab configuration is the incompatibility of the highly elliptical mode with normal resonator configurations which would result in poor beam quality, particularly in the width direction. However, for our application, a highly multi-mode flat-top output profile can actually be desirable for uniform-pumping of the Ho:YAG crystal to avoid thermal lens aberrations.

2.9 Conclusion

We have developed a power-scaling strategy for taking the 2- μ m output of Tm:YLF lasers into the 100 W regime. The strategy is based on scaling from carefully designed low-power laser experiments, which automatically include the various competing heat-deposition effects occurring in the laser system. In addition, an estimated quantum yield and upconversion parameter were deduced for several thulium concentrations, then used to predict the heat load and performance limitation for each crystal. Fracture has been observed in the 4 and 6 at.% rod, helping to define a figure of merit and thereby estimating the power scalability of Tm:YLF as a function of doping level. We find an optimum thulium doping level, providing the maximum output power before thermally induced fracture, of 2 at.%. Combining these values with simple scaling laws, we identify that the slab geometry is a better choice for power scaling to the 100 W regime due to the potentially higher stress fracture limit provided by distributing the heat load sideways.

Chapter 3

Power scaling of end-pumped Tm:YLF slab lasers

As we have seen in chapter 2, Tm:YLF rods, limited by thermally induced stress fracture, have difficulty in achieving an output power much greater than 20 W from a single rod laser. The highest power demonstrated, before this work, from a single gain element was by Budni [33, 89], who demonstrated 22 W from a single 3 at.% doped Tm:YLF rod, using undoped end-caps to help increase the stress fracture limit. In order to power scale Tm:YLF to power levels much greater than 20 W, this limitation must be overcome.

Power-scaling requires the determination of the underlying effects that generate heat and therefore stress, such as the quantum defect and upconversion, which would allow us to optimise the laser crystal dimensions, geometry and doping concentration. The results in chapter 2 provide an estimate for the heat power contribution from upconversion and the quantum defect, which when combined with the known fracture limits and laser performance characteristics, can allow us to predict maximum pump and output powers. Moreover, the calculations in section 2.7 predict that a 2 at.% doping concentration is the optimum doping in terms of distributing the heat power in direction of pump propagation while maintaining a good laser performance. In addition, they support the notion that the slab geometry provides better extraction of this heat than that of a rod, with output powers of much greater than 20 W being possible. Unfortunately, this geometry is not compatible with circular output modes, and tends to deliver non-diffraction limited and non-symmetric output without careful control. However, this is not necessarily a big drawback when used as a power-scaled pump source, as the effort to obtain diffraction-limited output can then rather be transferred to the final Ho:YAG laser.

In this chapter a plane-wave model is presented, which will be used to predict the slab laser performance. This is followed by a description of the experimental setup and a full characterisation of the Tm:YLF slab laser. The laser results and the fracture limit are then compared to the model and discussed, including suggestions for further power scaling and improving the beam quality for alternative applications. This laser was later used as a platform to scale the power of Ho:YAG lasers, as described in chapters 4 and 5.

3.1 Plane-wave analysis

Many models have been proposed for predicting laser performance [75–77, 90, 91], mostly based on rate equations including the spatial coupling of the pump and laser fields in the active host. The equations presented in section 2.1 are based on a model for predicting laser performance using rate equations derived by T.Y. Fan [90]. The model was originally derived for an end-pumped, quasi-three-level, Nd:YAG laser system and takes into account the spatial distribution and overlap of the pump and laser modes. It has been modified in section 2.1 to take account of upconversion and cross-relaxation in the thulium system. The model suits most of our needs but, unfortunately, it is difficult to use it to model a laser system whose spatial distributions for either the laser or pump radiation are not well defined, which is the case for our high-power diode-pumped slab laser, or if a significant number of ions were excited out of ground state, thus changing the absorption properties of the active media. In the experiments described in this chapter, the pump beam was a highly multi-mode, approximately top-hat, distribution and can be approximated as a simple plane wave. Similarly, the laser output is also expected to be multi-mode in nature. Thus, a simple plane-wave analysis can be used, while still providing a good prediction for the laser performance characteristics, such as threshold and expected output power as a function of pump power.

Presented here is a model based on Beach’s plane wave analysis [92] for the thulium laser system described in this chapter. The model takes into account ground-state depletion, gain saturation, and energy transfer mechanisms such as cross-relaxation and upconversion. Another benefit of this model is that it gives simple equations describing the conversion of the absorbed pump power into various output channels, namely fluorescence, quantum defect, upconversion loss, output power and intrinsic cavity loss. This is useful for estimating the thermal load when calculating the fracture limits of the crystal. It does not, however, provide the specifics of the spatial dependence of the excitation.

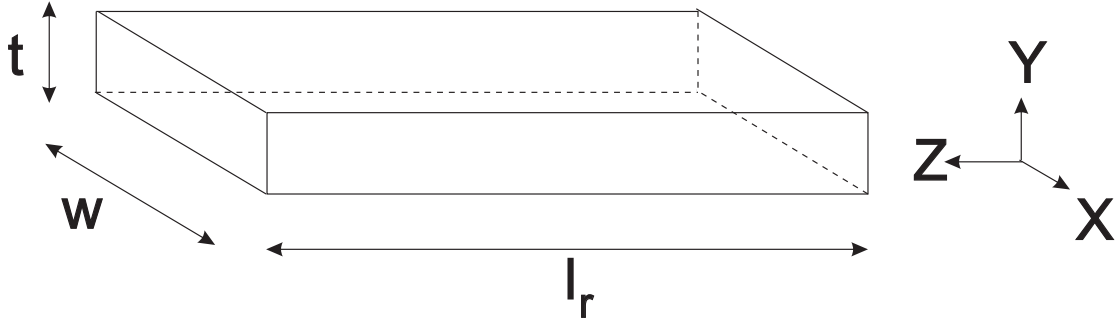


FIGURE 3.1: Slab dimensions and axes direction

The solution of this plane-wave analysis is a simple equation that relates the input pump power, output power, slope efficiency and threshold of the laser. This relationship is given by

$$P_o = \eta_s(P_p - P_{th}) , \quad (3.1)$$

where P_o is the laser output power, η_s is the laser slope efficiency, P_p is the diode pump power and P_{th} is the threshold pump power of the laser system. Normally, for a quasi-three-level laser system, the slope efficiency is expected to increase as the system is pumped higher above threshold, due to the effect of spatially varying ground state reabsorption [93]; this feature is not shown in the plane-wave model.

3.1.1 Single-pass absorption

Under plane-wave end-pumping, assuming the optic axis is parallel to the length of the laser crystal, l_r , with width, w , and thickness, t , as shown in figure 3.1, it will have a single-pass-absorption of the incident pump power, F_A , given by,

$$F_A = 1 - \exp \left(-\sigma_{abs}^{LB}(\lambda_p, T) \int_{z=0}^{z=l_r} [N_L(z) - \frac{f_3}{f_0} N_B(z)] dz \right) , \quad (3.2)$$

where $\sigma_{abs}^{LB}(\lambda_p, T)$ is the manifold absorption cross-section at the pump wavelength λ_p promoting an electron from lower laser manifold (L) to the upper pump manifold (B) as shown in figure 2.1 (from 3H_6 to 3H_4), $N_L(z)$ is the population density of the lower laser manifold, $N_B(z)$ is the population density of the upper pump manifold and the z -axis corresponds to integration along the length of the crystal. f_0 and f_3 are the Boltzmann occupation factors of the particular Stark levels involved in the pumping process in the lower laser manifold and the upper pump manifold, respectively. The ratio of these factors is equal to the manifold cross-section ratio given by [94]

$$\frac{f_3}{f_0} = \frac{\sigma_{em}^{BL}(\lambda_p, T)}{\sigma_{abs}^{LB}(\lambda_p, T)} , \quad (3.3)$$

where $\sigma_{em}^{BL}(\lambda_p, T)$ is the manifold emission cross-section from the upper pump manifold (B) to the lower laser manifold (L). Note that the notations used here are similar to the ones in chapter 2 (see figure 2.1) and differ slightly to those used by Beach [92].

Tm³⁺ ions excited to the 3H_4 energy state can undergo a cross-relaxation process (see thulium energy level diagram in figure 2.1) thus, it is possible to achieve quantum yields of up to 2 (see section 2.2.3). However, the population density in the upper two manifolds, N_B and N_A , can be assumed to be ~ 0 due to the much longer decay lifetime of the upper laser manifold, 3F_4 , (on the order of 10 ms) when compared to the effective lifetime of manifolds 3H_4 and 3H_5 (both on the order of μs) [7, 87]. Therefore, it is possible to assume that all the population lies within the two manifolds 3F_4 and 3H_6 , i.e.,

$$N_U(z) + N_L(z) = N_T, \quad (3.4)$$

where $N_U(z)$ is the population density in the upper laser level and N_T is the active ion doping density.

Key to this model is the definition of length-integrated inversion density, n_p , referenced to the Stark levels coupled by the pump radiation as a function of the length-integrated excited ion density, n_U , given by

$$\begin{aligned} n_p &= - \int_{z=0}^{z=l_r} [N_L(z) - \frac{f_3}{f_0} N_B(z)] dz, \\ &= - \int_{z=0}^{z=l_r} N_L(z) dz, \\ &= \int_{z=0}^{z=l_r} [N_U - N_T] dz, \\ &= n_U - N_T l_r, \end{aligned} \quad (3.5)$$

$$(3.6)$$

where l_r is the length of the crystal. Note the upper pump level population, N_B , is assumed to be empty as stated above. The length-integrated excited ion density, n_U , is given by the expression

$$n_U = \int_{z=0}^{z=l_r} N_U(z) dz. \quad (3.7)$$

The single-pass absorption in equation 3.2 can thus be simplified by substituting in equation 3.5, and can now be rewritten as

$$F_A = 1 - \exp(\sigma_{abs} n_p). \quad (3.8)$$

3.1.2 Rate of excitation

The rate of excitation is the rate at which photons are absorbed in the active medium, thus creating a population of ions excited to the upper laser level. This process involves the cross-relaxation process as described in section 2.2.2, and thus requires an extra parameter called quantum yield as shown in section 2.2.3, when compared to Beach's equation [92]. The rate at which the excited population is created, taking into account a double-pass pump configuration, is given by,

$$\begin{aligned} R_{ex} &= \eta_{QY}\eta_{del}\frac{P_p}{h\nu_p}F_A + \eta_{QY}\eta_{del}\frac{P_p}{h\nu_p}(1 - F_A)R_pF_A , \\ &= \eta_{QY}\eta_{del}\frac{P_p}{h\nu_p}F_A(1 + R_p(1 - F_A)) , \end{aligned} \quad (3.9)$$

where η_{QY} is the quantum yield, η_{del} is the pump delivery efficiency, h is Planck's constant, ν_p is the pump photon frequency, and R_p is the reflectivity of the pump reflector for a double-pass of the pump power. The pump delivery efficiency, η_{del} , includes losses through the optics chain from the diode to the input end of the active medium. This, when combined with the pump power, P_p , could be replaced by the incident power, P_{inc} .

3.1.3 Single-pass emission

In analogy to the single-pass absorption derived in section 3.1.1, the single-pass emission, F_B , can be written as

$$F_B = - \left(1 - \exp(\sigma_{em}^{UL}(\lambda_l, T) \int_{z=0}^{z=l_r} [N_U(z) - \frac{f_1}{f_2}N_L(z)]dz) \right) , \quad (3.10)$$

where $\sigma_{em}^{UL}(\lambda_l, T)$ is the manifold emission cross-section at the lasing wavelength, λ_l , from the upper laser manifold (U) to the lower laser manifold (L) (3F_4 to 3H_6). f_1 and f_2 are the Boltzmann occupation factor of the particular Stark levels involved in the lasing process for the lower and upper laser manifolds, respectively. The ratio of these factors is equal to the manifold cross-section ratio given by [94]

$$\frac{f_1}{f_2} = \frac{\sigma_{abs}^{LU}(\lambda_l, T)}{\sigma_{em}^{UL}(\lambda_l, T)} , \quad (3.11)$$

where $\sigma_{abs}^{LU}(\lambda_l, T)$ is the manifold absorption cross-section from the lower laser manifold (L) to the upper laser manifold (U).

The length-integrated inversion density referenced to the Stark levels coupled by the laser radiation, n_l , is given by

$$\begin{aligned}
 n_l &= \int_{z=0}^{z=l_r} [N_U - \frac{f_1}{f_2} N_L] dz \\
 &= \int_{z=0}^{z=l_r} [(1 + \frac{f_1}{f_2}) N_U - \frac{f_1}{f_2} N_T] dz \\
 &= (1 + \frac{f_1}{f_2}) n_U - \frac{f_1}{f_2} N_T l_r .
 \end{aligned} \tag{3.12}$$

Similar to equation 3.8, substituting equation 3.12 into equation 3.10 gives,

$$F_B = -(1 - \exp(\sigma_{em} n_l)) . \tag{3.13}$$

3.1.4 Rate of de-excitation

The rate of de-excitation includes all the losses within the crystal such as fluorescence and energy-transfer upconversion, and the stimulated emission that provides amplification of the laser signal and output coupling. Firstly, a lossless output coupler is assumed (one that only reflects and transmits, but does not scatter or absorb), thus the cavity power, P_{cav} , reflected back into the cavity by the output coupler of reflectivity, R_{oc} , is given by

$$P_{cav} = P_o \frac{R_{oc}}{1 - R_{oc}} , \tag{3.14}$$

where P_o is the output power.

Secondly, all passive cavity losses, excluding the output coupling and ground state re-absorption, are assumed to be located at the high reflector end of the laser cavity and equivalent to a one-way cavity transmission of T_c . Finally, similar to the rate of excitation, the de-excitation rate, R_{de-ex} , can be written as

$$\begin{aligned}
 R_{de-ex} &= \frac{P_o}{h\nu_l} \frac{R_{oc}}{1 - R_{oc}} F_B + \frac{P_o}{h\nu_l} \frac{R_{oc}}{1 - R_{oc}} (1 + F_B) T_c^2 F_B + \frac{n_U A}{\tau_{eff}} , \\
 &= \frac{P_o}{h\nu_l} \frac{R_{oc}}{1 - R_{oc}} F_B (1 + T_c^2 (1 + F_B)) + \frac{n_U A}{\tau_{eff}} ,
 \end{aligned} \tag{3.15}$$

where ν_l is the laser transition frequency, and A is the cross-sectional area of the excited pump area. Furthermore, τ_{eff} is the effective lifetime of the manifold depending upon radiative lifetime, τ_r , non-radiative decay lifetime, τ_{nr} , and other excited state energy transfer processes such as upconversion (assumed distributed uniformly along length of gain medium) given by

$$\frac{1}{\tau_{eff}} = \frac{1}{\tau_r} + \frac{1}{\tau_{nr}} + \gamma \frac{n_U}{l_r} , \tag{3.16}$$

where γ is the overall upconversion parameter accounting for all upconversion pathways from the manifold [9].

3.1.5 Steady-state operation

Under steady-state operation, the excitation and de-excitation rates are equal. Combining equations 3.9 and 3.15 gives

$$\eta_{QY}\eta_{del}\frac{P_p}{h\nu_p}F_A(1+R_p(1-F_A)) = \frac{P_o}{h\nu_l}\frac{R_{oc}}{1-R_{oc}}F_B(1+T_c^2(1+F_B)) + \frac{n_U A}{\tau_{eff}}. \quad (3.17)$$

This can be re-arranged into a form similar to equation 3.1 such that,

$$P_o = \eta_{mode}\eta_{QY}\eta_{del}\frac{1-R_{oc}}{R_{oc}}\frac{\nu_l}{\nu_p}\frac{F_A(1+R_p(1-F_A))}{F_B(1+T_c^2(1+F_B))} \times \left(P_p - \frac{n_U A}{\tau_{eff}}\frac{h\nu_p}{\eta_{QY}\eta_{del}}\frac{1}{F_A(1+R_p(1-F_A))} \right), \quad (3.18)$$

where η_{mode} is the mode-fill efficiency, which is introduced such that it takes into account the scenario where the laser mode does not completely fill the gain region.

Comparing equation 3.1 with equation 3.18, the threshold and slope efficiency come into their final forms, that is,

$$P_{th} = \frac{n_U A}{\tau_{eff}}\frac{h\nu_p}{\eta_{QY}\eta_{del}}\frac{1}{F_A(1+R_p(1-F_A))}, \quad (3.19)$$

$$\eta_s = \eta_{mode}\eta_{QY}\eta_{del}\frac{1-R_{oc}}{R_{oc}}\frac{\nu_l}{\nu_p}\frac{F_A(1+R_p(1-F_A))}{F_B(1+T_c^2(1+F_B))}. \quad (3.20)$$

As shown in the equations above, the upconversion, through the effective lifetime, affects the threshold but not the slope efficiency, while the quantum yield, cross-relaxation, is found to modify both.

3.1.6 Excited ion population at threshold

Under steady-state operation, the laser power should be the same after a round-trip in the cavity, giving the gain=loss condition. This can be re-expressed using the length-integrated inversion density,

$$e^{2\sigma_{em}n_l}T_c^2R_{oc} = 1, \\ n_l = \frac{1}{2\sigma_{em}^{UL}}\ln\frac{1}{T_c^2R_{oc}}, \quad (3.21)$$

and thus from equation 3.12 the length-integrated excited ion density is

$$n_U = \frac{1}{1 + \frac{f_1}{f_2}} \left(\frac{1}{2\sigma_{em}^{UL}} \ln\left(\frac{1}{T_c^2 R_{oc}}\right) + \frac{f_1}{f_2} N_T l_r \right) . \quad (3.22)$$

3.1.7 Output channels

After the pump power is absorbed, it is divided into different output channels determined by the active medium spectroscopy. As pump power is absorbed, a certain percentage of the pump power is first deposited into the crystal as heat due to the energy difference between the pump and laser photons. This is known as the quantum defect, and the power loss that goes into this process, P_{QD} , is given by

$$P_{QD} = \left(1 - \eta_{QY} \frac{\nu_l}{\nu_p} \right) P_p \eta_{del} F_A (1 + R_p (1 - F_A)) , \quad (3.23)$$

where the part outside the first bracket is essentially the absorbed pump power with double-pass pumping. Note that this is identical to equation 2.9 but using different notation.

The excited ions have a limited lifetime before their energy is released, that is the inverted population would decay exponentially via radiative or non-radiative pathways, in the absence of lasing and effects such as upconversion and cross-relaxation. The radiative decay would give out fluorescence at wavelengths corresponding to allowed transitions and with random propagation directions. It is purely a power loss process that does not create heat in the lattice. On the other hand, the non-radiative decay does transfer the energy to the lattice of the host medium in the form of phonons, thus generating heat. Fortunately, in Tm:YLF the non-radiative decay process is very weak from the upper laser level, when compared to fluorescence, and is therefore unimportant. The power converted into fluorescence, P_{fl} , is given in the form

$$P_{fl} = h\nu_l \frac{n_U A}{\tau_r} . \quad (3.24)$$

Note that τ_r is used in this equation instead of τ_{eff} that was used for calculating the laser performance. If τ_{eff} is used, it will also include the power loss due to upconversion.

Although τ_{eff} defines the effective lifetime of the upper laser manifold, it is useful to find the power loss due to upconversion separately. The power loss due to upconversion, P_{UC} , results in heat generation in the active media, as discussed in section 2.2.1, and is given by

$$P_{UC} = h\nu_l \gamma \frac{A n_U^2}{l_r} . \quad (3.25)$$

Note that this is identical to equation 2.4 but with different notations.

Under steady-state lasing, a certain percentage of the laser power escapes through the output coupler resulting in output power, P_o , and the rest remains in the cavity. Intrinsic cavity losses, such as scattering and absorption loss from coatings or crystal lattice can be described as another output channel. The power lost from the cavity given by,

$$P_{lost} = P_o \frac{R_{oc}}{1 - R_{oc}} (1 + F_B)(1 - T_c^2) , \quad (3.26)$$

where it is assumed that all the cavity losses have been combined into one loss component located between the high-reflective mirror and the active media for simplicity.

The output channels can be used as a check for the model such that no absorbed power goes missing. This is done using the simple equation

$$P_{abs} = P_o + P_{lost} + P_{QD} + P_{UC} + P_{fl} . \quad (3.27)$$

Moreover, as shown in the analysis in chapter 2, the heating power in the crystal is simply $P_{QD} + P_{UC}$, therefore these equations provide a way to estimate the heat deposition.

3.2 Experimental setup

In chapter 2 we have presented the performance characteristics of high-power Tm:YLF rod lasers. However, as discussed in section 2.7 the output power is limited to ~ 20 W per rod gain element, limited by thermally induced stress fracture. We also recommended that a slab geometry would prove better for power-scaling. Thus, the laser setup was redesigned, to use a slab geometry for the Tm:YLF crystal and we employ a simple cavity to explore the experimental limits of the thermal fracture and maximum achievable output power. In this section we describe the experimental setup for such a power-scaled Tm:YLF laser, and demonstrate five-fold improvement in output power over a single rod geometry.

3.2.1 Pump configurations

The pump source for Tm:YLF has significant restrictions on its spectral radiance and brightness due to the quasi-three-level nature of the $2 \mu\text{m}$ transition. A small spectral bandwidth well matched to Tm:YLF absorption is needed to provide good absorption over a short crystal length. A good pump beam quality is also desirable as it reduces

average pump size in the active medium, thus reducing the threshold pump power requirement.

3.2.1.1 Single diode stack pumping

Two different pump configurations have been used with this experiment. The first configuration consisted of a single vertical diode-bar array stack. The nLIGHT 6-bar, low-fill-factor stack¹ is mounted on a copper heat sink with water at a temperature of $\sim 17^\circ\text{C}$ flowing through its micro-channels. A $5\ \mu\text{m}$ water filter was used to filter out large particles to prevent blockage of the micro-channels, which may lead to overheating of the stack and thus damage the diodes. A de-ioniser was also employed in the water loop to maintain the water conductivity between 0.25-0.5 M Ω -cm, to prevent corrosion of the channels. Water pressure in the heat exchanger² is maintained at a flow rate of 2 litres/min for which a pressure drop of 32 psi across the heat exchanger was observed. The stack is driven by a Delta Elektronika power-supply³, capable of producing very stable voltage or DC current (0.004% – 0.010% over 8 hours after 1 hour warmup) with low ripple and spikes (ripple+noise, rms/peak-peak at 3.5/17 mV and 20/60 mA), for the ranges in voltage 0-45 V and current 0-70 A. The driver requires a three-phase input power supply, and has an operating efficiency around 90 %. When operating at a recommended maximum operating current of 50 A, the voltage drop across diodes and wire resistance was ~ 12 V. The diode stacks are contained in a box to prevent dust from covering the stack, with a hole to let the power out.

The water temperature was adjusted such that the stack operated at a wavelength of 792 nm at maximum pump power, which increased from a wavelength of 788 nm at threshold, and typically had a spectral bandwidth (FWHM) of 3 nm. The wavelength corresponds well with the measured Tm:YLF absorption cross-section for both polarisations, as shown in figure 3.2. The TM polarised stack gave a maximum output power of 300 W before the collimating lenses, corresponding to 50 W per bar.

Each low-fill-factor diode-bar has 19 emitters on a $500\ \mu\text{m}$ pitch, which allowed slow-axis (x-axis) collimation, therefore both fast (y-axis) and slow axes were collimated using micro lenses [95, 96]. As such, each bar of the stack was followed by an individual fast-axis collimating cylindrical lens, followed by a micro-lens array of cylindrical lenses to collimate the slow-axis of each emitter. The slow axis lenses were in the form of an array matched to the bar emitter array and fixed on a home-made mount that had adjustment in the two horizontal axes. An M^2 beam quality of 450 by 40 for the slow and fast axes

¹nLIGHT / Vertical stacked arrays / model: customized

²Thermo Neslab / model: System I water-water heat exchanger

³Delta Elektronika / model: SM45 70D

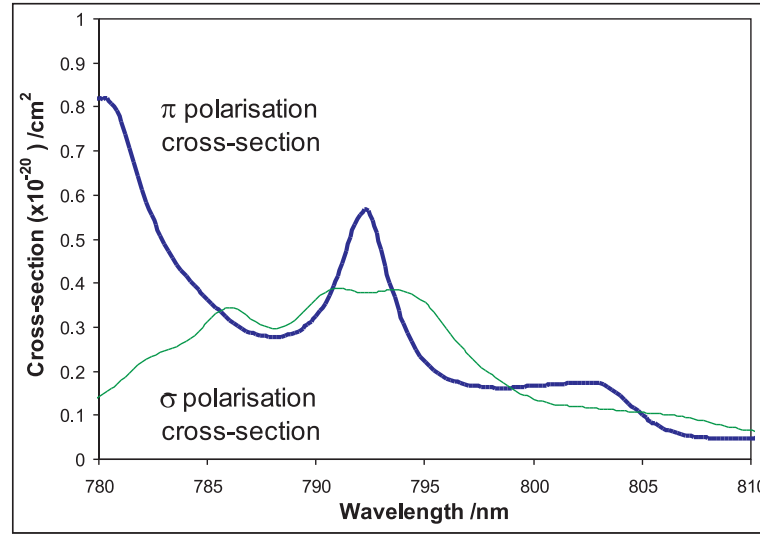


FIGURE 3.2: Tm:YLF absorption cross-section for a 2 at.%, 24 mm Tm:YLF rod measured by Mackenzie, J.I.

respectively, was measured with a beam profiler⁴ after a focussing lens. The beam profiler had a pyroelectric detector, suitable for high powers, with a 9 mm aperture and 5 μm slit for the two orthogonal axes. A high M^2 for the slow axis is well suited to the slab geometry as it allows uniform pumping with a quasi-top hat distribution. This is a significant simplification when compared to standard rod lasers, which normally require beam shaping to equalise the beam quality and size in the orthogonal axes.

Figure 3.3 illustrates the experimental setup of the optics after the micro-lensed diode stack. Cylindrical lenses, anti-reflection coated for 800 nm, were used to reformat the diode output beam size suitable for the slab. A telescope, consisting of a $f_{x1}=100$ mm and a $f_{x2}=80$ mm cylindrical lens, was used to demagnified the x-axis (slow axis) to a pump spot diameter ($\frac{1}{e^2}$ width of intensity) of ~ 8 mm. The first lens was placed 120 mm from the diode due to space limitation imposed by the diode box. The distance between the lenses was 180 mm, and the f_{x2} lens was a distance of ~ 100 mm from the slab input face. This result in the individual emitters re-imaged at a plane slightly before the input face of the slab to avoid local pumping hot-spots, which can occur if the individual diode emitters are re-imaged inside the YLF crystal. These hot-spots could cause non-uniform heat distribution and could potentially fracture the slab. Another cylindrical lens $f_y=250$ mm was used to focus the y-axis (fast axis) spot-size to a pump waist diameter of 0.74 mm, positioned at the farther end of the slab. The final incident power onto the slab was 242 W, giving an approximately collimated top-hat pump distribution in the x-axis and confocal pumping in the y-axis when double-passed. Double-pass pumping was achieved

⁴Photon inc / BeamScan controler model: 3088 / detector head: Pyroelectric heads, XYFIR/10Hz

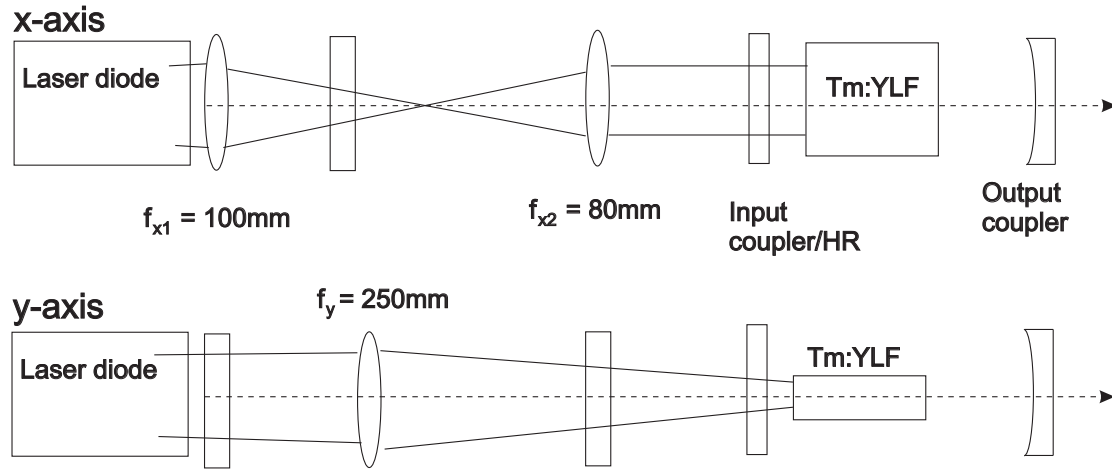


FIGURE 3.3: Pump configuration for end-pumped Tm:YLF slab laser described in section 3.2.2

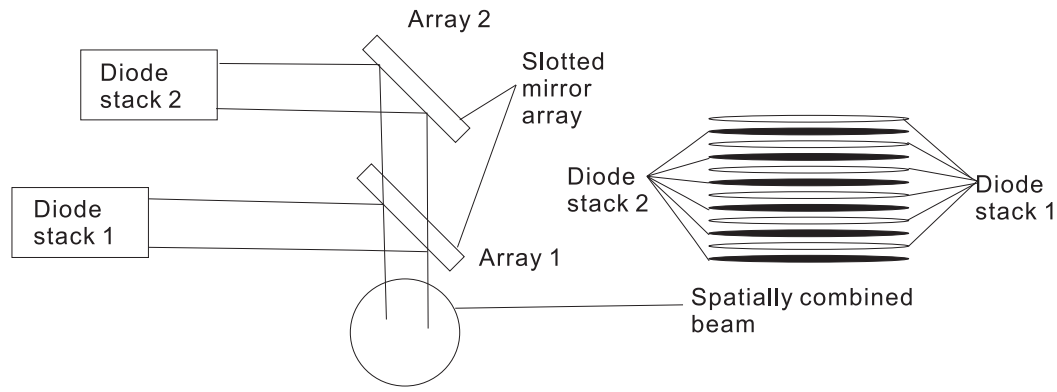


FIGURE 3.4: Spatial beam combination setup and output profile

via a pump-reflective coating on the slab end face, which will be discussed in sections 3.2.2 and 3.2.3.

3.2.1.2 Spatially multiplexed diode stack pumping

Two nLIGHT diode stacks with the same properties as described in the previous section were used as the pump source for a second pump configuration, where their output beams were spatially multiplexed. Spatial multiplexing is possible because of the separation between the diode bars in a stack, where the separation between the bars is of a similar dimension to the fast-axis collimated output of the diode bars themselves. These “dead” spaces could be filled with the output from another diode stack, to form a combined output beam like the one shown in figure 3.4. Combining the two pump sources in this way provides higher pump power without significantly degrading the beam quality.

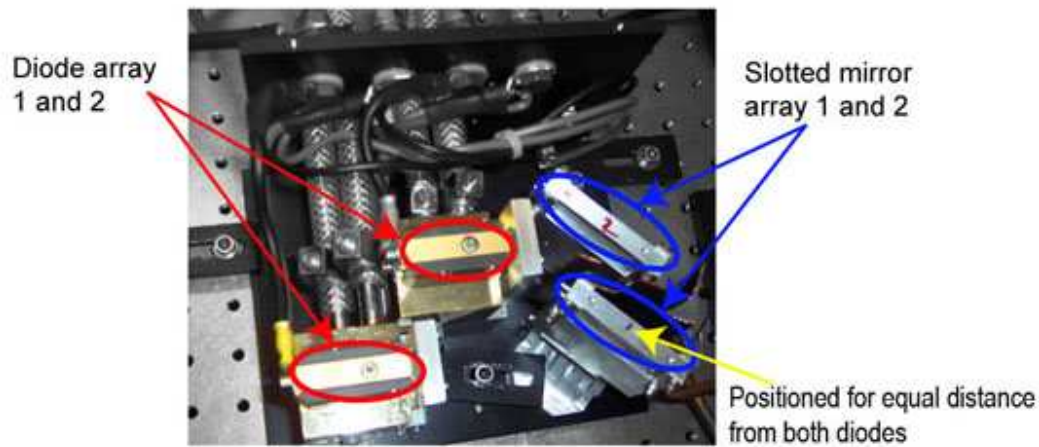


FIGURE 3.5: Photo of the diode box with slotted mirrors for spatial beam combination

The diode stacks were combined using slotted mirrors. The mirrors are BK7 slab-like mirrors, 40 mm-long, 5 mm-wide and 0.9 mm-thick, with one of the 40 mm x 0.9 mm surfaces coated highly-reflective at the diode wavelength for an angle of incidence of 45° . The thickness of the mirrors were designed to roughly equal to the height of the collimated beam of the diode bars, such that they can capture most of the power for the individual bar.

Two mirror mounts were designed by Dr J.I. Mackenzie, and assembled by me, to hold the slotted mirrors in the form of a vertical array. The mirrors were spaced ~ 0.9 mm apart, which is equal to their thickness, such that they can reflect power from one stack while letting the power from the other stack through between their gaps, relatively unattenuated. Each individual mirror could be aligned vertically such that the overall fast-axis beam quality could be optimised by removing the pointing errors of the collimated stacks. A second mirror array was placed such that the two diode pump beams would travel equal distances before exiting the diode box and allows pointing correction for the second diode as well. A photo of the setup is shown in figure 3.5. The mirror arrays were first optimised via their height such that the majority of the power gets reflected. With mirror array 1 in place, the slotted mirrors in mirror array 2 were tilted to get most of the power through the mirror array 1. A beam profiler⁵ was positioned at the focal plane of a cylindrical lens and the mirrors in the array were aligned to form the smallest spot size possible. The mirror array 2 was then aligned the same way as for mirror array 1.

⁵Photon inc / BeamScan controller model: 3088 / detector head: Pyroelectric heads, XYFIR/10Hz

The multiplexed output beam-quality was measured using a beam profiler. The beam quality was measured to be 360 in the fast-axis and 30 in the slow-axis. The fast-axis beam quality improvement is thought to be due to reducing the pointing errors between the respective bars, whereas the apparent and somewhat surprising slow-axis improvement may simply be due to the increased intensity at the center of the profile. The combined pump power of the two stacks after beam conditioning is 431 W, where the slotted mirrors incurred a ~ 10 % transmission/reflection loss. During operation, gradual degradation of beam quality of individual diode bars was observed.

A similar pump conditioning optical configuration as used for the single diode configuration was used in this dual-diode configuration. A cylindrical lens telescope was used to adjust the horizontal spot-size in the slow-axis and a further single cylindrical lens was used to focus the beam in the fast-axis, resulting in confocal pumping when the pump underwent a double-pass of the active media. Pump sizes of 16 mm x 0.7 mm and 13.2 mm x 0.7 mm ($\frac{1}{e^2}$ intensity diameters defined in ISO standard⁶) were used for comparative studies. The pump profile is similar to that described in the previous section, having a collimated top-hat distribution in the slow-axis and being confocally focussed in the fast-axis.

3.2.2 Laser configuration

The power scaling capability offered by the slab geometry was tested using a 2 at.% Tm-doped YLF slab of dimensions 9 mm-wide (c-axis) and 20 mm-long. As concluded in section 2.7, 2 at.% is the optimum doping for power-scaling, which should give the highest output power before fracture given the same pump configuration. The width of the slab was limited to <10 mm by the crystal suppliers and is dependent upon their maximum crystal boule size. The slabs were a-cut, and the c-axis was aligned with the width dimension. Therefore, the TM polarised diode beam experienced the absorption according to the σ polarisation curve ($E \perp c$ -axis) as shown in figure 3.2, which has a relatively broad absorption band and is relatively insensitive to the bandwidth of the pump, thus providing good absorption. The slab length was chosen to be ~ 2 absorption lengths long, sufficient to provide good absorption while not making the re-absorption losses and pump mode size too large. As per equation 2.14, thinner slabs have a higher pump power fracture limit, therefore the slab thickness was chosen to be as thin as possible, while still allowing the full pump beam to enter the slab and face given the pump beam quality, as such $t=1.5$ mm for our pump configuration.

⁶International standard ISO11146

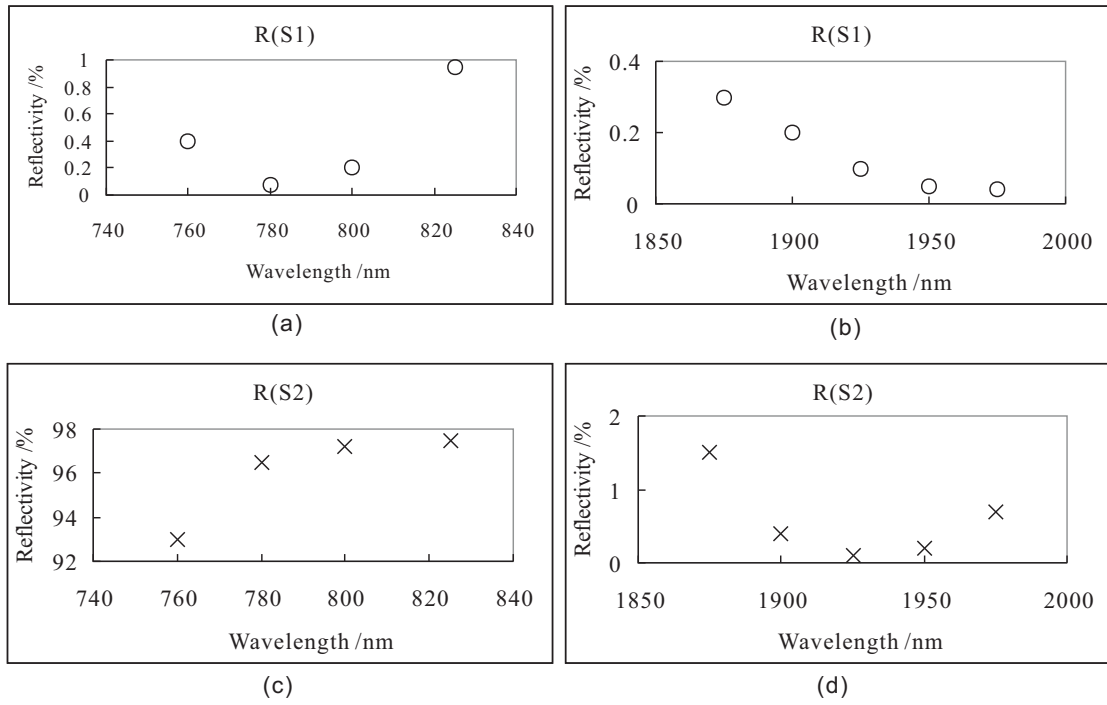


FIGURE 3.6: Tm:YLF slab coatings reflectivity, provided by slab vendor. (a) and (b) correspond to the anti-reflection coating reflectivity at 790 nm and 1900 nm respectively. (c) and (d) correspond to the pump-reflective coating reflectivity at 790 nm and 1900 nm respectively.

Both the input and output faces (9 mm by 1.5 mm) were polished to optical quality while the others fine ground to avoid parasitic lasing paths. The input face of the slab was anti-reflection coated at the pump and laser wavelength, and its output face was anti-reflection coated at the laser wavelength and had a $>90\%$ reflectivity at the pump wavelength, effectively allowing a double-pass of the pump. These characteristics were optimised for low loss at the laser wavelength, as shown in figure 3.6.

The slab was sandwiched between two water-cooled copper heat-sinks with large faces (9 mm x 20 mm) serving as thermally conducting surfaces. The heat sink was kept at a water temperature of $16\text{ }^{\circ}\text{C}$, and gold plated to prevent oxidation, which could otherwise reduce the thermal conductivity between the mount and the slab. Two pieces of 0.1 mm-thick indium foil were inserted between the mount and the crystal, compressed with ~ 10 kg of weight when mounted, for improved thermal contact⁷. The indium was not melted because previous attempts in melting the indium before mounting the crystal would either result in air bubbles between the slab and the indium, or areas where no indium existed. Both of these problems led to a degraded thermal contact, increasing the overall thermal resistance. Moreover, they can lead to local hot-spots in the crystal, causing thermally-induced stress fracture. Two metal plates were attached to the heat-sink before the input end of the slab, and positioned to block stray pump light from hitting

⁷<http://www.indium.com/TIM/solutions/heatspringtim1.php>

the indium. Sufficient pump power incident on the indium can ignite it, and deposit debris onto the surface of the slab. The entire water cooled copper mount was attached to a vertical translation stage to allow positioning of the slab in the pump beam path. The mount also had tilt adjustments to align the Tm:YLF slab to the pump beam.

As shown in figure 3.3, a simple two-mirror cavity was used, formed by a plane high reflectivity input coupling mirror and a 200 mm radius of curvature, 87 % reflectivity output coupler. The cavity is solely designed for power-scaling without any attempt to deliver diffraction-limited beam quality. The mirror-mirror separation was approximately 50 mm and the Tm:YLF crystal is positioned close to the input coupler.

According to our calculations, described in section 3.5, this should allow us to power-scale to the 50 W regime. In order to scale to the 100 W regime it is predicted that a higher aspect ratio pump, and thus a wider slab, would be required to increase the fracture limit.

3.2.3 Slab aspect ratio considerations

In order to scale to the 100 W regime, more pump power is required to be absorbed in the Tm:YLF slab. Therefore, it is important to increase the fracture limit. We know that the fracture limit for a uniformly end-pumped slab can be calculated using equation 2.14. All variables are dependent on the host material except for $\frac{w_p}{t}$. Therefore, it is important to increase the aspect ratio in order to increase the fracture limit.

One way of increasing the aspect ratio of the pump is to simply use a thinner slab. This requires a tighter focus of the pump y-axis (see figure 3.1 for axes definition) to a smaller spot-size, which is limited by the pump beam quality and the confocal pumping condition. The optimum doping concentration of 2 at.% and the length required to give sufficient absorption prevents the possibility of using a shorter slab, which would otherwise allow the use of a smaller pump waist. Pump guiding offers a solution to these problems. However, for YLF, pump guiding brings added complications due to its already low refractive index, which would require a cladding layering of even lower index such as MgF₂ or polymer films [97]. Water would be an interesting possibility except that this is known to slowly dissolve the host⁸.

Apart from narrowing the vertical pump size, using thinner or waveguide slab lasers, one may also make the pump wider. However, this requires a wider slab than was commercially available. YLF boules have two of the three axes limited to ~ 10 mm, and thus it is very difficult to obtain a wider slab than the ones used throughout this thesis.

⁸<http://www.leelaser.com/pdf/Nd-YLF%20vs%20Nd-YAG.pdf>

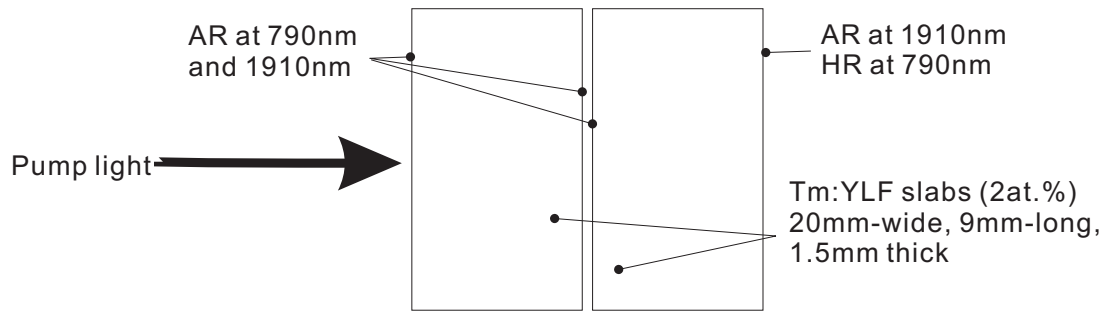


FIGURE 3.7: Tm:YLF two-slab system

The solution we employed was to have two slabs of similar dimensions, positioned one after another to form a larger slab, as illustrated in figure 3.7.

Slabs of dimensions 1.5 mm-thick (c-axis) by 20 mm-wide and 9 mm-long were used for our two-slab laser configuration, with a combined length of 18 mm. Both slabs have all sides fine ground except for the input and output faces, which were polished to optical quality. The c-axis is aligned to the thickness dimension of the slab, such that the TM polarized pump beam is aligned with the YLF π polarisation axis ($E//c$ -axis) (see figure 3.2). The absorption cross-section peak is higher for the π polarisation with respect to the σ polarisation. However, as the peak is narrower, according for the ~ 3 nm bandwidth of the diode output, the calculated double-pass absorption is only $\sim 2\%$ higher than for the other polarisation and including the difference in slab length. The first of the two slabs was anti-reflection coated at the pump and lasing wavelength on both polished surfaces. The second slab was anti-reflection coated at both wavelengths on the input face, while it was anti-reflection coated at the lasing wavelength but had $R > 90\%$ at the pump wavelength on the output face. The coating was optimized for low loss at lasing wavelength while still having as high a reflectivity as possible for the pump. Predictions based on a simple scaling law by doubling the x-axis pump size for this two-slab system leads to an expected threshold of 83 W of absorbed power, a fracture limited absorbed power of 330 W, and thus a maximum output power of 100 W, given a slope efficiency of 40.4 %.

3.3 Power-scaling of the single-slab geometry

In this experiment, the pump configuration described in section 3.2.1.1 was used in conjunction with the cavity described in section 3.2.2. A summary of the laser performance obtained is shown in table 3.1.

Threshold	P_{th}	52 W
Output power	P_o	68 W
Incident pump power	P_{inc}	242 W
Slope efficiency	η_s	40 %
Wavelength	λ_l	1909 nm

TABLE 3.1: Measured single Tm:YLF slab laser characteristics

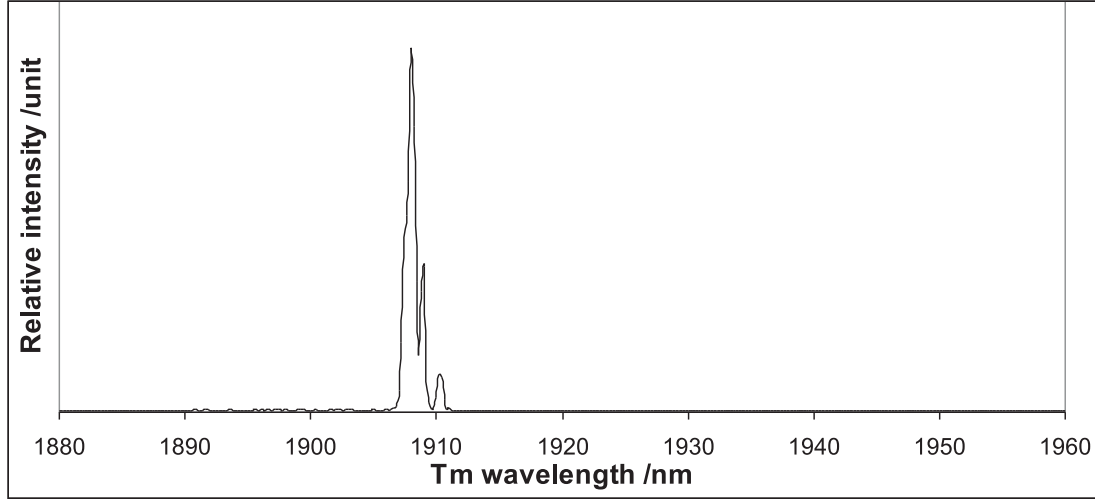


FIGURE 3.8: Measured Tm:YLF slab laser lasing wavelength (resolution: 0.2 nm)

A computer controlled monochromator⁹ of $f=0.5$ m was used to measure the output wavelength of the Tm:YLF slab laser. An extended-InGaAs photodetector¹⁰, operating over the spectral range from $0.8 \mu\text{m}$ to $2.6 \mu\text{m}$, was used for the measurement with both of the slits of the monochromator set to $50 \mu\text{m}$. The slit of the monochromator was positioned to be at the centre of the beam with broadband output couplers acting as attenuators before the slit to prevent saturation of the detector. The ${}^3F_4 \rightarrow {}^3H_6$ lasing wavelength was found to be at 1907 nm, as shown in figure 3.8, which matches the σ polarisation ($E \perp c$ -axis) emission peak of Tm:YLF and an absorption peak for the Ho:YAG. The output was polarised without any polarisation selection elements, which was expected due to the higher σ polarisation with respect to π polarisation gain spectrum in Tm:YLF (see figure 2.6). The spectrum consists of 3 peaks spanning across 4 nm with the majority of the intensity between 1907 and 1909 nm.

Laser output power as a function of incident pump power is represented by the data points in figure 3.9 for the Tm:YLF single slab laser system. The calculated small-signal, double-pass absorption is 95 % at 790 nm (for a 3 nm bandwidth), but is expected to drop to ~ 90 % at threshold due to GSD. The output power was maximised by optimising the output coupler reflectance, where only a few output couplers were tested according

⁹DongWoo Optron Co. / DM501

¹⁰Judson / J23TW266CR0252.4 / J23 series

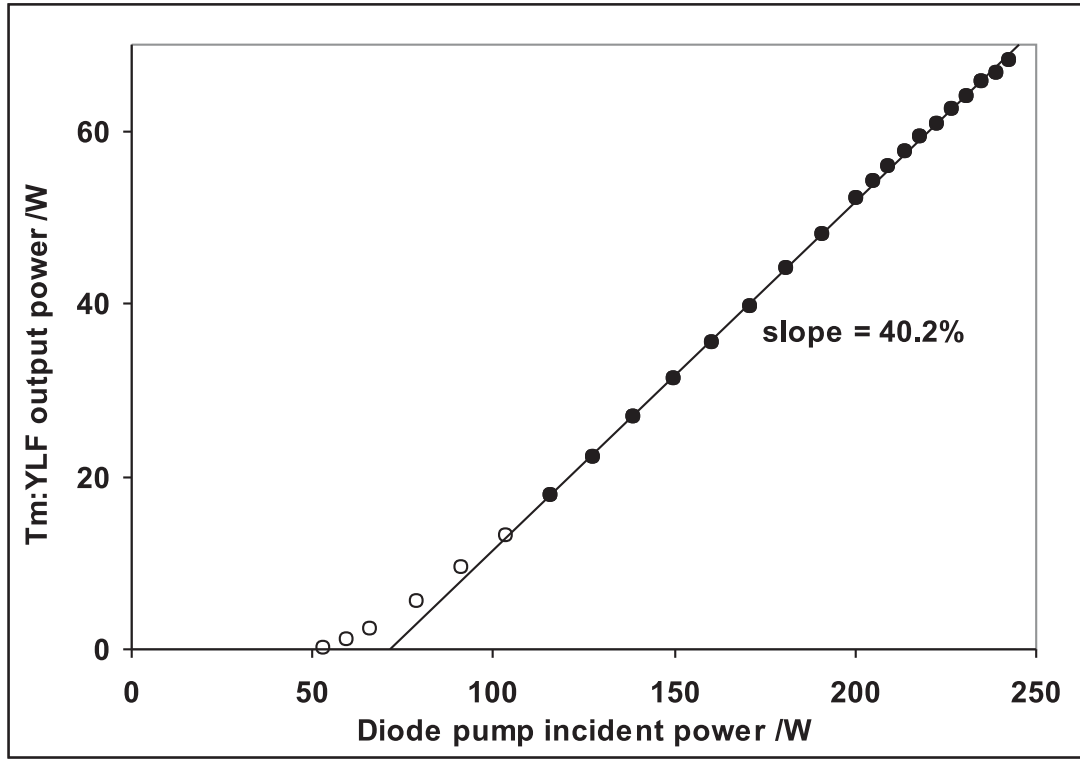


FIGURE 3.9: Laser performance of a single Tm:YLF slab laser system (see section 3.2.2)

to availability. The thulium power reached a promising output level of 68 W, limited only by the available pump power. This result is a three fold improvement over the single-rod geometry that was limited to power levels of ~ 20 W.

A linear fit to the data points for pump powers greater than three times threshold was used to estimate the slope efficiency, as it is expected to increase rapidly until the laser is operating several times above threshold, which is typical for quasi-three-level lasers [7, 93]. The slope efficiency was measured to be 40 %, which did not increase significantly with increasing output coupling transmission implying low cavity losses relative to the output coupling.

Equations from section 3.1.5 are used to estimate the expected performance of the laser system, where a calculated threshold pump power of 45 W was obtained using parameters listed in table 3.2. The cavity loss was estimated by counting the number of surfaces and assuming each surface gives ~ 0.3 % loss, and the cavity transmission, T_c , was calculated accordingly. If we allow free parameters be the effective lifetime, τ_{eff} , and mode-fill efficiency, η_{mode} , the model fits to the experimental effective threshold and slope efficiency for a lifetime of 8.8 ms and a mode-fill efficiency of 0.67. These are reasonable values given the plane-wave approximation. Note that the temperature rise

Description	Symbol	Value
Active ion density (cm^{-3})	N_T	2.64×10^{20}
Crystal length (cm)	l_r	2
Upper level effective lifetime (ms)	τ_{eff}	14
Emission Boltzmann ratio@T=300 K	F_{em}	0.117
Lasing wavelength (nm)	λ_l	1909
Pump wavelength (nm)	λ_p	790
Eff. emission cross-section (cm^2)	σ_{em}	2.3×10^{-21}
Eff. absorption cross-section (cm^2)	σ_{abs}	3.5×10^{-21}
Cavity transmission	T_c	0.992
Output coupler reflectivity	R_{oc}	0.87
Pump area (cm^2)	A	0.0465
Quantum yield (from chapter 2)	η_{QY}	1.68
Delivery efficiency	η_{del}	1
Mode-overlap efficiency	η_{mode}	0.67
Pump reflection	R_p	0.97

TABLE 3.2: Laser performance model parameter for Tm:YLF, mostly obtained from literature [7]

with increasing pump power, which leads to a change of Boltzmann fractional population, has not been taken into account in the modelling.

An average temperature of the slab, T_a , can be obtained using the equation [61]

$$T_a = T_c + \frac{Qt}{2} \left(\frac{1}{h_t} + \frac{t}{6\kappa} \right), \quad (3.28)$$

where T_c is the coolant temperature, h_t is the surface heat transfer coefficient, t is the slab thickness and κ is the thermal conductivity. The heat deposition per unit volume, Q , can be expressed as

$$Q(z) = \frac{P_h}{2w_{px}tl_r}, \quad (3.29)$$

where P_h is the heat deposition power and w_{px} is the pump width radius. Table 3.3 shows the parameters used for the average temperature modelling, where the dimensions and coolant temperature are from the setup used in this experiment. The thermal conductivity of YLF is obtained from [98], and the heat deposition density is simply the quantum defect at 250 W of incident diode power, using the quantum yield obtained in chapter 2. The average temperature of the slab is calculated to be 84 °C at full pump power. This would lead to an increase in the ratio of emission to absorption cross-section, F_{em} , from 0.117 to 0.155, and increasing the threshold pump power by nearly 15 %.

The distribution of power to different output channels is calculated using equations 3.23 to 3.26 and shown in figure 3.10, which shows that apart from the output power, the majority of the power is lost to the quantum defect, heating up the crystal. The figure also shows that the fluorescence is a fixed loss as the inversion is clamped, and the power

Description	Symbol	Value
Heat deposition density (Wcm^{-3})	Q	75
Crystal length (cm)	l_r	2
Pump width radius (cm)	w_{px}	0.4
Slab thickness (cm)	t	0.15
Coolant temperature ($^{\circ}\text{C}$)	T_c	16
Thermal conductivity of YLF ($\text{W cm}^{-1} \text{K}$)	κ	0.063
Surface heat transfer coefficient ($\text{W cm}^{-2} \text{K}^{-1}$)	h_t	0.4

TABLE 3.3: Parameters used for temperature modelling

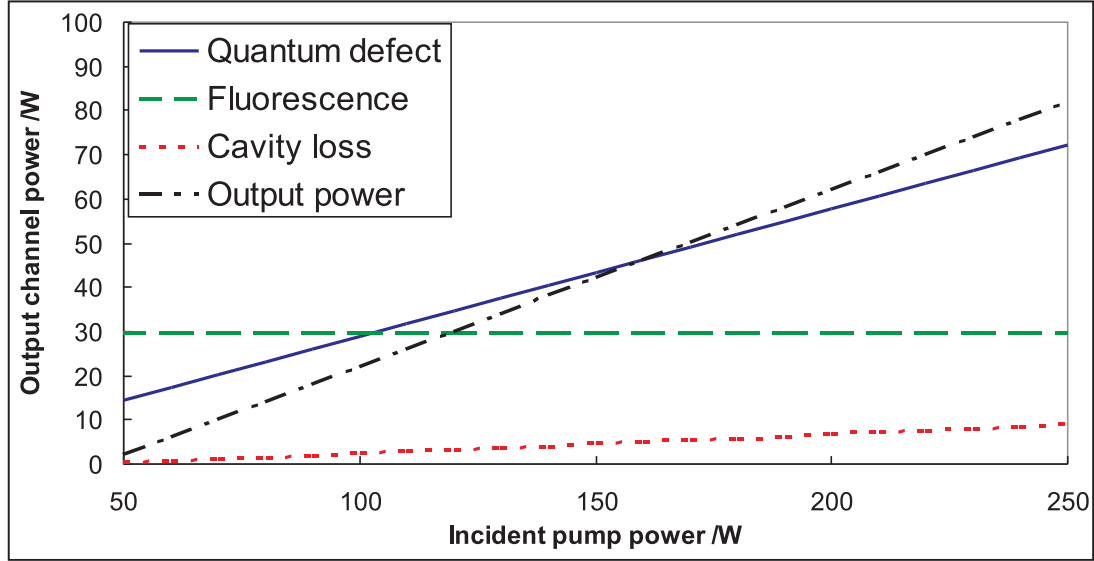


FIGURE 3.10: Calculated power in different output channels at various incident pump power

channelled to cavity loss is small when compared to the other output channels. Note we have assumed upconversion loss to be negligible for 2 at.%, as discussed in chapter 2, and thus is not included in the output channel graph.

The setup shown in figure 3.11 was used to investigate the lasing mode profile at the plane input coupler. In order to obtain an accurate profile, the output beam was imaged directly from the input coupler to avoid the imaging through the Tm:YLF slab, with its thermal aberrations. The input coupler was replaced by a plane mirror with a reflectivity of 94 % at the lasing wavelength, and high-transmission at the pump wavelength, to obtain a direct output from the plane mirror. The output coupler was also replaced by a 94 % reflective, 100 mm radius of curvature concave mirror, which gives a combined reflectivity of 12 %, to maintain an overall similar output coupling with the previous configuration. A 45° beam splitting mirror that was highly reflective at 2 microns, and had a transmission of ~ 90 % at the pump wavelength was inserted after the $f_x=80$ mm cylindrical lens as shown in figure 3.11, to prevent the thulium laser beam hitting the pump-diode and causing damage. The thulium power exiting from the “input coupler”

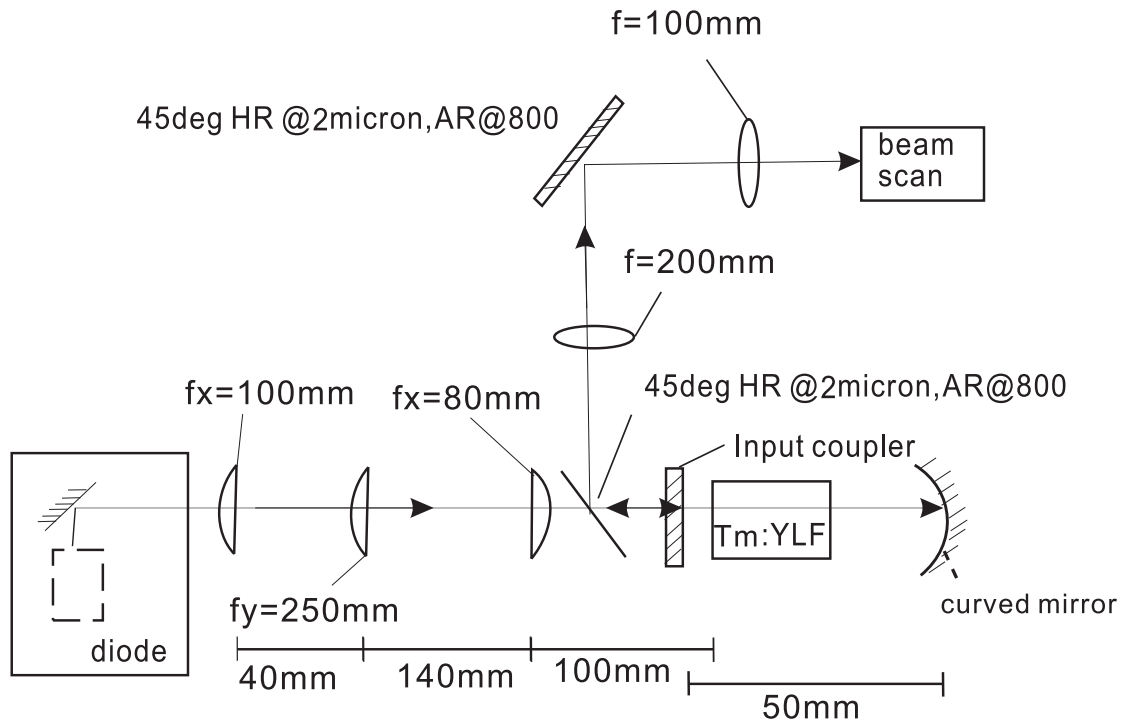


FIGURE 3.11: Experimental setup for measuring Tm:YLF slab laser beam quality and spot size in the cavity

was reflected into a reimaging system that produced a demagnified image of the cavity mode distribution at the plane mirror. The imaging telescope comprised two spherical lenses, $f=200\text{ mm}$ and $f=100\text{ mm}$ respectively, such that a beam profiler could be used to observe the near field distribution of the thulium output, and simultaneously, when scanned through the image, measure the M^2 by determining the Rayleigh range about the waist.

Two slightly wedged plane output couplers with reflectivity of 94 % were used for attenuation, to prevent damaging the beam profiler at high powers. The lasing mode was observed to nearly fill the slab aperture with a super-Gaussian-like profile in the plane of the slab and an approximate Gaussian profile in the vertical axis, as shown in figure 3.12, with corresponding M^2 values of 320 by 2.4. Note that the original power-scaling cavity uses a 200 mm radius of curvature concave mirror instead of 100 mm, which theoretically has a 30 % larger fundamental mode size, thus we would expect a somewhat better beam quality than measured in the second experiment.

The high M^2 for the horizontal mode is expected due to the much larger pump beam size compared to the fundamental cavity mode. After the laser reaches threshold, the gain outside the laser mode would keep on building up, providing gain to higher-order modes. The super-Gaussian-like profile was a result of the many high-order modes overlapping each other, whereas the vertical Gaussian mode was because the pump to laser mode

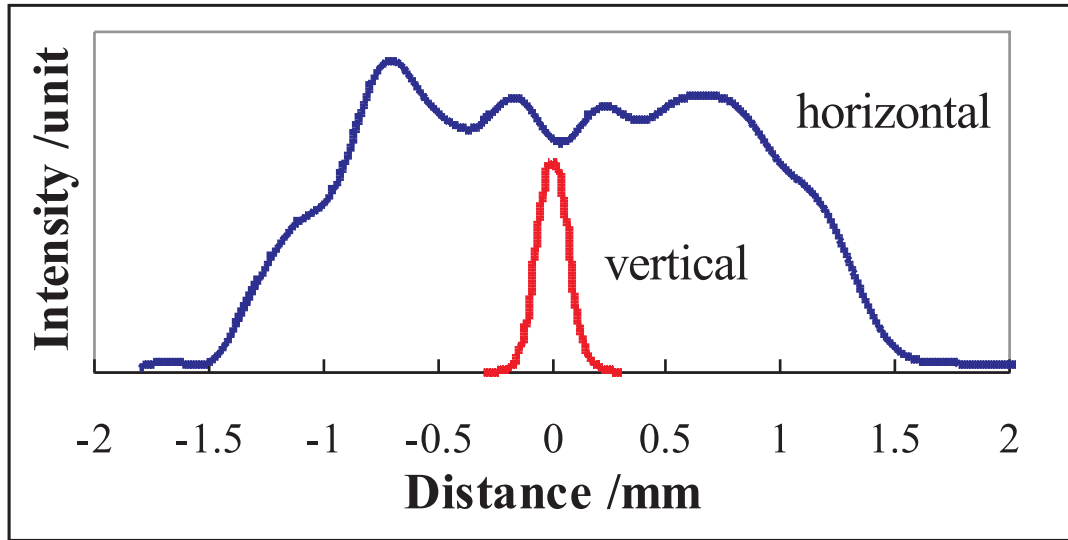


FIGURE 3.12: Measured Tm:YLF beam profile on plane input coupler

size ratio is closer to 1.0. It should be noted that further improvements in beam quality could be achieved by using different cavity designs, where a larger fundamental mode size is present in the active medium [99]. Moreover for the in-plane axis, the use of unstable resonator designs [65–67], multi-passes of the fundamental laser mode through the active medium [61, 68, 69] or an asymmetric mode cavity [70, 71] offer several solutions to high brightness from the slab lasers. Due to the reasonably high brightness of the pump diodes in the fast-axis, a cavity design that produces a mode with dimensions similar to that of the pump dimension would be relatively straight forward.

Measurement of both the diode and thulium power uses a 300 W power detector and a 3 significant figure digital meter. The measured power was stable to within 1 W for the diode power and 0.5 W for the thulium power, which has minimal effect on the laser performance result.

3.4 Power-scaling of a two-slab Tm:YLF laser

Although, as will be discussed in section 3.5, the single-slab configuration gave us an output power higher than the calculated fracture limit should have allowed, however it is not expected to deliver 100 W of output power without fracturing. Therefore, in order to further power scale safely into 100 W regime, a wider pump distribution was required to increase the aspect ratio. In this experiment, the pump configuration described in section 3.2.1.2 was used in conjunction with the cavity described in section 3.2.3.

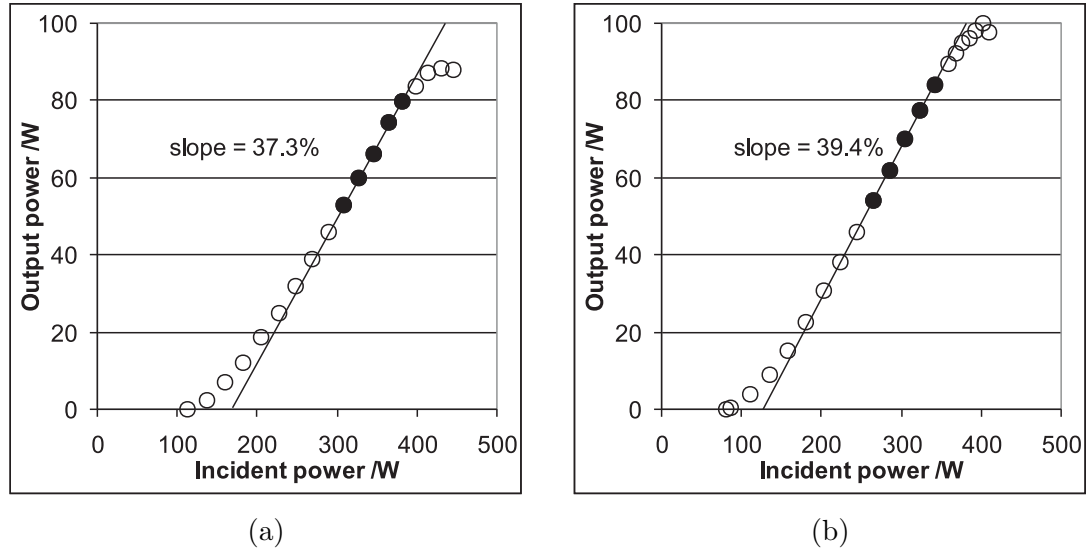


FIGURE 3.13: Laser performance of two-slab system that use (a) 16 mm (b) 13.2 mm diameter diode pump spot size

The two-slab laser was characterised and its performance is shown in figure 3.13. The slope efficiencies are 37.3 % and 39.4 % for the 16 mm and 13.2 mm pump diameters respectively. The small drop in efficiency with respect to the single-slab system is due to the increase in cavity loss from the extra surfaces. A thulium output power of 100 W is demonstrated with the 13.2 mm pump size for an incident pump power of 400 W. The observed threshold power for the 16 mm and 13.2 mm pump diameters are 112 W and 81 W respectively.

In both situations roll-over of the output power was observed, as shown in figure 3.13, starting at around the 400 W incident pump power level, limiting the maximum output power achievable; the roll-over power level is slightly higher for the larger pump size. This was not present in the single slab scenario where the pump diameter and power was half, i.e. 190 W, as shown in figure 3.9. There are various possible reasons for the roll-over. Firstly, the slab is now in “two-pieces” and as such its temperature profile is not smooth across the two slabs, which combined with additional lensing effects due to surface bulging from the extra surfaces could lead to the cavity becoming unstable. Another possibility is that the heat sinking could not cope with the higher thermal load. Figure 3.14 shows the temperature of the heat sink. The temperature increases linearly with pump power suggesting that the heat-sinking arrangement is sufficient. Finally, the change of diode pump wavelength at increased powers could also contribute to the roll-over. The pump wavelength for the diodes at maximum operating current was measured using an optical spectrum analyser¹¹ and found to be 788.3 nm and 792.6 nm, and the lasing wavelengths at which roll-over starts to occur is 787.8 nm and 792.0 nm for the

¹¹ANDO / model: AQ6317B

two diodes. Thus one pump wavelength going over the absorption peak while the other in a minima, as shown in figure 3.15, could lead to a reduction in absorption and explain the roll-over. Having not observed this effect in the single-slab system could be explained by the difference in the c-axis orientation that leads to a different absorption property as shown in figure 3.2. Unfortunately, a 790 nm half-waveplate was not available at the time and this was not verified experimentally. Note that the calculated saturated absorption at threshold for the wavelengths 788.3 nm, 792.0 nm and 792.6 nm are 88.2 %, 96.3 % and 94.6 % respectively.

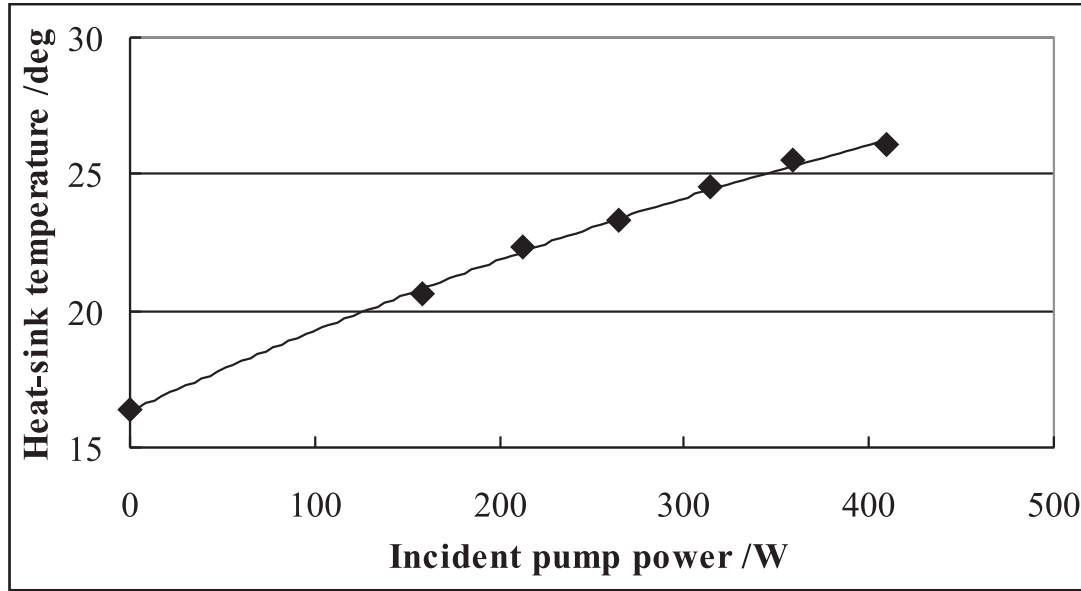


FIGURE 3.14: Measured temperature of heat-sink at different pump power

The measurement of the diode power uses a 1 kW thermal power detector while the thulium output power uses a 300 W power detector, both uses a 3 significant figure digital meter. The measured power was stable to within 1 W for the diode power and 0.5 W for the thulium power, which has minimal effect on the laser performance result.

3.5 Tm:YLF fracture limit

The estimated fracture limits were calculated for the current system, using the equations in section 2.4 and 2.7. Results are shown in table 3.5, with the other parameters used listed in table 3.4.

The 8 mm full width pump size corresponds to the single slab configuration. As shown in table 3.5 the expected maximum output power possible for the single-slab is only ~ 50 W, while nearly 70 W has been observed without fracture with such a slab. This

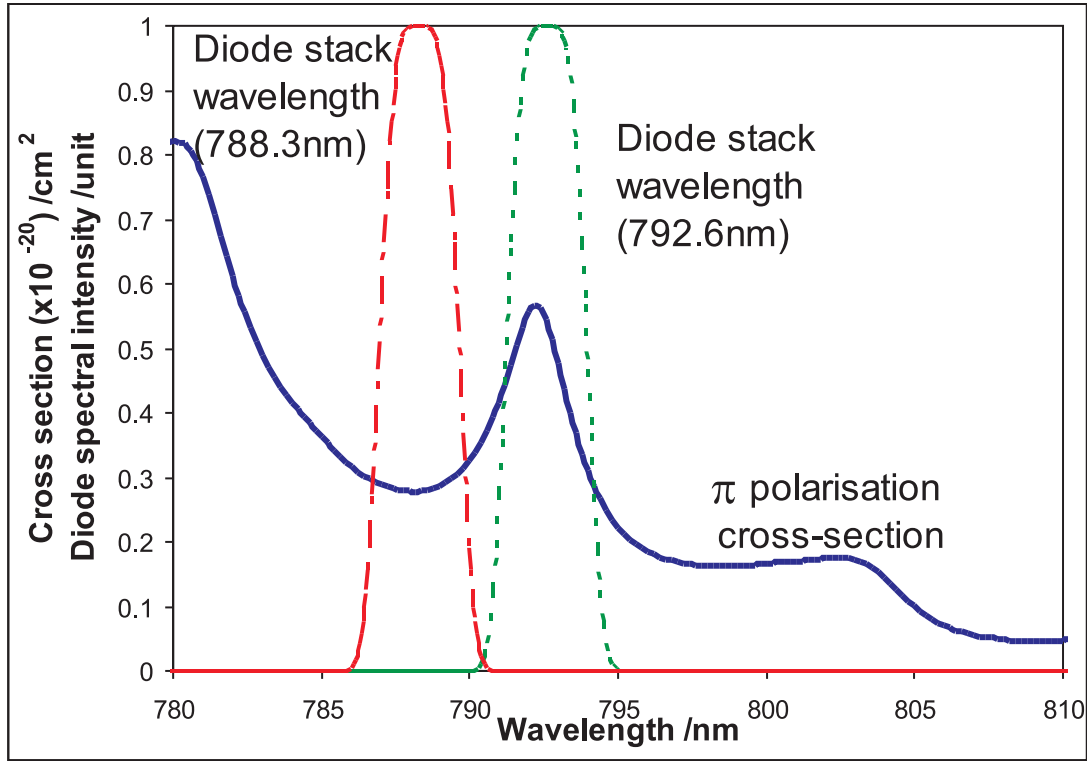


FIGURE 3.15: Measured Tm:YLF π polarisation absorption cross-section and measured diode pump wavelength with estimated profile for the two diode stacks at maximum operating power. Absorption cross-section was measured by Dr J.I. Mackenzie.

requires an absorbed power of over 220 W, much greater than the 158 W predicted to result in fracture. Moreover, both the 13.2 and 16 mm pump sizes have also absorbed a pump power much greater than the predicted fracture limit. These predictions were based on scaling from the rod laser results of chapter 2. The better than expected results are believed to be due to the better heat sinking in the case of the slab compared to the rod as the indium interface should have a much lower thermal resistance than the wax, or indeed small variations in other parameters such as surface finish. It may also be due to the fact that our slabs are not uniformly pumped and so the exact nature of the scaling from the rod results is not clear. However, when a 2 mm-thick slab was used in the same set-up, fracture was observed at an absorbed pump power level of 200 W. If we scale from this figure to our current single 1.5 mm slab the expected fracture point is 267 W of absorbed power with an output of 90 W.

3.6 Conclusion

In this chapter an end-pumped, power-scaled, CW Tm:YLF slab laser with good performance was demonstrated. Although power-scaling YLF active materials is usually

Rod parameters		
Quantum yield for 2 at. %	$\eta_{QY-2\%}$	1.68
Threshold for 2 at. % rod (W)	P_{th-rod}	6.2
Rod pump size (mm)	w_{p-rod}	0.47
Slope efficiency wrt P_{inc} (%)	η_{s-rod}	37
Length of rod (mm)	L_{rod}	24
Absorption	$\eta_{abs-rod}$	0.86
Fracture figure of merit (W/cm)	P_h/l_{abs}	10.6

Slab laser parameters		
Pump half width - x (mm)	w_{px}	4
Pump half width - y (mm)	w_{py}	0.37
Slab thickness (mm)	t	1.5
Absorption - double pass	η_{abs}	0.93 (18 mm slab)
Slope efficiency wrt P_{inc} (%)	η_s	40

TABLE 3.4: Tm:YLF slab fracture limit model parameters

Pump full width (mm)	P_h^{max} (W)	P^{th} (W)	P_{abs}^{max} (W)	P_{out}^{max} (W)
8	48	45	158	49
13.2	79	74	261	81
16	96	90	316	98
8 (slab thickness=2 mm)	36	45	119	32

TABLE 3.5: Predicted power-scaling using Tm:YLF two-slab laser with double passing, employing different pump widths and slab thickness

difficult due to its fragile mechanical properties, output powers of close to 70 W were achieved from a single gain component, limited by the available pump power. In addition, a two-slab Tm:YLF laser system was demonstrated with an output power reaching 100 W. These results illustrate the possibility of scaling the output power of Tm:YLF slab lasers in a straight-forward manner.

Results from modelling of the thermally induced stress fracture limit based on the rod laser results of chapter 2 were found to be lower than the experimental values. Therefore the slab geometry is shown to provide better thermal management properties, which lowers the stress within the crystal as discussed above. The thulium lasing wavelength at 1909 nm is suitable to act as a pump source for Ho:YAG, the primary interest in power-scaling this laser transition. This simple, compact, yet efficient high-power Tm:YLF laser is therefore an excellent pump source for Ho:YAG. In the following chapter, we look at this slab laser utilised in a novel intra-cavity pumping scheme for a side-pumped Ho:YAG laser.

Chapter 4

Intra-cavity side-pumping

As discussed earlier, different laser systems have been designed to achieve output from a Ho:YAG laser. Direct pumping of Ho:YAG, using 1.9 μm GaInAsSb and InGaAsP diodes has only been demonstrated at low power levels [32]. End-pumping has also been demonstrated using thulium-fibre lasers or Tm:YLF rod lasers [33, 34, 36, 52, 100, 101]. Co-doping with thulium enables pumping at common diode wavelengths associated with Tm^{3+} , whereby excitation of the Ho^{3+} is achieved through energy-transfer processes. However, co-doped materials typically suffer severe upconversion effects, which includes typical upconversion between neighbouring ions, thulium-thulium and holmium-holmium upconversion, and between neighbouring ions of different dopant, namely co-operative upconversion, thulium-holmium. This results in a significant reduction in the effective lifetime [102, 103] of the holmium 5I_7 manifold, the upper laser level of the 2 μm emission. Beside co-doping, one can also use two separate crystals sharing the same cavity, thus removing the problem of co-operative upconversion. However, this has limited power-scalability due to stress-fracture for end-pumped Tm:YLF rods [4], or if Tm:YAG is used it is still limited by thermal lensing [11]. Therefore, we propose a novel intra-cavity side-pumping scheme as an alternative route for power-scaling Ho:YAG.

Intra-cavity side-pumping is an architecture that has the advantages of co-doping while still maintaining a long upper laser level lifetime. Moreover, as the single pass absorption of the thulium output by the Ho:YAG need only be a few percent for intra-cavity pumping, it potentially allows for the use of low holmium doping concentrations, reducing the holmium-holmium upconversion, and leading to relatively uniform excitation of the Ho^{3+} ions. Thermal problems in the holmium rod are therefore minimised by having separate pump and laser crystals, and the orthogonal lasing axes of the side-pumping scheme decouples thermal effects in the thulium crystal from the holmium resonator. It is also a relatively compact device as no diode pump shaping optics are required. Finally,

it allows the use of a thulium slab pump laser, leading to improved power-scalability, as we have seen from the work of chapter 3.

Presented in this chapter are theoretical aspects underlying the experimental data of the intra-cavity side-pumping scheme, with particular attention paid to the thulium laser operating wavelength. Firstly, a modified plane-wave model for predicting the laser performance is described, extending the method introduced by Beach [92] and Mackenzie [104]. This is followed by a description of the experimental setup and the laser characterisation. The results are then compared to the model and various aspects, including power-scalability and possible laser performance improvements, are discussed.

4.1 Intra-cavity side-pumped plane-wave analysis

Different models have been proposed for laser performance modelling, some of which were specifically designed for intra-cavity pumping, such as the one by Schellhorn and Hirth [7]. The model is based on rate equations that take into account upconversion losses, spatial distribution and overlap of the pump and laser modes, as well as super-Gaussian distributions for the modes. Unfortunately, the spatial distributions of our system are not well defined, thus making it difficult to use. However, a plane-wave analysis is simple to implement, while still encapsulating all of the physical principles that govern the laser performance of the system, and as such still provides a reasonable prediction of threshold and the expected output power as a function of pump power, as it did for the Tm:YLF slab laser in chapter 3.

The model presented here is an extension of the model presented in section 3.1 to account for the intra-cavity pumping configuration described in this chapter. It takes into account ground-state depletion and gain saturation, and energy transfer mechanisms such as cross-relaxation and upconversion. Once again, the model is used to predict the relative powers for the various output channels. These outputs allow the estimation of the thermal load, as presented in section 3.1.7.

Figure 4.1 shows the axes and the notations for the dimensions of the slabs used in the model. The x-axis corresponds to the slow axis of the diode pump while the y-axis is parallel to the fast axis. The diode pump propagates along the z-axis, i.e. end-pumping the Tm:YLF slab of length, l_r^{Tm} . The thulium slab width, w^{Tm} , is parallel to the x-axis and has a thickness, t^{Tm} . The thulium beam propagates in the same direction as the diode pump and is partially absorbed when it passes through the width of the Ho:YAG slab, w^{Ho} . The Ho:YAG slab has a thickness t^{Ho} and the optical axis for the holmium laser is along its length, l_r^{Ho} .

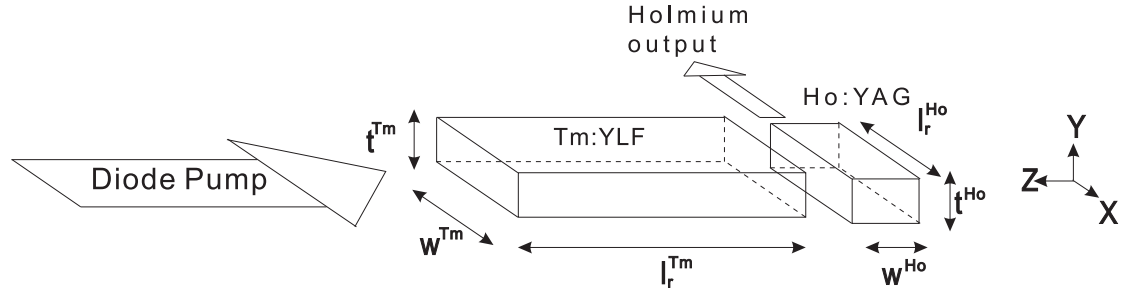


FIGURE 4.1: The axes and dimensions variables of the slabs used in the model

As in section 3.1, the laser performance requires equation 3.1 to relate the input pump power, output power and the slope efficiency. It can be shown that the laser performance of the intra-cavity side-pumped Ho:YAG system with respect to the diode power can be predicted using the equations

$$\eta_s^{Ho} = \eta_{mode}^{Ho} \eta_{mode}^{Tm} \eta_{QY}^{Tm} \eta_{del}^p \frac{\nu_{Ho}}{\nu_p} \frac{1}{R_{eff}^{Tm}(\lambda^{Tm}, T)} \frac{1 - R_{oc}^{Ho}}{R_{oc}^{Ho}} \frac{D_A^{Ho}(\lambda^{Tm}, T)}{D_B^{Ho}(\lambda^{Ho}, T)} \frac{D_A^{Tm}(\lambda^p, T)}{D_B^{Tm}(\lambda^{Tm}, T)}, \quad (4.1)$$

$$P_{th}^{Ho} = \frac{n_U^{Ho} A^{Ho}}{\tau_{eff}^{Ho}} \frac{h\nu_{Tm}}{D_A^{Ho}(\lambda^{Tm}, T)} \frac{D_B^{Tm}(\lambda^{Tm}, T)}{D_A^{Tm}(\lambda^p, T)} \frac{1}{\eta_{mode}^{Tm} \eta_{QY}^{Tm} \eta_{del}^p} \frac{\nu_p}{\nu_{Tm}} R_{eff}^{Tm}(\lambda^{Tm}, T) + \frac{n_U^{Tm} A^{Tm}}{\tau_{eff}^{Tm}} \frac{h\nu_p}{\eta_{QY}^{Tm} \eta_{del}^p} \frac{1}{D_A^{Tm}(\lambda^p, T)}, \quad (4.2)$$

where η_s^{Ho} is the slope efficiency of the holmium laser and P_{th}^{Ho} is the threshold of the holmium laser with respect to the diode pump power. Moreover, η_{mode}^{Tm} and η_{mode}^{Ho} are the mode-fill efficiencies for the thulium and holmium laser respectively, which is included to approximately account for the spatial overlap of the pump and laser mode profile, η_{QY}^{Tm} is the quantum yield of the thulium slab, η_{del}^p is the diode pump delivery efficiency which corresponds to the transmission of the optics chain between the diode laser and the Tm:YLF slab. On the other hand, ν_{Tm} , ν_{Ho} and ν_p are lasing frequencies of the thulium, holmium and diode pump respectively, R_{oc}^{Ho} is the reflectivity of the holmium output coupler, $D_A^{Tm}(\lambda^p, T)$ and $D_A^{Ho}(\lambda^{Tm}, T)$ are the double-pass absorption factors for the thulium and holmium systems respectively at the diode pump wavelength, λ^p , and thulium wavelength, λ^{Tm} , and a temperature T , $D_B^{Tm}(\lambda^{Tm}, T)$ and $D_B^{Ho}(\lambda^{Ho}, T)$ are the double-pass gain factors for the thulium and holmium systems respectively, Furthermore, A^{Tm} and A^{Ho} are the cross-sectional areas of the pump excitation for thulium and holmium respectively, τ_{eff}^{Tm} and τ_{eff}^{Ho} are the effective lifetimes for the upper laser levels of the thulium and holmium media respectively, as defined in equation 3.16, and h is Planck's constant.

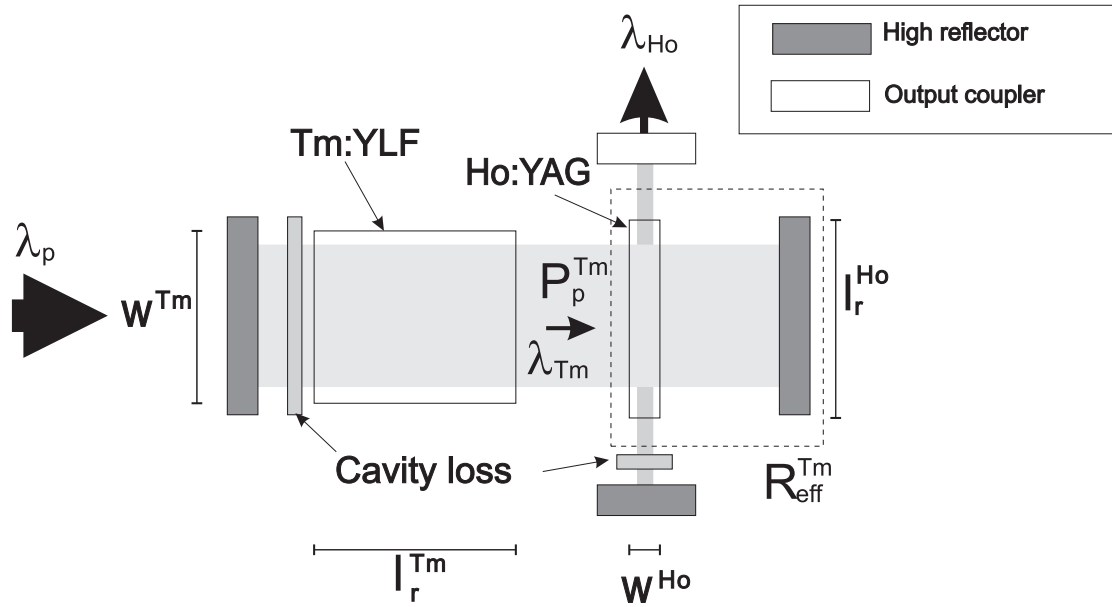


FIGURE 4.2: Intra-cavity elements for the laser cavity model. P_p^{Tm} is the one-way intra-cavity thulium power

$R_{eff}^{Tm}(\lambda^{Tm}, T)$ is the reflectivity of the effective output coupler for the thulium laser. As the thulium cavity uses two highly reflective mirrors, virtually no power comes out from the system as output, but is directly absorbed in the holmium crystal. Therefore, the holmium crystal and the following high reflective mirror may be considered as the effective output coupler of the thulium system as shown in figure 4.2. The effective output coupling reflectance is given by the double-pass transmission through the Ho:YAG slab, and the reflectance of the following mirror at the thulium wavelength, $R_p^{Tm}(\lambda^{Tm})$, defined by

$$R_{eff}^{Tm}(\lambda^{Tm}, T) = (1 - F_A^{Ho}(\lambda^{Tm}, T))^2 R_p^{Tm}(\lambda^{Tm}), \quad (4.3)$$

where $F_A^{Ho}(\lambda^{Tm}, T)$ is the single-pass absorption in the holmium crystal. It is assumed the reflectivity of the mirror following the Ho:YAG slab, $R_p^{Tm}(\lambda^{Tm})$, is wavelength dependent, which becomes important in terms of the wavelength of operation for the thulium system, as will be shown shortly.

Similarly, the laser slope efficiency and threshold for the thulium system can be predicted using the equations

$$\eta_s^{Tm} = \eta_{mode}^{Tm} \eta_{QY}^{Tm} \eta_{del}^p \frac{\nu_{Tm}}{\nu_p} \frac{1}{R_{eff}^{Tm}(\lambda^{Tm}, T)} \frac{D_A^{Tm}(\lambda^p, T)}{D_B^{Tm}(\lambda^{Tm}, T)}, \quad (4.4)$$

$$P_{th}^{Tm} = \frac{n_U^{Tm} A^{Tm}}{\tau_{eff}^{Tm}} \frac{h\nu_p}{\eta_{QY}^{Tm} \eta_{del}^p} \frac{1}{D_A^{Tm}(\lambda^p, T)}, \quad (4.5)$$

where η_s^{Tm} is the slope efficiency of the thulium system and P_{th}^{Tm} is the threshold pump power of the thulium system with respect to the diode pump power.

4.1.1 Absorption

In our configuration, the laser process commences with the diode pumping of the Tm:YLF slab. Using the assumption of plane-wave pumping, the thulium slab exhibits a single-pass absorption, F_A^{Tm} , given by,

$$\begin{aligned} F_A^{Tm}(\lambda^p, T) &= 1 - \exp \left(\int_{z=0}^{z=l_r^{Tm}} [-\sigma_{abs}^{Tm}(\lambda^p, T) N_L^{Tm}(z) + \sigma_{em}^{Tm}(\lambda^p, T) N_B^{Tm}(z)] dz \right) , \\ &= 1 - \exp \left(-\sigma_{abs}^{Tm}(\lambda^p, T) \int_{z=0}^{z=l_r^{Tm}} N_L^{Tm}(z) dz \right) , \\ &= 1 - \exp(\sigma_{abs}^{Tm}(\lambda^p, T) n_p^{Tm}) , \end{aligned} \quad (4.6)$$

where $\sigma_{abs}^{Tm}(\lambda^p, T)$ and $\sigma_{em}^{Tm}(\lambda^p, T)$ are the effective absorption and emission cross-sections respectively for Tm:YLF at the diode pump wavelength λ^p , $N_L^{Tm}(z)$ is the population density of the lower laser manifold (3H_6) of thulium, and $N_B^{Tm}(z)$ is the population density of the upper pump manifold (3H_4) of thulium, as shown in the energy level diagram in figure 4.3. Note that, due to fast thermal relaxation and the relatively long upper laser manifold (3F_4) lifetime [7, 87], all of the population is assumed to be in the upper and lower laser manifolds, that is the upper pump manifold (3H_4) is assumed to be empty, $N_B^{Tm}(z) \approx 0$, and the total population density of thulium, N_T^{Tm} , is equivalent to

$$N_T^{Tm} = N_U^{Tm}(z) + N_L^{Tm}(z) , \quad (4.7)$$

where $N_U^{Tm}(z)$ is the population density of the upper laser manifold.

The term n_p^{Tm} is the integrated inversion density along the direction of laser propagation, referenced to the manifolds coupled by the pump radiation (level N_L^{Tm} and N_B^{Tm}). Similarly to equation 3.5, n_p^{Tm} is given by

$$\begin{aligned} n_p^{Tm} &= - \int_{z=0}^{z=l_r^{Tm}} N_L^{Tm}(z) dz , \\ &= \int_{z=0}^{z=l_r^{Tm}} (N_U^{Tm}(z) - N_T^{Tm}) dz , \\ &= n_U^{Tm} - N_T^{Tm} l_r^{Tm} , \end{aligned} \quad (4.8)$$

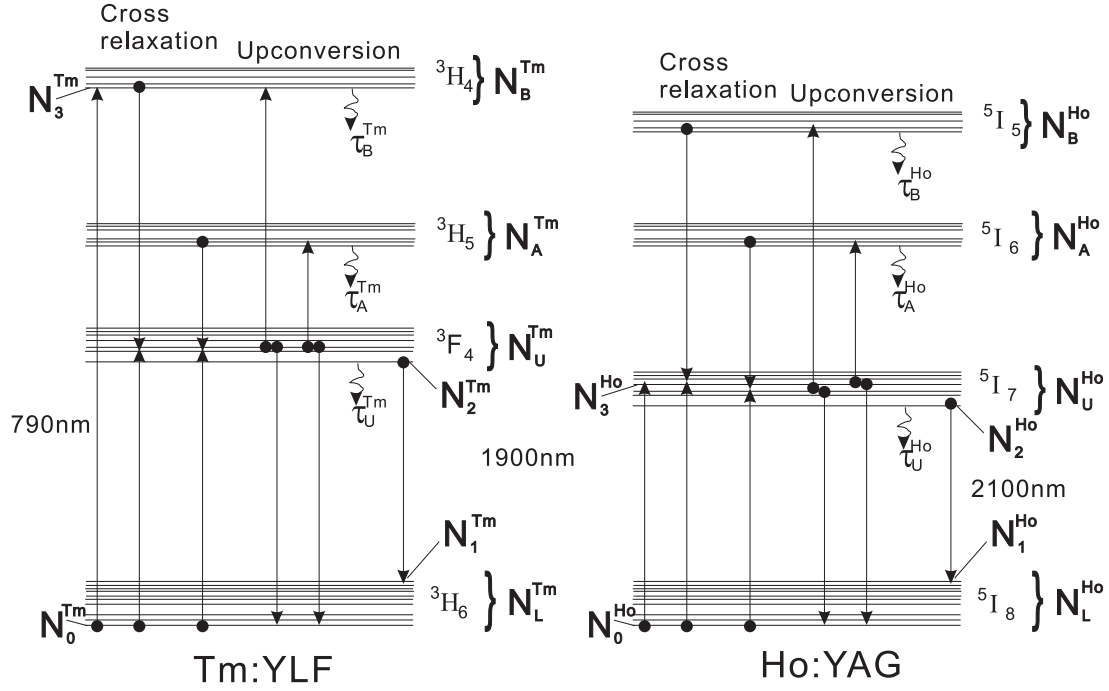


FIGURE 4.3: Energy level diagram of Tm:YLF and Ho:YAG

The integrated excited ion density, n_U^{Tm} , sums up the excited population over the length of the crystal that interacts with the laser field, given by

$$n_U^{Tm} = \int_{z=0}^{z=l_r^{Tm}} N_U^{Tm}(z) dz . \quad (4.9)$$

Similarly, the single-pass absorption across the Ho:YAG slab, F_A^{Ho} , at the Tm:YLF lasing wavelength is given by

$$\begin{aligned} F_A^{Ho}(\lambda^{Tm}, T) &= 1 - \exp \left(\int_{z=0}^{z=w^{Ho}} [-\sigma_{abs}^{Ho}(\lambda^{Tm}, T) N_L^{Ho}(z) + \sigma_{em}^{Ho}(\lambda^{Tm}, T) N_U^{Ho}(z)] dz \right) , \\ &= 1 - \exp \left(-\sigma_{abs}^{Ho}(\lambda^{Tm}, T) \int_{z=0}^{z=w^{Ho}} [N_L^{Ho}(z) - F_{abs}^{Ho}(\lambda^{Tm}, T) N_U^{Ho}(z)] dz \right) , \\ &= 1 - \exp(\sigma_{abs}^{Ho}(\lambda^{Tm}, T) n_p^{Ho}(\lambda^{Tm}, T)) , \end{aligned} \quad (4.10)$$

where $\sigma_{abs}^{Ho}(\lambda^{Tm}, T)$ and $\sigma_{em}^{Ho}(\lambda^{Tm}, T)$ are respectively the effective absorption and emission cross-sections, for Ho:YAG at the thulium lasing wavelength λ^{Tm} , $N_L^{Ho}(z)$ is the population density of the lower holmium laser manifold (5I_8) and $N_U^{Ho}(z)$ is the population density of the upper holmium laser manifold (5I_7). Note that N_U^{Ho} is used, in contrast to the thulium case, because we are interested in the in-band pumping process.

F_{abs}^{Ho} is the ratio of the effective emission cross-section to the absorption cross-section in holmium, therefore it is the ratio of the Stark level Boltzmann fractions of the population

distributions in the terminal and initial pump manifolds, given by [94]

$$\begin{aligned}
F_{abs}^{Ho}(\lambda^{Tm}, T) &= \frac{\sigma_{em}^{Ho}(\lambda^{Tm}, T)}{\sigma_{abs}^{Ho}(\lambda^{Tm}, T)} , \\
&= \frac{\exp\left[\frac{-1}{k_B T} \left(\frac{hc_0}{\lambda^{Tm}} - E_{5I7}^{Ho}\right)\right]}{Z_U^{Ho}(T)} \frac{Z_L^{Ho}(T)}{\exp\left[\frac{-1}{k_B T} (E_{5I8}^{Ho} - E_{5I7}^{Ho})\right]} , \\
&= \frac{Z_L^{Ho}(T)}{Z_U^{Ho}(T)} \exp\left[\frac{hc_0}{k_B T} \left(E_{5I7}^{Ho} - \frac{1}{\lambda^{Tm}}\right)\right] , \tag{4.11}
\end{aligned}$$

where c_0 is the speed of light in free space, k_B is the Boltzmann constant, and T is the temperature. Note that E_{5I8}^{Ho} and E_{5I7}^{Ho} is the energy of the lowest energy level, the zero-line energy, of the lower and upper laser manifold respectively, 5I_8 and 5I_7 . This assumes the absorption started from the lowest energy level of the lower laser manifold.

Z_L^{Ho} and Z_U^{Ho} are the holmium partition functions for the lower and upper manifolds respectively (5I_8 and 5I_7). The partition function of a particular manifold, Z , is given by the equation [94]

$$Z = \sum_k d_k \exp\left[\frac{-1}{k_B T} (E_k - E_{ZL})\right] , \tag{4.12}$$

where d_k and E_k is the degeneracy and energy of the Stark level, k , and E_{ZL} is the zero-line energy of the manifold. E_{ZL} equals E_{5I8}^{Ho} and E_{5I7}^{Ho} for Z_L^{Ho} and Z_U^{Ho} respectively.

The integrated inversion density for holmium, referenced to Stark levels coupled by the thulium pump radiation, n_p^{Ho} , similar to equation 3.5, is given by

$$\begin{aligned}
n_p^{Ho}(\lambda^{Tm}, T) &= - \int_{z=0}^{z=w^{Ho}} [N_L^{Ho}(z) - F_{abs}^{Ho}(\lambda^{Tm}, T) N_U^{Ho}(z)] dz , \\
&= \int_{z=0}^{z=w^{Ho}} (1 + F_{abs}^{Ho}(\lambda^{Tm}, T)) N_U^{Ho}(z) - N_T^{Ho} dz , \\
&= (1 + F_{abs}^{Ho}(\lambda^{Tm}, T)) n_U^{Ho} \frac{w^{Ho}}{l_r^{Ho}} - N_T^{Ho} w^{Ho} . \tag{4.13}
\end{aligned}$$

Note the integrated excited population density for holmium, n_U^{Ho} , is defined by the equation

$$n_U^{Ho} = \int_{x=0}^{x=l_r^{Ho}} N_U^{Ho}(x) dx , \tag{4.14}$$

which is along the optical axis of the holmium laser cavity, thus the fraction, $\frac{w^{Ho}}{l_r^{Ho}}$ is required in the n_p^{Ho} equation.

Again, as we are in-band pumping holmium, it is effectively a two-level system, thus the total population density for holmium, N_T^{Ho} , is given by

$$N_T^{Ho} = N_U^{Ho}(z) + N_L^{Ho}(z) . \quad (4.15)$$

D_A^{Tm} and D_A^{Ho} is defined as the double-pass absorption for the thulium and holmium respectively, which is given by the equations

$$D_A^{Tm}(\lambda^p, T) = F_A^{Tm}(\lambda^p, T) (1 + R_p(\lambda^p) (1 - F_A^{Tm}(\lambda^p, T))) , \quad (4.16)$$

$$D_A^{Ho}(\lambda^{Tm}, T) = F_A^{Ho}(\lambda^{Tm}, T) (1 + R_p^{Tm}(\lambda^{Tm}) (1 - F_A^{Ho}(\lambda^{Tm}, T))) , \quad (4.17)$$

where $R_p(\lambda^p)$ is the reflectivity of the coating at the end of the Tm:YLF slab at the diode wavelength and $R_p^{Tm}(\lambda^{Tm})$ is the reflectivity of the cavity mirror on the other side of the holmium slab with respect to the Tm:YLF slab.

4.1.2 Emission

The single-pass emission, as opposed to the absorption, from the thulium and holmium crystals, F_B^{Tm} and F_B^{Ho} , can be expressed as

$$\begin{aligned} F_B^{Tm}(\lambda^{Tm}, T) &= - \left(1 - \exp(\sigma_{em}^{Tm}(\lambda^{Tm}, T) \int_{z=0}^{z=l_r^{Tm}} [N_U^{Tm}(z) - F_{em}^{Tm}(\lambda^{Tm}, T) N_L^{Tm}(z)] dz) \right) , \\ &= - (1 - \exp(\sigma_{em}^{Tm}(\lambda^{Tm}, T) n_l^{Tm}(\lambda^{Tm}, T))) , \end{aligned} \quad (4.18)$$

$$\begin{aligned} F_B^{Ho}(\lambda^{Ho}, T) &= - \left(1 - \exp(\sigma_{em}^{Ho}(\lambda^{Ho}, T) \int_{x=0}^{x=l_r^{Ho}} [N_U^{Ho}(x) - F_{em}^{Ho}(\lambda^{Ho}, T) N_L^{Ho}(x)] dx) \right) , \\ &= - (1 - \exp(\sigma_{em}^{Ho}(\lambda^{Ho}, T) n_l^{Ho}(\lambda^{Ho}, T))) , \end{aligned} \quad (4.19)$$

where $\sigma_{em}^{Tm}(\lambda^{Tm}, T)$ and $\sigma_{em}^{Ho}(\lambda^{Ho}, T)$ are once again the effective emission cross-sections for the thulium and holmium media at the lasing wavelength of each laser, respectively.

The integrated inversion density, referenced to manifolds coupled by the laser radiation for both systems, n_l , similar to equation 3.12, is given by

$$\begin{aligned}
 n_l^{Tm}(\lambda^{Tm}, T) &= \int_{z=0}^{z=l_r^{Tm}} [N_U^{Tm}(z) - F_{em}^{Tm}(\lambda^{Tm}, T) N_L^{Tm}(z)] dz, \\
 &= \int_{z=0}^{z=l_r^{Tm}} [(1 + F_{em}^{Tm}(\lambda^{Tm}, T)) N_U^{Tm}(z) - F_{em}^{Tm}(\lambda^{Tm}, T) N_T^{Tm}] dz, \\
 &= (1 + F_{em}^{Tm}(\lambda^{Tm}, T)) n_U^{Tm} - F_{em}^{Tm}(\lambda^{Tm}, T) N_T^{Tm} l_r^{Tm}, \quad (4.20)
 \end{aligned}$$

$$\begin{aligned}
 n_l^{Ho}(\lambda^{Ho}, T) &= \int_{x=0}^{x=l_r^{Ho}} [N_U^{Ho}(x) - F_{em}^{Ho}(\lambda^{Ho}, T) N_L^{Ho}(x)] dx, \\
 &= \int_{x=0}^{x=l_r^{Ho}} [(1 + F_{em}^{Ho}(\lambda^{Ho}, T)) N_U^{Ho}(x) - F_{em}^{Ho}(\lambda^{Ho}, T) N_T^{Ho}] dx, \\
 &= (1 + F_{em}^{Ho}(\lambda^{Ho}, T)) n_U^{Ho} - F_{em}^{Ho}(\lambda^{Ho}, T) N_T^{Ho} l_r^{Ho}. \quad (4.21)
 \end{aligned}$$

$F_{em}^{Tm(Ho)}$ is the ratio of the emission cross-section and absorption cross-section at the lasing wavelength, or the ratio of the Boltzmann distribution factor of the laser manifold, given by the equations

$$\begin{aligned}
 F_{em}^{Tm}(\lambda^{Tm}, T) &= \frac{\sigma_{abs}^{Tm}(\lambda^{Tm}, T)}{\sigma_{em}^{Tm}(\lambda^{Tm}, T)}, \\
 &= \frac{\exp\left[\frac{-1}{k_B T} \left(E_{3F4}^{Tm} - \frac{hc_0}{\lambda^{Tm}} - E_{3H6}^{Tm}\right)\right]}{Z_L^{Tm}(T)} \frac{Z_U^{Tm}(T)}{\exp\left[\frac{-1}{k_B T} (E_{3F4}^{Tm} - E_{3F4}^{Tm})\right]}, \\
 &= \frac{Z_U^{Tm}(T)}{Z_L^{Tm}(T)} \exp\left[\frac{1}{k_B T} \left(\frac{hc_0}{\lambda^{Tm}} - E_{3F4}^{Tm}\right)\right], \quad (4.22)
 \end{aligned}$$

$$\begin{aligned}
 F_{em}^{Ho}(\lambda^{Ho}, T) &= \frac{\sigma_{abs}^{Ho}(\lambda^{Ho}, T)}{\sigma_{em}^{Ho}(\lambda^{Ho}, T)}, \\
 &= \frac{\exp\left[\frac{-1}{k_B T} \left(E_{5I7}^{Ho} - \frac{hc_0}{\lambda^{Ho}} - E_{5I8}^{Ho}\right)\right]}{Z_L^{Ho}(T)} \frac{Z_U^{Ho}(T)}{\exp\left[\frac{-1}{k_B T} (E_{5I7}^{Ho} - E_{5I7}^{Ho})\right]}, \\
 &= \frac{Z_U^{Ho}(T)}{Z_L^{Ho}(T)} \exp\left[\frac{1}{k_B T} \left(\frac{1}{\lambda^{Ho}} - E_{5I7}^{Ho}\right)\right], \quad (4.23)
 \end{aligned}$$

where $Z_U^{Tm}(T)$ and $Z_L^{Tm}(T)$ are the partition functions of the upper and lower laser manifold of thulium, E_{3F4}^{Tm} and E_{3H6}^{Tm} is the zero-line energy of the upper and lower laser manifold of thulium (3F_4) and E_{5I7}^{Ho} is the zero-line energy of the upper laser manifold of holmium (5I_7).

The double-pass gain for the thulium and holmium doped crystals, D_B^{Tm} and D_B^{Ho} respectively, are given by

$$D_B^{Tm}(\lambda^{Tm}, T) = F_B^{Tm}(\lambda^{Tm}, T)(1 + (T_c^{Tm})^2(1 + F_B^{Tm}(\lambda^{Tm}, T))) , \quad (4.24)$$

$$D_B^{Ho}(\lambda^{Ho}, T) = F_B^{Ho}(\lambda^{Ho}, T)(1 + (T_c^{Ho})^2(1 + F_B^{Ho}(\lambda^{Ho}, T))) , \quad (4.25)$$

where T_c^{Tm} and T_c^{Ho} are the one-way transmission of the thulium and holmium cavities respectively, assuming that all losses excluding output coupling and ground state re-absorption, are located at the plane high reflectance mirror end of the laser cavity, as shown in figure 4.2.

4.1.3 Rate of excitation and de-excitation

The rate of excitation for both the thulium and holmium systems, R_{ex}^{Tm} and R_{ex}^{Ho} , are similar to equation 3.9, given by the equations

$$R_{ex}^{Tm} = \eta_{QY}^{Tm} \eta_{del}^p \frac{P_p}{h\nu_p} D_A^{Tm}(\lambda^p, T) , \quad (4.26)$$

$$R_{ex}^{Ho} = \frac{P_p^{Tm}}{h\nu_{Tm}} D_A^{Ho}(\lambda^{Tm}, T) , \quad (4.27)$$

where P_p is the diode pump power. P_p^{Tm} is the one-way intra-cavity thulium power incident on the effective output coupler of reflectance, R_{eff}^{Tm} , as shown in figure 4.2.

In the holmium slab, the absorbed power excites the ions from the ground state, 5I_8 , directly to the upper laser level, 5I_7 ; thus the quantum yield is effectively unity. Moreover, the thulium pump power does not need to go through an optics chain before reaching the holmium doped crystal; thus the pump delivery efficiency is $\sim 100\%$.

As discussed in section 3.1.4, under steady-state operation, the de-excitation rates for both systems are given by

$$R_{de-ex}^{Tm}(\lambda^{Tm}, T) = \frac{P_p^{Tm} R_{eff}^{Tm}(\lambda^{Tm}, T)}{h\nu_{Tm}} D_B^{Tm}(\lambda^{Tm}, T) + \frac{n_U^{Tm} A^{Tm}}{\tau_{eff}^{Tm}} , \quad (4.28)$$

$$R_{de-ex}^{Ho}(\lambda^{Ho}, T) = \frac{P_o^{Ho}}{h\nu_{Ho}} \frac{R_{oc}^{Ho}}{1 - R_{oc}^{Ho}} D_B^{Ho}(\lambda^{Ho}, T) + \frac{n_U^{Ho} A^{Ho}}{\tau_{eff}^{Ho}} , \quad (4.29)$$

where P_o^{Ho} is the output power of the holmium laser.

4.1.4 Equating excitation and de-excitation rate

The one-way intra-cavity thulium laser power incident on the holmium doped crystal can be obtained by equating and rearranging equation 4.26 and 4.28 giving

$$P_p^{Tm} = \eta_{mode}^{Tm} \eta_{QY}^{Tm} \eta_{del}^p \frac{\nu_{Tm}}{\nu_p} \frac{1}{R_{eff}^{Tm}(\lambda_{Tm}, T)} \frac{D_A^{Tm}(\lambda^p, T)}{D_B^{Tm}(\lambda^{Tm}, T)} \left[P_p - \frac{n_U^{Tm} A^{Tm}}{\tau_{eff}^{Tm}} \frac{h\nu_p}{\eta_{QY}^{Tm} \eta_{del}^p} \frac{1}{D_A^{Tm}(\lambda^p, T)} \right], \quad (4.30)$$

where an additional term, η_{mode}^{Tm} , the mode-fill efficiency of the thulium system enters the equation by replacing P_p^{Tm} with $\frac{P_p^{Tm}}{\eta_{mode}^{Tm}}$, leading to the final form of the equation. The effective output power of the thulium laser, P_o^{Tm} , includes the power absorbed by Ho:YAG and that which is lost through the thulium cavity mirrors, and is related to the one-way intra-cavity thulium pump power by

$$P_o^{Tm} = (1 - R_{eff}^{Tm}(\lambda^{Tm}, T)) P_p^{Tm}. \quad (4.31)$$

Similarly for the holmium laser system, equating and rearranging equations 4.27 and 4.29 we find,

$$P_o^{Ho} = \eta_{mode}^{Ho} \frac{\nu_{Ho}}{\nu_{Tm}} \frac{1 - R_{oc}^{Ho}}{R_{oc}^{Ho}} \frac{D_A^{Ho}(\lambda^{Tm}, T)}{D_B^{Ho}(\lambda^{Ho}, T)} \left[P_p^{Tm} - \frac{n_U^{Ho} A^{Ho}}{\tau_{eff}^{Ho}} \frac{h\nu_{Tm}}{D_A^{Ho}(\lambda^{Tm}, T)} \right]. \quad (4.32)$$

Although the slope efficiency and threshold pump power for the holmium laser are obtained from equation 4.32 in terms of the thulium laser parameters, using a similar method to that above, it is more meaningful to derive an expression for the laser performance with respect to the diode pump power. Thus by substituting equation 4.30 into equation 4.32, we obtain the final form

$$P_o^{Ho} = \eta_{mode}^{Ho} \eta_{mode}^{Tm} \eta_{QY}^{Tm} \eta_{del}^p \frac{\nu_{Ho}}{\nu_p} \frac{1}{R_{eff}^{Tm}(\lambda_{Tm}, T)} \frac{1 - R_{oc}^{Ho}}{R_{oc}^{Ho}} \frac{D_A^{Ho}(\lambda^{Tm}, T)}{D_B^{Ho}(\lambda^{Ho}, T)} \frac{D_A^{Tm}(\lambda^p, T)}{D_B^{Tm}(\lambda^{Tm}, T)} \left[P_p - \frac{n_U^{Tm} w^{Tm} t^{Tm}}{\tau_{eff}^{Tm}} \frac{h\nu_p}{\eta_{QY}^{Tm} \eta_{del}^p} \frac{1}{D_A^{Tm}(\lambda^p, T)} - \frac{n_U^{Ho} w^{Ho} t^{Ho}}{\tau_{eff}^{Ho}} \frac{h\nu_{Tm}}{D_A^{Ho}(\lambda^{Tm}, T)} \frac{D_B^{Tm}(\lambda^{Tm}, T)}{D_A^{Tm}(\lambda^p, T)} \frac{1}{\eta_{mode}^{Tm} \eta_{QY}^{Tm} \eta_{del}^p} \frac{\nu_p}{\nu_{Tm}} R_{eff}^{Tm}(\lambda^{Tm}, T) \right]. \quad (4.33)$$

Comparing equations 4.30 and 4.33 with equation 3.1 allows us to obtain the laser performance equations for the thulium and holmium systems as given by equations 4.1 to 4.5.

4.2 Laser design

Using the equations described in the above section to model the laser performance of the intra-cavity side-pump configuration, it is possible to determine what are the effects of various cavity parameters. In this section parameters such as output coupling, Ho:YAG crystal dimensions and doping concentration are discussed and adjusted to optimise the cavity and Ho:YAG design in favour of the output power and slope efficiency.

Table 4.1 shows the parameters used for the modelling. The design of the Tm:YLF slab has been discussed in chapter 3, thus further details will not be discussed here. The Ho:YAG slab, on the other hand, has a length and thickness defined by the thulium laser pump profile. The length of crystal was designed to be slightly longer than the pump width to prevent its edges blocking the path of the thulium laser beam and affecting the laser performance, while the thickness is chosen so as to fit in the whole thulium pump beam. The width and doping concentration of the slab were flexible and were solely used to provide enough absorption in the holmium through the double-passing of the thulium pump beam. The relatively low single-pass cavity transmission for the thulium cavity was primarily due to the loss in the pump-reflective coating of the Tm:YLF slab. As shown in figure 3.6, the coating loss is ~ 0.5 % per pass, which unfortunately was higher than regular anti-reflection coatings. Moreover, the surfaces of the Ho:YAG also give extra losses, which were assumed to be ~ 0.3 % per pass for each surface. The model assumes room temperature operation at 300 K as the temperature rise is not known. In any case the calculated temperature rise was also rather small and its effect on laser performance was minor. The mode-fill efficiency used for the thulium is obtained in section 3.3, and is also used for the holmium as the exact value is unclear.

In the intra-cavity side-pumped configuration with the holmium positioned in the thulium cavity, changes in the holmium cavity can affect the thulium laser performance. Therefore when changing parameters of the holmium cavity, it is important to be aware of the effects the changes bring to both systems.

Description	Symbols	Tm:YLF	Ho:YAG
Doping concentration (at.%)	D	2	1
Total population density (cm^{-3})	N_T	2.62×10^{20}	1.38×10^{20}
Slab width (cm)	w	0.8	0.4
Slab length (cm)	l	2.0	1.0
Gain height (cm)	t	0.074	0.080
Cavity length (cm)	l_c	6.7	3.0
Fluorescence lifetime (ms)	τ	14	8.5
Single-pass cavity transmission	T_c	0.986	0.994
Crystal operating temperature (K)	T	300	300
Mode-fill efficiency	η_{mode}	0.67	0.67
Delivery efficiency	η_{del}	1	1

TABLE 4.1: Parameters used for intra-cavity modelling. Obtained from literature [7].

4.2.1 Gain and absorption for different holmium output coupler reflectivities

The first design parameter of interest is the output coupling of the holmium laser. Figure 4.4 shows how the gain and absorption for both systems change as a function of the holmium output coupling reflectivity. As expected, the gain of the holmium system increases significantly with increasing output coupler transmission (see figure 4.4(a)). As a result, the increased inversion leads to a stronger depletion of the holmium ground-state, and thus a reduction in thulium absorption in the holmium crystal. The reduction in absorption brings along reduced effective output coupling of the thulium cavity (see figure 4.4(b)), as expressed by equation 4.3. Although the change in reflectivity of the effective output coupling is small, it can be a significant effect on the thulium laser performance when the small output coupling is comparable to the total loss in the thulium cavity. Moreover, the broad gain spectrum in thulium allows the operating wavelength to shift, depending on cavity configuration, which can introduce significant performance changes as the absorption in holmium varies.

In order to observe the effect of an intra-cavity Ho:YAG gain element on the Tm:YLF lasing wavelength, a Ho:YAG rod was inserted into a Tm:YLF rod laser cavity previously described in section 2.5. The simple two-mirror cavity, 100 mm long, consisted of a plane mirror and a 200 mm radius of curvature concave mirror, both coated to be highly reflective at the thulium lasing wavelength. A 2 at%, 24 mm-long Tm:YLF rod, and two 0.5 at% Ho:YAG rods of lengths (0.6 cm and 1 cm), each mounted in water cooled copper heat sinks maintained at 16 °C, were used for the experiment. The operating wavelength of thulium shifted to 1951 nm compared to 1909 nm when either Ho:YAG rod was inserted into the cavity, as has been reported by other groups [4]. This shift in wavelength was due to the Tm:YLF laser selecting an operating wavelength

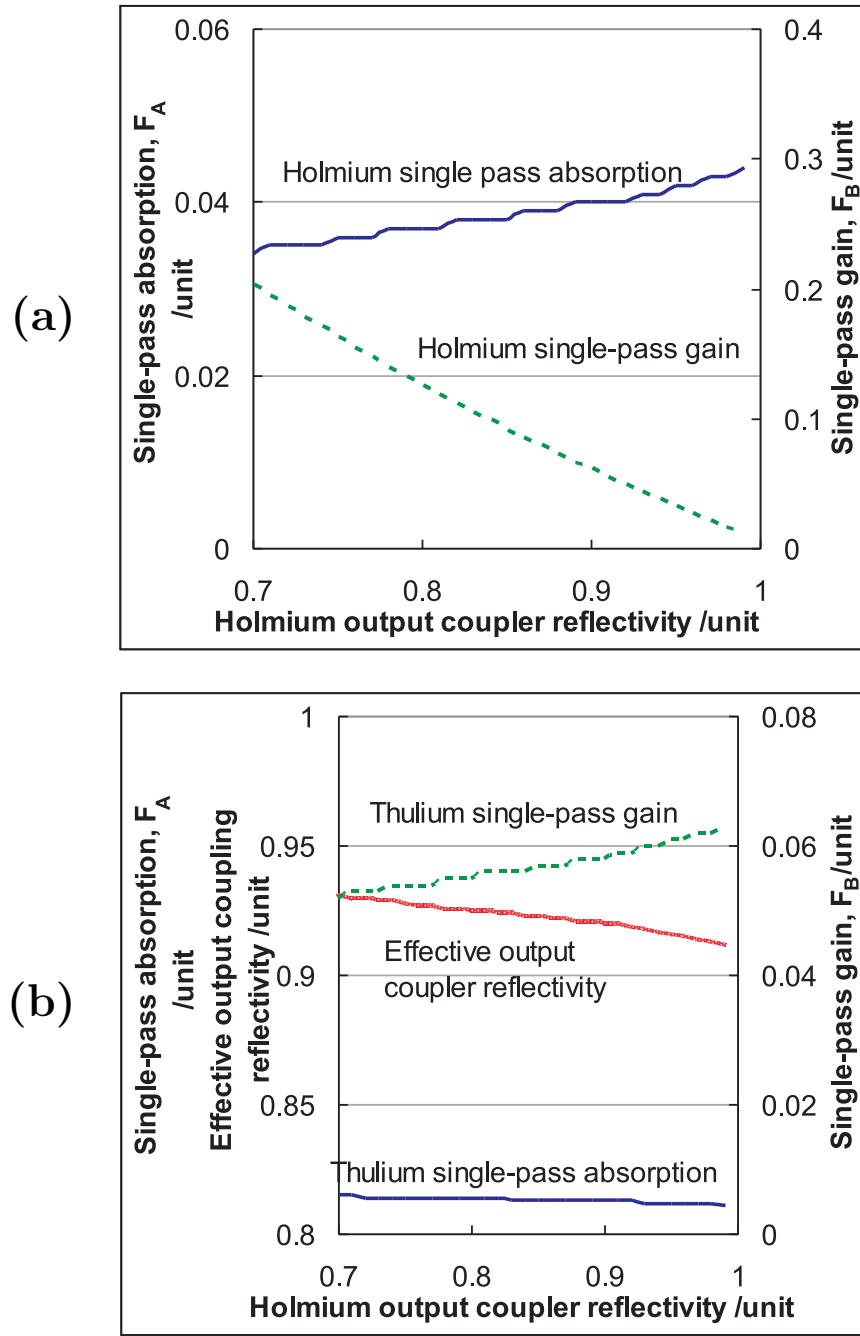


FIGURE 4.4: Effect of holmium output coupler reflectivity on gain and absorption for (a) holmium and (b) thulium system

that minimises the threshold condition, i.e. it automatically finds the lowest cavity loss condition at which it has sufficient gain, and therefore tries to avoid absorption of the Ho:YAG by using the broad gain spectrum available. Figure 4.5 shows that 1950 nm is the lowest absorption of the Ho:YAG spectrum while some thulium gain is still available. Unfortunately, this is not the desired operating wavelength as the absorption in Ho:YAG would be relatively low. Thus we employed a simple wavelength selection method of

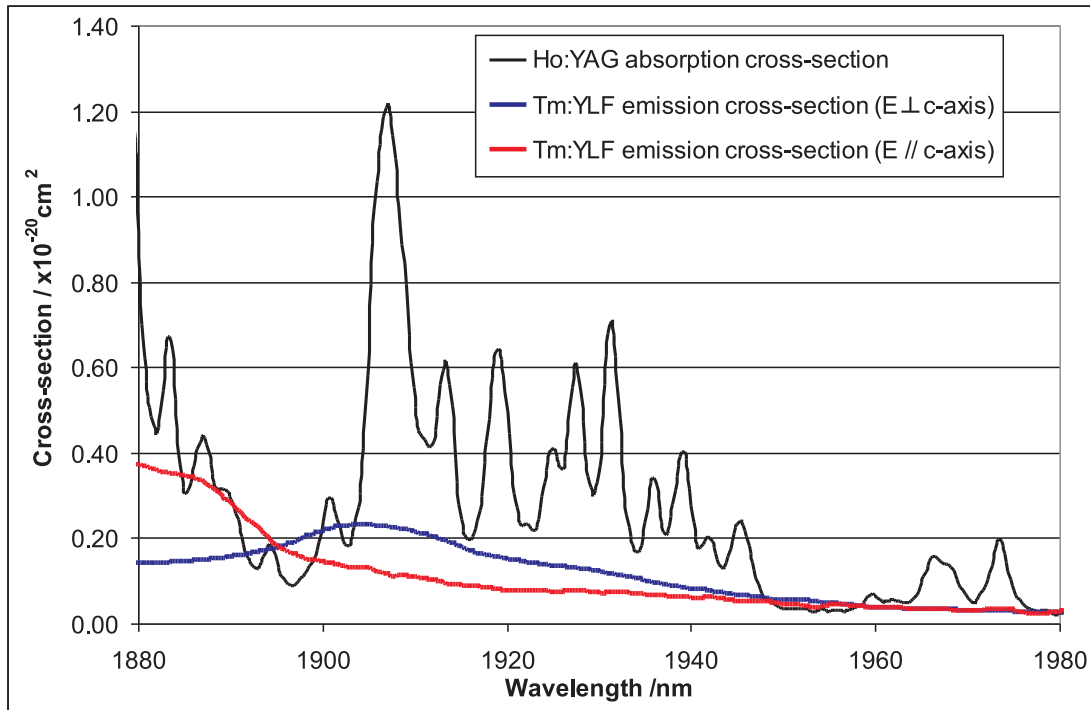


FIGURE 4.5: Tm:YLF emission cross-section from literature [87] for the two polarisations and measured Ho:YAG absorption cross-section

customised mirror coating, which prevents the thulium from lasing at this wavelength.

The purpose of the specially designed mirrors, which we will call “edge mirrors”, was to prevent the thulium laser wavelength from shifting to the longer wavelength of 1950 nm by increasing the transmission as shown in figure 4.6. The edge mirrors were employed in the thulium cavity, to force the thulium to lase at wavelengths < 1950 nm, and thus give higher absorption in the holmium. Moreover, the edge mirrors also prevent the holmium ions stimulating lasing in the wrong direction, since Tm:YLF can still have gain in the $2.1 \mu\text{m}$ region [87] and, if broadband high reflective coatings covering this band were used for the thulium laser, it could potentially reach threshold before the intended holmium laser cavity.

4.2.2 Holmium cavity optimisation

For the holmium optimisation, we choose a Ho:YAG slab of 1 at.% with a width of 0.4 mm to provide sufficient absorption as will be discussed in section 4.2.3. Figure 4.7(a) shows the predicted laser performance for the holmium system with respect to various output coupling values for the holmium laser cavity. It is clear that increasing the output coupling from zero improves the laser performance due to the higher output to cavity loss ratio, as shown in the slope efficiency curve. This starts to saturate when reflectivity

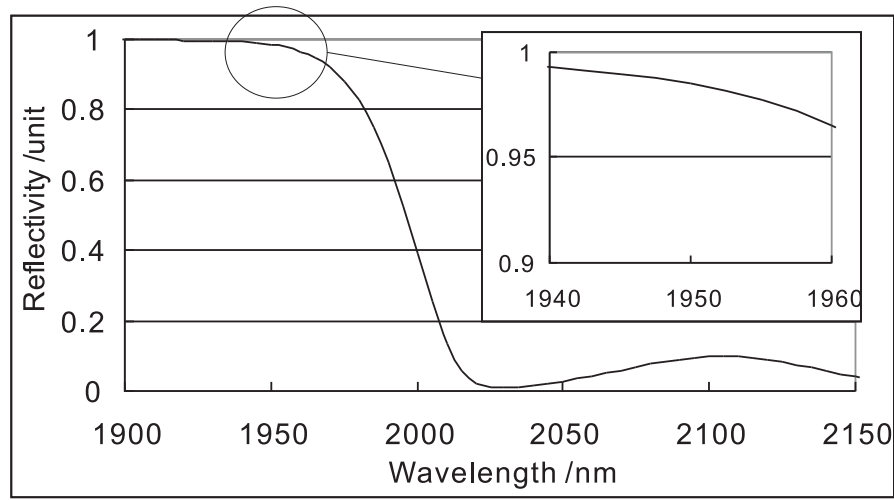


FIGURE 4.6: Theoretical reflectivity of “edge mirror”

of the output coupler reaches $\sim 95\%$, and is maximised at 90% . The output power prediction for the holmium laser suggests that the optimum output coupling reflectivity is $\sim 90\%$. For the optimum configuration the holmium laser was anticipated to have an 18% slope efficiency with respect to the diode incident power on the thulium slab and a maximum output power of 27 W with a diode-pump power threshold of 86 W . Note that the holmium lasing wavelength changes according to the output coupling, due to the quasi-three level nature of the transition, and for a 90% reflective output coupler, is expected to lase at 2097 nm .

The expected effective performance for the thulium laser is shown in figure 4.7(b), illustrating the dependence on the holmium output coupler reflectivity. The modelled thulium laser performance is weakly affected by the holmium output coupling. The thulium laser has a theoretical slope of 33% with respect to the diode incident power, slightly lower than the 40% slope efficiency obtained under normal operation with a 87% reflective output coupler. This is due to the increased loss from the extra surfaces and the lower output coupling. The 60 W effective thulium output power corresponds to the double-pass absorbed power in the holmium, but unfortunately it is not directly measurable experimentally. The thulium laser requires 57 W of diode pump power to reach threshold when a 90% reflective holmium output coupler is used for the holmium cavity. The thulium lasing wavelength is expected to shift to 1898 nm after the insertion of the holmium crystal (see figure 4.7(b)). This is different to the previous experimental and literature result as discussed in section 4.2.1, where a shift of wavelength to 1951 nm was observed. The difference was caused by the use of the customised coating edge mirror, which prevents the shift of wavelength to 1950 nm by introducing high transmission at that wavelength. The thulium lasing wavelength is thus forced to 1898 nm , the second lowest holmium absorption dip in this spectral region, giving a calculated double-pass

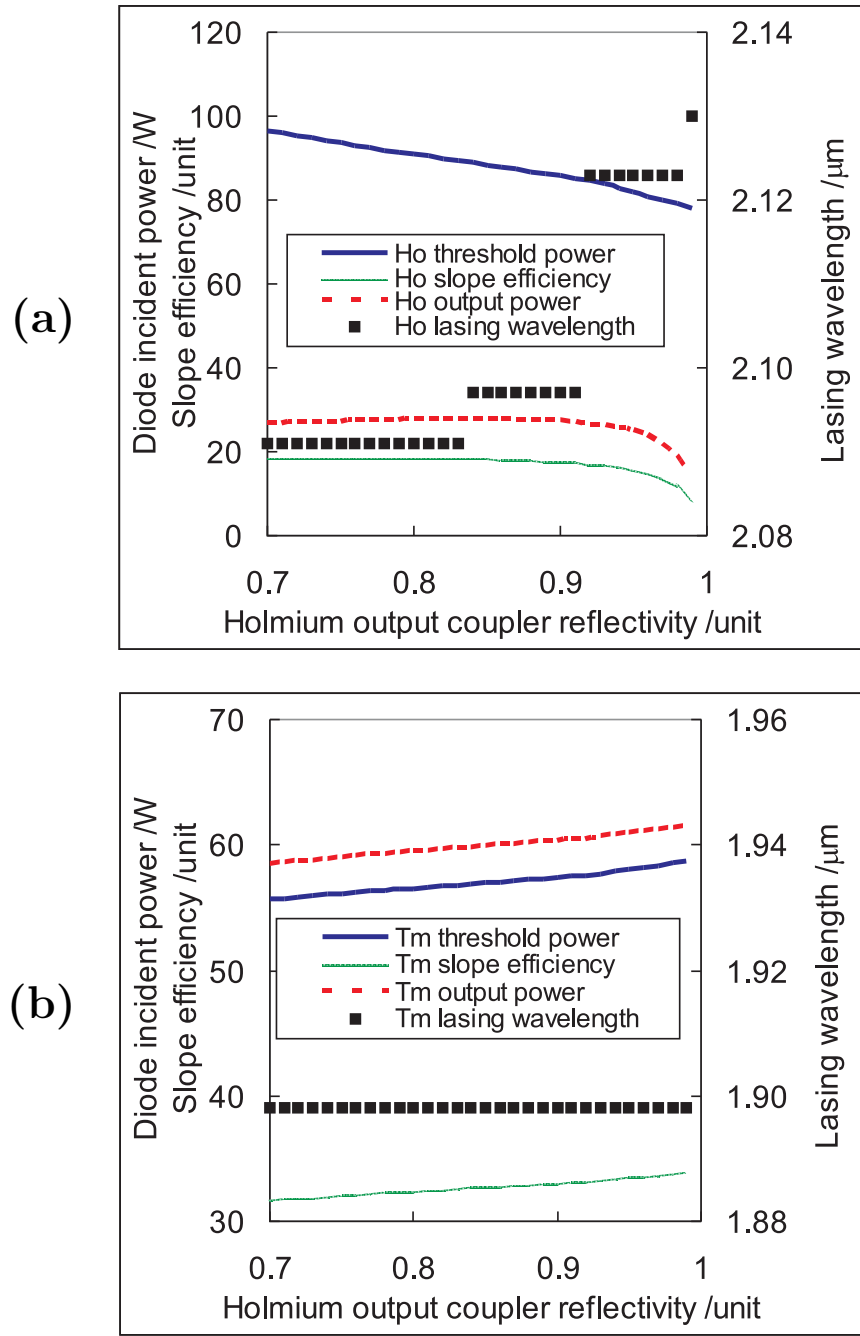


FIGURE 4.7: Calculated laser performance of (a) holmium system and (b) thulium system

absorption of $\sim 8\%$. Note that the threshold pump power for the intra-cavity system is higher than the 52 W for the standard thulium laser system with a 87 % reflective output coupler, even though the combined output coupling and loss is lower. The increase in threshold is due to the change in thulium lasing wavelength, where the shift to a shorter wavelength leads to increased population in the lower laser level.

4.2.3 Optimisation of the Ho:YAG slab design

The optimum output coupler is calculated above to be 90 % reflective and this is now used to model the laser performance for various holmium doping concentrations (0.5-2 at.%) and slab widths (0.2-1 cm), in order to maximise the laser performance. Too high a doping concentration would lead to high threshold and upconversion losses, thus increasing the heat deposition and reducing upper laser level lifetime. On the other hand, increasing the slab width would increase the difficulty in obtaining circular output, leading to a requirement for a more complicated holmium cavity design. Therefore, a balance between the two is required.

The calculated laser performance is shown in figure 4.8 for the different doping concentration and slab width combinations. It can be seen that the highest output power achievable is 28 W at the maximum diode pump power of 240 W, using a 0.2 mm-wide, 2 at.% doped Ho:YAG slab. The slope efficiency for this slab configuration was 17.5 %. Unfortunately, the holmium-holmium upconversion effect is not taken into account in this model as not all the required parameters were available, and the high doping concentration could have a relatively high upconversion loss. This loss will further increase the threshold, therefore we expect an optimum condition to be reached for low holmium concentration.

The next highest output power from the graph is a 0.4 mm-wide, 1 at.% doped Ho:YAG slab, which gives a predicted output power of 27 W, with a slope efficiency of 17.5 %. This slab has a slightly higher threshold pump power as the inversion along holmium is lower than the 0.2 mm wide, 2 at.% slab due to the lower doping concentration. It was chosen for our cavity design as it provides a high output power, a good slope efficiency and a low upconversion loss.

4.3 Intra-cavity side-pumping experimental setup

The architecture presented here is the intra-cavity side-pumping Ho:YAG laser system. The holmium crystal was positioned in the thulium cavity, side-pumped by the Tm:YLF slab laser, which was in turn end-pumped by a diode-stack. This cavity design allows the use of a moderate-brightness diode pump source for the Tm:YLF slab pump laser, and a low holmium doping concentration for reduced holmium-holmium upconversion effects, while maintaining a compact cavity design, as shown in figure 4.9.

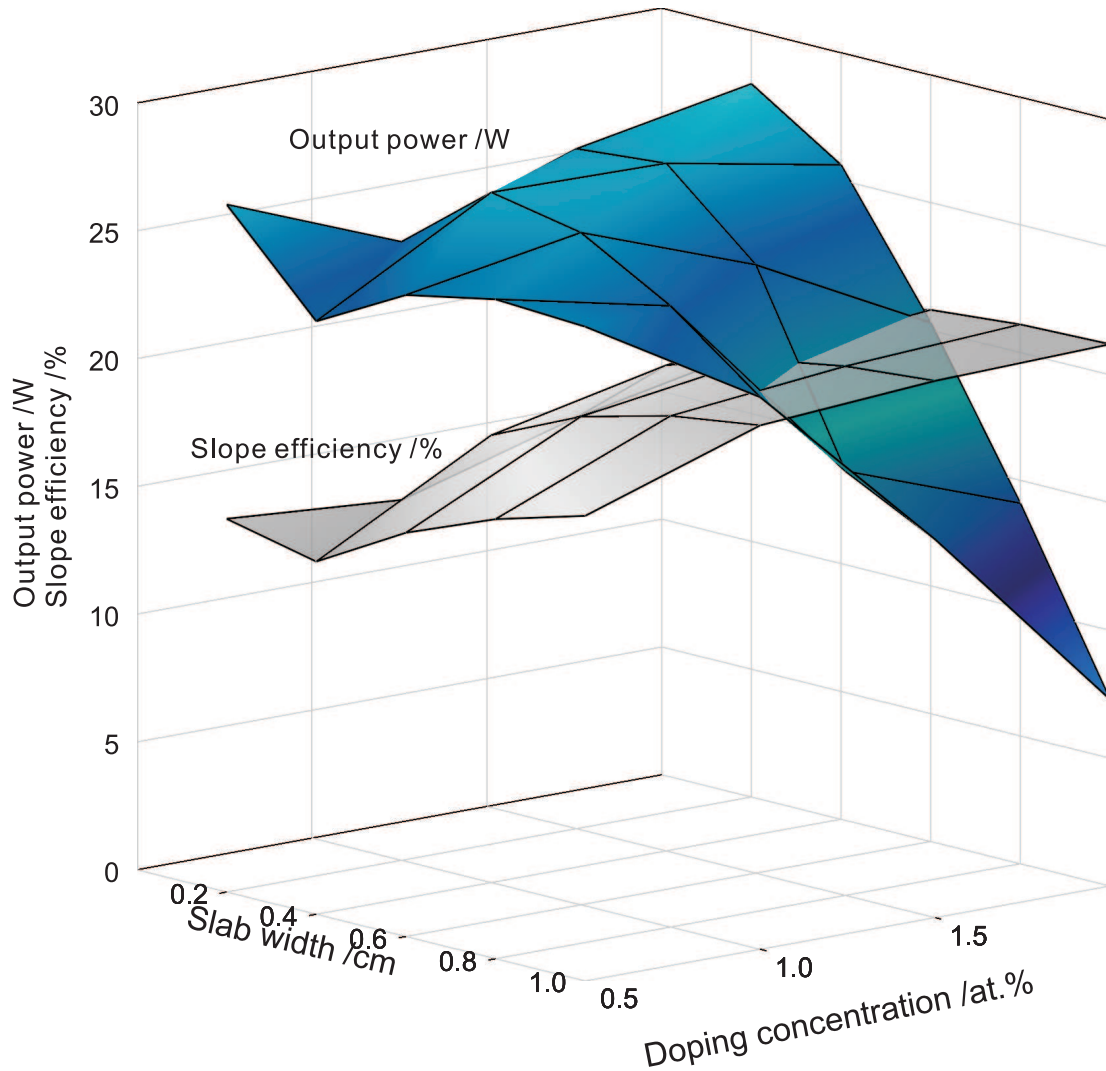


FIGURE 4.8: Calculated holmium laser performance as a function of Ho:YAG slab width and doping concentration

4.3.1 Pump laser

The laser diode pump source used in this section is identical to the one described in section 3.2.1.1, giving a total pump power of 242 W incident. The Tm:YLF slab is also similar to that described in section 3.2.2, except that it was 2 mm-thick. A 2 mm-thick slab was used instead of a 1.5 mm-thick slab because the 1.5 mm slab pump reflective coating was damaged during initial investigations by power spikes as will be discussed later in section 4.4.

The thulium cavity employed a simple two-mirror plane-concave cavity design that consisted of a plane pump-in-coupling mirror and another 100 mm radius of curvature concave mirror. Both mirrors have the edge mirror coating described in section 4.2. The Tm:YLF slab was positioned close to the plane mirror, followed closely by the Ho:YAG

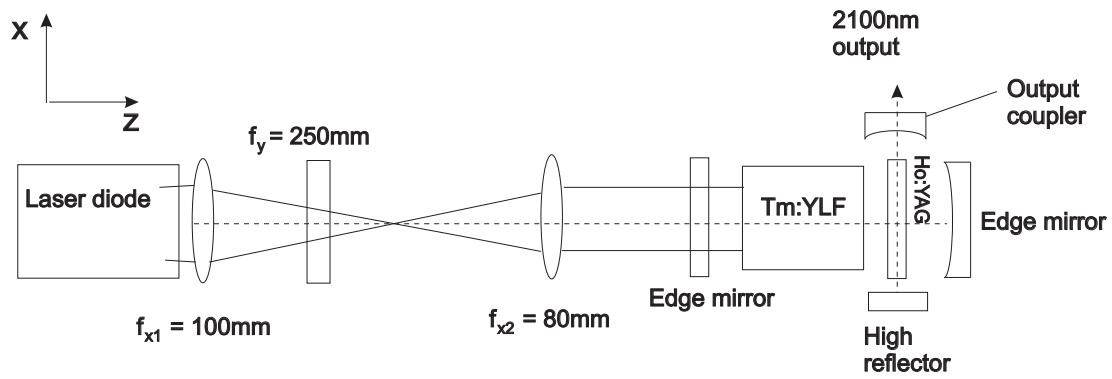


FIGURE 4.9: Intra-cavity side-pumping experimental setup

slab. The cavity length was ~ 67 mm, which was longer than that used in chapter 3, as was required to provide enough space for the Ho:YAG within the thulium laser cavity.

4.3.2 Holmium cavity

The Ho:YAG slab design is shown in figure 4.10. It is doped at 1 at.%, and is 10 mm-long, 4 mm-wide and 2 mm thick. The top and bottom surfaces were fine ground and the other surfaces were optically polished. The 10 mm by 2 mm surfaces were AR coated for 1900 ± 30 nm and the 2 mm by 4 mm surfaces are AR coated for 2100 ± 30 nm. The slab was mounted on an aluminium mount that was attached to the water-cooled thulium copper-mount for heat-sinking. A layer of 0.1 mm-indium foil is used for improved thermal contact between the aluminium mount and the Ho:YAG slab, and between the aluminium mount and the copper heat-sink.

A simple two-mirror cavity was employed for the holmium laser system. The plane mirror was coated with a broadband high reflectivity coating at $2 \pm 0.1 \mu\text{m}$, and the concave output coupler had a 50 mm radius of curvature with a measured reflectivity of 89 % at the holmium lasing wavelength. The cavity mirror-mirror separation was set to ~ 25 mm, to minimise the fundamental mode size and threshold, while maximising the overlap between the higher-order-modes and the excited volume. This simple cavity resulted in a very compact laser, as shown in the photo in figure 4.11, where the whole cavity was measured to be 3×7 cm only.

4.4 Intra-cavity side-pumped Ho:YAG experimental results

The Tm:YLF laser was observed to operate with a slope efficiency of 36.9 % with respect to the diode incident power, and a threshold incident diode-power of 52 W, without the

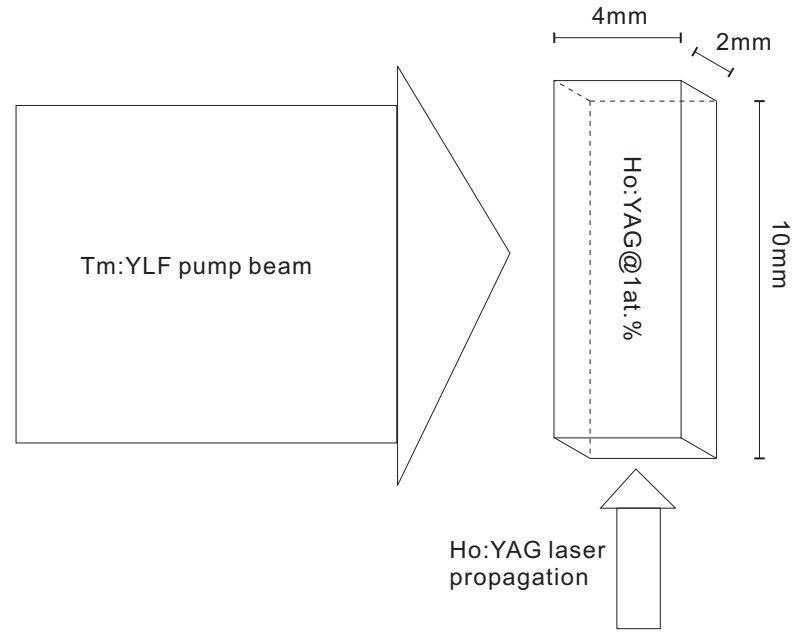


FIGURE 4.10: Ho:YAG slab design

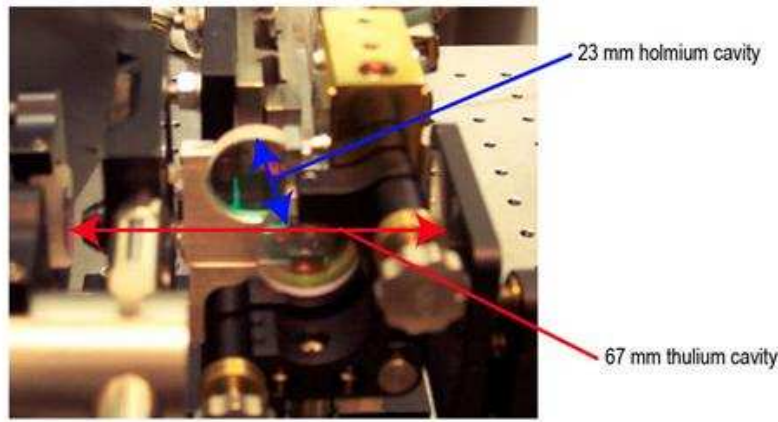


FIGURE 4.11: Photo of intra-cavity side-pumping cavity

Ho:YAG in the cavity, using a $\sim 87\%$ reflective, 200 mm concave output coupler, and a mirror-mirror separation of 50 mm. The slightly reduced slope with respect to the value reported in section 3.3 is assumed to be the result of a worse thermal contact between the slab and the heat-sink, as discussed in chapter 3, or due to higher losses caused by a collection of scratches on the Tm:YLF coatings as shown in figure 4.12. The damage were fine marks crossing the full width of the slab on the pump-reflective coatings of the Tm:YLF slab and were more dense at the top and bottom, as shown in figure 4.12(a). The damage was observed after the experiment thus the exact time of appearance and nature of the damage was not clear.

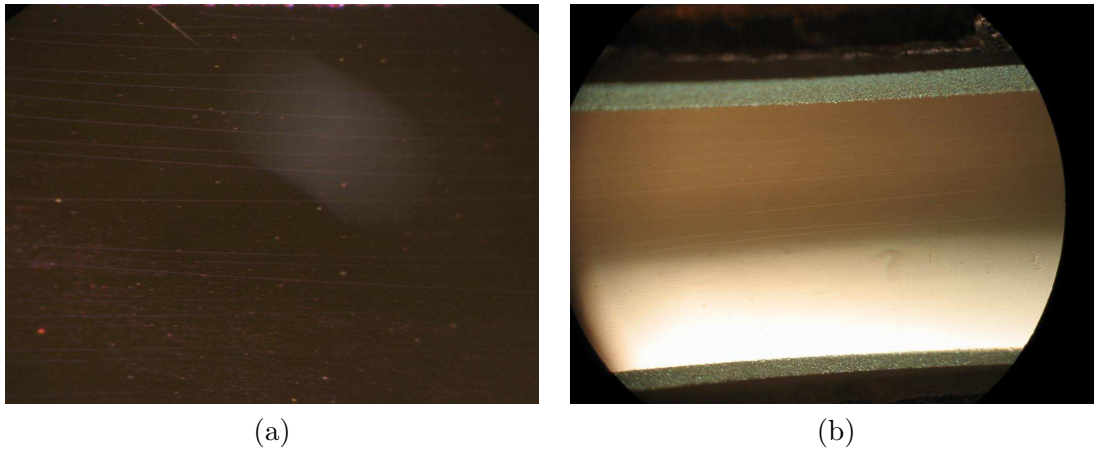


FIGURE 4.12: Damage on pump-reflective coatings of 2 mm thick Tm:YLF slab; (a) shows the damage distribution in detail and (b) shows the damage distribution along the thickness of the slab.

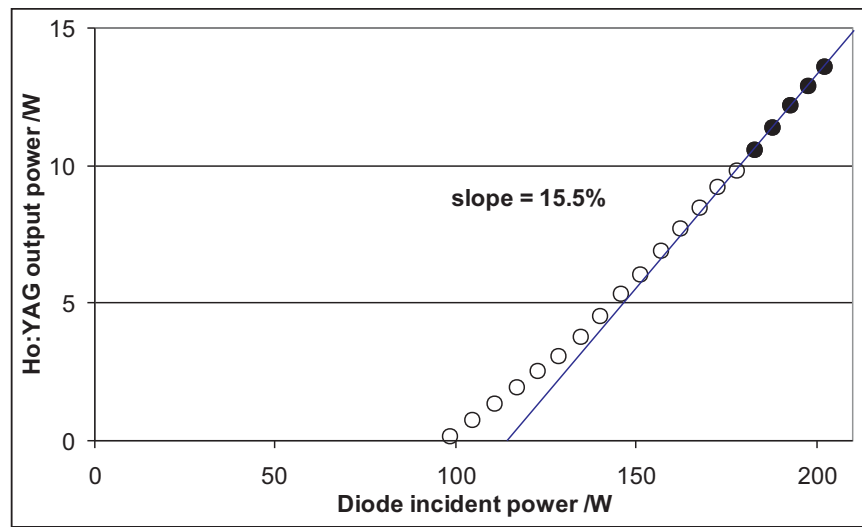


FIGURE 4.13: Laser performance of the intra-cavity side-pumped Ho:YAG laser

The measured laser performance of the intra-cavity side-pumped Ho:YAG laser is shown in figure 4.13. A slope efficiency of 15.5 %, with respect to the diode incident pump power, was found when fitted to the last five data points of the graph. Since the exact threshold of the Ho:YAG with respect to the thulium pump power is not easily quantifiable, the slope efficiency could not be fitted to three times the threshold pump power. The threshold in terms of incident diode power is ~ 95 W, while the maximum holmium laser output power was 13.6 W for 202 W of diode power. Note that the maximum diode pump power was not used due to the concern of possibly exceeding the fracture limit for the 2 mm-thick slab.

A computer controlled monochromator¹, of $f=0.5$ m, was used to measure the output

¹DongWoo Opttron Co. / DM501

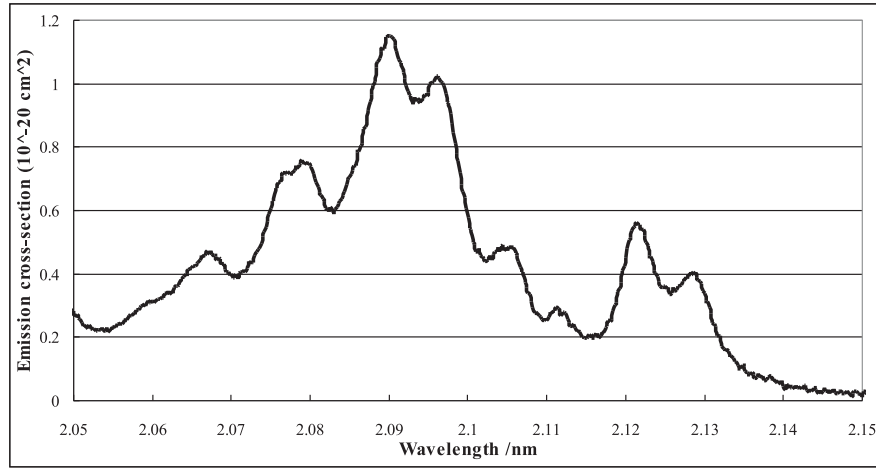


FIGURE 4.14: Emission cross-section of Ho:YAG. Obtained from literature [94].

wavelength of both slab lasers. An extended-InGaAs photodetector² was used for the measurement, and both of the slits of the monochromator were set to 50 μm . The holmium lasing wavelength was at 2097 nm, corresponding to one of the highest emission peaks for Ho:YAG, as shown in figure 4.14. The lasing wavelength of the thulium laser shifts from 1909 nm to 1897 nm, one of the absorption minima of the Ho:YAG absorption spectra, as shown in figure 4.5, after the holmium is inserted into the cavity. This should provide a double-pass absorption and hence an effective output coupling of $\sim 7.6\%$, which is $\sim 50\%$ of the output coupling transmission that was used in chapter 3 for the best Tm:YLF slab laser performance.

A beam profiler³ was used to estimate the beam size ($\frac{1}{e^2}$) and quality of the cavity mode in the holmium laser. The output coupler was changed from a 50 mm radius of curvature concave mirror to 100 mm concave such that a lens of $f=250$ mm could be used to compensate the divergence after the concave output coupler. The mode distribution on the plane high-reflector was re-imaged to half the original size at the beam profiler using a telescope consisting of two spherical lenses of $f=100$ mm and $f=200$ mm. Beam radii of 1910 μm by 250 μm were measured on the plane high-reflector suggesting that the higher-order-modes have filled out the gain region. The beam profile is shown in figure 4.15, and a M^2 beam quality of 140 by 1.7 was measured. Note that we were at this stage only interested in the power-scaling capability in this cavity design and thus no attempt at improving the beam quality had been made.

The curved edge mirror after the Ho:YAG was replaced by a 89 % reflective output coupler. A similar re-imaging arrangement to the one described above was used to measure the mode size of the thulium on the input coupler. It was found that the

²Judson / J23TW266CR0252.4 / J23 series

³Photon inc / BeamScan controler model: 3088 / detector head: Pyroelectric heads, XYFIR/10Hz

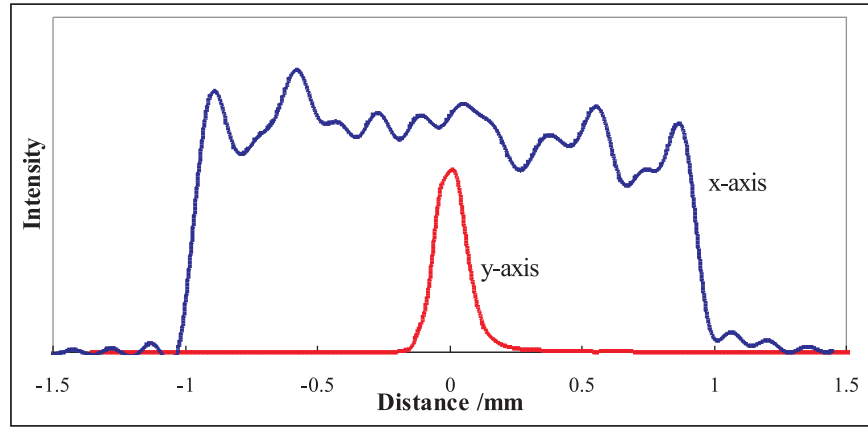


FIGURE 4.15: Measured beam profile of Ho:YAG on high reflective plane mirror

vertical spot size radius was $330\ \mu\text{m}$, without holmium in the thulium cavity, reducing to $220\ \mu\text{m}$ when the Ho:YAG slab was inserted.

Random power spikes were observed from the thulium laser when it was at a power level below the threshold of the holmium laser, or during the alignment of the Ho:YAG laser. The peak power of the spikes increased with pump power until the holmium laser threshold was reached. Regular Q-switched pulses have not been observed, which is consistent with the passive Q-switch second-threshold condition, as discussed in section 4.6. The spikes only exist because Ho:YAG is acting as a saturable absorber in the cavity, giving a varying loss, but it is not strong enough to fully Q-switch the system [105]. Damage to the pump-reflective coating of the Tm:YLF slab and the plane edge mirror were believed to be caused by the spikes. This suggests that the cavity configuration here is not suitable for low-repetition-rate pulsed operation of the holmium laser, as the Ho:YAG would act as a saturable absorber, Q-switching the thulium laser [105].

Note that the diode power was measured with a 300 W power detector with an accuracy to the nearest 1 W. The holmium output power uses a 100 W power detector that is accurate to the nearest 0.2 W. The affect of inaccurate reading to the result is small.

4.5 Laser result discussion and modelling

Although the available pump power was 240 W only 200 W was used, due to the concern of possibly exceeding the fracture limit for the 2 mm-thick slab as stated above. Modelling based on this pump power and an holmium output coupler of 89 % reflectivity predicts a threshold of 85 W for this configuration with respect to the diode incident pump power, which is close to the 95 W obtained in the experiment. The maximum

output power at 200 W of incident pump power was expected to be 20 W, while the experimental output power was lower at 13.6 W due to the lower measured slope efficiency of 15.5 % with respect to the theoretical value of 17.5 % and higher threshold.

The lower than predicted slope efficiency could be caused by not having sufficient pump power to get high enough above threshold for the slope efficiency to reach its best performance, which is expected to increase for a three-level laser system [93]. In addition the cavity losses for the thulium laser could have been significantly higher than assumed, possibly exacerbated by the apparent damage on the pump-reflective coatings. Another possibility is the shift in thulium lasing wavelength that result in a low holmium absorption, causing the thulium cavity being under-coupled. Note that the thulium lasing wavelength could shift to longer wavelengths if the thulium slab length or doping concentration increases. Moreover, the mode-fill factor used could be larger than the actual value, or the overlap between the thulium beam and its inversion could have been reduced because of the experimentally observed smaller vertical thulium beam size after the holmium was inserted.

The Ho:YAG crystal was moved up and down whilst the laser was operating and the monitored output power demonstrated that the reduced spot size was not due to hard aperturing by the holmium-doped crystal. Therefore, it is believed that the reduced thulium mode size was due to a soft-aperturing effect, where as the thulium starts lasing, it deplete the absorption in the Ho:YAG at the center of the thulium beam. This would form an effective output coupler with variable transmission across the vertical axis (fast-axis of diode), with minimum absorption, and thus loss, in the center. It is expected that as the pump power is increased, the intensity of the thulium beam will saturate the outer sections of the Ho:YAG crystal and should fill out all the pumped region.

4.6 Second threshold condition

Ho:YAG can be used as a saturable absorber for passive Q-switching Tm:YLF systems. It is therefore important that the thulium laser is operating below the Q-switch operating threshold, or the second threshold condition for passive Q-switching, which is defined by both the Tm:YLF and Ho:YAG design. The relationship of the design parameters are given by [106]

$$\frac{\alpha_a^{Ho} w^{Ho} \sigma_a^{Ho} A_g^{Tm}}{\alpha_g^{Tm} l_r^{Tm} \sigma_g^{Tm} A_a^{Ho}} > 2^* , \quad (4.34)$$

where α_a^{Ho} and w^{Ho} are the small-signal absorption coefficient and width of the holmium crystal. Furthermore, α_g^{Tm} and l_r^{Tm} are the small-signal gain coefficient and the length

of the Tm:YLF slab, σ_a^{Ho} and is the holmium absorption cross-section, σ_g^{Tm} is the thulium laser emission cross-section, A_g^{Tm} is the effective thulium laser beam area in the thulium slab and A_a^{Ho} is the effective holmium laser beam area in the holmium slab. The population reduction factor, 2^* , is equals to one for fast thermal relaxation, and two for slow thermal relaxation [106–108].

Figure 4.16 shows the passive Q-switched operating threshold condition for the intra-cavity system, assuming a 90 % reflective output coupler and a 4 mm-wide holmium slab. The figure suggests that thulium can lase at 1897 nm without exceeding the threshold for Q-switching. On the other hand, lasing wavelength at 1892 nm (π polarisation) and 1953 nm may cause Q-switching of the thulium depending on the thermal relaxation rate. This may be the cause of the power spikes as mentioned in section 4.4. Of the different potential thulium lasing wavelengths, 1953 nm has the lowest absorption, making it sensible to use edge mirrors to prevent lasing in the 1950 nm region. Moreover, equation 4.34 shows that increasing slab width or doping concentration, while keeping the thulium intact, would bring the laser closer to the Q-switch threshold. Therefore it is best to keep the holmium slab wide enough to achieve sufficient absorption while not too wide to start Q-switching the thulium system. Note that reducing the slab width to 2 mm would still give a similar result, therefore, the best option is to use a Ho:YAG slab 3-4 mm wide and utilise a thulium operating wavelength around 1.89 μm as opposed to the peak of the σ polarisation of Tm:YLF emission. It is worth noting that below a wavelength of 1.9 μm the stronger Tm:YLF may switch to the π polarisation.

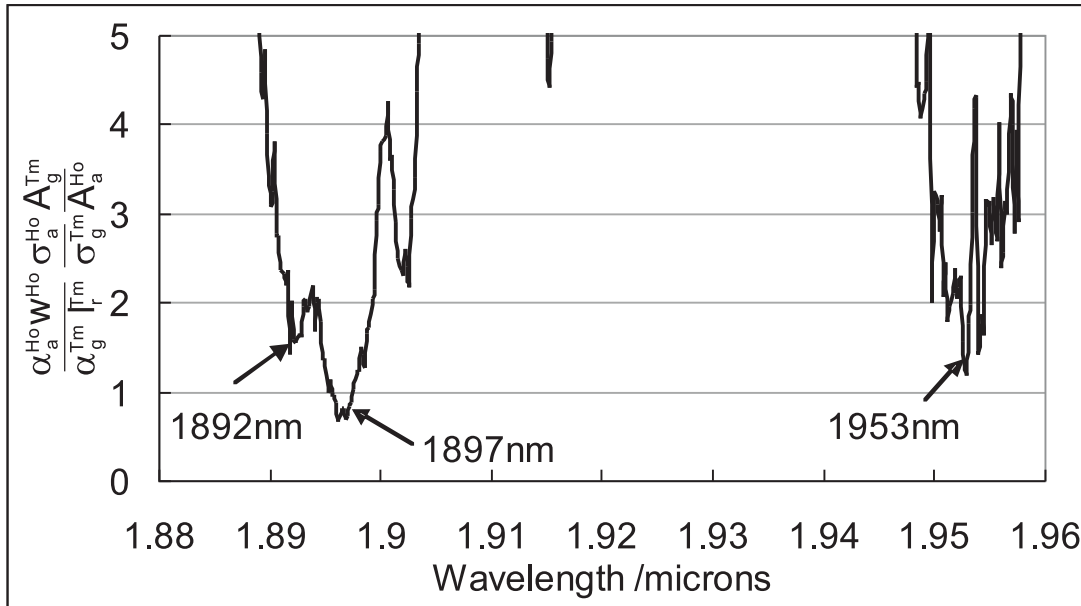


FIGURE 4.16: Calculated passive Q-switch operating threshold equality

4.7 Conclusion

In this chapter a novel Ho:YAG laser has been reported that uses an intra-cavity side-pumping design. This architecture has various benefits, such as compatibility with a power-scalable Tm:YLF slab laser, enabling the use of low holmium doping concentrations, and a compact and simple cavity configuration. A maximum output power of 13.6 W at 2.1 μm was achieved for 200 W of incident diode power, with good potential for further power scaling. Unfortunately, this is still slightly lower than the 19 W achieved by Budni [33] that has a slope efficiency of $\sim 24\%$ overall in an external diode end-pumping scheme. The overall slope efficiency was 15.5% with respect to the diode incident pump power, with a threshold diode pump power of ~ 95 W. The lasing wavelength of the thulium and holmium lasers was 1897 nm and 2097 nm respectively, which matches well with the modelling.

Power scaling in this geometry could be simply achieved by extending the length of the Tm:YLF slab, and side-pumping it. The increase in length of the Tm:YLF slab allows the use of multiple stacks along the sides, well within the fracture limit of a slab (see equation 2.14). As a result, this design allows a simple means of power-scaling the Tm:YLF laser through the increase in fracture limit by increasing in the pump volume. In the following chapter, we will look into how an externally-pumped Ho:YAG laser performed, comparing the results with the intra-cavity side-pumping scheme.

Chapter 5

Externally-pumped Ho:YAG laser

In the previous chapter a novel intra-cavity side-pumped cavity configuration was demonstrated as a platform for power scaling Ho:YAG lasers. One of the limitations in power-scaling Ho:YAG is the power-scalability of the Tm:YLF pump laser, which is limited by the fragile nature of the host and its consequent low stress fracture limit. The use of a slab laser in the intra-cavity side-pumping configuration helped overcome the limitation by increasing the thermally-induced stress fracture limit. Over 13 W of holmium output was achieved and 20 W is expected if a 1.5 mm-thick Tm:YLF slab is available.

Although intra-cavity side-pumping has proven successful with power-scaling and in the mean time provides various benefits over external pumping, it is still important to understand how it compares with external pumping in terms of laser performance and output power. Moreover, external pumping has applications where intra-cavity pumping could not be used, as discussed in section 4.4. Therefore, a Ho:YAG laser externally pumped by power-scaled Tm:YLF slabs is investigated in terms of laser performance and power-scalability.

In this chapter, a power-scaled Ho:YAG laser is demonstrated, externally pumped by two Tm:YLF slab lasers that are spatially multiplexed to form a single pump source. Due to the poor beam quality from a slab laser, a pump-guiding Ho:YAG rod is required. The laser is characterised via its laser performance and is matched against the plane-wave theory as described in chapter 3.1. Side-by-side comparison of the externally pumped rod laser and the intra-cavity side-pumping design are given in later sections, followed by a conclusion of the external pumping work.

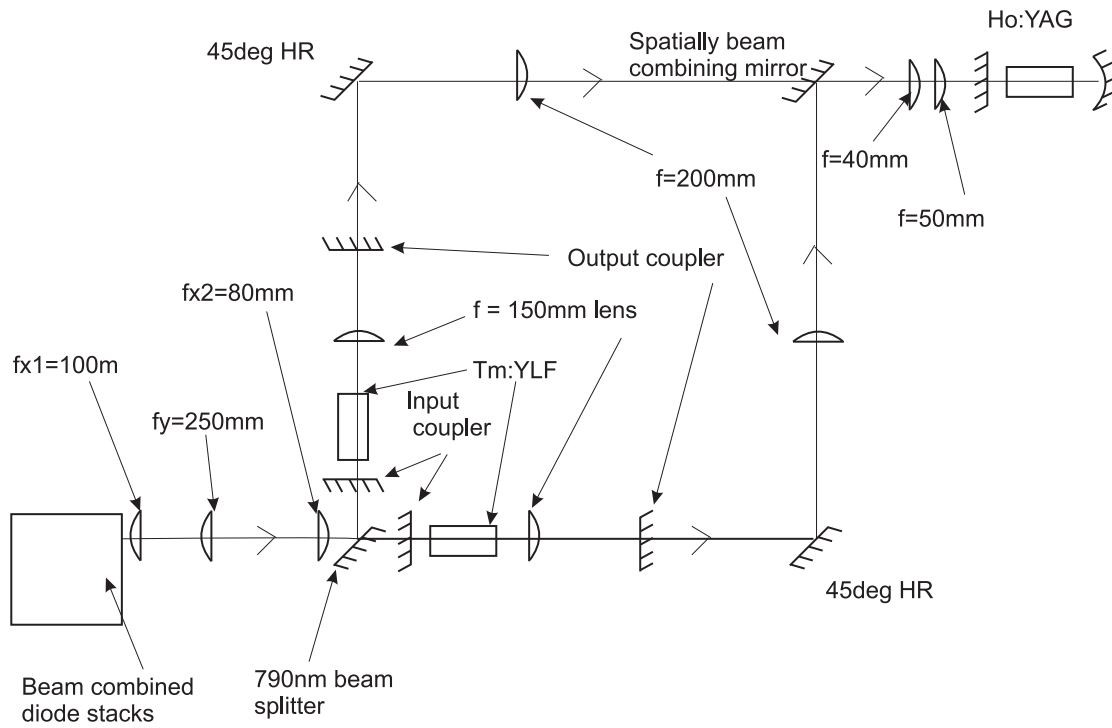


FIGURE 5.1: Experimental setup of pump-guiding Ho:YAG rod laser pumped by spatially beam-combined Tm:YLF slab laser

5.1 Externally-pumped Ho:YAG laser cavity

In this configuration the Ho:YAG rod laser was end-pumped by two spatially multiplexed Tm:YLF slab lasers, which were in turn end-pumped by a spatially multiplexed diode stack. Figure 5.1 shows the experimental setup from the diode pump source to the Ho:YAG laser, including the two thulium lasers and the optics used to focus the spatially multiplexed pump beam into the rod.

5.1.1 Pump configuration

The pump source used is identical to the one described in section 3.2.1.2, which gives a total pump power of 431 W at 790 nm, with a beam quality of 360×30 for the fast (y) and slow (x) axes respectively. The focusing system is as previously described until the 790 nm beam-splitting mirror. The mirror has a coating that goes to the edge, and was used to spatially split the pump beam from the diode stacks. The spatially multiplexed diode pump beam was split in the fast-axis before the input couplers of the Tm:YLF lasers, improving the pump beam quality to an estimated value of ~ 21 in the fast-axis for both pump beam. Due to fracture and laser performance considerations, the pump beam was not equally split but a larger portion goes to the thinner slab. This also results in slightly different pump waist diameters of 0.82 mm and 0.68 mm for the 1.5

mm and 2 mm thick slabs respectively. A 2 mm Tm:YLF slab was used instead of two 1.5 mm slabs as only one 1.5 mm slab was available.

5.1.2 Thulium pump

After the beam splitter, the two diode pump beams were used to pump two separate Tm:YLF slab lasers positioned at 90 degrees to each other. Two separate thulium lasers were used as a means of power scaling because the two-slab Tm:YLF slab configuration discussed in section 3.2.3 was not available at the time of experiment. Two separate thulium lasers also provide better overall beam quality when recombined, thus allowing the use of the thinnest Ho:YAG rod for minimum threshold.

The two Tm:YLF lasers consisted of a 1.5 mm-thick and a 2 mm-thick slab, both mounted on separate water-cooled copper heat sinks maintained at 15 °C; a configuration discussed in section 3.2.2. 0.1 mm-thick indium foil was sandwiched between the copper mount and the crystal for improved contact surfaces. The mount is gold plated to prevent oxidation of the copper, which could otherwise lead to reduction in thermal conductivity. Metal plates were attached to the input end of the mount to block any stray pump from hitting the indium, since the power from the stray pump could easily be sufficient to ignite and deposit the indium on the thulium slab surface. The mount was fixed to a translation stage that had vertical movement and tilt adjustment for aligning the slab in the pump beam path.

The Tm:YLF cavity used a plane input coupler that is highly reflective at the laser wavelength, and a plane output coupler with 88 % reflectivity, separated by a distance of 135 mm. A $f=150$ mm spherical lens was inserted into the cavity, 80 mm from the output coupler, to improve the output beam quality for pumping the thinnest Ho:YAG rod. This gave a calculated fundamental mode size of ~ 300 μm , resulting in a measured M^2 beam quality of 175×1.2 and 187×1.3 for the 1.5 mm and 2 mm slab respectively.

This cavity configuration gave a laser performance of 40 % slope efficiency with respect to incident pump power for the 1.5 mm slab, which matches well with previous results. An output power of 47 W was achieved with an incident pump power of 183 W. The threshold pump power was ~ 53 W, which is similar to the threshold pump power when compared to previous result in section 3.3. The threshold equation described in [75] is used to estimate the threshold power of this cavity, using previous and current experimental results and calculated fundamental mode sizes of 235 μm and 298 μm for the previous and current cavity configuration respectively. The threshold is estimated to be 59 W, where the increase in threshold comes from the increased pump and laser mode

sizes. The calculated threshold is higher than the threshold obtained experimentally, indicating the improved beam quality causes a slight improvement in the threshold pump power.

On the other hand, the 2 mm slab operated at only 25 % slope efficiency, much lower than expected. This could be due to thermal contact issues as discussed in section 3.3, but the problem was not solved after several mounting cycles. Another possible explanation is the damaged coatings mentioned in section 4.4 giving a higher cavity loss, but the exact reason is still unclear. The output power was 29 W at a pump power of 167 W. The incident threshold power was 49 W, slightly lower than the 1.5 mm slab due to the smaller pump size. The calculated threshold pump power is also 49 W, but according to the 1.5 mm slab result, the experimental threshold should be lower than the calculated one due to the improved beam quality. This suggested there could be a higher than expected loss in the cavity, which is also the cause of the reduced slope efficiency.

The characterisation of the Tm:YLF laser was not performed at their maximum pump power of 230 W and 196 W respectively for 1.5 mm and 2 mm slabs. This is because the relatively poor performance in the 2 mm slab could lead to increased heat deposition and so we were cautious with the pump power in case fracture occurred. The lasing wavelengths were 1909 nm for the 1.5 mm slab, and both 1907 nm and 1909 nm for the 2 mm slab.

The output from the two slab lasers was collimated and spatially multiplexed before coupling into the Ho:YAG rod as shown in figure 5.1. Two $f=200$ mm lenses were used for the collimation, one for each laser, positioned at 200 mm from the plane output coupler of the thulium lasers. High-reflectors at 45 degree incidence were used for turning the thulium beam, redirecting it to the spatially beam combining mirror. The thulium pump beam was spatially combined and focussed into the Ho:YAG rod using two lenses of focal lengths $f=40$ mm and $f=50$ mm. The resulting measured M^2 beam quality was 193×11 with a pump beam waist radius of 0.4×0.05 mm. The total transmission of the optics from the output coupler to after the holmium input coupler was ~ 96 %, giving a total thulium pump power of 73 W at 350 W of diode power. It should be noted that if two properly operating 1.5 mm-thick Tm:YLF slabs had been available then >100 W of thulium pump power should have been obtained.

5.1.3 Ho:YAG laser

Due to the relatively poor beam quality of the Tm:YLF slab laser output, it is difficult to use a standard Ho-doped rod. The beam quality in the x-axis (along slow-axis of diode) leads to a relatively large pump size, and the difference in beam quality between

the orthogonal axes results in an elliptical pump profile. The combined result would be a holmium laser with a high threshold and an elliptical output. Moreover, the beam also gives a very short Rayleigh range in the x-axis, which translates to a need for a short rod with high doping concentration for confocal pumping and efficient absorption of pump power. The increased doping concentration would introduce severe thermal problems, via increased upconversion loss [82], leading to increased threshold, strong thermal lensing and ultimately causing cavity instability at high pump powers, limiting the power-scalability of the system.

A solution to these problems is to use a pump-guiding Ho:YAG rod. Using a pump-guiding rod allows the use of a long rod, thus the doping concentration can be lowered. This effectively reduces the problem of upconversion which is especially important when Q-switched at low-repetition-rate where inversion density is high. As illustrated in figure 5.2(a), the pump beam is tightly focussed in the x-axis to a spot size that provides a long enough Rayleigh range to avoid hitting the contact face between the rod and the mount, which can cause pump power leakage. In the y-axis (along fast-axis of diode), the pump beam can either be over-focused, or collimated, shown in figure 5.2(b) and (c) respectively, to force the pump beam to bounce along the rod at small angles or fill up the rod, such that a circular pump spot would emerge, allowing a circular output beam. Both options will be investigated experimentally in sections 5.2 and 5.3. In the case of figure 5.2(b) the two spatial combined beams take different paths whereas in figure 5.2(c) the spatially multiplexing was such that the two beams follow the same path. Note that the diameter of a pump-guiding rod has a tighter limitation, unlike regular rods, as it effectively defines the threshold pump power requirement. Too small a rod and the pump beam would not be able to fully couple into the rod, and may also be limited by the manufacturing processes, whereas increasing the rod diameter would also increase the threshold significantly.

The Ho:YAG rod used for power-scaling in the CW regime was a 0.25 at.% doped rod with dimensions of 1.5 mm-diameter by 80 mm-long, where the diameter was the smallest possible, as limited by the fabrication processes. The rod was barrel polished with AR coatings on both ends at the pump and lasing wavelengths. The rod was surrounded by water in the copper mount with wax sealing both ends of the rod at the first and last mm to prevent water leakage as illustrated in figure 5.2. The water flows around the entire rod to act as a coolant as well as providing a refractive index difference for pump-guiding. Because of the large difference in refractive indexes between YAG and water, the NA of the rod is 1.26, which enables pump-guiding as long as the pump beam is coupled into the rod. The water temperature surrounding the rod was set to 20 °C, a slightly higher temperature than normal, to relax the stress on the rod caused by the mount, as the mount was heated up during the mounting process.

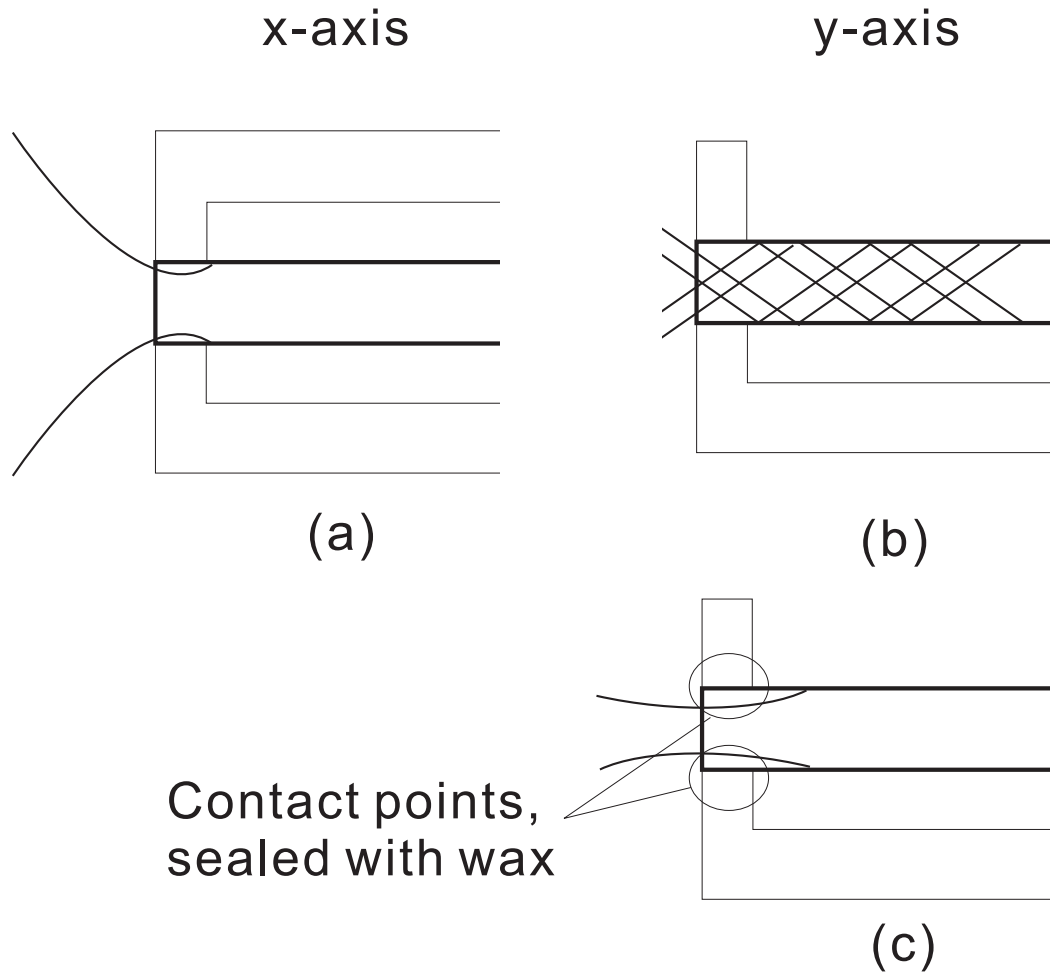


FIGURE 5.2: Thulium pump beam propagation path in holmium rod (a) in x-axis; (b) in y-axis using over-focussed pump; (c) in y-axis using collimated pump

The holmium cavity was a simple plane curved two-mirror cavity with a 100 mm mirror-mirror separation. The plane input coupler was coated for high-transmission at $1.9 \mu\text{m}$ on both sides and high-reflectivity at $2.1 \mu\text{m}$, and the 100 mm concave broadband output coupler was 89 % reflective at the holmium lasing wavelength. Although the output coupler provides over 90 % reflectivity at the thulium wavelength, the spot size was too large to be re-coupled into the Ho:YAG rod, thus the thulium pump was not double-passed.

5.2 Laser characterisation with focused y-axis thulium pump beam

In this setup the thulium pump was focused to a pump waist situated slightly into the rod, after which it bounces along the rod. The pump waist size in the x-axis was adjusted such that it gives a Rayleigh range long enough to avoid hitting the contact face between

the rod and the mount, which prevent power leakage from melting the wax, as shown in figure 5.2(a). The y-axis is tightly focussed, as illustrated in figure 5.2(b), such that the thulium pump beam is bounced along the rod to provide a relatively uniform pump inversion. To the first order approximation, where the lensing effect from the curvature of the rod surface is ignored, the pump beam is expected to bounce 9 and 4 times in the x and y-axis respectively before exiting the holmium rod. Although the number of bounces are small, the inversion profiles are different for both axes. The x-axis would give a relatively uniform inversion profile due to it being a single top-hat pump beam, filling out the rod. On the other hand, the y-axis would give an inversion with many gaps in between, like in figure 5.2(b), because the separate pump beams would go along different paths.

Figure 5.3 shows the laser performance of the Ho:YAG laser. The laser operated at a slope efficiency of 61 % with respect to the incident pump power, estimated by fitting to the last five points of the curve, and a threshold of 4.3 W incident power. The maximum output power achieved was 38 W with 73 W of incident thulium power, at a lasing wavelength of 2090 nm, measured using a computer controlled monochromator¹ and an extended-InGaAs photodetector². The single-pass absorption was measured to be 83 % at threshold pump power, indicating a 73 % slope efficiency with respect to the absorbed power. The output M^2 beam quality, measured using a beam profiler³, was 18.3×3.3 with a Gaussian-like profile in both axes but with expanded wings, as shown in figure 5.3. The expanded wings were due to the fundamental mode size being much smaller than the pump profile, thus higher-order modes started to lase when sufficient gain was reached. The relatively small vertical mode further suggested that most of the inversion was located in the center. Using this inversion profile and expanding the fundamental mode to achieve good beam quality is possible, but the non-uniform inversion profile could lead to local intensity peaks when Q-switched, which could be problematic. In order to get a more uniform pump profile, either focussing the vertical axis even more tightly or collimating the vertical axis to a size similar to the dimension of the rod would be required.

Parameters used for the modelling is shown in table 5.1, where the calculated threshold is 4.5 W using plane-wave analysis as described in section 3.1. The cavity transmission is calculated by assuming each surface gives 0.3 % loss per pass, including the input coupler. The pump radius uses rod diameter divided by π , and η_{QY} is set to 1 as no cross-relaxation process is involved in the pump-laser process. If we allow free parameters of the effective lifetime, τ_{eff} , and mode-fill efficiency, η_{mode} , the model fits to the

¹DongWoo Optron Co. / DM501

²Judson / J23TW266CR0252.4 / J23 series

³Photon inc / BeamScan controler model: 3088 / detector head: Pyroelectric heads, XYFIR/10Hz

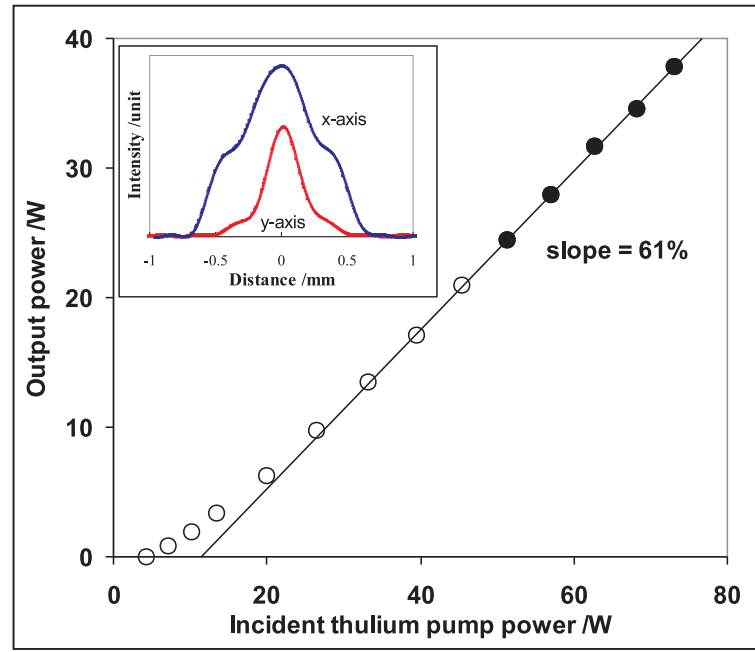


FIGURE 5.3: Measured Ho:YAG CW laser performance and beam profile

Description	Symbol	Value
Active ion density (cm^{-3})	N_T	3.45×10^{19}
Crystal length (cm)	l_r	8
Upper level effective lifetime (ms)	τ_{eff}	8.5
Emission Boltzmann ratio@T=300 K	F_{em}	0.1722
Lasing wavelength (nm)	λ_l	2090
Pump wavelength (nm)	λ_p	1909
Eff. emission cross-section (cm^2)	σ_{em}	12×10^{-21}
Eff. absorption cross-section (cm^2)	σ_{abs}	9×10^{-21}
Cavity transmission	T_c	0.992
Output coupler reflectivity	R_{oc}	0.89
Pump radius (cm)	w_p	0.048
Quantum yield	η_{QY}	1
Delivery efficiency	η_{del}	1
Mode-overlap efficiency	η_{mode}	0.86
Pump reflection	R_p	0

TABLE 5.1: Laser performance model parameters for Ho:YAG [7]

experimental effective threshold and slope efficiency for a lifetime of 3.4 ms and a mode-fill efficiency of 0.86. The difference in threshold is possibly due to pump power lost when being guided along the holmium rod, or some upconversion loss is present.

5.3 Laser characterisation with collimated y-axis thulium pump beam

In order to achieve a more circular output profile, the pump beam was collimated to a size similar to the rod, thus making the inversion in the holmium more evenly distributed along the vertical axis. A cylindrical lens of $f=35$ mm was inserted ~ 55 mm before the $f=40$ mm and $f=50$ mm lens (see figure 5.1), used to form a telescope for the vertical axis to re-collimate the pump beam to a size similar to the diameter of the rod. The resulting pump size was 0.39×0.40 mm with an M^2 of 195×41 , where the pump waist profile is shown in figure 5.4. Unfortunately the cylindrical lens was uncoated, giving a transmission of slightly larger than 90 % at the thulium pump wavelength, resulting in a reduction in pump power to 68 W incident. Measuring the pump profile after the uncoated lens, it was observed that a tail appeared on one side, possibly due to multiple reflections on the surfaces of the lens.

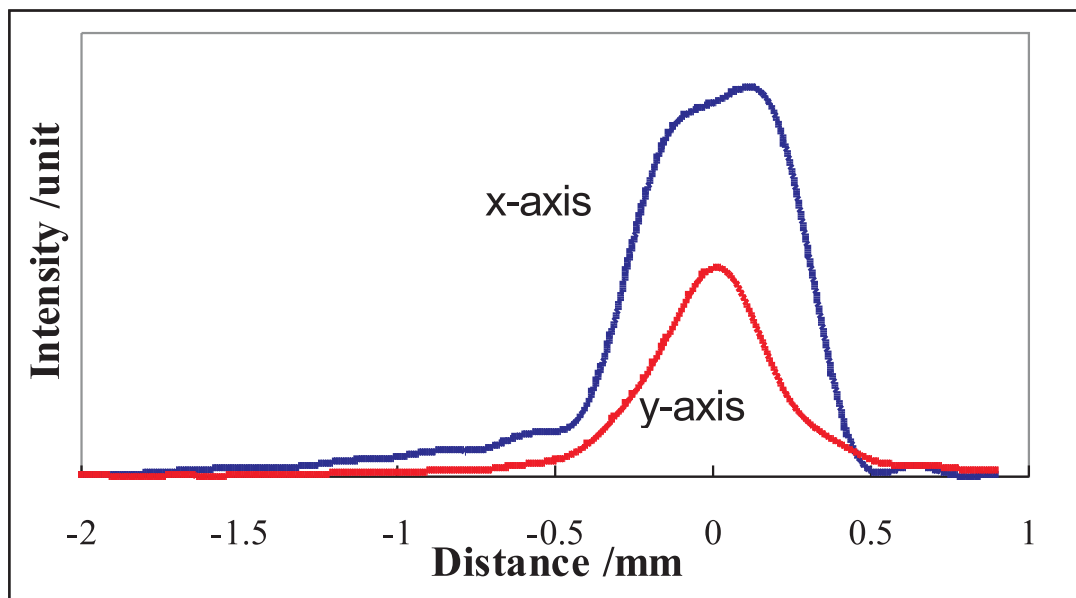


FIGURE 5.4: Measured collimated pump profile at pump waist

Despite the change in pump configuration, the laser performance remains similar to that found in section 5.2. A slight increase in threshold and single-pass absorption were observed. The threshold increased to 5.7 W while the absorption was measured to be 88 % at threshold pump power. The increase in threshold was due to the increased pump size, and the absorption was a result of lower ground state depletion also caused by increased pump size. As shown in figure 5.5, the slope, fitted with the last five points of the curve, is 61 %. A maximum output power of 34 W was achieved using the same cavity as described in section 5.2, with the lower output power a direct result of reduced

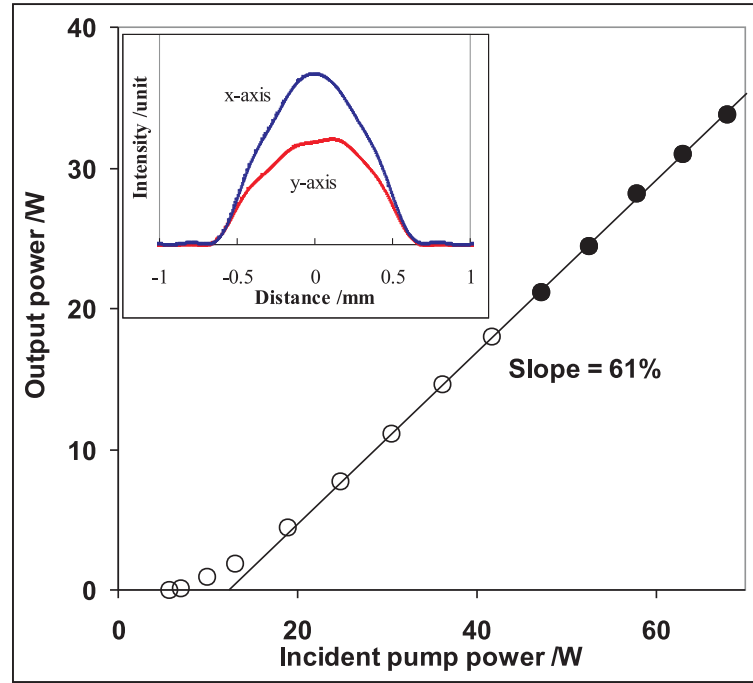


FIGURE 5.5: Measured Ho:YAG laser performance and output beam profile using collimated vertical axis pump beam

pump power. The M^2 was measured to be 16 x 18; thus a relatively circular mode was achieved, as shown in figure 5.5.

5.4 Plane-plane mirror cavity

In an attempt to improve the output beam quality, a plane-plane resonator design was employed for the holmium laser. The cavity consisted of a plane input coupler and a plane output coupler of high reflectivity and 82 % reflectivity respectively, at the holmium lasing wavelength. The cavity length was increased to 300 mm such that other optics could be fitted into the cavity in the future.

Although the beam quality was significantly improved to very close to diffraction limited with an M^2 of ~ 1.2 in both axes, the slope efficiency was reduced to only 37 % with respect to incident power, as shown in figure 5.6. Although the slope efficiency may increase as it is pumped higher above threshold, as was found in the earlier results, the roll-over of the output power, observed at ~ 45 W of incident power, restricted the power achievable from this setup to only 14.3 W at 68 W of pump power. A combined effect of the resonator design and the increased output coupling lead to an increase in threshold to 15 W, with a corresponding single-pass absorption of 82 % at threshold.

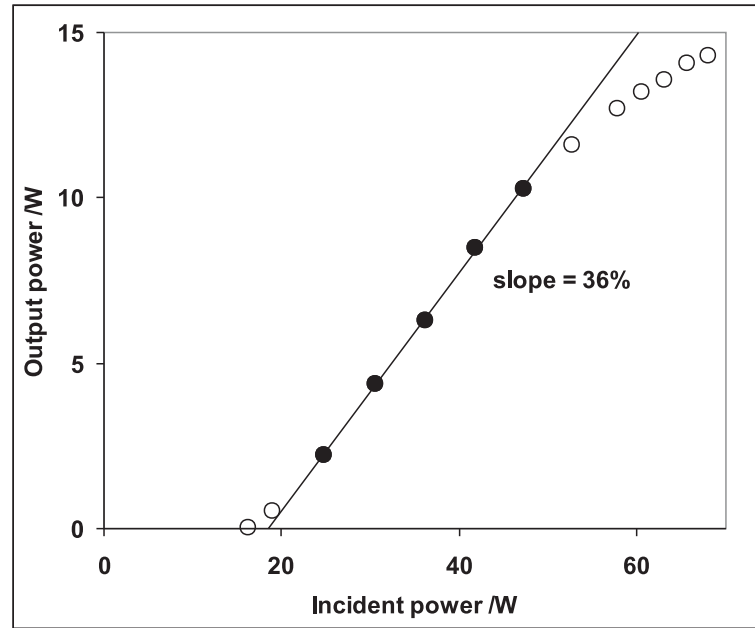


FIGURE 5.6: Measured laser performance of Ho:YAG using plane-plane cavity

Investigations to find the reason for the roll-over behaviour were carried out. The mirror-mirror separation was reduced to 100 mm, as instability of the cavity due to strong thermal lensing was suspected. Figure 5.7 shows how the cavity stability varies with thermal lens strength for the two cavity lengths, where the cavity is stable if the cavity stability is between 1 and -1 [108]. The thermal lens is dependent on three contributing factors; change of refractive index due to temperature gradient, change of refractive index due to thermal stress, and end-face bulging due to thermal expansion [84]. Since the refractive index change with temperature accounts for over 80 % of thermal lensing in YAG [109], it is the only part considered in our thermal lens estimation. The thermal lens focal length, f_{th} , can be estimated using the equation [84]

$$\frac{1}{f_{th}} = \frac{P_p \eta_a \eta_h}{K_c \pi w_p^2} \frac{dn}{dT}, \quad (5.1)$$

where P_p is the incident pump power, η_a is the absorption, η_h is the heat conversion coefficient, K_c is the thermal conductivity, w_p is the pump size radius and $\frac{dn}{dT}$ is the change of refractive index with temperature. The thermal lens focal length is estimated to be 400 mm and 256 mm respectively at a pump powers of 45 W and 70 W, using the parameters shown in table 5.2. The actual focal length is expected to be somewhat shorter due to contributions from the thermal stress and change of physical length. As shown in figure 5.7, the thermal lens brings the cavity stability of the 300 mm long cavity very close to the unstable limit of -1.

With the reduced mirror separation an improvement in laser performance was observed,

Description	Symbol	Value
Single-pass absorption (unit)	η_a	0.85
Heat conversion coefficient (unit)	η_h	0.09
Thermal conductivity ($Wcm^{-1}K^{-1}$)	K_c	0.14
Pump radius (cm)	w_p	0.048
Refractive index change with temperature (K^{-1})	$\frac{dn}{dT}$	7.3×10^{-6}

TABLE 5.2: Thermal lens modelling parameters

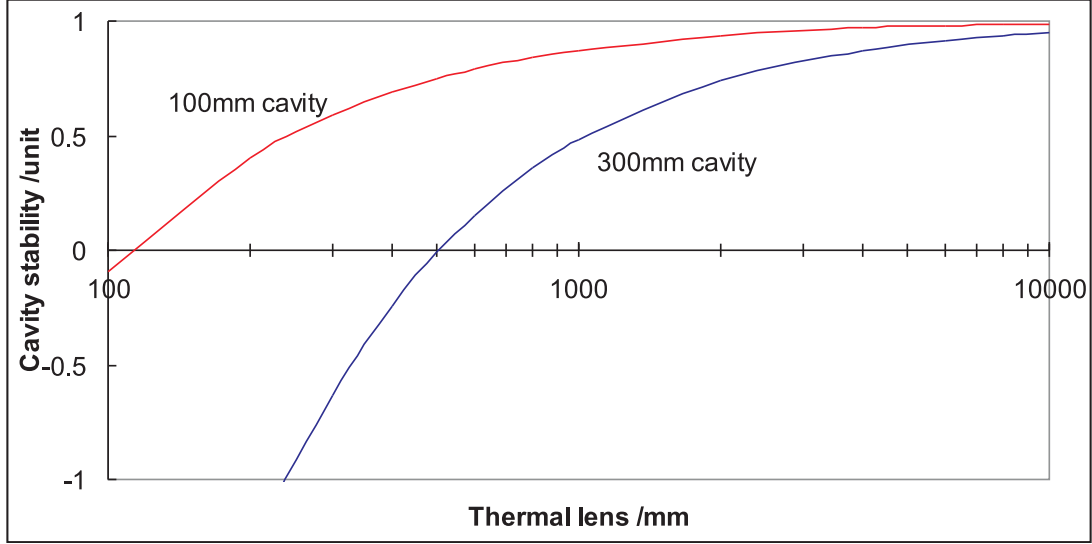


FIGURE 5.7: Cavity stability as a function of thermal lens

as shown in figure 5.8, giving a slope efficiency of 59 % at a threshold of 9.6 W. Due to the nature of a plane-plane mirror cavity, the stability of the cavity relies on the thermal lens of the active medium. Thus too strong a thermal lens would easily bring the long cavity into the unstable region, leading to roll-over of output power, while a shorter cavity can tolerate a higher lensing. The shortened cavity exhibits a single-pass absorption of ~ 85 % at threshold, and gives 31.6 W of output from 65.4 W of incident power.

The beam quality was not measured in the shorter cavity, but the increased performance suggests that the M^2 has increased to fill out the rod as the cavity length reduced. The drop in the available thulium pump power was due to occasional power spikes in the thulium cavity that caused coating damages on the thulium mirrors. These spikes seem to only occur during summer when humidity is high, and less frequently when nitrogen was used to flush the enclosed thulium cavity.

Thus, the plane-plane mirror cavity configuration, although successful in improving the beam quality, is limited in power-scalability due to the roll-over effect caused by thermal lensing. Therefore, other cavity configurations, such as an extended cavity with stable

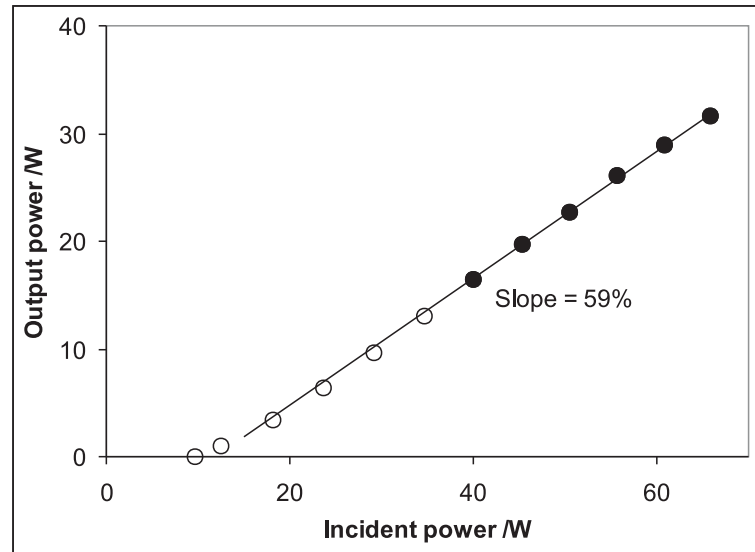


FIGURE 5.8: Output power of Ho:YAG plane plane cavity

operation over a wide range of thermal lens, or a weak concave mirror that supports a large fundamental mode, would provide a better path to improve beam quality and power-scalability of the system in future work.

Note that both the thulium and holmium output was measured using a 100 W power meter with a three significant figure digital meter. Both lasers give an output power reading that is accurate to within 0.2 W and the affect of inaccurate reading to the laser performance results are small.

5.5 Intra-cavity and external-pumping comparison

We have demonstrated two different Ho:YAG cavity designs, the intra-cavity pumping in chapter 4, and the external pumping in this chapter. Each design has its benefits and drawbacks as summarised in table 5.3.

Looking first at their performances, the external pumping scheme performs better than the intra-cavity pumping scheme, even after losses from the optics chain and unabsorbed power is included. The external pumping scheme gives a slope efficiency of 18.8 % with respect to the incident diode pump power. On the other hand, the slope efficiency for the same processes in the intra-cavity pumping scheme leads to a slightly lower performance of 15.5 %, as shown in section 4.4.

The lower performance was due to the wavelength shift and the extra loss-inducing surfaces in the cavity. The wavelength shift was caused by the insertion of Ho:YAG into the thulium cavity. Due to its broad gain spectrum, the thulium lases at a wavelength

	Intra-cavity pumping	External pumping
Overall Performance with respect to incident diode power	15.5 %	18.8 %
Thulium lasing wavelength	1897 nm	1909 nm
Cavity size	3×7 cm	Requires more space depending on focusing arrangement
Complications	Less optics required	Individual lasers can be tested separately
Holmium doping concentration	1 at.%, due to low absorption at thulium wavelength	0.25 at.% used, pumping guiding allow long rod
Output beam	Elliptical unless controlled , low abberations from uniform inversion	Circular, further abberations from thermal lens
Other losses	Extra coating loss in thulium cavity	Power loss in optics chain and unabsorbed power
Other	Intra-cavity element leads to power spikes	Can Q-switch at low-repetition-rate

TABLE 5.3: Comparison of internal and external pumping scheme summary

that has minimum absorption in the holmium, and thus lowest threshold. This shift in wavelength from 1909 nm to 1897 nm resulted in a calculated double-pass absorption in the holmium of only ~ 7.6 %. The cavity loss is also increased as the pump-reflective coating has a slightly higher loss of ~ 0.5 % per pass at 1897 nm (see figure 4.6), thus lowering the output to loss ratio and overall performance. As stated in section 4.7, the performance can be improved via wavelength selection elements, which can greatly increase the absorption, and to use a pump-reflective coating that has an appropriate center wavelength to reduce the loss.

The size of the two schemes differs significantly, mainly because of the optics required for coupling the pump into the holmium in the case of external pumping. The intra-cavity pumping scheme was very compact, measured to be ~ 3 by 7 cm, including both cavities, as it does not require any extra optics to couple the thulium output into the holmium. The final cavity size is expected to be larger due the extended cavity required for improving the holmium output beam quality. External pumping requires more space because of the focusing elements needed to couple the thulium pump into the Ho:YAG rod. Moreover, a slightly longer thulium cavity was needed for improving the thulium beam quality.

In terms of simplicity of the design, the intra-cavity pumping scheme leads by having less optics involved. However, the physics is more complicated as the Ho:YAG slab is an intra-cavity element to the thulium, thus both cavities have to be considered at the same

time. External pumping requires more optics in formatting the thulium pump beam, but the thulium and holmium laser can be characterised and optimised separately when required.

A higher holmium doping concentration was needed in intra-cavity pumping because of the low absorption exhibited by the shifted thulium wavelength. External pumping allows the use of low doping concentration when combined with pump-guiding, as the average pump-size no longer changes with the rod length. Low doping concentration benefits from minimised upconversion loss, which is especially important in high-energy Q-switch operation where high inversion is required and long effective lifetime is beneficial.

The external-pumping scheme had a better beam quality than the intra-cavity pumping in one of the axes when a simple two-mirror cavity was used. The output profile was circular which makes improving the beam quality, using an extended cavity or long curvature output coupler, simpler. Intra-cavity pumping gives a high M^2 and an elliptical output, which requires more complicated cavity design for fundamental mode operation [61, 65–70].

A major benefit of intra-cavity pumping is the ability of reusing unabsorbed pump power. However, the intra-cavity element acts as a saturable absorber that could cause power-spikes damaging the coatings on the mirrors and slab. This also limits the application for the holmium laser to CW or high-repetition-rate Q-switching operation.

5.6 Conclusion

A pump-guided Ho:YAG rod laser, externally pumped by two Tm:YLF slab lasers, was demonstrated in this chapter. A multi-mode output of 38 W holmium power was obtained with a slope efficiency of 61 % with respect to the incident thulium power. Higher holmium output power of at least 70 W would have been possible if another undamaged Tm:YLF slab had been available that could operate at the same performance as the current 1.5 mm Tm:YLF slab, delivering >100 W of thulium power in total. Nonetheless, this laser design is clearly suitable for power-scaled lasers due to the possibility of using spatial multiplexed Tm:YLF pump beam to provide sufficient pump power.

Roll-over was observed while trying to improve the beam quality of the Ho:YAG laser with an unstable plane-plane resonator of 300 mm physical cavity length. Further investigation suggests the thermal lensing of the laser rod may be too strong, leading to instability of the cavity. A comparison study of intra-cavity pumping and external pumping was performed, with benefits of each scheme listed. The externally pumped

Ho:YAG laser is seen to have advantages for low-repetition-rate Q-switched operation (which is required in many applications). Thus in the next chapter the pump-guided Ho:YAG rod arrangement is used for investigations into pulsed operation.

Chapter 6

A Q-switched Ho:YAG laser pumped by Tm:YLF slab lasers

Ho:YAG is a very useful laser source due to its many attractive properties and applications. Previous chapters have demonstrated power-scaled Ho:YAG lasers using various cavity configurations, for which over 13 W was obtained from an intra-cavity side-pumping configuration, and 38 W from an external end-pumping configuration. Although the power-scaled lasers provide a fairly high intensity, it is not sufficient for all the applications listed above.

Q-switching is a technique used to generate giant intensity pulses by squashing the CW energy into a very short period of time. This technique involves changing the Q factor (quality factor) of the cavity with the help of a Q-switch, such as a Pockel's cell, where the cavity is "switched off" by introducing high cavity loss to build up high inversion density, and is "switched on" by removing the induced loss to extract the inversion, rapidly forming a pulse. The longer the cavity is switched off, the greater the inversion, and the higher the output intensity. Unfortunately, one cannot allow the inversion to build up indefinitely because of spontaneous emission that is dependent on the population inversion and can equal the pump inversion rate when inverted population is high enough. Moreover, process such as upconversion that is also inversion dependent would further limit the maximum inversion possible. Consequently, Ho:YAG is a good Q-switching material as it has a relatively long upper laser level lifetime of 8.5 ms, which allows high inversion to be stored, and high-energy Q-switched pulses to be extracted.

Q-switching is a very important mode of operation as it opens up applications that are normally not possible with CW operation. Remote sensing, for example, benefits from increased propagation distance and signal density from the increased intensity, which allows a longer detection range, higher sensitivity and more accurate detection. Laser

cutting is another area where a short high intensity pulse is more effective than the same amount of laser energy distributed over time. Similarly, processes relying on non-linear effects, such as pumping of OPOs for tunable mid-IR sources, would also benefit from the higher intensity.

This chapter is concerned with Q-switched operation of an externally-pumped Ho:YAG laser. Presented in this chapter are some theoretical aspects of a Q-switched laser, and the Q-switching methods available. This is followed by a detailed description of the experimental setup of our Q-switched laser, and the performance obtained, including the CW performance, and the pulse width and pulse energy at various repetition rates when Q-switched.

6.1 Q-switching theory

The equations used for modelling the Q-switching process are based upon two basic rate equations. For CW pumping, the rate equation for the cavity photon density, $n(t)$, and the inverted population density, $N(t)$, can be expressed as [108]

$$\frac{dn(t)}{dt} = KN(t)n(t) - \frac{n(t)}{\tau_c} , \quad (6.1)$$

$$\frac{dN(t)}{dt} = R_p - \frac{N(t)}{\tau_{eff}} - 2^*Kn(t)N(t) , \quad (6.2)$$

where R_p is the pump rate and τ_{eff} is the effective upper laser level lifetime. $K = c\sigma$ is the coupling efficiency between the inversion and laser photons, c is the speed of light and σ is the emission cross section. In the case of fast thermal relaxation in the lower laser level, the lower laser Stark level remains constant all the time such that the parameter $2^* = 1$. However, there are cases where thermal relaxation in the lower laser level is slow when compared to the de-excitation rate during stimulated emission. Therefore, each de-excited ion would result in one less excited ion in the upper laser level, while creating one extra ion in the lower laser level. This would effectively reduce the population inversion at twice the speed, giving $2^* = 2$. Note that these equations were derived for four-level lasers, but are also applicable to three-level lasers when derived using equation A.16.

τ_c is the cavity photon lifetime and is given by the equation

$$\frac{1}{\tau_c} = \frac{c}{2l_{cav}}(L + T_{oc}) , \quad (6.3)$$

where l_{cav} is the cavity length, L is the intrinsic cavity loss and T_{oc} is the output coupler transmission.

Q-switching operates by modulating the cavity losses periodically as illustrated in figure 6.1(a). The cavity is initially held at a high loss with the gate closed, and there is no oscillation as shown in figure 6.1(c). During this period the inversion will accumulate to a higher level than under CW operation, as shown in figure 6.1(b), until the gate opens. Up to this point, we know that no laser intensity exists in the cavity thus $n=0$, and when combined with equation 6.2 it allows the calculation of the total population inversion at any point of time, t , while the gate is still closed using the equation

$$N(t) = R_p \tau_{eff} (1 - \exp(-t/\tau_{eff})) . \quad (6.4)$$

From the equation we can deduce that the inversion approaches a maximum of $R_p \tau_{eff}$ as the pump duration tends to infinity. It can also be seen that there is little to be gained from holding off the Q-switch for longer than a few τ_{eff} as the inverted population will not grow much further. Thus a laser material with a long upper laser level lifetime is beneficial in obtaining high energy Q-switched pulses as more energy can be stored.

Once the gate opens, the cavity loss is removed providing a suitable lasing environment. At this point, the inversion is accumulated to a high level, N_i , as shown in figure 6.1(b). The emission in the laser cavity builds up at a rapid rate, given the high inversion, resulting in a giant burst of energy, or a pulse, as shown in figure 6.1(c). The peak intensity in the pulse could generally be a few orders of magnitude higher than the CW operation level created using the same pump rate. The pulse reaches its peak when the gain equals the threshold gain, as it specifies the point where the gain is just sufficient to overcome the cavity loss and output coupling. Afterwards, as the gain is further depleted, the intensity would start to decrease forming the pulse shaped intensity burst as shown in figure 6.1(c). After the pulse, the gain is severely depleted to N_f , below threshold, and the lasing process stops. At this point, a CW state would be reached if the gate is left open in the low-loss state. However, a high-loss state should be restored via closing the gate to allow the inversion to recover to N_i and the Q-switch process repeats to generate a train of pulses.

In Q-switched operation, the pulse width is equally as important as the energy of the pulse since a short pulse width means a higher peak power. The pulse width of a certain cavity and pump power can be estimated using the equation [108]

$$\tau_p \approx \frac{r\eta(r)}{r - 1 - \ln(r)} \times \tau_c , \quad (6.5)$$

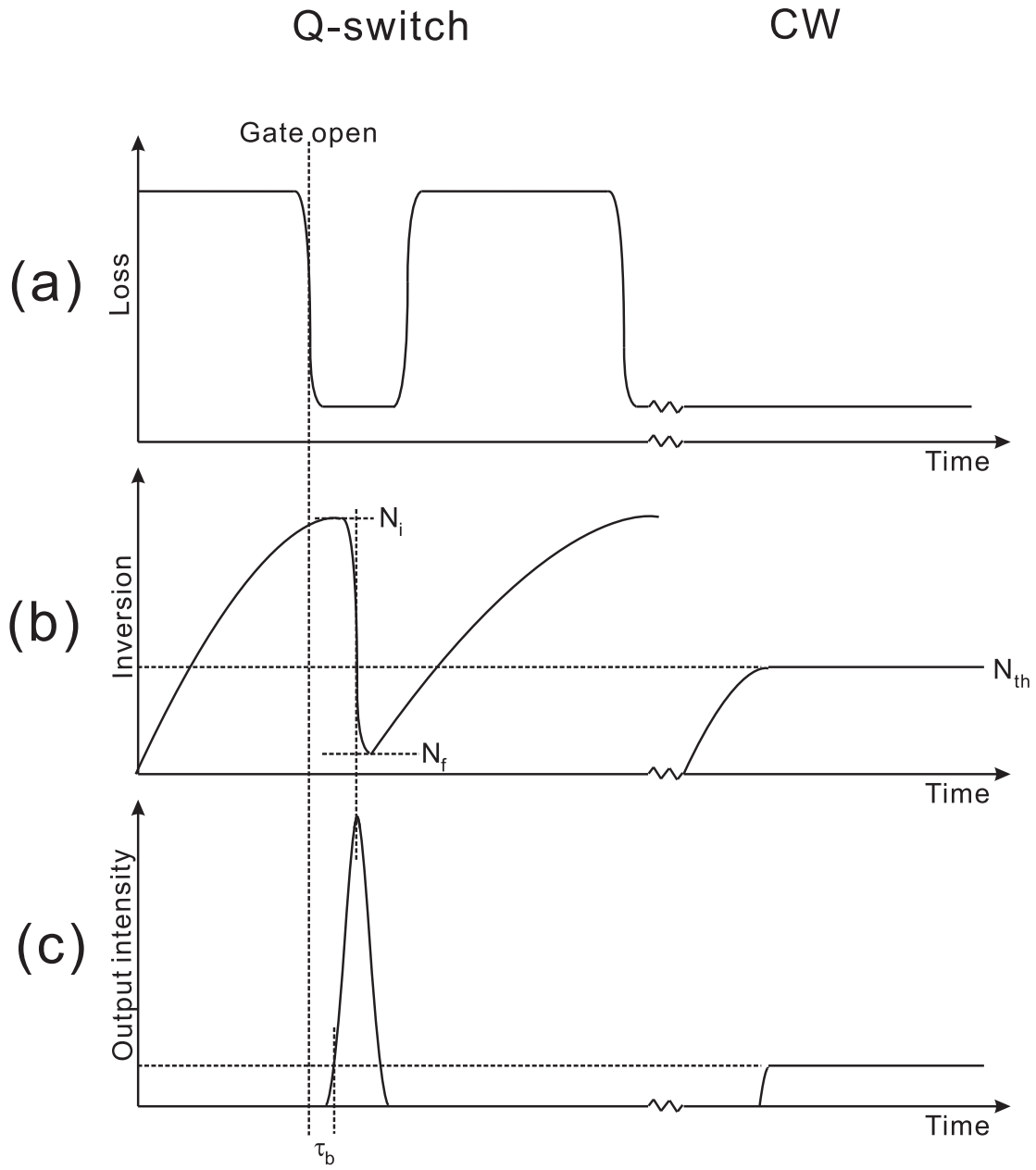


FIGURE 6.1: Loss, inversion and output intensity under Q-switch and CW operation (CW pumping)

where $r = \frac{N_i}{N_{th}}$ is the ratio of the initial inversion before switching to the threshold inversion. The extraction efficiency, $\eta(r)$, can be obtained using the equation [108]

$$1 - 2^*\eta(r) = \exp[-2^*r\eta(r)] \quad . \quad (6.6)$$

6.2 Q-switching method

As discussed in the previous section, Q-switching relies on the periodic modulation of the cavity loss to suppress lasing such that the inversion could be accumulated. Thus it is important that the induced cavity losses are high enough in the high loss state, otherwise CW leakage output would result. This leakage would clamp the inversion and thus reduce the energy per output pulse. The low loss state, on the other hand, is not as restrictive in terms of minimising loss since high transmission output couplers can be used in Q-switch systems, especially in low repetition rate Q-switching where high gain is available. A high transmission output coupler not only improves the laser performance, but also prevents optical damage on coatings by reducing the intra-cavity intensities. Another important property of a Q-switch is the switching time. The switching time has to be much shorter than the build-up time of the pulse, which can be defined as the time between the opening of the gate and the point at which the pulse intensity reaches the level under CW operation (see figure 6.1(c)). If the switching time is too long compared to the build-up time of the cavity, multiple peak pulses with low peak power could result [108, 110, 111] causing a reduction in energy per pulse.

There are various devices that could be used for Q-switching a laser. They are usually in the form of optical, mechanical or electrical switches. In this work we choose to work with an electro-optic Q-switch because of the fast switching time.

Of the various Q-switching methods, the electro-optic modulator (EOM) provides the best overall performance. It has the fastest switching time of ≤ 10 ns that allows high repetition rate Q-switching of 100 kHz, and a large hold-off ratio that prevents CW leakage while under high loss condition. Moreover, the use of the electro-optical switching method provides repeatability, and stability. However, an EOM is a relatively expensive solution due to the high cost from the electro-optical crystal and fast-rising, high-voltage pulse source. Another drawback is that the high-voltage source can produce severe electrical interference with other equipment, thus care has to be taken. Moreover, being an intra-cavity element and polarisation dependent, it requires a precise alignment.

An electro-optic Q-switch depends on the electro-optic effect to induce loss to the cavity. The electro-optic effect is the change in an optical property of a material when a electric field is applied. This can be in the form of absorption or refractive index change, and it is the latter which is used in electro-optic Q-switches. Electro-optic Q-switches are formed by an EOM and a polarisation selection element to introduce loss to the cavity. As a voltage is applied to the EOM, the refractive index changes and the material becomes birefringent. The birefringence is controlled such that it would rotate the polarisation of the incident beam by 90° through a double-pass in the high loss state. The polarisation

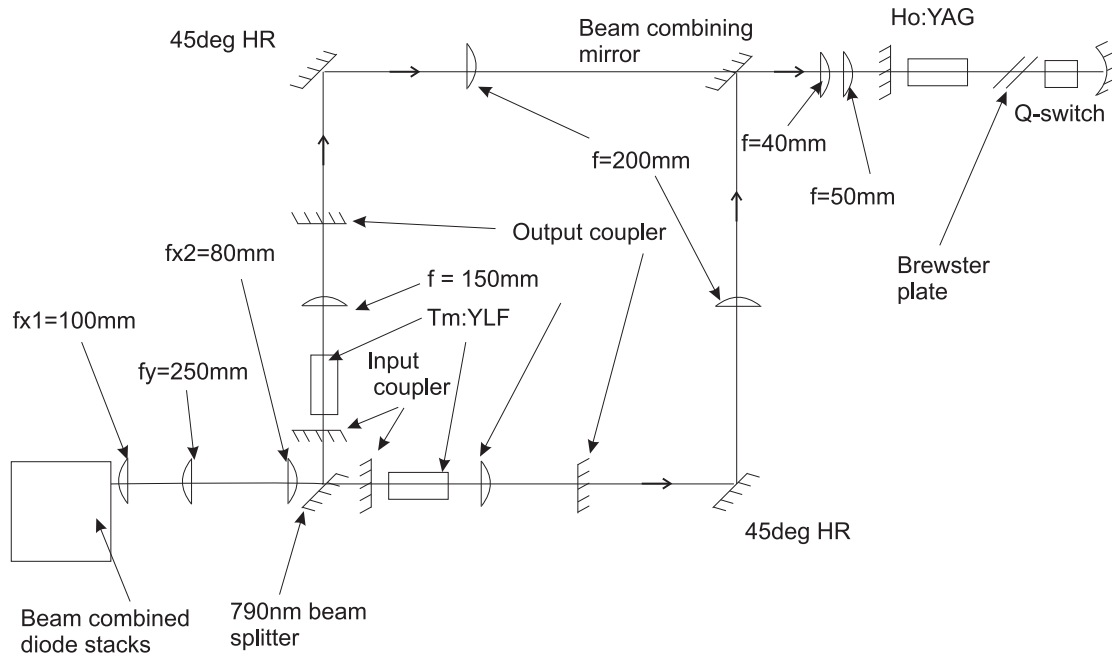


FIGURE 6.2: Q-switch cavity configuration and pumping arrangement

selection element is used in the setup for linearly polarising the cavity and rejecting the rotated beam out of the cavity, creating the high loss state for Q-switching.

The electro-optic crystal used in our EOM is rubidium titanyl phosphate (RTP), which offers high damage threshold (1.8 times higher than KTP¹), the possibility of operating in a high-repetition rate regime, and low power consumption². As RTP crystals are naturally birefringent, two RTP crystals are used in the Pockel's cell. The two RTP crystals are oriented 90° to each other such that whatever the polarisation rotation that occurred to the incident beam after the first crystal, is reverted and cancelled out after the second when no voltage is applied.

6.3 Q-switching experimental setup

The experimental setup used in this section is similar to the one described in section 5.1, where the pump-guided Ho:YAG rod laser was end-pumped by two spatially multiplexed, diode-pumped Tm:YLF slab lasers. The experimental setup is shown in figure 6.2, from the spatially multiplexed diode pump to the thulium lasers, to the Ho:YAG rod including all the optics used.

¹http://www.bjgot.com/crystal_nlo/rtp.html

²http://www.leysop.com/100khz_rtp_q-switch.htm

6.3.1 Pump configuration

The diode pump configuration was identical to the one described in section 5.1.1 and the thulium pump laser cavity configuration and the beam reshaping system used was the same as described in section 5.1.2. The difference in the combined thulium pump beams was that the incident angles on the focussing lens were parallel in the previous chapter, whereas, the incident angles used in this experiment were adjusted, using the beam combining mirror, to be slightly different to each other. This causes the two beams to intersect after their individual waists, reducing the beam quality of the vertical axis (fast-axis of diode). The lower beam quality causes the beam to diverge faster, allowing for more bounces in the Ho:YAG rod in an attempt to achieve a more uniform inversion. The M^2 beam quality of the combined Tm:YLF pump beam was measured to be 195 and 85 for the horizontal (along slow-axis of diode) and vertical axis respectively, and the pump power was 67 W. Note that the thulium laser is operated as a CW pump laser, which allows flexibility for the Q-switched system, such as the ease of changing Q-switch frequency.

6.3.2 Holmium cavity configuration

The holmium rod and mount used in these experiments are described in section 5.1.3, but with an increase of rod diameter to 2.5 mm due to the fact that 1.5 mm diameter rod was damaged by Q-switched pulses at ~ 13.5 mJ during preliminary experiments. The rod was 0.25 at.% doped, 80 mm long, barrel polished on the sides with anti-reflection coatings on both ends at the pump and lasing wavelengths, and was mounted in the same heat-sinking arrangement, with water surrounding the rod for pump-guiding, as described in section 5.1.3. The anti-reflection coatings on the holmium rod were designed and specified by the manufacturer to give a damage threshold of 500 MW cm^{-2} .

6.3.2.1 Laser cavity for CW performance characterisation

A simple two-mirror cavity, identical to the one described in section 5.1.3, was used for CW laser characterisation in order to compare the laser performance difference between the 1.5 mm and 2.5 mm holmium rod. The 100 mm-long cavity was formed by a plane input coupler and a 100 mm radius of curvature concave output coupler with 88 % reflectivity at the holmium lasing wavelength. Note that, although the physical distance matches the radius of curvature of the output coupler, the optical distance of the cavity is much shorter, thus the cavity is still within the stability limit.

6.3.2.2 Laser cavity for Q-switching

The Q-switch configuration, shown in figure 6.2, was a simple two-mirror plane-curve cavity, but with a longer cavity length of 220 mm when compared to the one described in section 6.3.2.1 in order to fit in the other optics for Q-switching. The plane input coupler had high transmission at the thulium pump wavelength, and high reflectivity at the holmium lasing wavelength, while the output coupler was a 500 mm radius of curvature concave mirror with 40 % reflectivity at the lasing wavelength. The high output coupling was chosen to prevent coating damage due to the high intensity Q-switch pulses.

A RTP Pockel's cell³ of 4 mm aperture, with a measured switching time of ~ 10 ns, was used for this experiment. It has attractive features such as a high damage threshold, not being dissolvable in water (thus a sealed housing is not required), and a low half-wave voltage (half that of Beta Barium Borate (BBO, or beta- BaB_2O_4)). As already noted, owing to its natural birefringence property, two separate rods, specially orientated, are required such that it would not induce polarisation rotation when no voltage is applied. This leads to slightly higher loss but this is not an important factor due to the high output coupling used.

The Q-switch was mounted on two translation stages and a mirror mount. This gives two orthogonal tilt adjustments and two positional adjustments in the plane perpendicular to the beam propagation for aligning the Pockel's cell in the beam path, and a rotational adjustment for aligning the axes of the RTP crystal to the cavity polarisation using a mirror mount. The Q-switch was positioned and tilted for optimum performance under CW lasing conditions, and the angle adjustment responsible for aligning the Q-switch optical axis to the cavity polarisation was optimised under Q-switch operation for the lowest hold-off voltage. A Q-switch driver⁴ was used to control the Q-switch, along with two uncoated YAG Brewster plates to linearly polarise the cavity and induce loss when the polarisation was switched by the Pockel's cell. The Brewster plates were inserted and the Brewster angle was found by minimising the reflected power and maximising the output power while under CW laser operation, and were fixed at this alignment throughout the experiment.

³Quantum technology / material: RTP / model: QR-4

⁴Quantum technology / model: HVP - 5 - 100K

6.4 CW performance comparison for different holmium rods

The CW laser performance of the 2.5 mm rod is compared to the 1.5 mm rod performance described in section 5.2, using an identical cavity, as described in section 6.3.2.1. The laser performance of this cavity with the 2.5 mm holmium rod is shown in figure 6.3.

The threshold was measured to be 14 W and the slope efficiency with respect to incident power was 46 %, calculated using the last five points of the graph. Note that the slope efficiency is lower than the 61 % slope with the 1.5 mm holmium rod. This is thought to be due to the slightly lower single-pass absorption of 81 % at threshold, and the fact that the laser was only operating at nearly 4 times above threshold, whereas the laser with the 1.5 mm-diameter holmium rod in section 5.2 was operating at nearly 6 times above threshold before it reached its optimum performance. The lasing wavelength was 2097 nm, measured using a f=0.5 m computer controlled monochromator⁵.

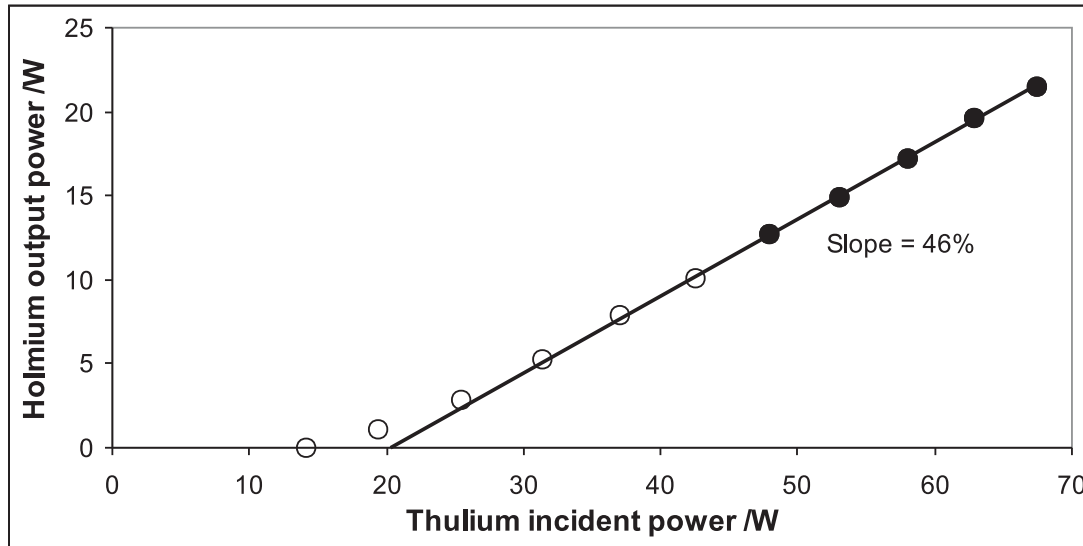


FIGURE 6.3: CW laser performance with 88 % reflectivity output coupler

6.5 CW performance comparison for different intra-cavity elements

The cavity described in section 6.3.2.2 was characterised, under CW operation and with various intra-cavity elements. The characterisation includes the basic cavity, a basic

⁵DongWoo Optron Co. / DM501

cavity with the addition of two Brewster plates, and the whole Q-switch configuration. The resultant laser performances are shown in figure 6.4.

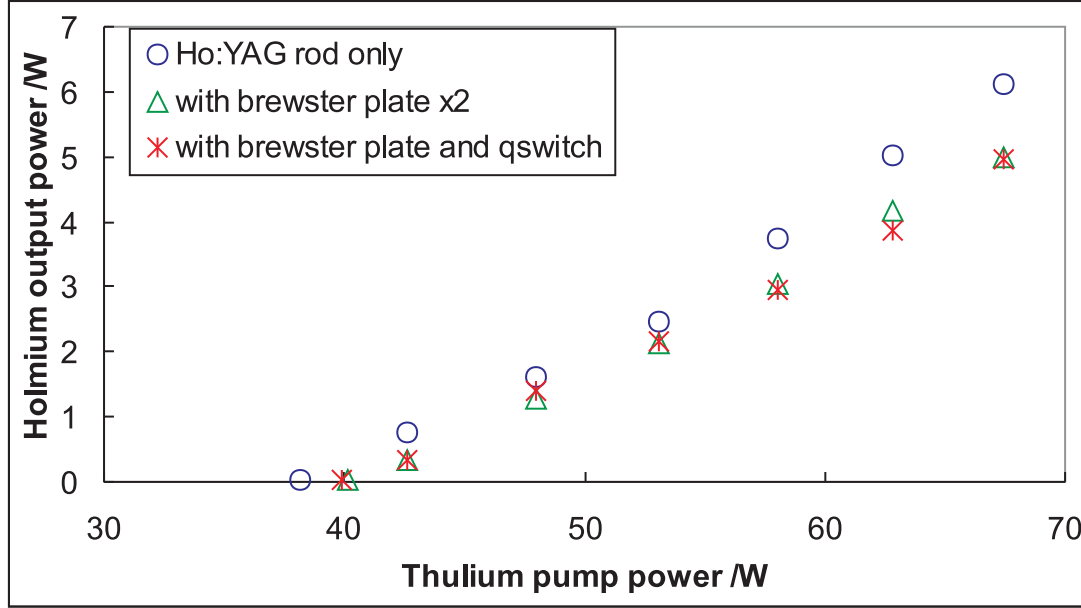


FIGURE 6.4: CW laser performance with various intra-cavity elements

The threshold for the plane cavity was increased to 38 W, where the increase in threshold was mainly due to the increase of the output coupling, and the change in fundamental mode size due to the increased cavity length and change in output coupler curvature. The threshold increases slightly to 40 W after two Brewster plates were inserted, and remains the same after the Q-switch was inserted. This suggested that the Q-switch has insignificant insertion loss, which is also shown in the similar output power. The increase in threshold after the insertion of the Brewster plates was due to depolarisation loss that normally exists in isotropic hosts such as YAG, and was caused by stress induced birefringence.

A first-order quarter waveplate at 2 μm was inserted between the input coupler and the holmium rod in an attempt to reduce the depolarisation loss [112]. Unfortunately, although the depolarisation loss was reduced by over 85 %, observed via the drop in reflected power from the first Brewster plate from 1 W to 0.15 W, the holmium output power only improved slightly (by 0.2 W). This is due to the fact that although the depolarisation loss was reduced, the intra-cavity loss was increased by the quarter waveplate. This suggests that the depolarisation loss caused by thermal stress is not significant at the current pump power level and further work did not use the quarter waveplate.

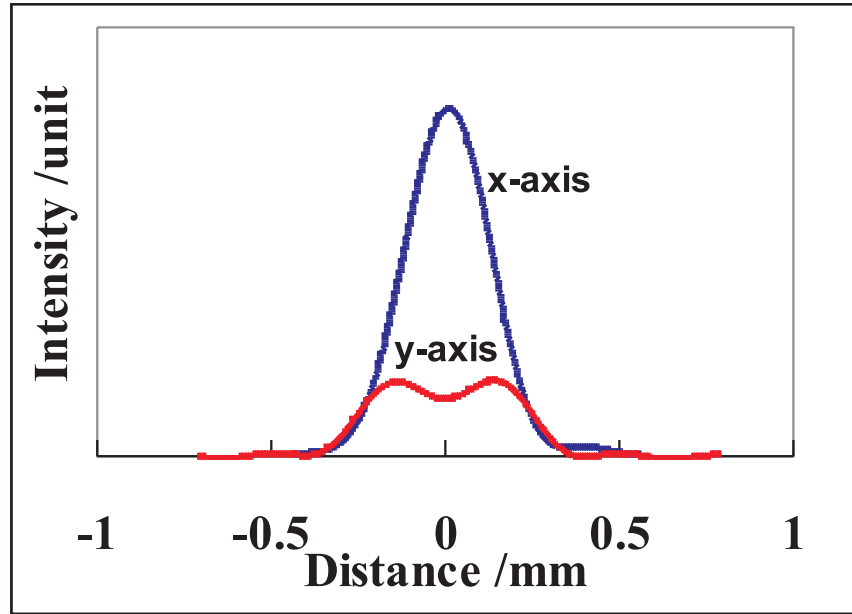


FIGURE 6.5: Measured beam profile on output coupler using 2.5 mm holmium rod under CW operation

The slope efficiency is not analysed here due to the fact that the laser is only operating at slightly above threshold. The laser output wavelength was measured to be at both 2090 and 2097 nm with similar intensities.

The beam profile on the output coupler is shown in figure 6.5, measured using a beam profiler⁶. A telescope was employed that was made up of two spherical lenses with focal lengths of $f=200$ mm and a $f=100$ mm. The telescope demagnifies and re-images the beam profile on the output coupler onto the beam profiler. A $f=250$ mm spherical lens was inserted directly after the concave output coupler as a correction lens, to remove the diverging effect that was caused by the concave output coupler. The M^2 beam quality was estimated to be 1×1.8 , through measuring the Rayleigh range and the beam waist. Note that the non-Gaussian beam profile in the vertical axis is likely to have been caused by the non-uniform pump profile. This suggests the beam quality is not poor enough to cause sufficient bounces to give uniform inversion.

6.6 Q-switching performance discussion

The cavity described in section 6.3.2.2 was used for Q-switched operation. The laser was characterised via the output pulse energy for the various Q-switching frequencies. The pulse energy was calculated from its operating frequency and the measured average

⁶Photon inc / BeamScan controller model: 3088 / detector head: Pyroelectric heads, XYFIR/10Hz

power, and it was experimentally confirmed that no CW leakage lasing occurred between pulses.

Figure 6.6 shows the measured output energy per pulse as a function of pump power when Q-switched at 20 Hz. The pulse energy increases linearly with pump power, and reaches a pulse energy of 14 mJ at a maximum thulium pump power of 58 W, where the reduced pump power was due to slotted mirrors misaligning. The effective threshold was 45 W, which roughly equals the effective threshold under CW operation, as illustrated in figure 6.6. The FWHM (full-width half maximum) pulse width shown in the figure was measured using an extended-InGaAs fast photodetector and a 500 MHz Tektronix digital oscilloscope⁷. The pulse width started from ~ 50 ns, and decreased toward a limiting value of ~ 17 ns.

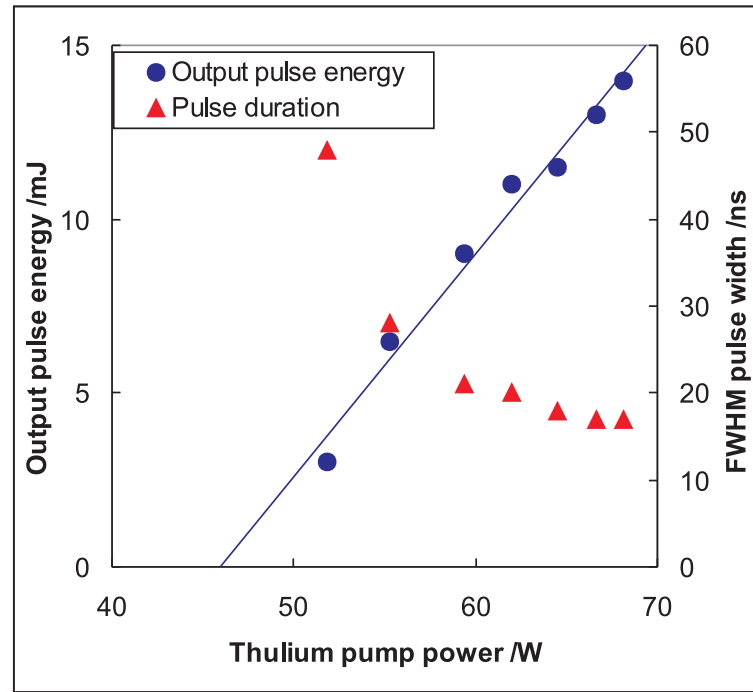


FIGURE 6.6: Measured pulse energy and pulse width at 20 Hz repetition rate as a function of pump power

The maximum pulse energy achievable was then measured for various repetition rates as shown in figure 6.7. As the repetition rate decreases, the time between pulses, and thus the pumping duration, increases. The longer pump duration allows more inversion to be stored, which leads to an increasing pulse energy. However, this does not increase indefinitely but is limited by the effective lifetime of the upper laser level, as shown in equation 6.4. The inversion would reach a maximum value of $R_p \tau_{eff}$ when the pump rate equals the decay rate. This is illustrated in figure 6.7 where the increase in pulse

⁷Tektronix / DPO 500MHz / model: TDS5052B

energy saturated below ~ 100 Hz. This saturation normally starts for pumping durations of approximately twice the effective upper laser level lifetime, as discussed in section 6.1.

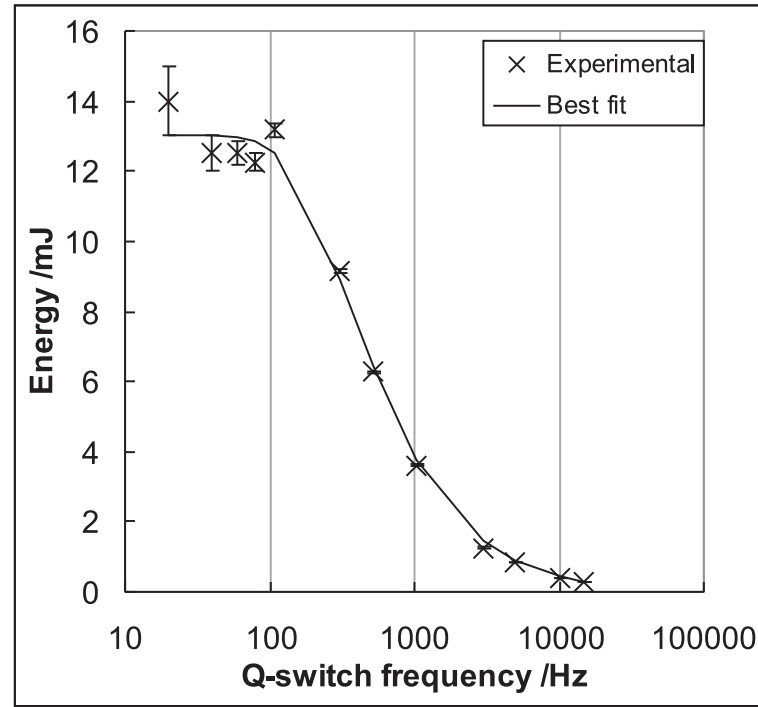


FIGURE 6.7: Measured Q-switch pulse energy as a function of Q-switch frequency

The pulse width was measured for various repetition rates at the maximum pump power, as shown in figure 6.8. The pulse width increases from 17 ns to 22 ns at ~ 300 Hz, and then it rises sharply to 600 ns at 15 kHz repetition rate. The increase in pulse width is expected and can be understood using equation 6.5. At low repetition rate, the initial inversion is much higher than the threshold inversion due to the long pump duration and energy storage lifetime. As the repetition rate increases, the initial inversion would decrease due to the shorter pump duration. Therefore, the increase in pulse width is expected for increasing repetition rate.

Equations 6.3 to 6.6 were used with the pulse width to estimate the number of times above threshold the initial inversion was. Given the cavity length was 220 mm, cavity loss $\sim 3\%$, a 60% transmission output coupler and 17 ns measured pulse width, the value of r was calculated to be ~ 2 . The extraction efficiency was calculated to be only $\sim 80\%$, where further increase in inversion to threshold ratio to three would allow near optimum extraction and reduced pulse width.

The temporal profiles were clean in all cases, where figure 6.9(a) shows the individual pulse temporal profile when Q-switched at 20 Hz, and figure 6.9(b) shows the pulse train

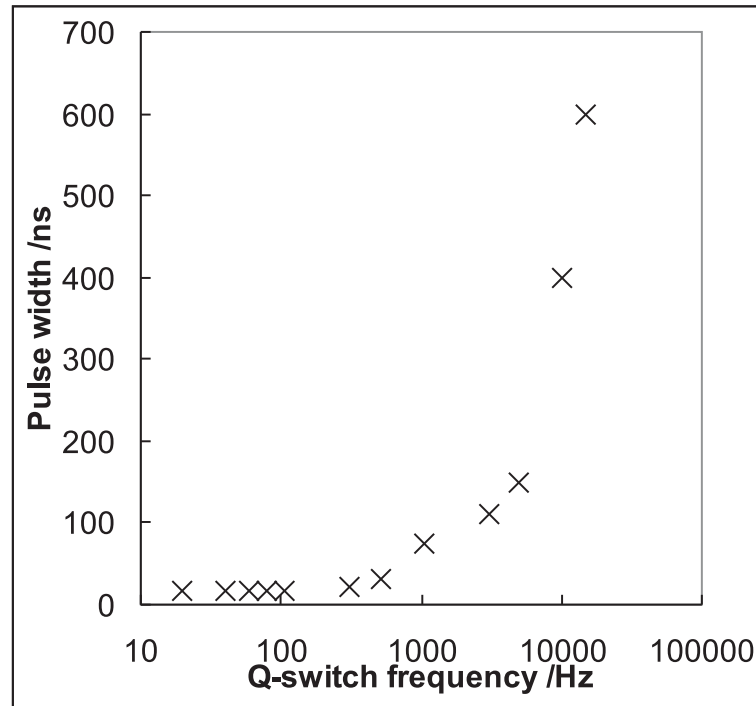


FIGURE 6.8: Measured pulse width as a function of Q-switch frequency at maximum thulium pump power

involved. The pulse profile was measured with the fast in-house photodetector and the pulse train was measured using a 100 kHz photodetector and a 100 MHz oscilloscope⁸. The build-up time increases from ~ 120 ns at 20 Hz up to $2.9 \mu\text{s}$ at 15 kHz.

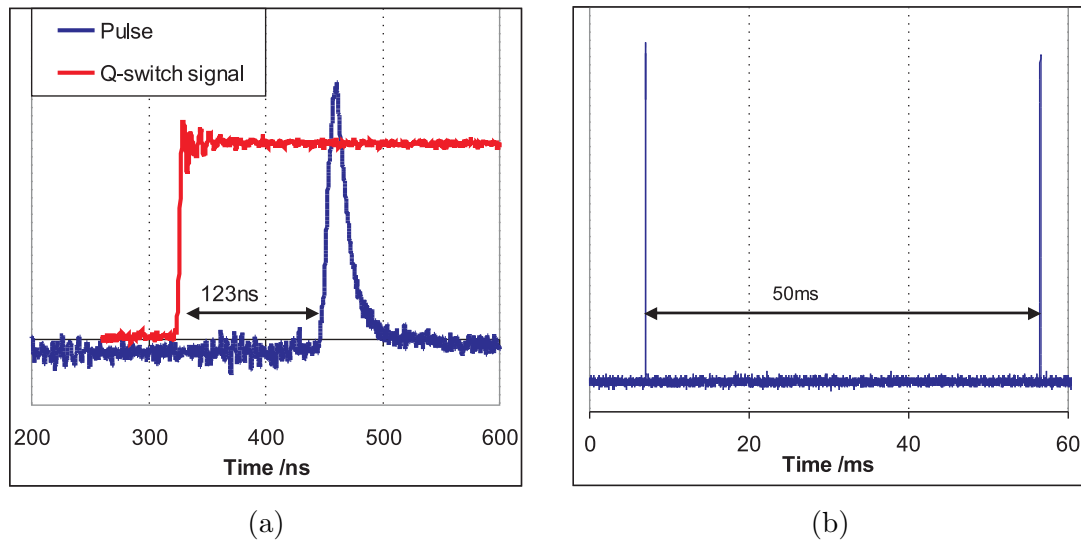


FIGURE 6.9: Measured Q-switch pulse at 20 Hz: (a) pulse profile and build-up time; (b) pulse train

⁸Tektronix / DPO 100MHz / model: TDS3102B

Note that the build-up time, T_b , can be estimated using the equation [108]

$$T_b = \frac{25 \pm 5}{r - 1} \times \tau_c . \quad (6.7)$$

In conjunction with the measured build-up time as shown in figure 6.9(a), the value of r was found to be ~ 1.5 , lower than the 2 predicted above with the pulse width. Beside the difference in the predicted initial inversion, both calculations suggested higher pump power is required for efficient operation.

The output beam quality for various Q-switching frequencies is shown in figure 6.10, measured using the moving knife-edge method⁹ at the maximum pump power. An $f=200$ mm lens was positioned 200 mm after the output coupler to focus the beam. A copper plate was slid in side-ways to block 16 % and 84 % of the power, using a translation stage, and the distance between these points was measured. The distance between the points is equal to the $\frac{1}{e^2}$ beam radius for Gaussian beam profile, and a series of spot-sizes was thus measured at different positions after the lens, before and after its focal point, to estimate the beam quality. The beam quality for the horizontal axis was close to diffraction limited, while the vertical axis was lasing with higher-order modes, which is similar to the CW case, as discussed in section 6.4. The slightly higher M^2 than in the CW case is possibly due to the fact that the available gain is higher, thus allowing higher-order-modes to build-up in the cavity. The sudden improvement in M^2 beam quality at the low repetition rate could be caused by a reduced gain. The high inversion especially in the center pump region leads to a high upconversion loss. The upconversion loss is converted directly to heat, raising the temperature of the rod. The temperature rise would increase the lower laser level population, which effectively reduces the gain available, resulting in an improved beam quality from the fewer higher order modes. However, more experimental results at low Q-switching frequencies would be required to confirm this behaviour. Note that even at this doping concentration, there is still upconversion possibilities due to the high inversion during Q-switched operation [8].

The holmium lasing wavelength was measured using a monochromator under Q-switched operation. The wavelength was measured to be 2090 nm from CW to 300 Hz, and 2097 nm when Q-switched at 20 Hz. The shift in lasing wavelength to a lower emission peak at low repetition rate (see figure 4.14 for emission spectra for Ho:YAG) further suggested that there is an increased in upconversion that leads to a temperature rise as discussed above. Therefore the lasing wavelength increases to reduce the lower laser level population.

⁹International standard ISO11146

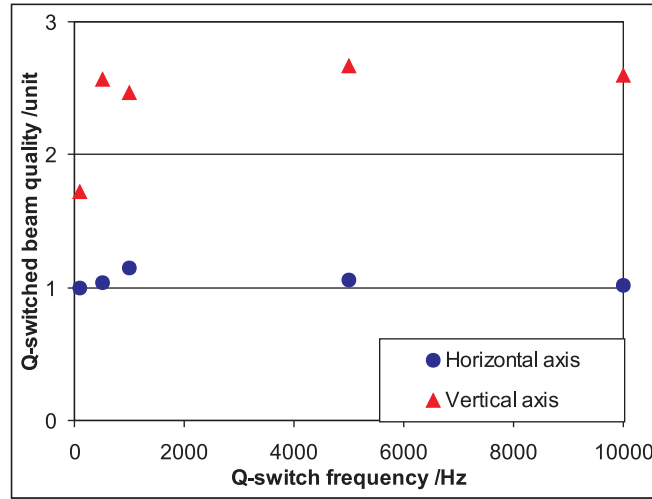


FIGURE 6.10: Measured beam quality of Q-switched output as a function of Q-switch frequency

Note that both the thulium and holmium output was measured using a 100 W power meter with a three significant figure digital meter. The thulium power was accurate to 0.2 W while the holmium power was 0.1 W due to different settings in the power meter. The thulium power has only small effect on the result while the holmium power result can be affected severely by the accuracy at low repetition rate when the average power is low.

6.7 Scaling prediction

A limiting factor in this experiment was the poor performance of the 2 mm thick Tm:YLF slab laser. If two 1.5 mm thick Tm:YLF slabs were available, each pumped with a separate diode stack, this should give us a combined thulium output power of over 120 W without fracture (68 W was demonstrated from a single slab without fracture in chapter 3). Following the trend in figure 6.6, it would give an output pulse energy of close to 50 mJ.

Given that the output from the Tm:YLF lasers were polarised, the output can be polarisation combined to pump the Ho:YAG rod. This would increase the available pump power to 240 W (four Tm:YLF slab lasers) without affecting the pump beam quality. Once again, following the trend of the figure 6.6, this would lead to pulse energies of over 120 mJ. Further power scaling can also be achieved by spatially multiplexing more Tm:YLF slab lasers as allowed by the diameter of the rod. Apart from the increased pump power, this would also provide a more uniform pump profile, which would result in a more Gaussian output profile. This improvement in pump power would add more

flexibility to the design of the holmium laser for obtaining higher pulse energies, such as using higher output coupling to prevent coating damages, or even further increase rod sizes if damage threshold of the coatings has been reached.

The scaling limit in this cavity design could come from the damage threshold of the coatings, or the thermal lens that could cause cavity instability, depending on cavity design. The number of slabs that can be used is limited by the rod size, where the 2.5 mm rod should allow 3-4 slab lasers to fit into the rod without any problem, due to the good vertical beam quality of the thulium. The holmium rod size could be limited by the cavity design, where larger rod size would require a more complex cavity in order to achieve good output beam quality.

6.8 Conclusion

In this chapter an externally pumped Q-switched Ho:YAG laser is demonstrated. Although the use of a 2.5 mm-diameter rod increased the threshold and reduced the performance, it is essential as it allows a larger spot-size to prevent the high intensities of the pulses from reaching the damage threshold of the coatings. Unfortunately, the poor performance of the 2 mm-thick Tm:YLF slab limited the maximum achievable pulse energy. The laser was characterised at various Q-switching repetition rates, giving a maximum pulse energy of 14 mJ with a pulse width of 17 ns at 20 Hz. This pulse energy was lower than the 50 mJ achieved at 60 Hz by Budni [113], using a diode-pumped Tm:YLF rod laser to externally pump the Ho:YAG laser at room temperature. However, our design allows the use of a CW Tm:YLF pump source, which gives flexibility in terms of repetition rate of the holmium laser. The lasing wavelength was at 2097 nm while the M^2 beam quality was estimated to be 1×1.7 using the knife edge method.

It was shown that a major advantage of this laser design is that it allows the use of Tm:YLF slab pump lasers. Moreover, because of the large rod diameter, multiple pump lasers can be used to obtain high energy Q-switch pulses. Smaller rods can be used if pump power is limited, but the pulse energy would be restricted by the damage threshold of the coatings. One may also use uncoated rods to improve the damage threshold while further increasing the output coupling to reduce the intra-cavity intensity to obtain higher Q-switch pulse energy. Thus the potential for power-scaling in this scheme seems very strong.

Chapter 7

Conclusions

7.1 Summary of work presented

Two power-scaling strategies for the Ho:YAG laser have been described in this thesis. Due to negligible absorption at commonly available laser diode wavelengths, an intermediate pump laser is required. Tm^{3+} doped materials offer reasonably efficient means to actively convert the output of high-power laser diodes from $\sim 0.8 \mu\text{m}$ to $\sim 1.9 \mu\text{m}$, where Ho:YAG has good absorption. Tm:YLF is the laser material of choice due to its lasing wavelength coinciding with a strong Ho:YAG absorption peak at $1.91 \mu\text{m}$. However, due to the fragile nature of YLF and a relatively low thermally-induced stress fracture limit, high-power operation of end-pumped Tm:YLF pump lasers are restricted to around 20 W for the single-rod geometry. In order to increase the Ho:YAG laser output, a power-scaled Tm:YLF pump laser was first required.

7.1.1 Tm:YLF pump laser design

A laser performance model was detailed in chapter 2 that accounted for the size, distribution, and overlap, of the pump and laser modes; reabsorption loss for a quasi-three-level laser system; and excited state upconversion and cross-relaxation processes. Various parameters were required that were not available in published literature, such as the upconversion rate and quantum yield versus doping level. However, our modelling suggested these parameters could be obtained through comparison of relative laser performance for similar crystals with different doping levels. In addition, the thermally-induced stress fracture limit dependent upon the laser performance was also required to find the power-scaling potential of the Tm:YLF laser system.

Thulium lasers using Tm:YLF rods of various doping levels were characterised through their threshold and slope efficiency. Their relative laser performance was used to find the required parameters including quantum yield and estimated upconversion loss. The fracture of a 6 at.% rod was used as a reference point to determine a figure of merit for thermal stress fracture limit at other doping concentrations. From these experiments we concluded that the 2 at.% doping concentration is the optimum doping concentration for the end-pumped configuration, where the optimum doping is defined as the maximum output power before fracture. An output power of 16 W was obtained from the 2 at.% rod, higher than the 15 W and 3 W obtained at the fracture point of 4 and 6 at.% rods respectively. Efficient performance was obtained with a slope efficiency of 48 % with respect to absorbed diode power, despite the relatively low doping level, demonstrating a strong cross-relaxation contribution enabling a quantum yield of ~ 1.7 . Unfortunately, the Tm:YLF rod laser is expected to have a maximum achievable output power of around 20 W, which is consistent with the work of Budni et al. [33, 89], who have demonstrated 22 W from a single 3 at.% doped Tm:YLF rod with undoped end-caps, which increase the stress fracture limit.

Therefore, knowing that a single Tm:YLF rod laser could not provide sufficient pump power to enable a 100 W class Ho:YAG laser, we resolved this issue by using a slab geometry. The slab geometry is known for its better thermal management and greater power handling capability. Moreover, the slab geometry has a similar shape to a diode laser bar, thus reducing the need of reshaping the pump light and simplifying the coupling optics with respect to rod or fibre lasers. Therefore the overall pumping configuration can be very efficient and at the same time provide a relatively uniform pump distribution that further eases the thermal management requirements within the gain medium.

A Tm:YLF slab laser was demonstrated at 100 W of output power at 1.91 μm , the highest known to date. This is a five-fold improvement over the rod geometry. In terms of laser performance, this corresponds to a slope efficiency of 40 % with respect to the incident diode power, and over 20 % optical to optical efficiency. The output intensity profile was essentially Gaussian in the vertical axis and top-hat in the horizontal, when a simple plano-concave cavity was used.

As the spatial profile is a complex combination of many higher-order cavity modes, at least in one axis, a plane-wave model was used to predict the laser performance. The plane-wave model is not only simpler, but also allows one to determine the relative powers in the different output channels; such as fluorescence, cavity loss, upconversion and the quantum defect. Consequently we could estimate the heat deposition in the laser crystal, which was useful in calculating the fracture limit for the slab configuration.

7.1.2 Intra-cavity side-pumping

An intra-cavity side-pumping scheme was demonstrated as a route toward a compact high-power Ho:YAG laser. Employing a Tm:YLF slab gain element, decoupled from the holmium laser cavity, this cavity offers the potential for further power-scaling as will be discussed in section 7.2.1.

At the time of this work, this was the first reported demonstration of an intra-cavity side-pumping scheme to our knowledge, and 13 W of holmium output was generated from the Ho:YAG slab for 200 W of incident diode power. The output beam was near-diffraction-limited in one axis, and moderately multi-mode in the other. A slope efficiency of 15.5 % with respect to the incident diode power on the Tm:YLF was obtained. As high as 20 W of output power was expected if a 1.5 mm Tm:YLF slab had been utilised, which unfortunately was not available at the time of this experiment. The holmium CW lasing wavelength was at 2097 nm, corresponding to the second highest emission peak in the 2.1 μm region. The thulium lasing wavelength shifted from 1910 nm for the simple two-mirror cavity and an output coupling of around 10 %, similar to the expected absorption peak by the holmium crystal, to 1897 nm when in the intra-cavity side-pumping configuration. Our plane-wave models confirmed such a shift was expected under certain conditions. Further improvements in output power and slope efficiency can be expected for a tailored thulium pump-reflective coating designed to optimise the thulium lasing wavelength when the holmium is in the cavity.

A plane-wave model for the intra-cavity side-pumping scheme was derived based on the work of Beach [92] and Mackenzie et al. [104]. The modelled laser performance was in fair agreement with the experiment. This model includes ground-state depletion, gain saturation and energy transfer mechanisms, such as upconversion and cross-relaxation. The modelled slope efficiency predicted was slightly higher than obtained experimentally, which was attributed to the fact that the laser was still relatively close to its threshold, where this modelling technique does not cater for the changing slope efficiency depending upon the laser intensity. It has also been shown that the wavelength of the thulium laser would shift to minimise the absorption by the Ho:YAG without active wavelength control in the cavity.

7.1.3 External pumping and Q-switching

Although the intra-cavity side-pumping scheme offers a power-scalable Ho:YAG laser, it is not particularly suitable for high-energy Q-switching operation. This is due to the Ho:YAG can act as a saturable absorber, which can cause un-controllable pulsing

of the Tm:YLF pump laser, as has been observed by Kieleck et al. [105]. Moreover, power spikes have been observed for the thulium laser when the holmium laser was below threshold, which damaged the coatings of the Tm:YLF slab. Therefore, changes to the cavity Q for either the thulium or holmium lasers make pulsed operation via this technique quite hazardous for the thulium pump laser.

To explore a second power-scaling strategy for the holmium laser we demonstrated a Tm:YLF slab laser end-pumping a pump-guided Ho:YAG rod laser. The pump-guiding rod was used to confine the multi-mode output of the Tm:YLF slab laser. Such a rod design not only allows the use of a simple slab based pump-laser, but also spatially multiplexed pump beams. An output power of 38 W has been demonstrated with a simple plano-concave two-mirror cavity, using 70 W of thulium incident power from two Tm:YLF slab lasers. The lasing wavelength of 2090 nm is at the highest holmium emission peak around the 2.1 μm region. The laser operated with a slope efficiency of 61 % with respect to the incident thulium laser power. The output profile was elliptical, but diffraction-limited beam quality can be expected from such a gain element by using more complicated resonator configurations such as an unstable resonator or a folded cavity.

To explore the energy storage potential of Ho:YAG in a pulse-mode operation, a Pockel's cell was used to Q-switch the Ho:YAG laser. The electro-optic material used was RTP, which had the benefit of low power consumption and high damage threshold. This laser was again pumped by CW Tm:YLF slab lasers, thus allowing the choice of the repetition rate via the voltage waveform applied to the Pockel's cell. A maximum Q-switch pulse energy of 14 mJ was obtained at a repetition rate of 20 Hz; it had a FWHM pulse-width of 17 ns. A further increase in pulse energy is possible with the higher pump powers, well within the damage threshold of the dielectric coatings within the cavity. The beam quality was diffraction-limited in the horizontal axis and slightly multi-mode in the vertical.

7.2 Future work

Although both the Tm:YLF slab laser and two different Ho:YAG laser configurations have been demonstrated with good laser performance, further improvements can be expected. Discussed here are the possibilities of improvements including power-scaling of Ho:YAG lasers, a different route to power-scaling Tm:YLF slab lasers, and improving the beam quality of the output from a slab laser.

7.2.1 Power-scaling Ho:YAG lasers

The power-scaling of the Ho:YAG lasers involved the scaling of the Tm:YLF pump laser. This can be achieved simply by combining several Tm:YLF slab lasers through spatial multiplexing or polarisation combination, or in the case of intra-cavity pumping where spatial multiplexing is not suitable, the scaling of the Tm:YLF slab pump laser itself.

7.2.1.1 Power-scaling Ho:YAG laser through spatially multiplex

Although the scaling of output power of Ho:YAG lasers is limited by the available pump power, spatially multiplexing several Tm:YLF slab pump lasers, as described in section 5, allow a much higher pump power to be used. Consider using both spatial multiplexing and polarisation combining, four Tm:YLF slab lasers can be used. Each can give ~ 70 W of pump power, resulting in a total pump power of 240 W as shown in figure 7.1. Following the trends in laser performance given in sections 5.2 and 6.6, the holmium laser is expected to give 140 W of CW output or 120 mJ pulse energy at 240 W of incident pump power. This is predicted using 1.5 mm diameter Ho:YAG rod for CW operation, and 2.5 mm rod for pulsed operation, which is also limited by the coating damage threshold. This strategy involves the increase in Ho:YAG rod diameter as more pump lasers are used.

7.2.1.2 Power-scaling Tm:YLF slab pump lasers

Power-scaling of the Tm:YLF slab laser can be achieved by increasing the area of the cooling faces with respect to the pumped volume. However, in an end-pumped configuration this would lead to further degradation in output beam quality. Thus one solution is to use a side-pumping scheme that has the benefit of increasing the pump volume simply by increasing the length of the slab, while additional pump modules could be installed along the sides. Although the increased slab length would lead to higher threshold power, it also increases the thermal fracture limit proportionally as the heat is more distributed, thus ultimately, higher output power can be achieved. A similar slab as described in chapter 3, a 20 mm-long, 1.5 mm-thick and 9 mm-wide slab but at an increased doping concentration of 4 at.% is used for comparison in terms of absorbed pump power before fracture. The increase in doping concentration led to a reduction in absorb power before fracture by ~ 30 %. However, due to doubling of the pump width, the fracture limit is also doubled. This gives a net increase of 40 % in absorbed power before fracture, allowing over 100 W of thulium output assuming the same threshold

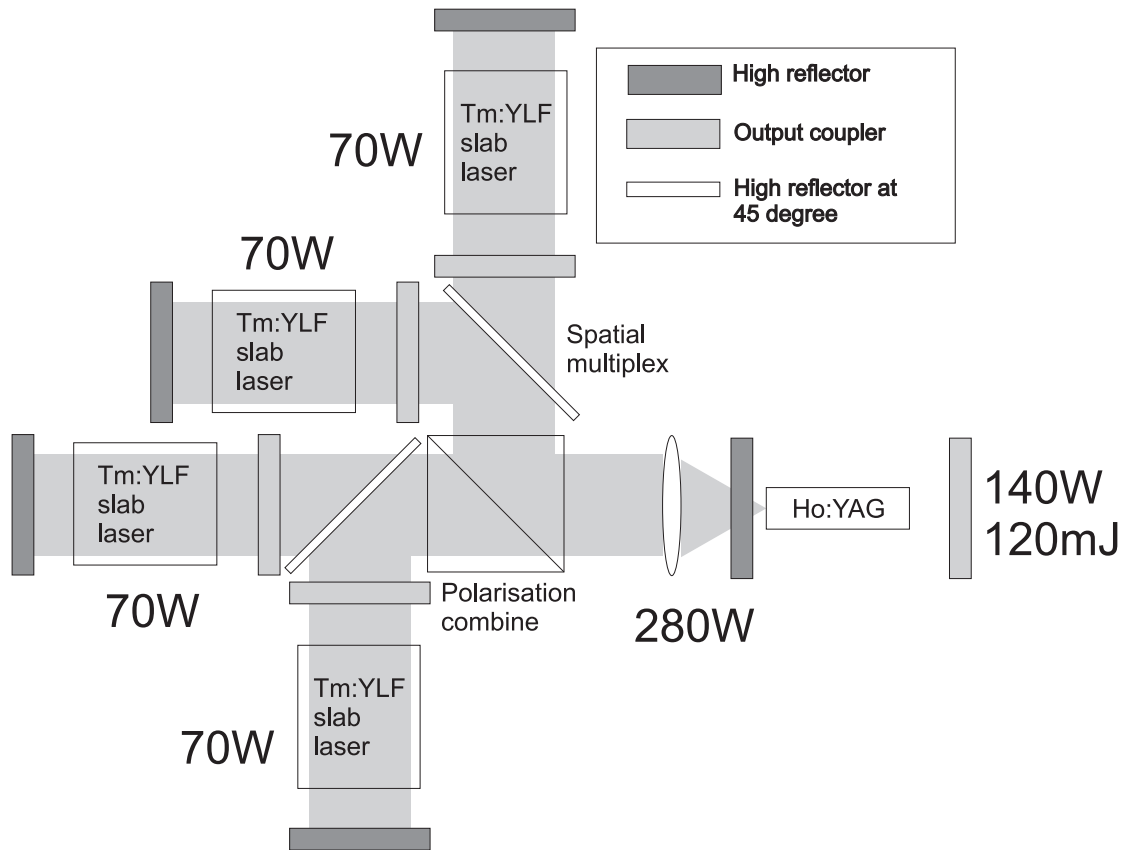


FIGURE 7.1: Spatially multiplex several Tm:YLF slab lasers

and slope efficiency. Moreover, the higher doping concentration is also expected to provide an improvement in slope efficiency from 40 % to 46 % which further increases the thulium output.

7.2.2 Slab lasers with good beam quality

Slab lasers have various benefits in high-power operation due to their good thermal management properties. Unfortunately, the highly multi-mode output restricts their applications. As such, improving the beam quality from a slab laser would bring solid-state lasers a big step forward in power-scaling applications.

Various techniques have been proposed in improving a slab laser beam quality. One of such is the hybrid stable-unstable resonator [65, 66], as shown in figure 7.3, where it is formed by two concave high reflectors, with a cavity length that leads to instability in the width axis and stable in the other. This relies on the difference of thermal lens in the orthogonal axes or the use of a cylindrical lens. In this cavity, the fundamental mode would start lasing and bounce between the high reflectors. It would be magnified in the horizontal axis, filling out the wide gain available after each double-pass, until it

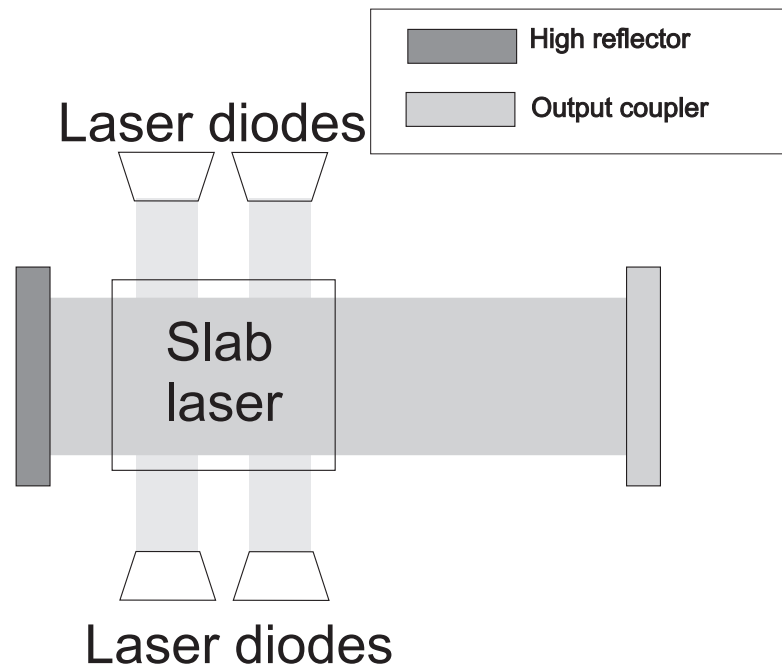


FIGURE 7.2: Side-pumped slab

reaches the 45 degree high reflector, and coupled out of the cavity. Note that the output coupling of the cavity depends on the radius of curvature of both high reflectors [66]. This strategy should allow the power-scaling of Tm:YLF lasers to the 100 W regime in a diffraction-limited beam, thus greatly improving the brightness.

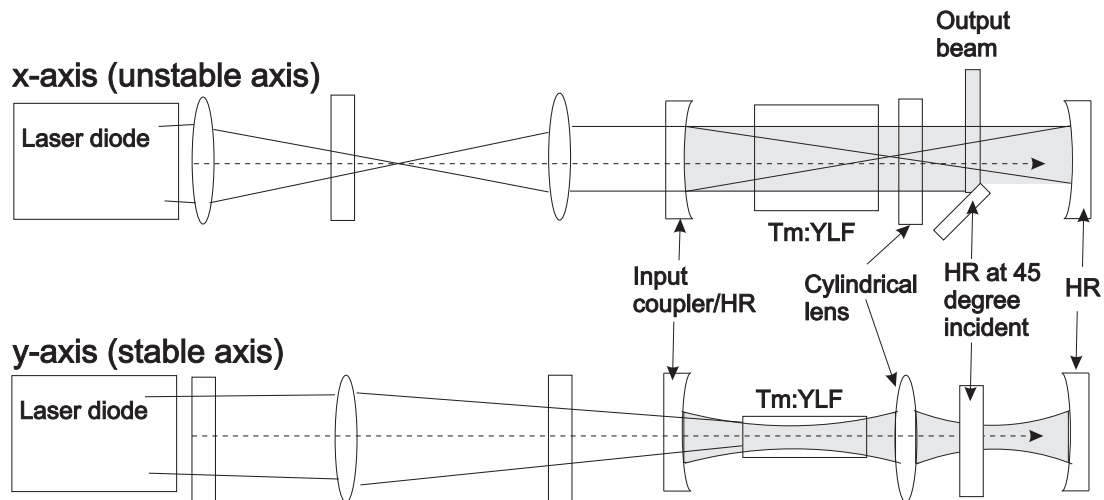


FIGURE 7.3: Hybrid stable-unstable resonator

Appendix A

Rate equation model

The rate equation model used here is based on the papers by Takunori Taira [76], but modified to account for upconversion and cross-relaxation. This approach was also employed by Bjurshagen [77, 114] for Nd:YAG in blue light generation. It takes into account reabsorption loss for a quasi-3-level system, upconversion, cross-relaxation, size of the pump and laser mode and, importantly, the distribution of pump and laser modes and their overlap in a longitudinally pumped laser. This model assumes fast thermal relaxation, no GSD and no diffraction inside the cavity. Although Tm:YLF exhibits cross-relaxation when operating at 1.9 μm , using a 790 nm pump source, which involves more than two manifolds in the overall pump-lasing process (see thulium energy level diagram in figure 2.1), the excitation density in the upper two manifolds, manifold 3H_4 and 3H_5 , can be assumed to be ~ 0 . This assumption is possible because of the much longer decay lifetime of the upper laser manifold (on the order of 10 ms), when compared to the effective lifetime of manifold 3H_4 and 3H_5 (both on the order of μs) [7, 87].

Figure A.1 is an energy level diagram based on a Tm:YLF system. In the diagram, N_U is the upper laser manifold population density, N_2 is the population density of the stark level in the upper laser manifold from which lasing occurs, N_L is the lower laser manifold population density and N_1 is the population density of the stark level in the lower laser manifold at which the laser transition terminates. The total population density, N_{total} , which is proportional to the doping concentration, is given by

$$N_{total} = N_U + N_L , \tag{A.1}$$

where we assume higher lying levels are quickly depopulated by non-radiative processes.

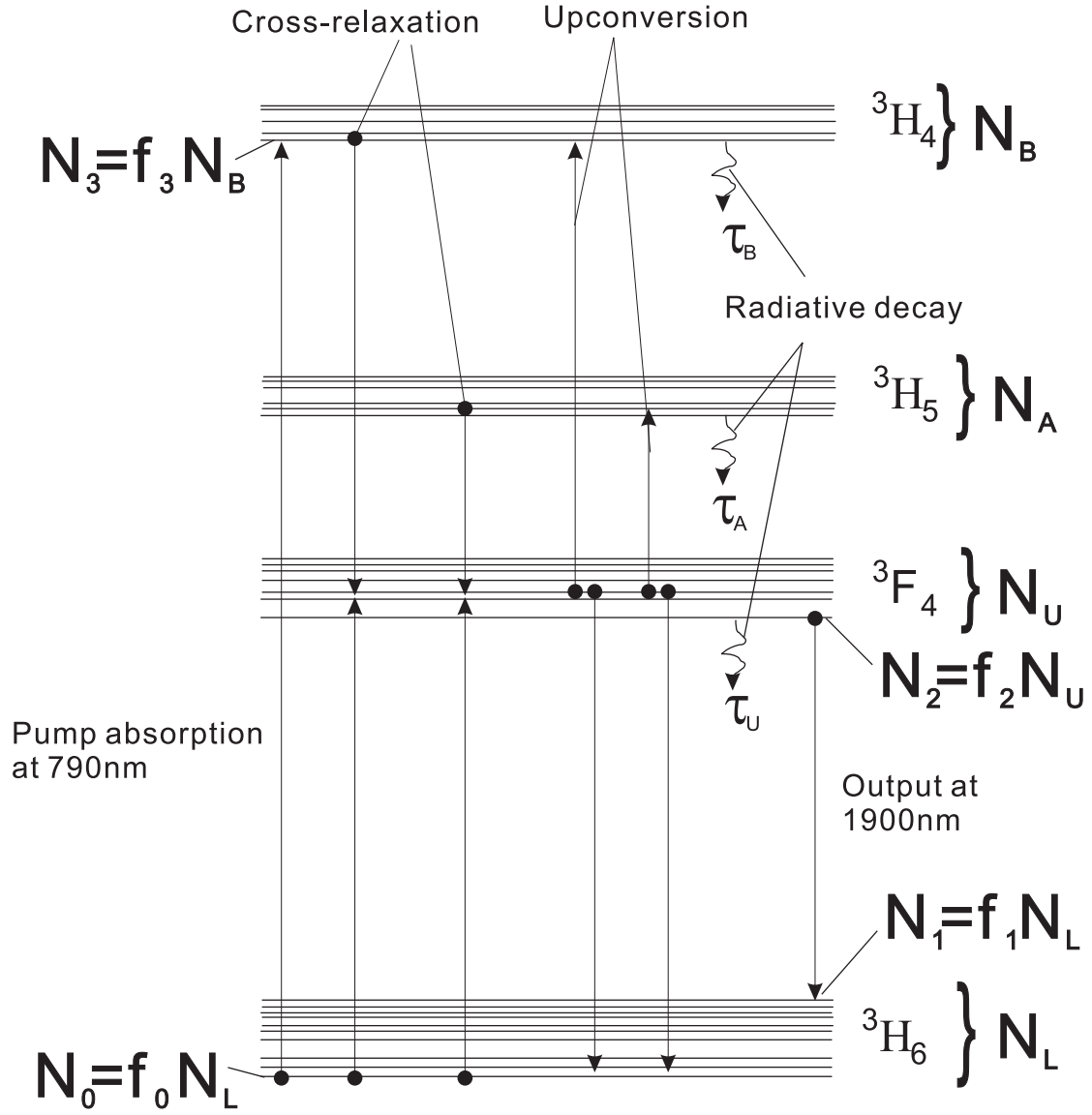


FIGURE A.1: Quasi-3-level energy level diagram based on Tm:YLF

The change of population density in the upper laser manifold, which takes into account the pump, fluorescence lifetime, upconversion and laser gain, is given by

$$\begin{aligned} \frac{dN_U(x, y, z)}{dt} = & Rr_p(x, y, z) - \frac{N_U(x, y, z) - N_U^0}{\tau_U} - \gamma(N_U(x, y, z) - N_U^0)^2 \\ & - \frac{c}{n} [\sigma_{em}(\lambda_l)N_U(x, y, z) - \sigma_{abs}(\lambda_l)N_L(x, y, z)] \Phi \phi_0(x, y, z), \end{aligned} \quad (A.2)$$

where τ_U is the lifetime of the upper manifold, γ is the manifold upconversion parameter, $\frac{c}{n}$ is the speed of light in the crystal, N_U^0 is the unpumped excited ion density in the upper laser manifold, which is assumed to be constant and independent of r and z for no GSD, r is the coordinate perpendicular to the propagation of the laser, z is the direction of

propagation, $\sigma_{em}(\lambda_l)$ is the effective emission cross section of the upper laser manifold at the lasing wavelength λ_l and $\sigma_{abs}(\lambda_l)$ is the effective absorption cross section at the lasing wavelength.

R is the rate of pumping to the upper manifold, which is given by

$$R = \frac{P_p \eta_a \eta_{QY}}{h\nu_p} , \quad (\text{A.3})$$

where P_p is the pump power, h is the Planck constant, ν_p is the pump photon frequency, η_{QY} is the quantum yield (which may be as high as 2 due to the “two for one” cross-relaxation process shown in figure A.1), and η_a is the fraction of pump absorbed with $\eta_a = 1 - \exp(-\alpha l)$ for a crystal of length l and pump absorption coefficient α .

$r_p(x, y, z)$ is the normalized spatial distribution of the pump such that,

$$\int \int \int_{crystal} r_p(x, y, z) dV = 1 . \quad (\text{A.4})$$

For a circular Gaussian beam, r_p is

$$r_p(x, y, z) = \frac{2\alpha}{\eta_a \pi w_p^2} \exp\left(\frac{-2(x^2 + y^2)}{w_p^2}\right) \exp(-\alpha z) , \quad (\text{A.5})$$

where w_p is the pump beam waist.

Φ is the total number of photons in the active medium,

$$\Phi = \frac{2P_o}{T_{oc} h\nu_L} \frac{l_{rod} n}{c} , \quad (\text{A.6})$$

where P_o is the output power, n is the refractive index of the crystal, l_{rod} is the active medium length, T_{oc} is the transmission of the output coupler and ν_L is the frequency of the laser photon. This assumes low output coupling thus photon density variation do not vary much within the active medium.

The spatial distribution of the laser photon field inside the active medium is given by ϕ_0 , and is normalized such that,

$$\int \int \int_{crystal} \phi_0(x, y, z) dV = 1 . \quad (\text{A.7})$$

For a circularly symmetric Gaussian beam with low output coupling, ϕ_0 is given by

$$\phi_0(x, y, z) = \frac{2}{\pi w_L^2 l_{rod}} \exp\left(\frac{-2(x^2 + y^2)}{w_L^2}\right) , \quad (\text{A.8})$$

where w_L is the laser beam waist

Similarly, for lower laser manifold, the rate of change of population density is given by

$$\begin{aligned} \frac{dN_L(x, y, z)}{dt} = & -Rr_p(x, y, z) - \frac{N_L(x, y, z) - N_L^0}{\tau_U} + \gamma(N_L(x, y, z) - N_L^0)^2 \\ & + \frac{c}{n} [\sigma_{em}(\lambda_l)N_U(x, y, z) - \sigma_{abs}(\lambda_l)N_L(x, y, z)] \Phi\phi_0(x, y, z) , \end{aligned} \quad (\text{A.9})$$

The Boltzmann occupation factor of the upper(lower) laser stark level, $f_{2(1)}$, within the particular stark levels involved in the laser transition are

$$N_{2(1)} = f_{2(1)}N_{U(L)} . \quad (\text{A.10})$$

It is known that the effective cross-sections are related to the spectroscopic cross-sections by

$$\sigma_{em}(\lambda_l) = f_2\sigma_{21}(\lambda_l) , \quad (\text{A.11})$$

$$\sigma_{abs}(\lambda_l) = f_1\sigma_{21}(\lambda_l) . \quad (\text{A.12})$$

Using equation A.10 to A.12 allows the stimulated emission part of the equation to be converted from using $N_{U(L)}$ to using $N_{1(2)}$ in the form

$$\begin{aligned} \sigma_{em}(\lambda_l)N_U(x, y, z) - \sigma_{abs}(\lambda_l)N_L(x, y, z) &= \sigma_{21}(\lambda_l)[f_2N_U(x, y, z) - f_1N_L(x, y, z)] \\ &= \sigma_{21}(\lambda_l)[N_2(x, y, z) - N_1(x, y, z)] . \end{aligned} \quad (\text{A.13})$$

In order to find the inversion density, equation A.2 and A.9 can be rewritten, using equation A.13, as

$$\begin{aligned} \frac{dN_2(x, y, z)}{dt} &= f_2 \frac{dN_U(x, y, z)}{dt} \\ &= f_2 Rr_p(x, y, z) - \frac{N_2(x, y, z) - N_2^0}{\tau_U} - \frac{\gamma}{f_2} (N_2(x, y, z) - N_2^0)^2 \\ &\quad - f_2\sigma_{21} \frac{c}{n} [N_2(x, y, z) - N_1(x, y, z)] \Phi\phi_0(x, y, z) , \end{aligned} \quad (\text{A.14})$$

$$\begin{aligned} \frac{dN_1(x, y, z)}{dt} &= f_1 \frac{dN_L(x, y, z)}{dt} \\ &= -f_1 Rr_p(x, y, z) - \frac{N_1(x, y, z) - N_1^0}{\tau_U} + \frac{\gamma}{f_1} (N_1(x, y, z) - N_1^0)^2 \\ &\quad + f_1\sigma_{21} \frac{c}{n} [N_2(x, y, z) - N_1(x, y, z)] \Phi\phi_0(x, y, z) . \end{aligned} \quad (\text{A.15})$$

Taking the difference between Equations A.14 and A.15, the rate of change of population inversion density, $\frac{d\Delta N}{dt}$ can be obtained. The resulting equation is

$$\begin{aligned} \frac{d\Delta N(x, y, z)}{dt} = & f R r_p(x, y, z) - \frac{\Delta N(x, y, z) - \Delta N^0}{\tau_U} - \frac{\gamma}{f} (\Delta N(x, y, z) - \Delta N^0)^2 \\ & - f \sigma_{21} \frac{c}{n} \Delta N(x, y, z) \Phi \phi_0(x, y, z) , \end{aligned} \quad (\text{A.16})$$

where $\Delta N(x, y, z) = N_2(x, y, z) - N_1(x, y, z)$ is the population inversion density, $\Delta N^0 \sim -N_1^0$ is the unpumped population inversion density and $f = f_1 + f_2$ is the sum of the fractional population of the upper and lower laser level.

To simplify the upconversion part of the rate equation, rearranging equation A.1 and expressing N_U and N_U^0 as a function of ΔN is required and is given by

$$\begin{aligned} N_{total} &= N_U + N_L = N_U^0 + N_L^0 , \\ \Rightarrow N_U - N_U^0 &= -(N_L - N_L^0) , \end{aligned} \quad (\text{A.17})$$

$$\begin{aligned} \Delta N = N_2 - N_1 &= f_2 N_U - f_1 N_L , \\ \Rightarrow f_2 N_U - f_1 N_{total} + f_1 N_U &, \\ \Rightarrow f N_U - f_1 N_{total} &, \\ N_U &= \frac{\Delta N + f_1 N_{total}}{f} , \end{aligned} \quad (\text{A.18})$$

$$\text{similarly } N_U^0 = \frac{\Delta N^0 + f_1 N_{total}}{f} , \quad (\text{A.19})$$

Taking the difference between $\frac{dN_2}{dt} - \frac{dN_1}{dt}$, the upconversion part goes through the following steps

$$\begin{aligned} & -\frac{\gamma}{f_2} (N_2(x, y, z) - N_2^0)^2 - \frac{\gamma}{f_1} (N_1(x, y, z) - N_1^0)^2 , \\ \Rightarrow & -\gamma [f_2 (N_U - N_U^0)^2 + f_1 (N_L - N_L^0)^2] , \\ \Rightarrow & -f \gamma (N_U - N_U^0)^2 , \\ \Rightarrow & -f \gamma \left(\frac{\Delta N + f_1 N_{total}}{f} - \frac{\Delta N^0 + f_1 N_{total}}{f} \right)^2 , \\ \Rightarrow & -\frac{\gamma}{f} (\Delta N - \Delta N^0)^2 , \end{aligned} \quad (\text{A.20})$$

Under steady-state, ΔN remains constant, which leads to $\frac{d\Delta N}{dt} = 0$. Let $k = (\Delta N(x, y, z) - \Delta N^0)^{-1}$ in equation A.16 allows one to obtain ΔN in the following expression [114],

$$\Delta N = \Delta N^0 + \frac{2f\tau_U Rr_p - 2f\tau_U \sigma_{21} \frac{c}{n} \Phi \phi_0 \Delta N^0}{1 + f\tau_U \sigma_{21} \frac{c}{n} \Phi \phi_0 + \sqrt{(1 + f\tau_U \sigma_{21} \frac{c}{n} \Phi \phi_0)^2 + 4\gamma\tau_U (\tau_U Rr_p - \tau_U \sigma_{21} \frac{c}{n} \Phi \phi_0 \Delta N^0)}} , \quad (\text{A.21})$$

where only the negative solution is required under lasing conditions as the positive solution is not physically meaningful.

In the absence of upconversion, setting $\gamma = 0$, equation A.21 becomes

$$\Delta N = \frac{f\tau_U Rr_p + \Delta N^0}{1 + f\tau_U \sigma_{21} \frac{c}{n} \Phi \phi_0} , \quad (\text{A.22})$$

which is identical to the form given by Takunori Taira [76].

Under steady-state lasing condition, gain \times passive round-trip transmission = 1, and the gain is given by

$$\text{gain} = \exp \left(2\sigma_{21} l_{rod} \int \int \int_{cavity} \Delta N(x, y, z) \phi_0(x, y, z) dV \right) . \quad (\text{A.23})$$

Here we have considered the gain along the whole cavity. However, because the inversion only exists within the laser crystal, this could be simplified by integrating within the crystal volume boundary.

On the other hand, the passive round-trip transmission of the cavity, T , is given by

$$T = R_{oc} \exp(-L) , \quad (\text{A.24})$$

where R_{oc} is the reflectance of the output coupler and $\exp(-L)$ includes all other loss factors. Rearranging equations (A.23) and (A.24) leads to

$$2\sigma_{21} l_{rod} \int \int \int_{crystal} \Delta N(x, y, z) \phi_0(x, y, z) dV = L - \ln R_{oc} . \quad (\text{A.25})$$

By substituting equation (A.21) into equation (A.25) we can numerically find the output power, P_o , for a given pump power, P_p .

Threshold power, P_{th} , occurs at $P_o = 0$. Setting $P_o = 0$ would result in $\Phi = 0$ according to equation A.6. This would result in the following inversion density equation

$$\Delta N = \Delta N^0 + \frac{2f\tau_U Rr_p(x, y, z)}{1 + \sqrt{1 + 4\gamma\tau_U^2 Rr_p(x, y, z)}} . \quad (\text{A.26})$$

The threshold can then be calculated by substituting ΔN into equation A.25. In the case where upconversion is ignorable, the equation is

$$P_{th} = \frac{h\nu_p V_{eff}}{2\sigma_{21} l_{rod} \eta_{QY} \eta_a f \tau_U} [L - \ln(R_{oc}) - 2\Delta N^0 \sigma_{21} l_{rod}] , \quad (\text{A.27})$$

where V_{eff} is the effective volume defined by [73]

$$V_{eff} = \frac{1}{\int \int \int_{crystal} r_p(x, y, z) \phi(x, y, z) dV} . \quad (\text{A.28})$$

This is the same as the threshold equation proven by Takunori Taira [76] that is suitable for arbitrary pump profile. The threshold that includes upconversion is more complex and has to be solved numerically. However, it can be approximated using the effective lifetime as described in section 2.2.1.

There is no simple equation for calculating the slope efficiency when upconversion is taken into account as a separate process, thus it is included in the form of effective lifetime given by equation 2.3. The slope efficiency is derived by substituting equation A.22 into equation A.25 giving

$$2\sigma_{21} l_{rod} \int \int \int_{crystal} \frac{f R r_p(x, y, z) \tau_{eff} + \Delta N^0}{1 + f \sigma_{21} \tau_{eff} \frac{c}{n} \Phi} \phi_0(x, y, z) dV = L - \ln R_{oc} . \quad (\text{A.29})$$

To solve equation A.29, the following parameters are defined

$$F = \frac{2f \sigma_{21} l_{rod} \tau_{eff}}{L - \ln R_{oc}} R , \quad (\text{A.30})$$

$$S = f \sigma_{21} \tau_{eff} \frac{c}{n} \Phi , \quad (\text{A.31})$$

$$B = \frac{-2\sigma_{21} l_{rod} \Delta N^0}{L - \ln R_{oc}} , \quad (\text{A.32})$$

where F is a normalized variable proportional to pump power, S is a normalized variable proportional to internal laser power and B is the ratio of reabsorption loss to fixed cavity loss.

Substituting equation A.30 to A.32 into equation A.29 and rearrange would give

$$F = \frac{1 + B \int \int \int_{crystal} \frac{\phi_0(x, y, z)}{1 + S \phi_0(x, y, z)} dV}{\int \int \int_{crystal} \frac{r_p(x, y, z) \phi_0(x, y, z)}{1 + S \phi_0(x, y, z)} dV} . \quad (\text{A.33})$$

This equation follows Taira's work [76] instead of Risk's [75], which allows arbitrary mode distribution. Note that at threshold there will be no laser photon in the cavity.

Setting $S=0$ for equation A.33 would also result in the same threshold equation as equation A.27.

The slope efficiency, defined as the change of output power with pump power, is given by

$$\eta_s = \frac{dP_o}{dP_p} = \eta_a \eta_{QY} \frac{\nu_L}{\nu_p} \frac{T_{oc}}{L - \ln(R_{oc})} \frac{dS}{dF} . \quad (\text{A.34})$$

$\frac{dS}{dF}$, known as the mode-coupling efficiency, is obtained by differentiating and rearranging equation A.33 resulting in

$$\frac{dS}{dF} = \frac{1 + B \int \int \int_{crystal} \frac{\phi_0(x,y,z)}{1+S\phi_0(x,y,z)} dV}{F \int \int \int_{crystal} \frac{[Fr_p(x,y,z)-B]\phi_0^2(x,y,z)}{[1+S\phi_0(x,y,z)]^2}} \quad (\text{A.35})$$

Appendix B

Publication list

B.1 Journal publications

- S. So, J.I. Mackenzie, W.A. Clarkson, J.G. Betterton, E.K. Gorton, “A power-scaling strategy for longitudinally diode-pumped Tm:YLF lasers”, *Applied Physics B-Lasers and Optics*, vol. B84, pp389, 2006.
- S. So, J.I. Mackenzie, D. P. Shepherd, W.A. Clarkson, J.G. Betterton, E.K. Gorton, J.A.C. Terry, “Intra-cavity side-pumped Ho:YAG laser”, *Optics Express*, vol. 14, pp10481, 2006.

B.2 Conference publications

- J.I. Mackenzie, S. So, D.P. Shepherd, W.A. Clarkson, “Comparison of laser-performance for diode-pumped Tm:YLF of various doping concentrations”, *Advanced Solid-State Photonics*, Vienna, Austria, 2005.
- S. So, J.I. Mackenzie, D.P. Shepherd, W.A. Clarkson, “Power scaling strategy for longitudinally diode-pumped Tm:YLF lasers”, *CLEO/Europe*, Munich, Germany, 2005.
- S. So, J.I. Mackenzie, D.P. Shepherd, W.A. Clarkson, J.G. Betterton, E.K. Gorton and J.A.C. Terry, “Power-scalable Ho:YAG Slab Laser, intracavity side-pumped by a Tm:YLF Slab Laser”, *Advanced Solid-State Photonics*, Incline Village, Nevada, 29 Jan 2006.

References

- [1] R.H. Hoskins and B.H. Soffer. *8B7 - energy transfer and CW laser action in $\text{Ho}^{3+}:\text{Er}_2\text{O}_3$* . IEEE J Quantum Elect., 2(8):253, 1966.
- [2] R. L. Remski, Jr. James, L. T., K. H. Goen, B. Di Bartolo, and A. Linz. *Pulsed laser action in $\text{LiYF}_4:\text{Er}^{3+}$, Ho^{3+} at 77°K*. IEEE Journal of Quantum Electronics, QE-5(5):214, 1969.
- [3] A. C. Everitt and E. D. Fletcher. *The performance of the holmium³⁺ in yttrium aluminium garnet laser*. In Mullard Research Laboratories annual review, page 28. Mullard Res. Labs, 1969. Copyright 1970, IEE 174571.
- [4] M. Schellhorn, A. Hirth, and C. Kieleck. *Ho : YAG laser intracavity pumped by a diode-pumped Tm : YLF laser*. Optics Letters, 28(20):1933–1935, 2003.
- [5] A. Rapaport, S. Zhao, G. Xiao, A. Howard, and M. Bass. *Temperature dependence of the 1.06- μm stimulated emission cross section of neodymium in YAG and in GSGG*. Applied Optics, 41(33):7052–7, 2002.
- [6] J. Yu, U. N. Singh, N. P. Barnes, J. C. Barnes, M. Petros, and M. W. Phillips. *An all solid-state 2- μm laser system for space coherent wind lidar*. In 2000 IEEE Aerospace Conference, Mar 18-25 2000, volume 3 of IEEE Aerospace Conference Proceedings, pages 27–33, Big Sky, MT, 2000.
- [7] M. Schellhorn and A. Hirth. *Modeling of intracavity-pumped quasi-three-level lasers*. IEEE Journal of Quantum Electronics, 38(11):1455–1464, 2002.
- [8] N. P. Barnes, B. M. Walsh, and E. D. Filer. *Ho : Ho upconversion: applications to Ho lasers*. Journal of the Optical Society of America B-Optical Physics, 20(6):1212–1219, 2003.
- [9] G. Rustad and K. Stenersen. *Modeling of laser-pumped Tm and Ho lasers accounting for upconversion and ground-state depletion*. IEEE Journal of Quantum Electronics, 32(9):1645–1656, 1996.

- [10] M. Sjöholm, P. Weibring, H. Edner, and S. Svanberg. Atomic mercury flux monitoring using an optical parametric oscillator based lidar system. *Optics Express*, 12(4):551–556, 2004.
- [11] C. Bollig, R. A. Hayward, W. A. Clarkson, and D. C. Hanna. 2-W Ho:YAG laser intracavity pumped by a diode-pumped Tm:YAG laser. *Optics Letters*, 23(22):1757–1759, 1998.
- [12] D. K. Killinger and Chan Kin Pui. Solid-state lidar measurements at 1 and 2 μm . In *Laser Radar VI*, 23-25 Jan. 1991, volume 1416 of *Proc. SPIE - Int. Soc. Opt. Eng. (USA)*, pages 125–8, Los Angeles, CA, USA, 1991.
- [13] S. W. Henderson, C. P. Hale, J. R. Magee, M. J. Kavaya, and A. V. Huffaker. Eye-safe coherent laser radar system at 2.1 μm using Tm,Ho:YAG lasers. *Optics Letters*, 16(10):773–5, 1991.
- [14] M. Henriksson, M. Tiihonen, V. Pasiskevicius, and F. Laurell. Mid-infrared ZGP OPO pumped by near-degenerate narrowband type-I PPKTP parametric oscillator. *Applied Physics B: Lasers and Optics*, 88(1):37–41, 2007.
- [15] Philip E. Cassady, Ronald Murata, Sean McKenna, M. John Yoder, William E. Keicher, Philip M. Blumenau, Daniel H. Leslie, and Douglas G. Youmans. Laser radar technology for airborne theater missile defense. In *Applied Laser Radar Technology II*, Apr 20 1995, volume 2472 of *Proceedings of SPIE - The International Society for Optical Engineering*, pages 50–61, Orlando, FL, USA, 1995. Society of Photo-Optical Instrumentation Engineers, Bellingham, WA, USA.
- [16] A. Charlton, M. R. Dickinson, T. A. King, and A. J. Freemont. Holmium YAG and erbium YAG laser interaction with hard and soft tissue. In *Proceedings of Laser-Tissue Interaction II*, Jan 21-23 1991, volume 1427 of *Proceedings of SPIE - The International Society for Optical Engineering*, pages 189–197, Los Angeles, CA, USA, 1991. Publ by Int Soc for Optical Engineering, Bellingham, WA, USA.
- [17] T. Y. Fan, G. Huber, R. L. Byer, and P. Mitzscherlich. Spectroscopy and Diode Laser-Pumped Operation of Tm, Ho-YAG. *IEEE Journal of Quantum Electronics*, 24(6):924–933, 1988.
- [18] Adam C. Mues and Bodo E. Knudsen. Holmium:YAG laser in clinical urology. *Biophotonics International*, 14(7):44, 2007.
- [19] M. R. Treat, M. C. Oz, and H. W. Popp. 2.15 micron laser welding of gallbladder tissue. In *Laser Surgery: Advanced Characterization, Therapeutics and Systems*, 15-18 Jan. 1989, volume 1066 of *Proc. SPIE - Int. Soc. Opt. Eng. (USA)*, pages 137–40, Los Angeles, CA, USA, 1989.

- [20] B. M. Antipenko, Yu D. Berezin, V. A. Buchenkov, V. M. Zhurba, T. I. Kiseleva, V. V. Lazo, A. A. Nikitichev, and V. A. Pis'mennyi. *Pulse-periodic holmium laser for medial applications*. Soviet Journal of Quantum Electronics, 19(11):1509–11, 1989.
- [21] John N. M. D. Kabalin. *Clinical development of holmium:YAG laser prostatectomy*. In Lasers in Surgery: Advanced Characterization, Therapeutics, and Systems VI, Jan 27-30 1996, volume 2671 of Proceedings of SPIE - The International Society for Optical Engineering, pages 292–299, San Jose, CA, USA, 1996.
- [22] Ralf Brinkmann, Dirk Theisen, Tobias Brendel, and Reginald Birngruber. *Single-pulse 30-J holmium laser for myocardial revascularization - a study on ablation dynamics in comparison to CO₂ laser-TMR*. IEEE Journal on Selected Topics in Quantum Electronics, 5(4):969–980, 1999.
- [23] Mehmet C. Oz, Michael R. Treat, Steven K. Libutti, Howard W. Popp, Larry S. Bass, and Sulli Popilskis. *Preliminary report: laser welding and fibrinogen soldering are superior to sutured cholecystostomy closure in a canine model*. In Proceedings of Laser Surgery: Advanced Characterization Therapeutics, and Systems II, Jan 14-19 1990, volume 1200 of Proceedings of SPIE - The International Society for Optical Engineering, pages 55–59, Los Angeles, CA, USA, 1990. Publ by Int Soc for Optical Engineering, Bellingham, WA, USA.
- [24] R. Beck and K. Guers. *Ho laser with 50-W output and 6.5% slope efficiency*. Journal of Applied Physics, 46(12):5224–5225, 1975.
- [25] Haim Lotem, Yeshoshua Kalisky, Jacob Kagan, and D. Sagie. *2 μ m holmium laser*. IEEE Journal of Quantum Electronics, 24(6):1193–1200, 1988.
- [26] H. O. Teichmann, E. W. Duczynski, and G. Huber. *17 J Ho-laser at 2 microns*. In High Power Solid State Lasers, 19-20 Sept. 1988, volume 1021 of Proc. SPIE - Int. Soc. Opt. Eng. (USA), pages 74–81, Hamburg, West Germany, 1989.
- [27] E. P. Chicklis, C. S. Naiman, R. C. Folweiler, and J. C. Doherty. *Low-threshold room-temperature lasing action in Ho³⁺:YLF and YAG*. In Digest of technical papers of the 1971 IEEE/OSA conference on laser engineering and applications, 2-4 June 1971, Digest of technical papers of the 1971 IEEE/OSA conference on laser engineering and applications, page 41, Washington, DC, USA, 1971. IEEE.
- [28] C. Li, D. Shen, J. Song, N. Kim, and K. I. Ueda. *Flash-lamp pumped high-power Cr-Tm:YAG and Cr-Tm-Ho:YAG lasers operating at 2 μ m wavelength*. In Advanced High-Power Lasers, 1-5 Nov. 1999, volume 3889 of Proc. SPIE - Int.

- Soc. Opt. Eng. (USA), pages 274–8, Osaka, Japan, 2000. SPIE-Int. Soc. Opt. Eng.
- [29] R. Allen, L. Esterowitz, L. Goldberg, J. F. Weller, and M. Storm. Diode-pumped 2 μm holmium laser. *Electronics Letters*, 22(18):947, 1986.
- [30] R. C. Stoneman and L. Esterowitz. Intracavity-pumped 2.09- μm Ho:YAG laser. *Optics Letters*, 17(10):736–738, 1992.
- [31] R. A. Hayward, W. A. Clarkson, and D. J. Hanna. High-power diode-pumped room-temperature Tm:YAG and intracavity-pumped Ho:YAG lasers. In *Proceedings of Topical Meeting on Advanced Solid-State Laser (ASSL 2000)*, 13-16 Feb. 2000, OSA Trends in Optics and Photonics. Advanced Solid State Lasers. Vol.34. Proceedings, pages 90–4, Davos, Switzerland, 2000. Opt. Soc. America.
- [32] C. D. Nabors, J. Ochoa, T. Y. Fan, A. Sanchez, H. K. Choi, and G. W. Turner. Ho:YAG laser pumped by 1.9- μm diode lasers. *IEEE J Quantum Elect.*, 31(9):1603, 1995.
- [33] P. A. Budni, M. L. Lemons, J. R. Mosto, and E. P. Chicklis. High-power/high-brightness diode-pumped 1.9- μm Thulium and resonantly pumped 2.1- μm Holmium lasers. *IEEE Journal of Selected Topics in Quantum Electronics*, 6(4):629–635, 2000.
- [34] N. P. Barnes, W. A. Clarkson, D. C. Hanna, V. Matera, and B. M. Walsh. Tm:glass fiber laser pumping Ho:YAG and Ho:LuAG. In *Conference on Lasers and Electro-Optics Europe, Conference on Lasers and Electro-Optics Europe - Technical Digest*, page 530, Baltimore, MD, 2001. Institute of Electrical and Electronics Engineers Inc.
- [35] A. Abdolvand, D. Y. Shen, L. J. Cooper, R. B. Williams, and W. A. Clarkson. Ultra-efficient Ho:YAG laser end-pumped by a cladding-pumped Tm-doped silica fiber laser. In *2003 OSA Topical Meeting on Advanced Solid-State Photonics (ASSP)*, 2-5 Feb. 2003, *2003 OSA Topical Meeting on Advanced Solid-State Photonics (ASSP) (Trends in Optics and Photonics Series Vol.83)*, pages 7–12, San Antonio, CA, USA, 2003. Optical Soc. of America.
- [36] D. Y. Shen, A. Abdolvand, L. J. Cooper, and W. A. Clarkson. Efficient Ho:YAG laser pumped by a cladding-pumped tunable Tm:Silica-fibre laser. *Applied Physics B-Lasers and Optics*, 79(5):559, 2004.
- [37] Ian Elder, Dan Thorne, Ian Jones, and David Bell. Thulium fibre laser pumped mid-IR source. *Proceedings of SPIE - The International Society for Optical Engineering*, 6397:639703, 2006.

- [38] C. K. Asawa, A. I. Braunstein, D. P. Devor, V. Evtuhov, and A. L. Gentile. *Holmium-2 micron pumped optical parametric oscillator. Technical Report AFAL-TR-74-318, Hughes Res. Labs., Malibu, CA, USA, 1974.*
- [39] D. P. Devor. *Development and applications of 2.1- μ m holmium lasers. In 1973 IEEE/OSA Conference on Laser Engineering and Applications Digest of Technical Papers, 30 May-1 June 1973, 1973 IEEE/OSA Conference on Laser Engineering and Applications Digest of Technical Papers, pages 46–7, Washington, DC, USA, 1973. IEEE.*
- [40] V. A. French and R. C. Powell. *Laser-induced grating measurements of energy migration in Tm, Ho:YAG. Optics Letters, 16(9):666–8, 1991.*
- [41] Guenter Huber, Peter Mitzscherlich, Tso Y. Fan, and Robert L. Byer. *Energy transfer and inversion saturation in Tm,Ho:YAG. Journal of Luminescence, 40-41:509–510, 1987.*
- [42] B. M. Antipenko, A. S. Glebov, T. I. Kiseleva, and V. A. Pis'mennyi. *2.12- μ m Ho:YAG laser. Soviet Technical Physics Letters, 11(6):284–5, 1985.*
- [43] Mark Storm, Leon Esterowitz, and Milan Kokta. *2- μ m room temperature laser operation of Cr:Tm:Ho:YAG. In Conference on Lasers and Electro-Optics - Digest of Technical Papers., page 360, Baltimore, MD, USA, 1987. Optical Soc of America, Washington, DC, USA.*
- [44] S. Imai, T. Yamada, Y. Fujimori, and K. Ishikawa. *A 20 W Cr³⁺, Tm³⁺, Ho³⁺:YAG laser. Optics and Laser Technology, 22(5):351–3, 1990.*
- [45] T. Y. Fan, G. Huber, R. L. Byer, and P. Mitzscherlich. *Continuous-wave operation at 2.1 μ m of a diode-laser-pumped, Tm-sensitized Ho:Y₃Al₅O₁₂ laser at 300K. Optics Letters, 12(9):678–80, 1987.*
- [46] G. J. Kintz, L. Esterowitz, and R. Allen. *CW diode-pumped Tm³⁺, Ho³⁺:YAG 2.1 μ m room-temperature laser. Electronics Letters, 23(12):616, 1987.*
- [47] S. W. Henderson and C. P. Hale. *Tunable single-longitudinal-mode diode laser pumped Tm:Ho:YAG laser. Applied Optics, 29(12):1716–18, 1990.*
- [48] G. Kintz, I.D. Abella, and L. Esterowitz. *Upconversion coefficient measurements in Tm³⁺, Ho³⁺: YAG at room temperature. In Proceedings of International Conference on Lasers 87, page 398. STS Press, 1988.*
- [49] E. C. Honea, R. J. Beach, S. B. Sutton, J. A. Speth, S. C. Mitchell, J. A. Skidmore, M. A. Emanuel, and S. A. Payne. *115-W Tm:YAG diode-pumped solid-state laser. IEEE Journal of Quantum Electronics, 33(9):1592–1600, 1997.*

- [50] A. Dergachev, K. Wall, and Moulton P.F. A CW side-pumped Tm:YLF laser. *Advanced Solid-State Lasers*, 2002.
- [51] C. Kieleck, A. Hirth, and M. T. Schellhorn. Performances of Ho : YAG laser intracavity-pumped by a diode-pumped Tm : YLF laser. In *Laser Optics 2003: Solid State Lasers And Nonlinear Frequency Conversion*, volume 5478 of *Proceedings Of The Society Of Photo-Optical Instrumentation Engineers (SPIE)*, pages 8–14. *SPIE-Int. Soc. Opt. Eng.*, 2004.
- [52] E. Lippert, G. Arisholm, G. Rustad, and K. Stenersen. Fiber laser pumped mid-IR source. In *OSA Topical Meeting on Advanced Solid-State Photonics (ASSP)*, 2003 *OSA Topical Meeting on Advanced Solid-State Photonics (ASSP) (Trends in Optics and Photonics Series Vol.83)*, page 292, San Antonio, CA, USA, 2003. *Optical Soc. of America*.
- [53] T. Y. Fan, A. Sanchez, and W. E. DeFeo. Scalable, end-pumped, diode-laser-pumped laser. *Optics Letters*, 14(19):1057–9, 1989.
- [54] R. Martinsen. Highly efficient, high-power pump diodes from 790 nm to 2 μ m. In *The Institution of Engineering and Technology Seminar on High Power Diode Pumped Lasers and Systems*, 5 Dec. 2006, *The Institution of Engineering and Technology Seminar on High Power Diode Pumped Lasers and Systems*, pages 55–6, London, UK, 2006. *Inst. of Eng. and Technol.*
- [55] W. A. Clarkson and D. C. Hanna. Two-mirror beam-shaping technique for high-power diode bars. *Optics Letters*, 21(6):375–377, 1996.
- [56] P. L. Fuhr. Polarization power summing in laser diode communication systems. In *Laser Diode Optics*, 13-14 Jan. 1987, volume 740 of *Proc. SPIE - Int. Soc. Opt. Eng. (USA)*, pages 70–6, Los Angeles, CA, USA, 1987.
- [57] I. F. Elder and J. Payne. Diode-pumped, room-temperature Tm:YAP laser. *Applied Optics*, 36(33):8606–8610, 1997.
- [58] A. Braud, P. Y. Tigreat, J. L. Doualan, and R. Moncorge. Spectroscopy and CW operation of a 1.85 μ m Tm : KY₃F₁₀ laser. *Applied Physics B-Lasers and Optics*, 72(8):909–912, 2001.
- [59] I. Sokolska, W. Ryba-Romanowski, S. Golab, M. Baba, and T. Lukasiewicz. Spectroscopic assessment of LiTaO₃ : Tm³⁺ as a potential diode-pumped laser near 1.9 μ m. *Journal of Applied Physics*, 84(9):5348–5350, 1998.
- [60] W. Koechner. *Solid-State Laser Engineering*. *Springer Series in Optical Sciences*. Springer, 5 edition, 1999.

- [61] J. M. Eggleston, T. J. Kane, K. Kuhn, J. Unternahrer, and R. L. Byer. *The Slab Geometry Laser .1. Theory*. IEEE Journal of Quantum Electronics, 20(3): 289–301, 1984.
- [62] W.S. Martin and J.P. Chernoch. patent, US #3,633,126: *Multiple internal reflection face pumped laser*, 1972.
- [63] W. B. Jones, L. M. Goldman, J. P. Chernoch, and W. S. Martin. *The mini-FPL-A face-pumped laser: concept and implementation*. In 1972 international quantum electronics conference, digest of technical papers. (abstracts only), 8-11 May 1972, volume QE-8 of IEEE J. Quantum Electron. (USA), pages 534–5, Montreal, Que., Canada, 1972.
- [64] T. S. Rutherford, W. M. Tulloch, E. K. Gustafson, and R. L. Byer. *Edge-pumped quasi-three-level slab lasers: Design and power scaling*. IEEE Journal of Quantum Electronics, 36(2):205–219, 2000.
- [65] Hengli Zhang, Daijun Li, Peng Shi, Rober Diart, Alexander Shell, Claus R. Haas, and Keming Du. *Efficient, high power, Q-switched Nd:YLF slab laser end-pumped by diode stack*. Optics Communications, 250(1-3):157, 2005.
- [66] Du Keming, Wu Nianle, Xu Jiandong, J. Giesekus, P. Loosen, and R. Poprawe. *Partially end-pumped Nd:YAG slab laser with a hybrid resonator*. Optics Letters, 23(5):370, 1998.
- [67] P. G. Gobbi, S. Morosi, G. C. Reali, and A. S. Zarkasi. *Novel unstable resonator configuration with a self-filtering aperture: experimental characterization of the Nd:YAG loaded cavity*. Applied Optics, 24(1):26, 1985.
- [68] W. M. Tulloch, T. S. Rutherford, E. K. Gustafson, and R. L. Byer. *CW high-power conduction-cooled edge-pumped slab laser*. In Solid State Lasers VIII, volume 3613 of Proc. SPIE - Int. Soc. Opt. Eng. (USA), page 2, San Jose, CA, USA, 1999. SPIE-Int. Soc. Opt. Eng.
- [69] Jr. Shine, R. J., A. J. Alfrey, and R. L. Byer. *A 40W CW, TEM₀₀ mode, diode-laser-pumped, Nd:YAG zig-zag miniature-slab laser*. In Solid State Lasers and Nonlinear Crystals, volume 2379 of Proc. SPIE - Int. Soc. Opt. Eng. (USA), page 112, San Jose, CA, USA, 1995.
- [70] J. I. Mackenzie and W. A. Clarkson. *Novel stable resonator concept for efficient axisymmetric output from lasers with a planar gain medium*. In Conference on Lasers and Electro Optics, Long Beach, 2006.

- [71] J. I. Mackenzie and W. A. Clarkson. *Circular beams from slab lasers*. In *Europhoton*, Pisa, 2006.
- [72] DC Shannon, DL Vecht, S Re, J Alonis, and RW Wallace. *High average power diode-pumped lasers near 2 μ m*. *Proc SPIE*, 1865:164–173, 1993.
- [73] Ken'ichi Kubodera and Kenju Otsuka. *Single-transverse-mode LiNdP₄O₁₂ slab waveguide laser*. *Journal of Applied Physics*, 50(2):653, 1979.
- [74] Peter F. Moulton. *Investigation of the Co:MgF₂ laser system*. *IEEE J Quantum Elect.*, QE-21(10):1582, 1985.
- [75] W. P. Risk. *Modeling of longitudinally pumped solid-state lasers exhibiting reabsorption losses*. *Journal of the Optical Society of America B-Optical Physics*, 5(7):1412–1423, 1988.
- [76] T Taira, W. M. Tulloch, and R. L. Byer. *Modeling of quasi-three-level lasers and operation of CW Yb:YAG lasers*. *Applied Optics*, 36(9):1867–1874, 1997.
- [77] S. Bjurshagen, D. Evekull, and R. Koch. *Efficient generation of blue light by frequency doubling of a Nd:YAG laser operating on ⁴F_{3/2}, ⁴I_{9/2} transitions*. In 2002 Spring Meeting of the Quantum Optics Section of the German Physical Society, volume B76 of *Appl. Phys. B, Lasers Opt.* (Germany), page 135, Osnabruck, Germany, 2003. Springer-Verlag.
- [78] P. J. Hardman, W. A. Clarkson, G. J. Friel, M. Pollnau, and D. C. Hanna. *Energy-transfer upconversion and thermal lensing in high-power end-pumped Nd : YLF laser crystals*. *IEEE Journal of Quantum Electronics*, 35(4):647–655, 1999.
- [79] S. R. Bowman, G. J. Quarles, and B. J. Feldman. *Upconversion losses in flashlamp-pumped Cr, Tm:YAG*. In *OSA Proceedings on Advanced Solid-State Lasers*. Vol.13. *Proceedings of the Topical Meeting*, *OSA Proceedings on Advanced Solid-State Lasers*. Vol.13. *Proceedings of the Topical Meeting*, page 169, Sante Fe, NM, USA, 1992. *Opt. Soc. America*.
- [80] G.J. Kintz. *Highly efficient CW 2- μ m laser*. In *OSA annual meeting*, 1990.
- [81] G Rustad. *Modeling and experimental investigation of laser-diode end-pumped and side-pumped thulium- and holmium doped lasers*. *PhD thesis*, University of Oslo, 1994.
- [82] L. B. Shaw, R. S. F. Chang, and N. Djeu. *Measurement of up-conversion energy-transfer probabilities in HoY₃Al₅O₁₂ and TmY₃Al₅O₁₂*. *Physical Review B*, 50(10):6609–6619, 1994.

- [83] R Paschotta, J. Aus der Au, and U Keller. *Thermal effects in high-power end-pumped lasers with elliptical-mode geometry*. IEEE J Quantum Elect., 6:636–642, 2000.
- [84] L. Yan and C.H. Lee. *Thermal effects in end-pumped Nd:Phosphate glasses*. Journal of Applied Physics, 75(3):1286–1292, 1994.
- [85] H. Vanherzeele. *Thermal lensing measurement and compensation in a continuous-wave mode-locked Nd:YLF laser*. Optics Letters, 13(5):369, 1988.
- [86] C. Pfister, R. Weber, H. P. Weber, S. Merazzi, and R. Gruber. *Thermal beam distortions in end-pumped Nd:YAG, Nd:GSGG, and Nd:YLF rods*. IEEE J Quantum Elect., 30(7):1605, 1994.
- [87] B. M. Walsh, N. P. Barnes, and B. Di Bartolo. *Branching ratios, cross sections, and radiative lifetimes of rare earth ions in solids: Application to Tm^{3+} and Ho^{3+} ions in $LiYF_4$* . Journal of Applied Physics, 83(5):2772–2787, 1998.
- [88] G. Armagan, A. M. Buoncristiani, A. T. Inge, and B. Di Bartolo. *Comparison of spectroscopic properties of Tm and Ho in YAG and YLF crystals*. In OSA Proceedings on Advanced Solid-State Lasers. Vol.10. Proceedings of the Topical Meeting, OSA Proceedings on Advanced Solid-State Lasers. Vol.10. Proceedings of the Topical Meeting, page 222, Hilton Head, SC, USA, 1991. Opt. Soc. America.
- [89] LA Pomeranz, P. A. Budni, M. L. Lemons, C. A. Miller, J. R. Mosto, TM Pollak, and E. P. Chicklis. *Power scaling performance of Tm:YLF and Tm:YAlO lasers*. OSA Trends Opt. Photon., 26:458–462, 1999.
- [90] T. Y. Fan and R. L. Byer. *Modeling and CW operation of a Quasi-Three-Level 946 nm Nd:YAG Laser*. IEEE Journal of Quantum Electronics, 23(5):605–612, 1987.
- [91] Y. F. Chen, Y. P. Lan, and S. C. Wang. *Influence of energy-transfer upconversion on the performance of high-power diode-end-pumped CW lasers*. IEEE J Quantum Elect., 36(5):615, 2000.
- [92] R. J. Beach. *CW theory of quasi-three level end-pumped laser oscillators*. Optics Communications, 123(1-3):385–393, 1996.
- [93] P. Peterson, A. Gavrielides, and P. M. Sharma. *CW theory of a laser diode-pumped two-manifold solid state laser*. Optics Communications, 109(3-4):282, 1994.

- [94] S. A. Payne, L. L. Chase, L. K. Smith, W. L. Kway, and W. F. Krupke. *Infrared cross-section measurements for crystals doped with Er^{3+} , Tm^{3+} , and Ho^{3+}* . *IEEE Journal of Quantum Electronics*, 28(11):2619–2630, 1992.
- [95] Raymond J. Beach, Mark A. Emanuel, Barry L. Freitas, Jay A. Skidmore, Nils W. Carlson, William J. Bennett, and Richard W. Solarz. *Applications of microlens-conditioned laser diode arrays*. In *Micro-Optics/Micromechanics and Laser Scanning and Shaping, Feb 7-8 95*, volume 2383 of *Proceedings of SPIE - The International Society for Optical Engineering*, pages 283–297, San Jose, CA, USA, 1995. *Society of Photo-Optical Instrumentation Engineers*, Bellingham, WA, USA.
- [96] J. J. Snyder, P. Reichert, and T. M. Baer. *Fast diffraction-limited cylindrical microlenses*. *Applied Optics*, 30(19):2743–7, 1991.
- [97] S. Yamakawa, T. Kinoshita, K. Sasaki, and T. Taniuchi. *Design and analysis of monolithic Q-switch $\text{Nd}^{3+}:\text{YLF}$ waveguide laser using poled-polymer film as guiding layer*. *Electron. Commun. Jpn. 2*, *Electron. (USA)*, 81(2):9, 1998.
- [98] T. M. Pollak, W. F. Wing, R. J. Grasso, E. P. Chicklis, and H. P. Jenssen. *CW laser operation of $\text{Nd}:\text{YLF}$* . In *CLEO '81. Conference on Lasers and Electro-Optics, 10-12 June 1981*, volume QE-18 of *IEEE J. Quantum Electron. (USA)*, pages 159–63, Washington, DC, USA, 1982.
- [99] L. McDonagh, R. Wallenstein, R. Knappe, and A. Nebel. *High-efficiency 60W TEM_{00} $\text{Nd}:\text{YVO}_4$ oscillator pumped at 888 nm*. *Optics Letters*, 31(22):3297, 2006.
- [100] Espen Lippert, Stephane Nicolas, Gunnar Arisholm, Knut Stenersen, and Gunnar Rustad. *Midinfrared laser source with high power and beam quality*. *Applied Optics*, 45(16):3839, 2006.
- [101] M. Schellhorn. *Performance of a $\text{Ho}:\text{YAG}$ thin-disc laser pumped by a diode-pumped 1.9 μm thulium laser*. *Applied Physics B-Lasers and Optics*, 85(4):549, 2006.
- [102] Norman P. Barnes, Elizabeth D. Filer, Clyde A. Morrison, and Chang J. Lee. *$\text{Ho}:\text{Tm}$ lasers I: theoretical*. *IEEE J Quantum Elect.*, 32(1):92, 1996.
- [103] Chang J. Lee, Gooywan Han, and Norman P. Barnes. *$\text{Ho}:\text{Tm}$ lasers II: experiments*. *IEEE J Quantum Elect.*, 32(1):104, 1996.
- [104] J.I Mackenzie, Cheng Li, D. P. Shepherd, R. J. Beach, and S. C. Mitchell. *Modeling of high-power continuous-wave $\text{Tm}:\text{YAG}$ side-pumped double-clad waveguide lasers*. *IEEE J Quantum Elect.*, 38(2):222–230, 2002.

- [105] Christelle Kieleck and Antoine Hirth. *Investigations of a Q-switched Ho:YAG laser intracavity-pumped by a diode-pumped Tm:YLF laser*. In *Solid State Lasers and Amplifiers*, Apr 27-29 2004, volume 5460 of *Proceedings of SPIE - The International Society for Optical Engineering*, pages 56–63, Strasbourg, France, 2004. *International Society for Optical Engineering*, Bellingham, WA 98227-0010, United States.
- [106] Yen-Kuang Kuo and Yi-An Chang. *Numerical study of passive Q switching of a Tm:YAG laser with a Ho:YLF solid-state saturable absorber*. *Applied Optics*, 42(9):1685, 2003.
- [107] Yen-Kuang Kuo, Man-Fang Huang, and Milton Birnbaum. *Tunable Cr^{4+} :YSO Q-switched Cr:LiCAF laser*. *IEEE J Quantum Elect.*, 31(4):657, 1995.
- [108] A.E. Siegman. *Lasers*. University Science Books, 1986.
- [109] Z. Xiong, Z. G. Li, N. Moore, W. L. Huang, and G. C. Lim. *Detailed investigation of thermal effects in longitudinally diode-pumped Nd:YVO₄ lasers*. *IEEE J Quantum Elect.*, 39(8):979, 2003.
- [110] R.J. Collins and P. Kisiuk. *Control of inversion population in pulsed optical masers by feedback modulation*. *Journal of Applied Physics*, 33(6):2009–2011, 1962.
- [111] R. Scheps and J. F. Myers. *Performance of a diode-pumped laser repetitively Q-switched with a mechanical shutter*. *Applied Optics*, 33(6):969, 1994.
- [112] W. A. Clarkson. *Thermal effects and their mitigation in end-pumped solid-state lasers*. *Journal of Physics D-Applied Physics*, 34(16):2381–2395, 2001.
- [113] P. A. Budni, C. R. Ibach, S. D. Setzler, E. J. Gustafson, R. T. Castro, and E. P. Chicklis. *50-mJ, Q-switched, 2.09- μm holmium laser resonantly pumped by a diode-pumped 1.9- μm thulium laser*. *Optics Letters*, 28(12):1016–18, 2003.
- [114] S. Bjurshagen and R. Koch. *Modeling of energy-transfer upconversion and thermal effects in end-pumped quasi-three-level lasers*. *Applied Optics*, 43(24):4753, 2004.